A study of the fatigue life of an aluminium alloy with particular reference to buckling.

Wyse, R. J.

Award date:
1970

Awarding institution:
University of Bath

A STUDY OF THE FATIGUE LIFE OF AN ALUMINIUM ALLOY WITH PARTICULAR REFERENCE TO BUCKLING

submitted by R.J. Wyse
for the degree of Ph. D.
of the Bath University of Technology
1970

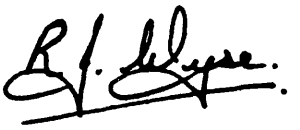

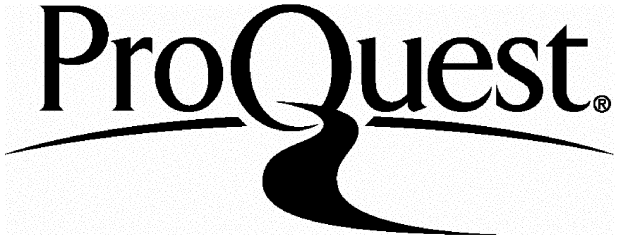

SUMMARY

The thermal fatigue problem associated with the operation of supersonic transport aircraft has been studied, both analytically and experimentally, by mechanical simulation of the thermal stress conditions, with particular respect to the effect of displacement controlled buckling on the fatigue life of simple notched sheet coupon specimens.

The design and manufacture of a special fatigue testing machine is described, in which the sheet specimens were subjected to constant amplitude displacement controlled cycling over a range of mean displacement, including various degrees of buckling. A comprehensive programme of tests on buckling and non-buckling strut specimens, at both room temperature and a constant elevated temperature of 150°C, is reported.

A simple analysis of the displacement controlled buckling of a slender encastré strut has been satisfactorily developed, and the effects of initial curvature and end alignment errors are shown to alleviate the peak stress conditions applicable to an initially straight perfectly aligned strut.

Using the stress-displacement relationships derived from this theoretical buckling analysis, which have been correlated with experimentally measured stresses, two methods of fatigue life prediction are compared, and the results are correlated with the fatigue lives achieved in the experimental investigation. From this correlation, three main conclusions are drawn:

(i) Accurately determined surface stresses are essential in order to achieve realistic fatigue life predictions for a buckling strut.

(ii) Cyclic buckling does not of itself introduce any significant life reduction phenomenon.

(iii) The mode of failure of a buckling strut changes as the cyclic buckling is made more significant, and it tends towards a finite fatigue life with increasing compression.

Examination of related work on thermal fatigue testing demonstrates the damaging influence of cyclic temperatures and the differences between thermal stress and mechanical stress fatigue.

CONTENTS

NOTATION

	A	Cross sectional area
	E	Young's modulus
	E_s	Secant modulus
	I	Moment of inertia
	K	Stiffness
	K_t	Elastic stress concentration factor
	L	Strut length
	M	Bending moment
	$\overline{M}$	Bending moment due to unit specimen load
	P	End load
	$\overline{P}$	End load due to unit specimen load
	Q	End displacement
	R	Radius of curvature
	X	Redundant load
	a	Length
	b	Central lateral deflection
	c, m	End alignment parameters
	e	Axial strain
	h	Half thickness of strut
	i, n	Integers
	s	Length
	x	Displacement
	x, y	Co-ordinate axes
	α	Specimen displacement accuracy tolerance
	δ	Relative displacement
	σ	Stress
	θ	Angle
Suffices:	o	Original conditions, unit specimen load
	1	Current conditions, unit redundant load
	1, 2, 3	Redundant loads
	A, B, C	Channel identities
	m	Machine
	s	Specimen

1.0 INTRODUCTION

This investigation forms part of a complex research programme into the behaviour of aluminium alloy structures subjected to the operating environment of supersonic transport aircraft, and has particular reference to the "Concorde". The occurrence of relatively high temperature differences throughout the aircraft structure, due to kinetic heating of skin surfaces at supersonic speeds, introduces structural behaviour phenomena which are rarely present in the operation of subsonic aircraft. These phenomena may be classified into four broad categories:

(i) the effect of temperature on material properties;

(ii) creep and its interaction with fatigue loading;

(iii) thermal stress as a loading action due to temperature gradients;

(iv) thermal fatigue caused by the cyclic variation of temperature.

The work reported was confined to making a contribution towards the understanding of category (iv).

Typical temperature and thermal stress variations of the aircraft skin and internal structure are shown in Figures 1.1 and 1.2, the temperature gradients and resultant thermal stresses being caused by relative masses, joint conductivities, shielding etc., which are likely to be most severe in wing masked areas of the fuselage and at the centre of deep webs in the wing structure, as indicated in Figure 1.3. The magnitude of the compressive thermal stress in the internal structure during deceleration introduces the possibility of local buckling, which may significantly alter the shape and magnitude of the stress variation of the unstable element. Local buckling having occurred, a stress redistribution to adjacent elements takes place until equilibrium is reached, in which the resultant additional compressive displacement causes lateral deflection of the centre of the buckled element. This may result in significant bending stresses being produced on opposite surfaces of the buckled element. The possible shape of the final stress variation of the unstable element is shown in Figure 1.4.

This unfavourable thermal stress cycle may be eliminated in some instances by the use of open braced shear webs or by

corrugated panels; in the latter case the thermal stress is relieved by bending of the curved surfaces of the corrugations, rather than by buckling of a straight element. Both these techniques may result in penalties of weight and fabrication complexity, and the use of corrugations is likely to concentrate the buckling effect into the edges of the corrugated sheet, where a joint with another member is made. In addition, structures such as pressure bulkheads and fuel tank walls require continuous structure and these solutions are often unacceptable. These structures therefore have an additional factor to be included in their design criteria: that of requiring a safe life under fatigue conditions caused by cyclic thermal stresses.

In order to determine whether or not this thermal stress fatigue problem could be handled using existing mechanical stress fatigue data, environmental fatigue tests on idealised structures have been performed, of which the two major tests are summarised below:

(i) I section beam and panel tests

The deep web structure of the wing was idealised into a simple I section as shown in Figure 1.5, which was then subjected to an idealised thermal cycle similar to that shown in Figure 1.1, where the flanges represented the external skin and the web represented the internal structure. No mechanical loads were applied, so that the stress cycle measured at the centre of the web of $-3,000$ lb.f./in.^{2} $\pm$ 14,300 lb.f./in.^{2} (tension +ve) was produced entirely by thermal effects, the high compressive stress during cooling being associated with severe web buckling. A life of 62,000 cycles was predicted from cold fatigue coupon tests, but the first crack at the edge of an unloaded hole in the web was observed after 12,000 cycles, the entire web failing after 18,500 cycles. Further tests on three similar structures, including panels, have been made, from which average life reduction factors on the predicted cold fatigue life of 6 for I section beams and 12 for skin-stringer panels under thermal cycling have been observed.

Environmental fatigue tests on small notched sheet coupon

specimens in tensile creep and fatigue conditions had shown a life reduction factor of between 2 and 3, and it was suggested that the further life reduction may be associated with the cycling buckling in the compression phase of the cycle.

(ii) Fuselage side panel tests

The wing masked area of the fuselage was idealised into a three bay skin-stringer panel as indicated in Figure 1.6, and tested under thermal cycling conditions, using a three stage heating and cooling cycle:

Stage 1: outer bays 1 and 3 were heated with radiant lamps.

Stage 2: inner bay 2 was heated with radiant lamps while the outer bays 1 and 3 were cooled with refrigerated air.

Stage 3: inner bay 2 was cooled with refrigerated air.

Very severe buckling of the inner bay skin was observed, and failure occurred due to cracking through a line of spot welds between the skin and a reinforcing plate, where the measured stress cycle was $2,000 \text{ lb.f./in.}^2 \pm 12,400 \text{ lb.f./in.}^2$. The predicted life, from room temperature tests on coupon specimens, was 60,000 cycles compared with an experimental life of 8,000 cycles, giving a life reduction factor of 7.5.

As a result of these tests a fundamental research programme was designed to investigate the thermal fatigue behaviour of this material, with particular respect to the effect of repeated buckling in compression. This programme was divided into two major sections:

(i) thermal cycling of coupon specimens, to be undertaken by the British Aircraft Corporation Ltd., at Filton (subsequently conveniently referred to as B.A.C.);

(ii) mechanical cycling of coupon specimens at room temperature and at constant elevated temperature, undertaken by Bath University of Technology, which is the work described in this report.

This particular division of the research was as a result of previous experience of thermal cycling, which had indicated the need for very long cycle times in order that a reasonable minimum temperature could be achieved without the use of expensive forced cooling equipment. Consequently, on grounds of time and cost, the present work was devoted to the mechanical simulation of the thermal stress cycle with a much shorter cycle time.

With totally unrestrained structural elements, the temperature cycle shown in Figure 1.1 would cause a thermal expansion of the skin relative to the internal structure during the acceleration phase, and a relative thermal contraction during the deceleration phase. However, since the structural elements are coupled, the internal structure restrains the relative thermal expansion and contraction of the skin to some degree, such that the skin is subjected to a compressive strain and the internal structure is subjected to a tensile strain during acceleration, and the situation is reversed during deceleration. With an elastic structure, these thermally induced strains result in the thermal stress variations shown in Figure 1.2. Fatigue critical areas are generally those containing some local stress concentration which may produce local plasticity and creep when subjected to the thermal stress cycle of Figure 1.2. Strain hardening or softening properties of the material may also contribute to local stress redistribution so that the local thermal stress variation becomes non-elastic and history dependant, and not as the elastic curve shown in Figure 1.2. However, since the origin of the loading action is the constant amplitude temperature cycle, even the locally non-elastic structural elements are subjected to a constant amplitude thermal strain cycle and the fatigue problem becomes one of cyclic strain fatigue rather than cyclic stress fatigue. Thus the experimental investigation has to be made in a special fatigue testing machine using strain or displacement controlled cycling, and theoretical estimates of cyclic stress levels for fatigue life predictions must be made on a displacement basis, rather than the usual load basis.

At the beginning of the investigation a literature survey of the published work on thermal fatigue was made and is included in Appendix 1; the main findings are briefly summarised below:

(i) materials tested: stainless and other special steels, titanium, nickel, aluminium alloy.

(ii) test temperatures: 300°C to 600°C.

(iii) an empirical relationship was derived by Coffin of the form:-

$$N^{K}\Delta\varepsilon_{p} = C$$ where N = no. of cycles to failure

$\Delta\varepsilon_{p}$ = plastic strain per cycle

K, C = material constants

The value of C varied between 0.043 and 1.91 while K varied between 0.35 and 0.82 for the range of materials tested.

(iv) for a given number of cycles to failure, more plastic strain could be sustained under load cycling than under thermal cycling; for nickel 21 times, for steel 2.3 times. No reasons for these differences are given.

At the time of this literature survey (September, 1965), little work had been published on aluminium alloys at temperatures relevant to the operating conditions of the Concorde; also the design of test specimens had been such as to avoid buckling in compression. These findings tended to underline the relevance of the work undertaken at Bath University.

The work of this investigation was divided into five principal sections:

(i) theoretical analysis of the buckling behaviour of an unstable structural element;

(ii) prediction of fatigue lives from theoretical stress levels;

(iii) design and manufacture of a special fatigue testing machine;

(iv) execution of an economic test programme;

(v) correlation of predicted and experimental fatigue lives and the application of these results to other thermal fatigue tests.

Figure 1.7 indicates in block diagram form the subjects covered in this report and the manner in which they are related so as to contribute towards the understanding of the problems of thermal fatigue.

2.0 THE DESIGN, MANUFACTURE AND COMMISSIONING OF A DISPLACEMENT CONTROLLED FATIGUE TESTING MACHINE

2.1 INTRODUCTION

In order to achieve both a reasonably short test period and to highlight the anticipated phenomenon, a fairly severe constant amplitude strain cycle of $\pm$0.2% over a range of mean strain from +0.2% to -0.2% was selected. A constant elevated temperature was selected at 150°C since considerable creep and mechanical strength data on the standard Concorde material CM001 sheet was already available at that temperature. The design of the fatigue testing machine was then based on the following requirements:

(i) displacement controlled cycling of sheet coupon specimens.

(ii) generation of a constant amplitude displacement cycle over a range of mean displacement.

(iii) slow speed cycling to avoid dynamic effects within both the machine and the specimen, but with the ability to easily vary the cycling speed.

(iv) the ability to maintain the specimens at a constant elevated temperature of 150°C.

(v) the ability to perform reversed cycling without backlash at zero load.

(vi) the ability to test three specimens simultaneously under nominally identical conditions.

(vii) an approximate sine wave displacement curve to represent the idealised internal structure thermal strain cycle, corresponding to the thermal stress cycle shown in Figure 1.4.

(viii) the facility to monitor test conditions in order to determine the peak specimen stresses.

A review of several simple loading and deforming techniques was made to select the system most suited to the design requirements; also to manufacturing simplicity and cost.

(i) dead weight system, in which the dead weight is applied to and removed from the specimen by the cycling unit. A possible arrangement using pulleys and counterbalanced weights to provide reversed cycling, is indicated in Figure 2.1.

(ii) coiled spring system, in which the specimen is loaded by cyclic straining of a coiled spring. A possible system using preloaded springs to provide reversed cycling and physical stops to provide displacements limitations is indicated in Figure 2.2.

(iii) resonating spring system, e.g. the Vibraphore machine, which operates between approximately 2,000 to 8,000 cycles/minute.

(iv) rotating crank, or cam with a follower linked to the specimen, producing a displacement cycle.

(v) hydraulic system, using an approximate servo feedback system.

(vi) motorised screwjack, with an approximate servo feedback system.

Techniques (i) and (iii) were unable to produce the required displacement cycle; in addition, the cycling speed of (iii) was excessive for this application. Techniques (v) and (vi) required expensive auxiliary equipment and a servo feedback channel for each specimen. A preliminary specification for a hydraulic system with servo feedback had an estimated cost of £3,500 per unit of three channels. A rotating cam and follower system was preferred to a coiled spring system with physical stops since it was more suited to the basic design requirements, giving simplicity of design and manufacture, and hence low cost.

2.2 THEORETICAL BASIS FOR DESIGN

Under test, specimen displacement is the difference between the input displacement and the testing machine displacement due to the application of the specimen load. For totally elastic conditions, a unique relationship between load and displacement exists for both the specimen and the machine, and the ratio of the specimen displacement

to the input displacement is of a constant value. However, under fatigue cycling, microscopic stress concentrations in a plain specimen, and the deliberate stress concentration in a notched specimen cause local yielding and plasticity, and under high temperature conditions, the occurrence of creep further destroys the overall elastic behaviour of the specimen. These two phenomena cause the specimen load to be history dependent and the ratio of specimen displacement to input displacement to be no longer of a constant value. Thus during a fatigue test with a constant amplitude input displacement cycle, the specimen displacement cycle amplitude varies throughout the test as a result of the effect of the history dependent specimen load on the testing machine displacement cycle amplitude.

A suitable feedback system could be used to adjust the amplitude of the input displacement cycle to maintain a constant amplitude specimen displacement cycle, but such a system would be both complex and expensive and would also be dependent on the sensitivity of the displacement measuring equipment, which would be required to determine small changes in an already small quantity.

Alternatively, the specimen displacement cycle amplitude may be maintained effectively constant by designing the testing machine to have a very high stiffness, so that it suffered negligible displacement under all specimen loads. Although absolutely infinite stiffness is not a practical proposition, by accepting a small finite accuracy tolerance on the specimen displacement cycle amplitude, a ratio of required machine stiffness to specimen stiffness may be derived to assist in the design of an acceptable testing machine. Considering the idealised displacement controlled testing machine shown in Figure 2.3, where spring 's' represents the specimen and spring 'm' represents the machine,

$$P_s = K_s x_s = P_m = K_m x_m$$

and $$x = x_s + x_m$$

hence $$x_s = x . \frac{K_m}{K_m + K_s}$$

$$\text{or} \quad \frac{x}{x_s} = \frac{K_s}{K_m} + 1$$

For a finite accuracy tolerance of α %:

$$\frac{x}{x_s} = \frac{100}{100 - \alpha} = \frac{K_s}{K_m}$$

$$\text{i.e.} \quad \frac{K_s}{K_m} = \frac{\alpha}{100 - \alpha}.$$

For a testing machine fabricated from n components:

$$x_m = \frac{P}{K_1} + \frac{P}{K_2} + \ldots\ldots + \frac{P}{K_n}$$

$$= P\left[\frac{1}{K_1} + \frac{1}{K_2} + \ldots\ldots \frac{1}{K_n}\right] = \frac{P}{K_m}$$

$$\text{i.e.} \quad \frac{1}{K_m} = \sum_{i=1}^{n} \frac{1}{K_i}.$$

For an overall accuracy tolerance of α %, and each component designed to the same tolerance, then:

$$\underline{\underline{K_i = \frac{n(100 - \alpha).\ K_s}{\alpha}}}$$

Considering the component 4 of the possible practical arrangement of a simple testing machine indicated in Figure 2.4, and assuming that it suffers axial loading only,

$$K_4 = \frac{A_4 \cdot E_4}{L_4} \; ; \; K_s = \frac{A_s \cdot E_s}{L_s} \; ; \; n = 6$$

$$\text{thus} \quad A_4 = A_s \cdot \frac{6(100 - \alpha)}{\alpha} \cdot \frac{E_s}{E_4} \cdot \frac{L_4}{L_s}$$

$$\text{For } \alpha = 1\% \qquad \underline{\underline{A_4 = 594 \cdot A_s \cdot \frac{E_s}{E_4} \cdot \frac{L_4}{L_s}}}$$

This simple analysis indicates the degree of difficulty of achieving a highly accurate specimen displacement cycle and indicates that the force loop around the specimen must be maintained as short as possible.

$$\text{i.e.} \quad L_4 \simeq L_s$$

In practice however, L_4 is likely to be considerably greater than L_s in order to introduce the strain input mechanism; with $L_4 = 2L_s$

$$A_4 = 1088 \cdot A_s \cdot \frac{E_s}{E_4}$$

In this particular application, some relief is afforded by the ratio of the Young's Moduli: for an aluminium alloy specimen and steel machine, the ratio is approximately equal to 0.3.

$$\text{Hence } A_4 \simeq 326\ A_s$$

For α = 5%, the appropriate area ratio $\frac{A_4}{A_s}$ becomes equal to 68.5, a more practical figure. The testing machine must still be of quite massive proportions.

2.3 PRACTICAL CONCEPT

The original B.A.C. Test Schedule[5] specified a sheet specimen having a working area 6" x 6" to represent part of a deep web. This was modified to 10" x 2" x 0.069" thickness to enable a large overall displacement to be used with a relatively low load. The $\pm$ 0.2% strain amplitude on the 10" long specimen resulted in an overall elastic displacement amplitude of $\pm$ 0.020" and a corresponding load amplitude of $\pm$2,800 lb. f. A mechanical lever system with a 50:1 displacement magnification was used to link the specimen to the rotating cam, resulting in a cam displacement of $\pm$ 1.00", and enabling a high degree of accuracy of the input displacement cycle to be achieved. This lever system also reduced the cam face loads to $\pm$ 56 lb. f.

The combined requirements of low cost and the ability to test three specimens simultaneously under nominally identical conditions suggested that they should be loaded by a common cycling unit ; three displacement channels were positioned radially around a central cam unit, each being placed 120^{o} apart from the other two. The general arrangement of the resulting testing machine is shown in Figures 2.5 and 2.6. This physical arrangement had four particular advantages:

(i) all three specimens were subjected to the same input displacement cycle.

(ii) the maximum load on the machine frame was reduced by the out of phase loading of the three specimens.

(iii) the three dimensional machine frame was stiffer than a two dimensional frame constructed from the same sections.

(iv) all the specimens could be enclosed by a single cylindrical furnace, for the elevated temperature tests, as shown in Figure 2.6 .

2.4 STRUCTURAL ANALYSIS

The complete testing machine was analysed using the unit load theorem in order to determine the overall machine displacement, and by comparison with the specimen displacement, to determine the machine to specimen stiffness ratio and specimen displacement accuracy tolerance. The testing machine displacement was calculated from the expression:

$$\delta = \int \frac{M\bar{M}}{EI}\, ds + \int \frac{P\bar{P}}{AE}\, ds$$

having first determined the redundant loads and the complete bending moment and end load distributions. This analysis is described in detail in Appendix 2.

The above expression may also be used to assist in the initial detail design before determination of the redundant loads if the assumption can be made that the effect of these redundant loads on the moment and end load distributions is negligible.

i.e. $M \simeq \bar{M}$ and $P \simeq \bar{P}$

Hence $$\delta \simeq \int \frac{\bar{M}^2}{EI} ds + \int \frac{\bar{P}^2}{AE} ds.$$

The value of the redundant load calculated in Appendix 2, as 0.627% of the specimen load, supports the validity of this assumption for this particular structure. Hence the basis for initial detail design was to match the variations of $\bar{M}^2$ and I, $\bar{P}^2$ and A and also to achieve a 1% component displacement. Figures 2.11 and 2.14 show the relevant variations around the machine frame and mechanism respectively, indicating good agreement, at least in shape.

2.5 DETAIL DESIGN

The design work described in this section is of components that required detail design in addition to that performed in the structural analysis of the machine frame and mechanism, which came under three headings:

(i) specimen holders

(ii) bearings

(iii) drive unit

2.5.1 Specimen Holders

The specimen holders were designed on the past experience of the grips of the Vibraphore fatigue testing machines, where the specimen load is applied through shear on tightly clamped faces.

The clamping bolts pass through oversize holes in the specimen to ensure that it is not loaded locally by contact with the bolt. The dimensions of the specimen holders, shown in Figure 2.23, were largely dictated by the physical dimensions of the available structural steel bolts capable of producing the necessary clamping force to resist slipping movement of the specimen. These dimensions result in a strain of 103.6×10^{-6} in the specimen holders under the action of the design maximum specimen load of 7,000 lb.f. This strain was used to monitor the peak stress levels in the specimen under fatigue testing conditions, which is descibed in Section 3.3.3.

2.5.2 Bearings

The service conditions of the bearings in the lever system of high reversed load, slow movement and minimal rotation proved to be too arduous for ball races, roller bearings and needle rollers, due to the likelihood of fretting. Metal backed rubber bushes were also considered but rejected as being unable to provide the necessary radial stiffness, Glacier D.U. dry plain bearings being selected as the only reasonable solution.

To meet the requirement of zero backlash during load reversal, each bearing was designed as a preloaded unit with a split housing, as shown in Figure 2.23, splitting the wrapped bearing shells to form semi-cylindrical bearing caps. The two halves of the bearing housing were assembled using specially waisted bolts, which performed two functions:

(i) they produced a preload in excess of the maximum bearing load ensuring positive contact between the bearing and journal during load reversal.

(ii) the elastic extension of the waisted section of the bolt allowed the anticipated wear of the bearing shells to be taken up without reducing the preload to below its design value.

Reference was made to a paper concerned with the theoretical torque-tension relationships of bolts[6], but the large number of unknown

factors made it unsuitable for practical design purposes. Consequently, the torque-tension relationship for these special bolts was determined experimentally to ensure that the specified tension could be achieved in each bearing housing. Typical torque-tension curves are shown in Figure 2.19.

2.5.3 Drive Unit

The drive unit, shown in Figure 2.21, consists of a $\frac{1}{2}$ H.P. electric motor driving a single circular profile cam through a 60:1 reduction gearbox. Different cycling speeds are achieved by the use of different pulleys between the motor and gearbox. Three cam followers are spring loaded against the cam face which transmit the input displacement cycle to the ends of the three lower levers through steel slides in phosphor bronze guides. A turn-buckle enables various mean displacements to be applied to the lever system. In order to achieve a very long service life for the drive unit, a number of detail design points were considered:

(i) the common spring attachment point, for preloading the cam followers, was positioned at the centre of the cam, rather than at the centre of rotation, in order that the cyclic straining of the springs would be a minimum, ensuring a long life for the springs and both their attachment points.

(ii) the spring tensioning bolts and the bearing cap common spring attachment point were case hardened to resist wear and fretting fatigue due to the slight rotation of the springs in their location holes.

(iii) the cam face was machined as a ring, case hardened and ground to a circular profile before being assembled onto the cam body.

(iv) steel and phosphor bronze were used as slider and guide, with brass strips being used to retain the slider in the guide. These strips were readily replaced when appreciable wear had occurred.

2.5.4 Manufacturing Drawings

Manufacturing drawings of the entire fatigue testing machine, reproduced in Figures 2.20 to 2.28, were prepared by a consultant designer from detailed drawings, showing all the major design features, prepared by the author.

2.5.5 Manufacture

Since the stiffness of a normal bolted joint is likely to change when subjected to reversed loading, unless it is correctly preloaded, it was decided to use welding as the major fabrication technique for the machine frame and the mechanism levers to ensure constant stiffness during operation. Stress relieving after welding was used to reduce the possibility of residual stresses, produced during welding, affecting the machine stiffness; this process was the major cause of an eleven week delay in final delivery.

The bearing journals were shrink fitted into the levers by immersing the journals for ten minutes into a solution of solid carbon dioxide dissolved in acetone before hand fitting into the corresponding bores.

In all other respects the manufacture of two units of three channels each was quite straightforward, and was completed within six months of the date of placing the contract for manufacture.

2.5.6 Specimen Manufacture

The specimens were cut from 1.6 mm. sheet along the direction of rolling and milled to size in batches of three. A small drilling jig, shown in Figure 2.29, was manufactured and used to position the central stress concentration, the oversize clamping bolt holes and the location holes for accurate alignment of the specimens in the lower specimen holder.

2.6 CALIBRATION

After final assembly of the machines in the laboratory and an initial period of running in, the two machines were calibrated to determine the degree to which the design specification had been

achieved, in terms of specimen displacement accuracy and the accuracy of the specimen temperature distribution. It was later discovered that the specimen displacement accuracy calibration had been performed incorrectly, so it was repeated at the end of the test programme. The results of this later calibration are reported here.

2.6.1 Input Displacement Cycle

The displacement cycle produced by the circular profile cam is shown in Figure 2.30 and compared with a true sine wave, fulfilling one of the design requirements of Section 2.1. In Figure 2.30A, the two curves are compared on a rotation basis, indicating that the circular profile cam produces a significantly larger displacement in compression than in tension. This was adjusted by arranging for the locating pin in the drive unit slider and guide to make the neutral position at mid displacement rather than at 0^{o} rotation. The resultant displacement curve with equal amplitudes in tension and compression is again compared with a sine wave in Figure 2.30B.

2.6.2 Specimen Displacement Accuracy Tolerance

The calibration of each channel was carried out by determining the relationship between input and output displacements under three conditions:

(i) without a specimen

(ii) with a specimen restrained from buckling

(iii) with a specimen free to buckle

Test (i) was used to determine the true geometric lever ratio, including the effects of manufacturing tolerances on the lever dimensions and friction within the preloaded bearing units. This latter effect could not be readily assessed during the design stage due to a lack of relevant information. Test (ii) determined the lever ratio with the levers loaded, by including lever and machine frame deflections, the loading being nominally identical in tension

and compression by restraining the specimen from buckling and allowing the full compressive load to be developed. Test (iii) determined the change in lever ratio from tension to compression when the buckling of the specimen restricted the compressive load to a relatively low value, such that the testing machine deflections were insignificant compared with those produced in the tension phase. Typical calibration curves are shown in Figure 2.31, the result of test (iii) being vertically displaced for clarity, and the results for all six channels are summarised in Figure 2.32.

2.6.3 Temperature Distribution

To achieve a temperature distribution with a low gradient over the centre section of the specimen, a series of tests was made, in which the following parameters were varied:

(i) the number of quartz infra red heater elements.

(ii) the position of the heater elements relative to the specimens.

(iii) the masking of the heater elements to modify the output temperature distribution.

(iv) the masking of the specimens with black heat resistant paint to vary the heat absorption along the specimen.

In addition, the specimen setting up procedure required a situation that resulted in little change in temperature distribution due to the bolting up of the top end of the specimen, with the specimen hot. The temperatures were measured at twelve positions using chromel-alumel thermocouples and an ice-water cold junction, the thermocouple outputs being measured on a null-point potentiometer bridge. The thermocouples themselves were regularly calibrated against accurate thermometers using an oil bath held at 150^{o}C and the ice-water cold junction.

A typical temperature distribution for a straight specimen is shown in Figure 2.33, indicating a reasonably flat distribution, particularly along the centre line with the hole being within $\pm$ 2^{o}C of the specified temperature. During buckling tests the lateral

displacement of the centre of the strut towards the heater elements caused a further cyclic temperature variation of $\pm 1.5^{o}C$. Figure 2.34, a photograph of the furnace with two panels removed, indicates the relative positions of the specimens and heater lamps, and the masking with black paint used to achieve the optimum temperature distribution.

2.7 INSTRUMENTATION

Three particular areas of instrumentation are described:

(i) fatigue life measurement

(ii) temperature control

(iii) specimen buckling conditions

2.7.1 Fatigue Life Measurement

The specimen fatigue lives were measured in terms of the number of cycles to complete failure, rather than to an arbitrary crack length, using six electric impulse counters. Each counter was associated with an automatic failure indicator: the breaking of a continuity wire attached across the minimum nett area of the specimen de-energised a relay which isolated the counter, preventing further cycles from being counted, although the fatigue testing machine continued to operate.

As this system is dependent on the tensile fracture of the continuity wire, it was not operative for tests that were largely compressive, where the crack propagation and total failure were checked visually. A diagram of the automatic system is shown in Figure 2.35.

2.7.2 Temperature Control

Since individual specimen temperatures fluctuated by approximately $\pm 1.5^{o}C$ during buckling, furnace control through a single thermocouple attached to the centre of one specimen resulted in a virtually unstable control loop, as the cycling speed was not

matched to the response speed of the controller. This problem was overcome by controlling on the mean temperature of the three specimens by using three thermocouples wired in parallel. Since the temperature fluctuations of the three specimens were out of phase by 120^{o}, this technique minimised the effect on the temperature controller and a long term temperature variation of the furnace as a whole of better than $\pm 1.0^{o}C$ was achieved. The controller, a 3 phase 21 KVA West Guardsman stepless unit with three saturable reactors, was tapped to 4 KVA and connected to six 1 KW heaters in parallel such that it controlled at approximately 40% of the maximum output, resulting in high sensitivity and a uniform temperature distribution over the centre of each specimen.

2.7.3 Specimen Buckling Parameters

In order to check the theoretical analysis of the buckling behaviour of a strut under displacement controlled conditions, presented in Section 3, the behaviour was determined experimentally in Channel No. 1, using the instrumentation shown in Figure 2.36. Specimen end load was measured using a four arm fully active semi-conductor strain gauge bridge mounted on the minimum section of the upper specimen holder, the output being measured on an S.E.L. transducer/converter amplifier and a digital voltmeter. Surface strain measurements were made using wire strain gauges attached to the mid point of the specimen, their separate outputs being measured on a Tinsley strain measurement bridge. The results of the tests are reported and discussed in Section 3.

2.8 DISCUSSION

Several significant features of the design work are discussed in this section, and a number of practical recommendations to improve the performance of the testing machine are made.

Theoretical Analysis

The structural analysis of the complete testing machine was performed using the unit load theorem (after the initial detail design had been completed), in order to determine the overall machine to specimen stiffness ratio and the theoretical specimen displacement accuracy tolerance. The detail design of the various components was based on an allowable deflection under load equal to 1% of the rotation or movement of the component during loading. For fixed components, in particular the machine frame elements, a deflection equal to 1% of the total specimen displacement was permitted.

The testing machine, idealised into a line diagram indicating the approximate neutral axes of the machine frame, as shown in Figure 2.7, was divided into two systems: a basic system of a single channel containing mechanism loads only, and a redundant system of three channels containing the redundant loads at the common centre joint, as indicated in Figure 2.8. The displacement analysis was based on the compatability of the relative displacements of the centre joint in the two systems of loading. Referring to Figure 2.8 and denoting:

δ as the relative displacement at joint F

δ_{10} as the relative displacement at joint F_1 with unit specimen load

δ_{11} as the relative displacement at joint F_2 with unit redundant load,

then $\delta = \delta_{10} + x\,\delta_{11} = 0$

where x = magnitude of the redundant load for unit specimen load.

δ_{10} and δ_{11} were determined by applying the unit load theorem to each system in turn, and the magnitude of the redundant load was determined from the compatability equation. The complete moment and end load distributions for the complete structure are given by

$$M = M_o + xM_1; \qquad P = P_o + xP_1,$$

and are shown in Figure 2.13, where

M_o and P_o are the moment and end load distributions of the basic system

M_1 and P_1 are the moment and end load distributions of the redundant system.

Application of the unit load theorem to the complete system, including the loading mechanism, enabled the relative displacement of the entire machine between the specimen holders to be determined, from which the overall machine to specimen stiffness ratio and specimen displacement amplitude accuracy were deduced.

Machine displacement $\delta_m = \int \frac{M\bar{M}}{EI}\, ds + \int \frac{P\bar{P}}{AE}\, ds$

i.e. $\delta_m = \int \frac{(M_o + xM_1)M_o}{EI}\, ds + \int \frac{(P_o + XP_1)P_o}{AE}\, ds$.

Specimen displacement $\delta_s = \frac{PL_s}{A_s E_s}$.

$$\text{Stiffness ratio} = \frac{\delta_s}{\delta_m}.$$

Accuracy of specimen displacement amplitude α is given by:

$$\alpha = \left(1 - \frac{\delta_s}{\delta_s + \delta_m}\right) \times 100\%.$$

Figure 2.18 lists the machine component displacements, from which

$\delta_m = 0.5224 \times 10^{-6}$ ins.

$\delta_s = 6.84 \times 10^{-6}$ ins.

Stiffness ratio = 13.1

$\alpha = 7.1\%$

Application of the displacement expression to the complete testing machine with the complete moment and end load distributions required the matching of the variations of MM_o and I, PP_o and A for the optimum design to minimise δ. Figures 2.15 to 2.17 indicate the variations in terms of $\frac{MM_o}{I}$, $\frac{PP_o}{A}$ indicating the components that contribute significantly to the overall machine displacement, as listed in Figure 2.18. Two components, the specimen holders and the machine frame side member, contribute approximately 75% of the total displacement and require particular comment. These two components form the major part of the force loop around the specimen, noted as a particularly critical part of the machine in Section 2.2, their comparatively large displacements being the result of having lengths considerably in excess of the specimen length. This feature was the result of a non-structural requirement; that of accommodating the furnace within this region, as shown in Figure 2.34.

The similarity of the total displacements of the machine frame and the mechanism, as indicated in Figure 2.18, is probably fortuitous, and no estimate of the contribution of the bearings has been included, due to a lack of information concerning the friction coefficient and the stiffness of the composite p.t.f.e./bronze/steel bearing shells. The effect of bearing friction is to oppose the movement of the mechanism and so increase the loads required to transmit the input displacement to the specimen, whilst the effect of the bearing radial stiffness is to contribute some small displacement to the overall machine displacement. The displacements for each of the bell crank lever main bearings are estimated as being less than half the displacement of the cam follower link, indicated in Figure 2.18. These have negligible effect on both the machine to specimen stiffness ratio and on the specimen displacement accuracy tolerance; hence the omission from the detailed analysis is of little significance.

Correlation of Experimental and Theoretical Stiffness Ratios

The calibration curves for all three test conditions, shown in Figure 2.31, indicate good linearity, the absence of backlash at

zero load, only a small hysteresis loop caused by bearing friction, and the change in response due to loads in the testing machine. The reciprocals of the slopes of the curves are equal to the effective lever ratios, which are the attenuation factors between the input displacement and specimen displacement amplitudes. Thus a decrease in slope implies a higher lever ratio due to the proportion of the input displacement amplitude lost as machine displacement. The slopes of the curves are equal to the actual specimen displacement amplitudes, and the difference between the slopes of tests (i) and (ii) is equal to the machine displacement under load. For the buckling condition, test (iii), which is displaced vertically for clarity, the response in tension is very similar to that of the loaded condition test (ii), while in compression the response approaches that of the unloaded condition, test (i), due to the low buckling load producing almost negligible machine displacements. Thus this calibration curve exhibits a significant change in slope at zero load, which implies an apparent change in machine to specimen stiffness ratio, but which is due to the change in loading condition. From these slopes, the machine to specimen stiffness ratios and specimen displacement accuracy tolerances have been calculated, and summarised in Figure 2.32.

The results for channels 1 and 4, which appear to be considerably different from the other four channels, are not fully representative as it was discovered that in both cases the preloading bolts at the lower end of the bell crank lever had released their design preload. This had the effect of reducing the frictional opposition to rotation, resulting in apparently higher stiffness ratios, even higher than the theoretical values, and a change in stiffness ratio at zero load. Had the calibration tests been correctly carried out at the beginning of the test programme, it is most likely that this fault would not have occurred. The fault also suggests that the torque of all preloading bolts should be checked frequently, and possibly that the bolts themselves should be replaced at regular intervals.

The variation of the results among the remaining four channels is reasonably small; the mean value of the stiffness ratio being 9.22

compared with the theoretical value of 13.1, and the mean value of the specimen displacement accuracy tolerance being 9.95% compared with a theoretical value of 7.1%. The differences between the theoretical and experimental values are the result of four major factors which are extremely difficult to quantify, and so are only discussed in a qualitative manner:

(i) errors in the theoretical idealisation of the machine, in particular the use of engineer's bending theory on large built up structures, and the location of the neutral axis of the frame side member in the built up region.

(ii) the omission of the effect of bearing friction on the load distribution throughout the machine.

(iii) the possible relaxation of the loads in the preloaded bolts to varying degrees, as discovered in channels 1 and 4.

(iv) the quasi-static method of machine calibration in which the displacement cycle was divided into 40 equal increments, the measuring dial gauges being read after each increment. In this way, the machine had to overcome static friction for each increment, rather than a continuous dynamic friction. Had it been practical to carry out a dynamic calibration test, the lower sliding friction would have permitted a greater specimen displacement, resulting in a higher machine to specimen stiffness ratio. In addition, a dynamic test would have been more relevant to the actual operation of the fatigue testing machine.

Although the effect of the bearing friction in producing the calibration curve hysteresis loop is in general fairly small, its practical effect, and its effect on (ii) and (iv) above, would be diminished by the replacement of the plain Glacier D.U. bearing shells by the later Glacier D.X. bearing shells. These bearings are of similar construction to the D.U. bearings except that the

p.t.f.e. bearing surface is liberally indented with small recesses for grease lubrication. It is anticipated that the use of these bearings would reduce the frictional effects throughout the machine and improve still further on its performance.

It is important to consider the implications of the derived values of the machine to specimen stiffness ratio and the specimen displacement accuracy on the performance of the machine as a fatigue testing device. Considering first the room temperature tests, the majority of the test conditions within the selected total strain range of +0.4% to -0.4% produce peak nett area stresses below the yield stress of the material and hence the overall displacement behaviour is elastic. Local plasticity may occur around the central hole and particularly in the vicinity of the tip of a propagating fatigue crack, but until this crack has propagated virtually the full width of the specimen, the bulk of the material remains elastic and the specimen stiffness remains constant. Thus in the crack propagation phase of a fatigue test, the machine to specimen stiffness ratio, and therefore the specimen displacement amplitude, remains constant until the very end of the test when the extreme fibres become plastic due to the high stress concentration factor associated with the crack tip. The fatigue crack does, however, have an adverse effect. Since the overall elastic displacement is maintained constant, the load is reduced in proportion to the loss of cross sectional area caused by the propagation of the fatigue crack. As a consequence of the reduction of load, the proportion of the input displacement absorbed by the machine is also reduced, so increasing the specimen displacement. From the crack propagation data presented in Figure 4.9, it may be observed that the crack length is less than 10% of the specimen width at 60% life, and that it does not reach 50% of the specimen width until 95% of the life has elapsed. Since the specimen displacement is changed by 9.95% by the load falling to zero (specimen displacement accuracy), at 60% life the load and machine displacement are reduced by 10% and the specimen displacement is increased by approximately 1%. Similarly at 95% life, the load and machine displacement are reduced by 50%, and the specimen displacement is increased by approximately 5%. Thus

for room temperature testing, the high relative stiffness of the machine to the specimen maintains the applied displacement conditions constant during the crack propagation phase, changes in excess of 5% only occuring in the last 5% of the fatigue life. This is in marked contrast to the situation when using a load controlled testing machine.

With elevated temperature tests, the occurrence of cyclic creep strain on nett cross sectional area in the highly stressed portions of the displacement cycle results in a reduction of the peak loads early in the fatigue life, and an overall depression of the cycle towards a lower stressed condition, as indicated in Figure 2.37. In addition to the slight increase in displacement amplitude due to the decreased loads, as discussed above, cyclic creep strain may also introduce the possibility of buckling in an otherwise unbuckled strut if the depression of the stress cycle takes it below the local buckling stress.

In the buckled condition, the load on the nett area is restricted to a low value, such that the effects of crack propagation and cyclic creep strain on nett area would have an insignificant effect on the cyclic displacement conditions.

2.9 CONCLUSIONS

A displacement controlled fatigue testing machine with a high relative stiffness to the fatigue specimen has been designed and manufactured, and calibration tests have demonstrated a good correlation with the theoretical idealisation and that all the initial design requirements have been met satisfactorily.

The high relative stiffness enables the machine to maintain a constant amplitude displacement cycle to a high order of accuracy throughout a fatigue test, including the crack propagation phase. Under room temperature conditions, changes in the displacement amplitude of the order of 5% are not produced until 95% of the total fatigue life has elapsed. Under constant elevated temperature conditions, cyclic creep strain depresses the mean load, but the displacement amplitude is held constant, as in the room temperature tests.

The low loads associated with buckling reduce these changes, so that the displacement conditions for a buckling strut are maintained even more accurately than for a non-buckling strut. This special testing machine therefore very accurately fulfills its design task, i.e. to provide a means of determining the effect of cyclic buckling on the fatigue life of an aluminium alloy under constant displacement amplitude cycling. The machine may also be used to investigate the fatigue behaviour of material adjacent to a severe stress concentration, where the input parameter is the elastic cyclic straining of the bulk of the material away from the stress concentration. Tests can also be carried out at both room temperature and constant elevated temperatures, enabling some aspects of creep fatigue interaction phenomena to be investigated.

3.0 A THEORETICAL ANALYSIS OF THE BEHAVIOUR OF A SLENDER ENCASTRÉ STRUT UNDER DISPLACEMENT CONTROLLED CONDITIONS

3.1 INTRODUCTION

This analysis investigates the relationship between applied end displacement, end load, buckling parameters and surface stress to assist in the analysis of large structures subject to thermal cycling, and to provide data for fatigue life prediction of the specimens used in the associated experimental programme.

The strut behaviour may be conveniently divided into two regimes: non-buckling behaviour in tension and in compression with suitable lateral restraint, and behaviour under buckling conditions.

3.2 NON-BUCKLING BEHAVIOUR

In this regime, the relationships between end displacement, end load and surface stress, under static conditions, are given simply by:

$$\text{displacement } Q = \pm \frac{PL}{AE_s},$$

$$\text{and } \sigma = \pm \frac{P}{A},$$

where the use of E_s includes loading beyond the elastic limit.

3.3 BUCKLING BEHAVIOUR

3.3.1 Conventional Approach

The conventional approach to the buckling problem has been to consider it as one of stability under load, where the critical load is such to cause the strut to maintain any slight increase in lateral deflection after the removal of the corresponding lateral load, the lateral deflection itself being an indeterminate quantity. This implies that the end displacement, which is geometrically related to the lateral deflection, is also an indeterminate quantity during buckling, so that this approach is of no value for the analysis of displacement controlled buckling conditions.

The indeterminate nature of the lateral deflection is the result of using the approximate expression for the curvature of a loaded strut:

$$\frac{1}{R} = \frac{d^2y}{dx^2},$$

and $$M = -EI\frac{d^2y}{dx^2}.$$

Use of the exact expression for curvature:

$$\frac{1}{R} = \frac{d\theta}{ds}$$

yields the precise shape of the curved strut, known as the "elastica". The solution involves the use of elliptic integrals and assessment of the effects of initial curvature and alignment errors is not easily handled, so a simpler approximate analysis has been made in order that practical cases may be conveniently analysed. The elastica solution, given in Ref. 7, has been retained as a comparison for an initially straight strut to assess the magnitude of error introduced by the assumptions made in the simpler analysis.

3.3.2 An Analysis of the Buckling Behaviour of a Slender Encastré Strut under Displacement Controlled Conditions

This analysis is given in detail in Appendix 3.

Geometric relationship

The geometric relationship between end displacement, central lateral deflection and end load is obtained by integration of an expression which considers the contribution to the end displacement and total compressive strain of a small elemental length of strut, as shown in Figure 3.1, where:

$$\delta Q = (\delta s - \delta x) - (\delta s_o - \delta x_o) + \delta e$$

where δQ = elemental contribution to the end displacement Q

δe = elemental contribution to the total axial compressive strain under the action of the associated end load P

Suffix o indicates the original unloaded curved condition.

Use of the approximate relationship:

$$ds = \left[1 + \left(\frac{dy}{dx}\right)^2\right]^{\frac{1}{2}} dx$$

and retention of only the first term in the expansion of the square root yields:

$$Q = \frac{1}{2}\int_0^L \left(\frac{dy}{dx}\right)^2 dx - \frac{1}{2}\int_0^{L_o} \left(\frac{dy_o}{dx}\right)^2 dx + \frac{P}{AE}\int_0^L dx$$

Determination of the end load

The end load is determined by the use of the engineer's bending theory expression and the appropriate boundary conditions. For an encastré strut with initial curvature, as shown in Figure 3.2:

$$M = -EI\left[\frac{d^2y}{dx^2} - \frac{d^2y_o}{dx^2}\right]$$

$$\text{also } M = P\left[y - \frac{b}{2}\right]$$

$$\text{thus } P = \frac{-EI}{\left[y - \frac{b}{2}\right]} \cdot \left[\frac{d^2y}{dx^2} - \frac{d^2y_o}{dx^2}\right]$$

Thus both the end displacement and end load are related directly to the assumed shape of the strut in the curved condition.

Alignment errors

The unloaded shape of an encastré strut with initial curvature, misalignment due to slope of the strut axis and due to parallel relative displacement of the strut ends, as shown in Figure 3.3, can be expressed as:

$$y_o = \frac{b_o}{2}\left[1 - \cos\frac{2\pi x}{L_o}\right] + \frac{c}{2}\left[1 - \cos\frac{\pi x}{L_o}\right] + mx$$

Assuming that the form of the strut is preserved on loading and that only the coefficients in the above expression vary, the loaded shape may be expressed as:

$$y = \frac{b}{2}\left[1 - \cos\frac{2\pi x}{L}\right] + \frac{c}{2}\left[1 - \cos\frac{\pi x}{L}\right] + mx,$$

c and m being independent of the loaded condition of the strut.

Application of these two expressions to the general expressions for end displacement and end load yields:

$$Q = \left[\frac{1}{1 + \frac{m^2}{2}}\right] \cdot \left[\frac{\pi^2}{4} \cdot \left(\frac{b^2}{L} - \frac{b_o^2}{L_o}\right) + \frac{c^2\pi^2}{16}\left(\frac{1}{L} - \frac{1}{L_o}\right) + \frac{PL}{AE}\right]$$

$$P = \frac{P_E \cdot \left[\frac{L_o^2}{L^2} - \frac{b_o}{b}\right]}{\left[1 + \frac{c}{b}\cos\frac{\pi}{4} + \frac{mL}{2b}\right]}$$

where $P_E = \frac{4\pi^2 EI}{L_o^2}$, the Euler load for an encastré strut.

Surface stresses

The surface stress on either face of the curved strut at mid length is given by:

$$\sigma = \frac{-P}{A} \pm \frac{Mh}{I}$$

i.e. $$\sigma = P_E\left[\frac{L_o^2}{L^2} - \frac{b_o}{b}\right] \cdot \left[\pm\frac{hb}{2I} - \frac{1}{A\left[1 + \frac{c}{b}\cos\frac{\pi}{4} + \frac{mL}{2b}\right]}\right]$$

Results

The above expressions were applied to a simple strut with the same physical dimensions as the specimen used in the experimental investigation, namely 10" x 2" x .069"; E having been determined as 10.575×10^6 lb.f./in.^{2}.

The separate effects of each of the alignment parameters on the

buckling behaviour of the simple strut are shown in Figures 3.4 to 3.7, and are compared with the behaviour of an initially straight strut in each case. In Figure 3.8 the effects of four combinations of alignment error are again compared with the behaviour of an initially straight strut; in each case the maximum value of each of the alignment errors used in Figures 3.4 to 3.7 has been taken to determine any significant interaction effects.

3.3.3 Discussion

Results of the simple buckling analysis

The analytical expressions relating the behaviour of an initially straight strut may be derived from the general expressions by putting the three alignment parameters equal to zero, i.e.:

$$Q = \frac{\pi^2 b^2}{4L} + \frac{PL}{AE}$$

$$\text{and} \quad P = P_E \cdot \frac{L_o^2}{L^2}$$

Thus the geometric relationship between the end displacement and the central deflection is parabolic, the offset from the origin shown in Figure 3.4 being the result of the compressive axial end displacement under the action of the Euler load. The end load expression implies that the end load in the buckled condition is equal to the theoretical Euler load for the strut reduced in length by the end displacement taken up by the buckle,

$$\text{i.e.} \quad P = \frac{4\pi^2 EI}{L_o^2} \cdot \frac{L_o^2}{L^2}$$

$$\text{i.e.} \quad P = \frac{4\pi^2 EI}{L^2}.$$

The effect of initial curvature is to reduce the effective stiffness of the strut, such that the end load is decreased for a given end displace-

ment, as shown in Figure 3.4. Since the end displacement and central deflection are related by a geometrical expression, the only effect of initial curvature is to cause a smaller axial compressive displacement due to the reduced end load. In Figure 3.4 the apparent central deflection, that is the measureable change in central deflection excluding the initial central deflection due to initial curvature, is plotted against end displacement, as this is the appropriate plot to compare with experimental results. The effects of axis slope and parallel displacement of the strut ends are similarly shown in Figures 3.5 and 3.6 where only the end load is significantly affected; in each case the end load is reduced in magnitude. The surface stresses produced in the initially straight strut are compared in Figure 3.7 with those produced in the struts with each of the alignment parameters, their highest values being used to highlight the effects. The initially straight strut stresses appear as a parabola with the horizontal axis displaced by the direct end load stress. The effect of a .050" initial deflection is to reduce the surface stresses by approximately 10% at .060" end displacement, while the effect of axis slope and parallel end displacement of similar magnitudes is to increase the stresses by approximately 2%, except at very small end displacements where the effect is larger.

Under experimental conditions, it is most likely for all three alignment parameters to be present in varying degrees, and it is almost certain that initial curvature will accompany either of the other two alignment parameters. Figure 3.8 shows the effects of four combinations of alignment errors, indicating that the end load is increasingly reduced by an increase in alignment errors. Case D is of interest in that the opposite signs of m and c simulate the situation of a strut with its ends in line but rotated with respect to each other. This causes the axis to assume a second mode buckled shape, increasing the effective stiffness and resulting in higher end loads than for the other combinations shown. However, the initial curvature term dominates the results, and the increase in surface stress due to axis slope and parallel end displacement is outweighed by the decrease in stress due to initial curvature, so that all the stress curves are virtually identical to the curve with initial

curvature only shown in Figure 3.7. Thus, for all practical cases, the initially straight strut produces the most severe surface stresses, the reduction due to alignment errors varying from 25% in the lightly buckled condition to 10% in the significantly buckled condition, for alignment parameters each equal to .050" on a 10" strut length.

Correlation with the elastica solution

The exact elastica and approximate cosine solutions to the buckling of an initially straight encastré strut are compared in Figures 3.9 and 3.10, in which the variations in end load, central deflection and surface stresses are plotted over a very much greater range of end displacement than that used in the experimental investigation. As anticipated with an approximate analysis, the cosine solution overestimates the increase in end load with increasing end displacement, the error being approximately 10% with an end displacement of 0.5". Over the experimental range of 0" to 0.040", however, the error is only 0.6%. The two central deflection curves are in very close agreement, the divergence of the cosine solution due to the overestimated axial compressive displacement only becoming discernible at a central deflection greater than 1.00". In Figure 3.10 the surface stress curves have been plotted for an end displacement range equal to twice the experimental range as the curves become unrealistic at an end displacement of approximately 0.15" due to the material yield point being reached. The two solutions agree very closely, the cosine solution having a typical error of 3% at 0.020" end displacement due to the overestimated end load.

It is therefore concluded that the approximate cosine solution to the buckling of an initially straight encastré strut correlates very well with the exact elastica solution, over ranges considerably larger than those used in this experimental investigation, although both solutions are limited for very large deflections by the assumption that the material remains elastic. The approximations made in the cosine solution, particularly the use of the engineer's bending theory expressions, introduce errors in surface stresses of only approximately 3%.

Correlation with experimental results

During the period of manufacture of the two fatigue testing machines, the buckling behaviour was briefly investigated in an Avery fatigue testing machine, using the mean stress screw adjustment to statically produce the specimen input displacement. Measurements of end displacement, apparent central lateral deflection and end load were made, the latter by the use of a calibrated load all mounted in series with the specimen. Similar tests were later carried out in Channel No. 1 of the special fatigue testing machines; end load in this instance being measured by the semi-conductor strain gauge bridge mounted on the upper specimen holder. The results of these tests are compared with the cosine solution in Figure 3.11.

The apparent central deflection v. end displacement curves for all tests correlate well with the cosine solution for an initially straight strut, indicating that the experimental initial central deflections were quite small and that the presence of a central hole in some specimens has no significant effect on the geometric relationship between end displacement and central deflection. The end load v. end displacement curves show considerably more variation, the Avery machine tests achieving between 88% and 77.5% of the Euler load for an initially straight strut. Since the method of gripping the specimen involved the use of tapered wedges, it is most likely that considerable end misalignment could have occurred, resulting in the lower end loads as predicted by the cosine solution, and indicated in Figures 3.5, 3.6 and 3.8. Other sources of error are variations in the free length of the strut, since the Euler load is inversely proportional to the square of the free length, and errors in the calibration of the load cell operating over only one twentieth of its normal working range. Within the scope of experimental accuracy, therefore, these tests indicate good correlation with the approximate cosine solution.

The end load v. end displacement curve for the test in Channel No. 1 shows a significantly different response in achieving a maximum of 58% of the Euler load and then decreasing with increasing end displacement. It is thought that this response is more a function of

the problems associated with the strain gauge bridge rather than implying considerable non-elastic specimen behaviour; the peak stresses are estimated to be -4,800 lb.f./in.^{2} on the concave surface and 2,300 lb.f./in.^{2} on the convex surface. Even with a theoretical stress concentration factor of 3.0, the maximum surface stresses are considerably lower than the material yield stress. Since the strain on the gross section of the specimen holder for the Euler buckling load was estimated as only 3.4 μ strain, the semi-conductor strain gauges were positioned on the minimum nett section, as shown in Figure 3.13, where the peak strain was estimated as 6.8 μ strain, ignoring any stress concentration effects. However, this location was also subjected to the maximum bending strains produced by tightening the specimen bolts and the absence of repeatability in the tightening process made calibration extremely difficult. It was also observed that the strain gauge bridge output tended to drift upwards with time under constant load, in contrast with the downward drift shown in Figure 3.11. Since the strain gauges are constructed as a temperature compensated pair with a temperature coefficient of resistance of $\pm$1.8 μ strain/^{o}C and are attached to a substantial steel block, it is unlikely that the drift shown in Figure 3.11 was due to temperature changes. Although the test has demonstrated the feasibility of measuring peak loads in a very stiff machine, the present equipment does not have sufficient accuracy or repeatability to greatly assist in the correlation of the test results with the cosine solution.

As a consequence of the difficulties encountered in measuring end load in the special fatigue testing machine and in determining the end alignment parameters for the Avery machine, specimen surface strains were determined directly from a strain gauged specimen in Channel No. 1 and are compared with cosine and elastica solutions in Figure 3.12. The results correlate reasonably well with the theoretical solutions for an initially straight strut, the experimental stresses being between 15% higher at .005" end displacement and 5% higher at .040" end displacement. These variations would appear to be mainly due to the effects of combinations of end alignment errors rather than specimen initial curvature. As shown in Figures 3.7 and 3.8, parallel

end displacement errors combined with slope errors of the opposite sign have the effect of increasing the strut stiffness and hence end load for a given end displacement, and thus increasing the surface stresses. An attempt to optimise the values of the three alignment errors to fit these experimental results, using at least mean squares method on a digital computer, had to be abandoned due to the vast number of possible combinations, and the variability of experimental end alignment conditions.

In the absence of a direct method of assessing the end alignment errors present in a given test and as the specimen initial curvature would appear to be negligible, the specimens were assumed to be straight and perfectly aligned in the theoretical stress estimates used in the analysis of the test results in Section 4. The errors incurred in the stress estimates as a result of these assumptions would appear to be only slight, as indicated by Figure 3.12.

Although the correlation between the test results and the two theoretical solutions is not totally conclusive, sufficient agreement has been found to give a reasonably high degree of confidence in the application of the approximate cosine solution to the analysis of encastré struts with various end alignment parameters. In the majority of practical combinations of these parameters, the cosine solution predicts lower surface stresses than for an initially straight strut. For design purposes therefore, it would be more appropriate to neglect initial curvature and end alignment errors, which is in contrast with the usual design assumption made when considering struts.

3.4 CONCLUSIONS

A simple approximate cosine solution to the buckling of an encastré strut has been shown to be sufficiently accurate to readily handle most realistic analytical cases. It has also been shown that the solution to an initially straight strut is the most conservative for design purposes, except in a number of exceptional circumstances. Since the chosen range of test conditions does not introduce any significant amount of plasticity on the nett area of the test specimens at room temperature, their response is almost entirely elastic, and

the presented solution applies equally to static and cyclic buckling conditions. The effect of cyclic creep strain during elevated tempeatures has not been evaluated.

4.0 FATIGUE LIFE INVESTIGATION

This section is divided into three convenient parts:

(i) experimental investigation

(ii) empirical fatigue life prediction techniques

(iii) correlation and discussion of the results.

4.1 EXPERIMENTAL INVESTIGATION

A programme of fatigue tests using a constant amplitude displacement cycle (nominally $\pm 0.020''$) over a range of mean displacement was performed in the two special testing machines described in Section 2. In the major portion of the programme, the specimen was free to buckle in compression, but for a small number of tests the specimen was restrained from buckling by the use of a simple jig shown in Figure 4.1. The tests were carried out at constant temperatures of $20^{\circ}C$ and $150^{\circ}C$, the latter to provide initial data on the simulation of thermal strain cycling.

4.1.1 Specimens

Simple sheet specimens 10" x 2" x 0.069" were cut from two 6' x 5' sheets of aluminium alloy, specification CM001/1D, both sheets being drawn from the same batch. A central 0.125" diameter hole was drilled and reamed using the drilling jig shown in Figure 2.30 to provide a stress concentration factor of 2.82 based on nett cross sectional area. The chemical composition, heat treatment and basic mechanical properties of the material, including the static tensile strengths of both plain and notched specimens, are summarised in Figure 4.2. A typical stress-strain curve for the material is shown in Figure 4.3.

4.1.2 Test Programme and Procedures

The detailed test programme is given in Figures 4.4 to 4.6.

Room temperature tests

The following setting up procedure was applied to each of the three testing channels in turn:

(i) the straining mechanism was set to a neutral position located by pins through the slider and guide and through the lower end of the bell crank lever.

(ii) the specimen was located in the specimen holders on two dowel pins to provide axial alignment, and the specimen bolts inserted and tightened to a preset torque. With non-buckling tests, the edges of the specimen were lightly greased with a molybdenum disulphide grease and inserted into the restraining jig as shown in Figure 4.1, before being located in the specimen holders.

(iii) having positioned a 0.0001" division dial gauge against one of the lower specimen bolts to measure displacement over the specimen length, the required mean displacement was applied to the specimen by means of the turnbuckle, having removed the bell crank lever locating pin.

(iv) the locating pin in the cam follower slider block was then removed and the cam was rotated to the mid-stroke position for the adjacent channel and the setting up procedure was repeated.

(v) the continuity wires across the specimen minimum cross sectional area were soldered into the cycle counting circuit shown in Figure 2.35, the relays energised and the counters zeroed. The fatigue testing machine motor was then started to commence the test, which continued until all three specimens had completely fractured.

(vi) actual test conditions were determined from peak displacement readings taken over four consecutive cycles within the first 30 cycles. The dial gauges were then removed to prevent them from being subjected

to fatigue damage.

(vii) crack length measurements during early tests were made using a travelling microscope mounted against the machine frame.

(viii) completely fractured specimens were removed without stopping the testing machine in order to limit the surface damage caused by the relative movement of the two fracture surfaces.

150° tests

The thermal expansion of the specimens and holders necessitated a slightly different setting up procedure. Having inserted the specimens into the holders as in the room temperature tests, the following procedure was adopted:

(i) the upper specimen bolts were slackened to allow the relative thermal expansions to cause the specimen to slide within the upper holder.

(ii) having repeated the setting up procedure and slackening of the upper bolts for all three specimens, the continuity wires were soldered and three control thermocouples were attached, one to each specimen. The furnace wall panels were positioned and the furnace and control system turned on for a three hour stabilising period.

(iii) the levers of Channel No. 4 were returned to the neutral position and the locating pins re-inserted. The upper specimen holder bolts were rapidly tightened through special cutouts in the furnace wall, the bell crank lever locating pin was removed and the required mean displacement was applied by means of the turnbuckle. In this instance the dial gauge was positioned against the bearing journal immediately below the specimen holder, as it was impractical to place the dial gauge inside the furnace.

(iv) the slider locating pin was then removed and the cam rotated to repeat the process for Channels Nos. 5 and 6. The whole procedure was carried out as quickly as possible to limit the amount of creep deformation before starting the fatigue test, and to subject all three specimens to the same prior treatment.

4.1.3 Test Results

Nominal and actual test conditions and fatigue lives, measured in terms of the number of cycles to complete failure, are tabulated in Figures 4.4 to 4.6 and are shown in Figure 4.7 as a plot of mean displacement against fatigue life, in which comparatively low scatter is demonstrated.

Micrographic examination of the fracture surfaces was beyond the scope of this investigation; however, careful macrographic study of all the specimens revealed the following features:

(i) the initial crack originated at opposite sides of the central hole, the fracture surface being normal to the surface of the specimen. In a number of tests in severe compression, failure occurred at the edge of the specimen holders.

(ii) the fatigue crack changed from being normal to the specimen surface to two surfaces inclined at the characteristic 45° to the specimen surface a short distance away from the central hole. The exception was for buckling specimens at $20^{\circ}C$ under a compressive mean displacement, where the fracture surface remained normal to the specimen surface for the majority of the specimen width.

(iii) the fatigue crack had a relatively smooth profile for tensile mean displacements and a noticeably meandering profile for compressive mean displacements.

Figure 4.8 indicates the macrographic features of the specimen fractures.

Crack length measurements were made for a number of the

earlier buckling tests at 20°C, using a travelling microscope mounted on a platform attached to the machine frame. The results are shown in Figure 4.9, where the ratio of crack length to specimen width is plotted against percentage of total fatigue life, for correlation purposes. The expected trend of high crack propagation rates associated with high tensile stresses is demonstrated, although there is considerable variation between two specimens tested under nominally identical conditions. As the initial cracks were not detected until 60% of the total fatigue life had elapsed, it was not practical to extrapolate back to the crack origin, and so these crack length measurements were discontinued. Fatigue lives are therefore quoted in terms of the number of cycles to complete failure.

4.2 EMPIRICAL FATIGUE LIFE PREDICTION TECHNIQUES

Two empirical techniques for fatigue life prediction were based on theoretical stresses derived in Section 3, and compared with the experimental lives achieved in the test programme. The prime concern was not to establish an accurate prediction technique but to determine whether or not buckling introduces a fatigue phenomenon which cannot be assessed using conventional fatigue life prediction techniques. The two techniques used were:

(i) the direct application of experimental fatigue data published by B.A.C.

(ii) a more general prediction technique developed by Heywood[8].

4.2.1 Stress Conditions

In Section 3 the use of a straight, perfectly aligned strut in the stress estimates for the theoretical fatigue life analysis was justified by reference to experimental stress measurements. This condition represents the most conservative life estimates, alignment errors and initial curvature resulting in an improvement in fatigue life for the same applied displacement conditions.

The table of experimental test conditions in Figures 4.4 to 4.6

shows a variation of alternating displacement amplitude, both within each channel and through the range of mean displacement, partly as a result of the small changes in stiffness in the buckling and non-buckling modes. This variation in displacement amplitude is plotted in Figure 4.10, from which it may be observed that 90% of the tests are included in an amplitude range of $\pm$0.0165" to $\pm$0.020". The two limits of this amplitude range were therefore used in the fatigue life prediction techniques in order to most conveniently cover the range of experimental data.

Figure 4.11 shows the variation of surface stress and nett area stress with end displacement for both non-buckling and buckling struts, the straight, perfectly aligned strut solution being used in the latter case. For constant amplitude displacement cycling, the variations in both mean and alternating stress with mean displacement may be determined from these curves, for each of four cases:

(i) non buckling strut

(ii) buckling strut, concave surface

(iii) buckling strut, neutral axis (mean stresses)

(iv) buckling strut, convex surface

For convenience, the variations in mean and alternating stress are plotted against mean displacement for $\pm$0.020" displacement amplitude in Figures 4.12 and 4.13, the curves for $\pm$0.0165" displacement amplitude being similar. Apart from the change in stress variation due to buckling relative to the non-buckling strut, the most significant feature is the situation on the convex surface, which suffers two tensile cycles. The first is due to the direct tension part of the displacement cycle, while the second is the result of bending in the buckled condition; each of these cycles is associated with separate mean and alternating stresses, as indicated in Figures 4.12 and 4.13.

The stress variations for both displacement amplitudes are also tabulated in Figures 4.19 and 4.20.

4.2.2 B.A.C. Fatigue Data

The current B.A.C. fatigue data contained in the Design Data Handbook[9] for light alloy sheet with unloaded holes was used. As

the test conditions were significantly more severe than those normally encountered in aircraft design, this data was extended to cover higher mean and alternating stresses by extrapolation and crossplotting, the final extrapolated curves being shown in Figure 4.14. Since this data is applicable to nett area stresses, the reduction in area due to a 0.125" diameter hole was used to determine the relevant nett area stress conditions.

The predicted fatigue lives for the four cases analysed, for each of the displacement amplitudes, are given in Figures 4.15 and 4.16, the results for the $\pm$0.020" displacement amplitude being plotted in Figure 4.17. In the case of the convex surface of the buckling strut, a linear cumulative damage law was applied to the contributions from the two stress cycles indicated in Figures 4.12 and 4.13 to determine the resultant fatigue life.

4.2.3 Heywood's Prediction Technique

This technique is fully described in Ref. 8 and only the additional specific information required to apply the technique to the present investigation is discussed here. The technique is based on empirical expressions describing the observed fatigue behaviour of plain coupon specimens, and is applied to notched coupons by means of four stress concentration factors in order to maintain a general and comparative approach.

The plain specimen fatigue data is described by expressions on page 39 of Ref. 8, and is related to the ultimate tensile strength of the material. The basic data for the CM001/1D material used in the test programme was derived from these expressions, and is plotted in Figure 4.18.

For notched specimens, four stress concentration factors are used (pages 155-156, Ref. 8), which anticipate the effects of:

(i) stress gradient effects at the notch for zero mean stress

(ii) plastic flow at the notch for zero mean stress for less than 10^7 cycles

(iii) reduction in static strength due to the presence of the notch

(iv) additional plastic flow associated with a non-zero mean stress.

The numerical values of these concentration factors given in Ref. 8 have been used in this analysis.

In applying these factors to the basic fatigue data, an iterative technique is used, as one of the above factors as a function of the required fatigue life. This iterative technique was handled conveniently and accurately by a special algol computer programme used on an Elliott 803 digital computer, with which the following additional input data was used:

(i) K_t = 2.82 for non-buckling strut,

(ii) K_t = 1.95 for bending surface of buckling strut,

(iii) E = 10.575×10^6 lb.f./in.^{2} determined experimentally.

For a surface stress cycle containing both direct tension and compression in bending, the value of K_t was made to vary linearly between 2.82 and 1.95 with the proportions of direct tension and bending in the cycle.

This fatigue life prediction technique was applied to the four cases detailed in Section 4.2.1 for both values of the displacement amplitude, and a linear cumulative damage law was applied to the convex surface of the buckling strut, as in Section 4.2.2. The results are given in Figures 4.19 and 4.20, and the results for the $\pm$0.020" displacement amplitude are plotted in Figure 4.17.

4.3 CORRELATION OF EXPERIMENTAL RESULTS WITH PREDICTIONS

Since the prediction curves for $\pm$0.020" displacement amplitude shown in Figure 4.17 exhibit a considerable degree of overlap, for clarity the correlation with the experimental results is divided into four sections:

(i) non-buckling strut

(ii) buckling strut, concave surface

(iii) buckling strut, convex surface

(iv) buckling strut at 150°C

The prediction curve for the neutral axis of the buckling strut indicates longer lives than for either the concave or convex surfaces, for all values of mean displacement, hence correlation with the experimental results is inappropriate in terms of a life reduction phenomenon.

4.3.1 Non-Buckling Strut

The results of both the B.A.C. and Heywood's fatigue life prediction techniques for displacement amplitudes of $\pm$0.0165" and $\pm$0.020" are compared with the experimental fatigue lives for the non-buckling strut in Figure 4.21. Although the shape of the B.A.C. curves correlates reasonably well with the trend of the test results, the slope is slightly low. The Heywood curves demonstrate poor correlation in terms of shape, slope and magnitude, being very pessimistic, particularly for tensile mean displacements. Reference to Figure 4.10 indicates that in general the displacement amplitudes for these tests (solid points) were closer to $\pm$0.0165" than to $\pm$0.020", so that the fatigue results would be expected to lie closer to the $\pm$0.0165" curve than to the $\pm$0.020" curve of Figure 4.21. However, in the mean displacement range from +0.010" to -0.005", this is not the case, the test lives being less than even those predicted by the $\pm$0.020" curve using the B.A.C. data, the $\pm$0.0165" predictions being optimistic by a factor of approximately 2. In addition, only three test conditions gave lives greater than those predicted by the B.A.C. data.

4.3.2 Concave Surface of a Buckling Strut

The appropriate prediction curves are compared with the test results in Figure 4.22. The B.A.C. curves correlate well in shape, slope and magnitude for tensile mean displacements, but they do not correlate with the trend of the results with compressive mean displacements, which appear to become asymptotic to a finite life of less than 10^6 cycles, rather than an infinite life as suggested by the prediction curves. This suggests the possibility of a change in the mode

of failure as the mean displacement is made more compressive, which is discussed more fully in Section 4.4. The Heywood prediction curves correlate well in terms of shape, but the slope is significantly lower than that of the mean of the test results, such that the predicted lives only compare at all reasonably over a small range of mean displacement. The variation of displacement amplitude with mean displacement is more appreciable in these tests (Figure 4.10) which is seen in the increased scatter of the fatigue life results in Figure 4.22.

4.3.3 Convex Surface of a Buckling Strut

The 20°C buckling test results are compared with the appropriate prediction curves in Figure 4.23. The rather unusual shape of the curves is the result of the convex surface being subjected to two tensile cycles, as discussed in Section 4.2.1. With tensile mean displacements, the major part of the fatigue damage is caused by the direct tension cycle, while with compressive mean displacements more severe than approximately -0.008" the bending tension cycle predominates. This causes the fatigue damage to be increased as the mean displacement is made more compressive, until the entire cycle is in the buckled condition. Below this, the alternating stresses are reduced, as shown by Figure 4.13, and the fatigue life is increased. For mean displacements between 0" and -0.008" each cycle contributes significantly to the total fatigue damage, which has been calculated using Miner's linear cumulative damage law.

The correlation with the test results is in general poor, except with high tensile mean displacements, when the B.A.C. curves correlate reasonably well. The B.A.C. curves are optimistic for mean displacements in the range +0.010" to -0.005", but then become severely pessimistic as the buckling is increased. However, the curves do support the experimental trend towards a finite life with increasing compression, as discussed in Section 4.4. Due to the low slope of the Heywood curves, very poor correlation is obtained, and the curves grossly exaggerate the fatigue damage caused by the bending tension for severely buckled tests.

4.3.4 Buckling Strut at 150°C

The results for the 150° buckling strut tests are plotted on Figure 4.22 where close agreement with the B.A.C. prediction curve for 20°C is demonstrated. These lives are consistently lower than the 20°C test lives, the difference being greatest with high tensile mean displacements. It is thought that the time exposure at high stress and 150°C was not long enough for any significant creep damage to have occurred, but rather that the life reduction factor of 1.4 was the result of the effect of the high temperature relaxing the beneficial compressive residual stresses around the stress concentration. As the mean displacement was made more compressive, the peak tensile stress was reduced, reducing the residual compressive stress around the stress concentration, so that the effect of the high temperature was also reduced, as shown in Figure 4.22.

4.4 DISCUSSION

4.4.1 Correlation between Predictions and Experimental Results

In general, the test results correlate better with the B.A.C. data predictions than with the Heywood data predictions. This is primarily because the B.A.C. data is based on an expression derived by Heywood[10] correlating the fatigue test results for a wide range of aluminium alloy joints, but subsequently adjusted to fit a relatively small number of test results for unloaded hole specimens in CM001 type alloys. In light of this, the following discussion is only concerned with the correlation with the B.A.C. fatigue data predictions, although comments on Heywood's technique will be included at the end of this section.

Non-buckling tests

Comparison of the B.A.C. fatigue data with the most directly relevant test results, those for the non-buckling tests, in Figure 4.21, reveals a consistent indication that the B.A.C. fatigue data is generally

optimistic. With a displacement amplitude of $\pm$0.0165", which from Figure 4.10 more closely describes the actual test conditions than a displacement amplitude of $\pm$0.020", the B.A.C. fatigue data is optimistic by a factor of between 2 and 3 for mean displacements between +0.010" and -0.005", decreasing to 1 outside this range. For convenience, this factor has been termed the "life correction factor" to distinguish it from life reduction factors due to cyclic buckling, elevated temperature etc. With the limited test results available for comparison with the B.A.C. fatigue data, it has not been possible to conclusively determine the source of this life reduction factor, but the following points may each contribute towards the overall effect:

(i) The alternating stress of $\pm$18,600 lb.f./in.^{2} appropriate to $\pm$0.0165" displacement amplitude lies towards the extreme limit of the published B.A.C. fatigue data, as shown in Figure 4.14. The process of extrapolation of the fatigue data into this high stress region is thought to be the main source of the observed difference from the non-buckling test results.

(ii) The possibility that the specimens used in establishing the B.A.C. fatigue data had significantly different values of the stress concentration factor to those used in this investigation. Although details of the B.A.C. specimens have not been formally published, it is thought that 2.6 is a typical value of K_t, compared with 2.82 for the specimens used in this investigation. This feature may have contributed to the optimism of the B.A.C. fatigue data.

(iii) The possibility of a frequency effect on the fatigue lives. If the B.A.C. fatigue data was generated by tests on a Vibraphore machine, the relatively high frequency of 2,000 cycles per minute compared with the 12 cycles per minute used in the investigation may have contributed towards longer fatigue lives.

A further point has been considered, but must be discounted as its effect is to make the fatigue life predictions conservative, rather than optimistic. The crack propagation phase under displacement controlled cycling is likely to be longer than that under load controlled cycling, which is the basis of the B.A.C. fatigue data. Under displacement controlled cycling, the bulk of the material ahead of the propagating fatigue crack remains elastic, tending to produce a constant propagation rate; under load controlled cycling the nett cross sectional area is reduced by the propagating crack so that the nett area stress is continually increased through the crack propagation phase, accelerating the propagation rate. Thus application of load controlled fatigue data to displacement controlled fatigue tests should produce marginally conservative life predictions because it underestimates the crack propagation phase.

From Figure 4.10 it may be seen that errors in the test displacement amplitudes have been taken into account by using displacement amplitudes of $\pm$0.0165" and $\pm$0.020" for fatigue life prediction, so that the bulk of the test results should lie between the two prediction curves.

Buckling tests

From Figure 4.17 it may be observed that the minimum predicted life under cyclic buckling conditions is given by the concave surface for mean displacements greater than -0.007", and by the convex surface for mean displacements less than -0.007". It is therefore reasonable to construct a predicted minimum life curve for all mean displacements, which would be expected to correlate most closely with the whole range of buckling test results. This minimum predicted life curve shown in Figure 4.24 appears to be optimistic for most tensile mean displacements and for compressive mean displacements above -0.007", but considerably conservative for all compressive mean displacements below -0.007". The implied change in the mode of failure, from crack nucleation and propagation initially on the concave surface to occurring initially on the convex surface, is supported by the change in appearance of the specimen fracture

surfaces as the mean displacement was made more compressive, as discussed in Section 4.1.3 and shown in Figure 4.8. In addition, it was observed that the crack was significantly longer on the convex surface than on the concave surface when the specimen was subjected to considerable cyclic buckling.

Assuming that the life correction factor determined from the non-buckling test results is applicable to all fatigue life estimates made with the B.A.C. fatigue data, it is necessary to establish a reasonable basis from which to apply it to the buckling test predictions, in order to determine any further life reduction factor due to cyclic buckling. Since the stress conditions appropriate to the non-buckling strut are significantly different from those for the buckling strut with the same mean displacement, the simple basis of using the variation of the life correction factor with mean displacement is unreasonable. The only significant variable parameter in the non-buckling tests, apart from the mean displacement, was the mean stress, and the variation of the life correction factor with mean stress, shown in Figure 4.25, is an estimate of the error of the B.A.C. fatigue data for a constant alternating stress of $\pm$ 18,600 lb.f./in.^{2} In the absence of any data on the variation of the life correction factor with alternating stress, it is assumed that the life correction factor can be applied to the buckling test predictions through the appropriate mean stress. This produces the factored curve B of Figure 4.24.

It has already been observed that the alternating stress of $\pm$ 18,600 lb.f./in.^{2} is near the extreme limit of the published B.A.C. fatigue data and it is anticipated that the life correction factor would be reduced with lower alternating stress levels, because of the availability of actual test results for direct correlation, rather than extrapolation. It is therefore most likely that the application of the derived variation in life correction factor with mean stress to the buckling test predictions over-corrects these predictions for mean displacements below -0.010", where the alternating stresses are significantly less than $\pm$ 18,600 lb.f./in.^{2}, as seen from Figure 4.16. The more appropriate factored minimum life curve of Figure 4.24 is

therefore probably coincident with curve B for tensile mean displacements and for compressive mean displacements above -0.010", but lies between curves A and B for more compressive mean displacements. This makes the most relevant predicted minimum life curve conservative for all tests in which buckling occurs.

There are, however, at least four further reasons why the B.A.C. fatigue data can be expected to produce conservative life predictions when applied to cyclic buckling conditions.

(i) The omission of the change in stress concentration factor due to cycling from direct tension into either tension or compression due to bending in the buckled condition. This change in stress concentration factor, from 2.82 to 1.95, would have an increasing effect as the specimen becomes increasingly buckled, i.e. as the mean displacement is made more compressive, causing the fatigue life predictions to be progressively increased, and its effect would be greatest on the bending tension cycle suffered by the convex surface.

(ii) The lower crack propagation rate under displacement controlled cycling compared with the rate under load controlled cycling has already been discussed. However, since the non-buckling tests were displacement controlled, this effect has been included in the life correction factor. With severe buckling test conditions, the crack having nucleated on the convex surface has to propagate through the thickness of the material in addition to along its surface. The propagation through the thickness of the material has to be achieved under retarding conditions, as the stresses at the neutral axis and on the concave surface are much lower than those on the convex surface. The evidence of the longer crack lengths on the convex surface to those on the concave surface suggests that the crack propagates along the convex surface only until such time as the local bending stiffness is sufficiently reduced as to increase the neutral axis and concave surface stresses to propagate the crack

through the thickness of the material and along the concave surface. Thus the crack propagation phase of the test is further increased for severe cyclic buckling conditions, making the B.A.C. fatigue data predictions conservative.

(iii) The extrapolation of the B.A.C. fatigue data into compression, where it has not been confirmed by appropriate test results on CM001 type alloys. This is evidenced by the discontinuity at zero mean stress in the B.A.C. fatigue data (Figure 4.21) and is anticipated to lead to conservative life estimates for compressive mean stresses. Since compressive mean stresses occur only for mean displacements between 0" and -0.006" for the minimum life curve (Figure 4.16) this effect is confined to a relatively small section of Figure 4.24.

(iv) The use of Miner's linear cumulative damage law to add the damage contributions of the direct tension cycle and bending tension cycle suffered by the convex surface. It has been assumed that the summation of the damage contributions should be equal to 1.0 at failure, but many researchers have found that this summation may have values ranging between 0.5 and 3.0, and possibly greater, depending on the particular test conditions.

It is therefore concluded that the factored minimum life curve B of Figure 4.24 is conservative, particularly for compressive mean displacements, although it is not possible to quantify the degree of conservatism present with the available data. It is unlikely, however, to exceed a factor of 10, which would be necessary to make the predictions optimistic in the severely buckled condition.

Buckling becomes a feature of the fatigue test cycle with mean displacements of less than approximately +0.019", increasing progressively as the mean displacement is reduced and made more compressive. Since the factored minimum life curve is conservative for all mean displacements where buckling is present, it is concluded that cyclic buckling does not introduce any significant life reduction factor.

In connection with the general analysis of buckling fatigue tests, two significant points should be noted. Firstly, without the non-buckling test results to compare with the B.A.C. fatigue data, a life reduction factor as high as 3 at zero mean stress would have been incorrectly attributed to cyclic buckling. Secondly, the results also indicate the importance of using surface stresses rather than mean stresses, determined either analytically or from strain gauge measurements on separate surfaces. The use of the average reading of a pair of back to back strain gauges, which is usual practice when determining end load stresses, implies stresses on the neutral axis in the buckled condition. Life estimates based on these would be optimistic by factors of approximately 2.2 at zero mean displacement, 3.6 at -0.005" and 154 at -0.010" mean displacement. (Figure 4.17)

Comparing the test results for the buckling and non-buckling conditions in Figure 4.7, it may be observed that allowing the specimen to buckle results in a longer fatigue life, but it anticipated that this result would be reversed for mean displacements below -0.020", i.e. with the specimen completely buckled. This is also shown by the unfactored B.A.C. fatigue data predictions in Figure 4.17, although in this case the buckling life is longer than the non-buckling life only for mean displacements between 0" and -0.011". Both the test results and the factored predictions in Figure 4.24 indicate a finite life with increasing compression for the buckling strut, as distinct from the trend towards an infinite life with the non-buckling strut. In the absence of stress data for the buckled condition, or in ignorance of the possibility of buckling with these particular test conditions, fatigue life predictions based on the non-buckling strut conditions would not be conservative should buckling occur, except for mean displacements more compressive than -0.007", as demonstrated by curve C of Figure 4.24. This is due to the life correction factor applicable to the non-buckling strut fatigue life predictions.

4.4.2 Effect of Variations in Displacement Amplitude

In order to achieve a reasonably short test period, the nominal displacement amplitude for the experimental investigation was selected as $\pm$0.020". By reference to Figures 4.12, 4.13 and 4.15, it may be observed that the alternating stress is increased by 12% and the mean stress is reduced by 16.5% at +0.014" mean displacement due to buckling, relative to the non-buckling stress conditions. The resultant fatigue life estimate for the buckling strut is less than that for the non-buckling strut by a factor of 1.23 (Figure 4.17). Since a displacement amplitude of $\pm$0.020" (i.e. $\pm$0.2%) is considerably more than that expected in the actual aircraft structure, it is instructive to consider the effect of lower displacement amplitudes on the stress changes due to buckling, and the consequent reduction in fatigue life estimates for a buckling strut, relative to a non-buckling strut subjected to the same displacement amplitudes.

It may be seen from Figure 4.26 that there is an increase in the percentage changes in both alternating stress and mean stress with decreasing displacement amplitudes. These two stress variations exert opposing influences on the fatigue life predictions, the former producing shorter lives, the latter producing longer lives. Since, with the B.A.C. fatigue data, fatigue lives are more sensitive to variations in alternating stress than to variations in mean stress, the comparatively smaller increases in alternating stress dominate the larger reductions in mean stress. The nett result is that the fatigue life estimates for the buckling condition are consistently lower than those for the non-buckling condition. The third curve in Figure 4.26 indicates that this reduction in life is approximately 20% for displacement amplitudes between $\pm$0.020" and $\pm$0.010". Below this the stresses for the non-buckling condition are close to the fatigue limit of the material, such that infinite lives are predicted and the percentage change in life predictions due to buckling also becomes infinite. The actual buckling life estimates are of the order of 4×10^5 and 2×10^6 cycles for displacement amplitudes of $\pm$0.008" and $\pm$0.006" respectively, which are outside the area of practical interest.

It is therefore concluded that the general trend of results obtained in detail for a displacement amplitude of $\pm$0.020" is applicable to smaller displacement amplitudes where the fatigue life estimates are in the range 10^3 to 10^6 cycles.

4.4.3 Heywood's Fatigue Life Prediction Technique

As noted at the beginning of this section, the generally poor correlation of the Heywood predictions with the test lives is the result of using fatigue data applicable to a wide range of aluminium alloys. However, the technique is more flexible than the direct application of the B.A.C. fatigue data, and it is thought that if suitable plain specimen fatigue data for CM001 type alloys was used with the Heywood technique, better test result correlation would be possible, particularly with compressive mean displacements, by incorporating the change in stress concentration factor.

It has not been possible to make these refined fatigue life predictions for two reasons.

(i) The published B.A.C. fatigue data for plain specimens has been derived from test results for a range of light alloy materials, with no specific correlation with CM001 test results. In light of the significant differences between the B.A.C. fatigue data for unloaded holes in CM001 sheet and the Heywood fatigue data for a range of aluminium alloys, it is quite likely that the use of the B.A.C. plain material fatigue data could result in similar errors to those shown in this analysis.

(ii) Although the non-buckling test results of this investigation could be used to work back to the basic data, the tests were all at a single alternating stress level, which would prevent the overall fatigue master diagram similar to Figure 4.18 from being generated.

4.5 CONCLUSIONS

It is convenient to group the conclusions of this section of the report under the headings of fatigue behaviour and fatigue life predictions.

4.5.1 Fatigue Behaviour

1. The main conclusion is that cyclic buckling under elastic conditions does not introduce any significant life reduction phenomenon into the fatigue behaviour of CM001 type aluminium alloys that cannot be assessed using current fatigue life prediction techniques.

2. The mode of failure of a strut under cyclic buckling conditions changes as the cycle becomes increasingly buckled, from crack initiation on the concave surface to crack initiation on the convex surface, due to the bending tension cycle suffered by the convex surface in the significantly buckled condition. This also causes the buckling strut to have a finite fatigue life with increasing compression, in contrast with the trend towards an infinite life with the non-buckling strut.

3. In order to determine realistic life estimates for the buckling strut, accurately determined surface stresses for both the concave and convex surfaces must be used, rather than the mean stress based on the buckling load and the nett cross sectional area.

4.5.2 Fatigue Life Predictions

4. By comparison with the non-buckling test results the B.A.C. fatigue data is optimistic at high alternating stress levels, by a maximum factor of 3 at zero mean stress.

5. When applied to the fatigue conditions of a displacement controlled cyclically buckling strut, the B.A.C. fatigue

data is conservative, particularly with compressive mean displacements. This is largely due to the change in stress concentration due to bending in the buckled condition, and also the different crack propagation characteristics under displacement controlled cycling compared with load controlled cycling, the latter being the basis of the fatigue data.

6. The trend towards a finite fatigue life with increasing compression for the buckling strut shown by the test results is supported by the fatigue life predictions.

7. The non-buckling strut life estimates are non-conservative when compared with the buckling test results. Since the buckling life estimates are also less than those for the non-buckling conditions with relatively high tensile mean displacements, the possibility of buckling must be carefully assessed in order to achieve a conservative design for a fatigue critical structure.

8. The effect of the changed stress conditions due to buckling on the non-buckling fatigue life estimates is calculated to be similar for displacement amplitudes in the range of $\pm$0.010" to $\pm$0.020".

9. The fatigue response of CM001 aluminium alloy is not accurately described by Heywood's fatigue data. However, it is anticipated that more accurate life predictions, particularly for the significantly buckling strut, would be obtained by using Heywood's prediction technique with the appropriate CM001 fatigue data.

5.0 GENERAL DISCUSSION

5.1 APPLICATION OF THE FATIGUE TEST RESULTS TO THE CONCORDE AIRCRAFT THERMAL FATIGUE PROBLEM

In terms of life reduction, two results are particularly relevant to the thermal fatigue tests on I beams and fuselage side panels referred to in Section 1. Firstly, cyclic buckling does not introduce any significant life reduction phenomenon. This result is based on the accurate knowledge of the cyclic surface stress conditions, which may present considerable difficulty in either calculation or measurement for a more complex structure than the simple coupon specimen. However, the strain gauge measurements in the thermal fatigue tests were in general made close to the location of failure, resulting in reasonable confidence in the stresses used for fatigue life prediction. Thus it is unlikely that errors in stress determination would have contributed significantly to the deduced life reduction factors of 6 and 12.

Secondly, a life correction factor of approximately 2.8 for mean stresses of 2,000 lb.f./in.^{2} and -3,000 lb.f./in.^{2} (Figure 4.25), based on the comparison between the B.A.C. fatigue data and the non-buckling test results, would appear to be applicable. Applying this factor to the thermal fatigue test results, life reduction factors of 2.15 for I beams and 4.3 for panels remained unexplained.

5.2 FURTHER SOURCES OF LIFE REDUCTION FACTORS

Three further features of these thermal fatigue tests may be examined as possible sources of life reduction factors, using the results of two additional current B.A.C. thermal fatigue investigations, but due to a lack of directly relevant experimental data, each of the features listed below can only be discussed qualitatively.

(i) creep and relaxation effects at 170°-190°C.

(ii) the effect of cyclic temperatures as distinct from cyclic thermal stress.

(iii) the application of mechanical stress fatigue data to thermal fatigue tests.

5.2.1 Creep and Relaxation Effects at 170°-190°C

As noted in Section 4.3.4, the residual stresses around a stress concentration significantly affect the role of that concentration as a nucleus for crack initiation. The most beneficial effects are obtained from compressive residual stresses, produced by the application of high tensile stresses during fatigue cycling. The effect of constant elevated temperature on this situation is two-fold: the occurrence of creep strain limits the peak tensile stress generated, so that the compressive residual stress is reduced; and compressive creep will cause this compressive residual stress to be further relaxed. Thus the beneficial effect of compressive residual stresses is reduced by the application of elevated temperatures.

In the coupon specimen tests reported here, the specimens suffered both tensile and compressive stresses at a constant elevated temperature of 150°C, in contrast to the thermal fatigue tests on the I beams and panels, where the stress was generally compressive when the specimens were at temperatures of 170°C to 190°C. It is extremely difficult to determine whether or not these latter conditions would result in the same life reduction factor of 1.4 deduced for the coupon tests (Section 4.3.4) due to the complex relationship between temperature, time and stress under creep conditions.

5.2.2 The Effect of Cyclic Temperatures as Distinct from Cyclic Thermal Stresses

In current research investigations supported by B.A.C. and the Ministry of Technology[11], notched sheet coupons and riveted lap joints in CM001 sheet have been subjected to fatigue tests which represent the operating environment of the Concorde, in a special facility known as the Avro Rig. The effect of a temperature cycle on the fatigue life under a mechanical stress cycle representing an aircraft flight cycle, shown in Figure 5.1, is currently being studied by comparing the fatigue lives with and without the temperature cycle, over a range of maximum temperatures. Figure 5.2 indicates the general trend of the results for two stress conditions, one with a

tensile stress (as opposed to a compressive stress in the thermal fatigue tests discussed above) and one with nominally zero stress during the elevated temperature cruise period of 60 minutes. Compared with the cold fatigue life, the inclusion of a tensile creep stress improves the fatigue life for maximum temperatures less than 145°C, but the life reduces rapidly above this temperature. The tests with a nominally unloaded condition during the elevated temperature cruise period show a consistent reduction in life, becoming more severe with increasing temperature. Both these effects are more marked with the notched coupon specimens, possibly due to the influence of the glue-like interfaying compound in the riveted joint specimens. In order to determine the time dependence of the most damaging effect with nominally zero load at temperature, 8 further notched coupon specimens were tested at 120°C and 150°C with cruise times of 15 minutes and 0 minutes, i.e. cooling started immediately the required maximum temperature had been achieved. The resultant life reduction factors were:

1.92 with 0 minutes at 150°C

1.16 with 0 minutes at 120°C

1.61 with 15 minutes at 150°C

1.56 with 15 minutes at 120°C

Comparing these results with those of Figure 5.2, two features may be noted:

(i) The 60 minute cruise period is more damaging than either the 0 minute or 15 minute cruise periods.

(ii) At 150°C the 0 minute cruise is more damaging than the 15 minute cruise, but the situation is reversed at 120°C.

Two conclusions may be drawn: the damaging influence is not simply related to cruise time, and that simple temperature cycling without any significant cruise period can cause reductions in fatigue life.

5.2.3 The Application of Mechanical Stress Fatigue Data to Thermal Stress Fatigue Tests

The assumption that the above technique is valid has been made in the analysis of the thermal fatigue tests described in Section 1, and has also been investigated in the analysis of a series of combined mechanical and thermal fatigue tests on simple box structures[12]. The fabricated box specimens were approximately 16" square and 10' long, as indicated in Figure 5.3, and were designed to be sufficiently deep so as to develop significant thermal stresses when subjected to temperature cycles similar to those shown in Figure 1.1. Typical test cycles are shown in Figure 5.4, where the mechanical stress cycle represents the ground to air loading and gusts, and the thermal cycle represents the acceleration and deceleration thermal stresses. Three test cycles were defined, with the accelerated cycle theoretically producing twice the fatigue damage of the basic cycle, in order to investigate the technique for accelerating thermal fatigue tests. The increased damage of the accelerated cycle was achieved by including two mechanical stress flight cycles and an increased amplitude temperature cycle into each test cycle. The third test cycle was defined as having the accelerated temperature cycle associated with only one mechanical stress cycle, in order to extend the correlation of cumulative damage calculations with actual test results.

The most significant fatigue cracks occurred in the riveted butt strap joint in the tension skin (Figure 5.3). The test lives were all less than the predictions based on measured stresses and the appropriate mechanical stress fatigue data. These results are further analysed in Figure 5.5, where the comparison is made on the basis of the thermal fatigue damage per test cycle sustained in each test. The correlation between the predicted and test values is much better with the accelerated and mixed cycles than with the basic cycle, the predicted value for the latter condition being less than half the corresponding test value. As a consequence, the thermal fatigue acceleration factors (the ratios of accelerated to basic thermal

fatigue damage) are totally different, being 3.16 by prediction compared with 1.90-1.97 by test.

The consistently low values of the predictions indicate the possible existence of an additional damaging factor associated with thermal fatigue. Comparison of the basic and accelerated results indicates that this damage factor is not simply related to temperature; from this small number of results, the damage factor appears to be worse at 110°C with a temperature range of 122°C than at 135°C with a temperature range of 165°C. This is in direct contrast to the effect of temperature cycling discussed previously and illustrated in Figure 5.2. It is therefore concluded that the fatigue data for thermal stress cycling may be significantly different from the corresponding mechanical stress fatigue data, and the assumption that thermal fatigue can be analysed using mechanical stress fatigue data can introduce damage factors of approximately 2.0.

5.3 SUMMARY OF ALL THE OBSERVED LIFE REDUCTION FACTORS

In addition to the life correction factor applicable to the B.A.C. unloaded hole fatigue data, deduced from the non-buckling test results, three particular features of the thermal fatigue tests on I beams and fuselage side panels have been examined, and are considered as possible sources of further life reduction factors.

(i) Creep and relaxation effects at the relevant constant temperatures of 170°C to 190°C would significantly reduce the beneficial effects of compressive residual stresses around stress concentrations.

(ii) Cyclic temperatures have been shown to produce life reductions in both notched sheet coupons and riveted joint specimens, dependent on the magnitude of the applied stress during the elevated temperature exposure, and on the maximum temperature achieved.

(iii) The analysis of thermal fatigue tests on deep boxes has shown that the B.A.C. mechanical stress fatigue data

does not accurately describe the behaviour of thermal stress fatigue cycling.

The origin and nature of each of these four life reduction factors are tabulated in Figure 5.6.

It may be observed from Figure 5.6 that the variations of the effects of the life reduction phenomena with temperature are not all similar, and there is probably considerable overlap and interaction in a realistic thermal fatigue test. In addition, the scatter normally associated with fatigue testing makes isolation of each of these features extremely difficult. However, it is thought that the combination of these effects relevant to the thermal fatigue tests on I beams and panels would be sufficient to account for the outstanding life reduction factors of 2.15 and 4.3.

To improve the understanding of the thermal fatigue problem in CM001 type alloy structures, further work on three particular effects would appear to be necessary:

(i) the establishment of relevant thermal stress fatigue data.

(ii) the effects of temperature exposure on residual stresses around stress concentrations.

(iii) the refining of the basic mechanical stress fatigue data, particularly at high stress levels.

Work on the effect of temperature cycling on fatigue is continuing, and is being extended to include temperatures and stresses more appropriate to the actual operating environment of the Concorde, which must also be a feature of the test conditions of (i) and (ii) above.

5.4 MAIN FEATURES OF THE RESEARCH WORK

It is convenient to list the features under the headings of testing machine, buckling analysis, and fatigue life analysis.

Testing Machine

A special fatigue testing machine to perform displacement controlled cycling on sheet specimens has been satisfactorily designed, manufactured and used in this investigation into the effect of buckling

on fatigue life. The accuracy of the machine is such that errors in specimen displacement conditions are maintained to less than 5% until 95% of the life, including the crack propagation phase, has elapsed. This accurate control of the test conditions has assisted in achieving the very low scatter of fatigue life test results, which has in turn assisted in the analysis of trends of these test results.

Buckling Analysis

A simple approximate solution to the displacement controlled buckling of an encastré strut has been developed and shown to be sufficiently accurate to be used with confidence in the analysis of most practical cases of buckling of slender struts. It has also been shown that the solution to the initially straight perfectly aligned strut is the most conservative for fatigue design purposes, and that alignment errors and initial curvature reduce the peak stresses and therefore produce a beneficial effect on the fatigue life under cyclic buckling. This analysis provided the fatigue stress conditions which enabled the observed change in mode of failure, from crack initiation on the concave surface to crack initiation on the convex surface of a buckling strut, and the observed trend towards a finite life with increasing compression to be predicted and understood.

Fatigue Life Analysis

Comparison of the fatigue test results with the fatigue life predictions has shown that cyclic buckling does not introduce any significant life reduction factor. By comparison with the non-buckling test results, the B.A.C. fatigue data has been shown to be optimistic at high alternating stress levels, by a factor of 3 at zero mean stress. When applied to the fatigue conditions of a displacement controlled cyclically buckling strut, the same data is found to be understandably conservative, particularly for compressive mean displacements, due to the change in stress concentration factor due to bending in the buckled condition, and the difference in crack propagation characteristics under displacement controlled cycling from load controlled cycling. The fatigue life estimates for the non-buckling

condition were found to be non-conservative when applied to the buckling test results. Since with relatively high tensile mean displacements the predicted buckling life is less than that for the non-buckling condition, the possibility of cyclic buckling must be carefully assessed in order to achieve a conservative design for a fatigue critical structure. It is anticipated that better life estimates, particularly for the buckling condition with compressive mean displacements, could be achieved by using Heywood's fatigue life prediction technique with specialised fatigue data appropriate to CM001 aluminium alloy.

6. CONCLUSIONS

1. Accurately determined surface stresses are essential in order to achieve realistic fatigue life estimates for a buckling strut.

2. Given conclusion 1 above, it has been shown that cyclic buckling does not introduce any significant life reduction phenomenon.

3. The mode of failure of a buckling strut changes as the buckle is made more significant, and the trend is towards a finite fatigue life with increasing compression.

4. The effect of constant elevated temperature of 150^{o}C on the fatigue lives was comparatively small, reducing them by approximately 40%.

5. Related work on thermal fatigue demonstrates the damaging influence of cyclic temperatures and the difference between thermal stress and mechanical stress fatigue.

6. A satisfactory simple analysis of displacement controlled buckling has been developed to produce the accurate surface stress data required for the fatigue life analysis.

7. A special displacement controlled fatigue testing machine has been satisfactorily designed, manufactured and utilised in this investigation.

8. Further work on the differences between thermal stress and mechanical stress fatigue, and on the effect of temperature exposure on residual stresses is seen to be necessary.

7. ACKNOWLEDGEMENTS

The author wishes to thank Professor J. Black, Mr. T. Adam, Mr. S. Butler and Dr. J.W.L. Warren (Bath University of Technology) for their encouragement and guidance throughout the progress of this work, and Mr. E. Millard and Mr. F. Bundy for their assistance with the experimental investigation.

Thanks are also expressed to Mr. N.F. Harpur, Dr. T.W. Coombe and Mr. J. Rillett (B.A.C., Filton) for arranging financial support for the period of the investigation, for their interest and permission to include in this report current B.A.C. work on the thermal fatigue problem.

The work was performed under Ministry of Technology Agreement No. PD/112/04, and permission to publish this work is gratefully acknowledged.

8. REFERENCES

1. M. Lazenbury, C. Mills 'Thermal fatigue test on a shear panel' British Aircraft Corporation Test Report No. SST/B76A-02/0102 July 1963 and Addendum 1, November 1964.

2. P. Westmoreland, S. Butler 'Thermal fatigue panel - technical appraisal of results' British Aircraft Corporation Report No. SST/B72D/6/TA/6.10.1, 16 October 1965.

2. P. Westmoreland, K. Amor, S. Butler 'Thermal fatigue test on idealised fuselage side panel' British Aircraft Corporation Report No. SST/B72D-6/TA/6.10.2, 19 October 1965.

4. C.S. Rostron 'Summary of test results for structures subjected to rapid accelerated thermal fatigue cycles' British Aircraft Corporation Report No. SST/B72-6/6.6.2 Report No. 2, January 1965.

5. S. Russell, S. Butler 'Proposals for detail specimen tests for environmental testing programme ' British Aircraft Corporation Report No. SST/B72D-6/2.4.11.6, 15 January 1965.

6. P.J. Gill 'Torque-tension relationships in bolts' Engineering Materials and Design, May 1966.

7. S. Timoshenko, J. Gere 'Theory of elastic stability' Engineering Societies Monographs, McGraw Hill Book Co. Inc. 1961.

8. R.B. Heywood 'Designing against fatigue' Chapman and Hall 1962.

9. British Aircraft Corporation Ltd. Structural Design Data, Volume 3.

10. R.B. Heywood 'Correlated fatigue data for aircraft structural joints' A.R.C. CP 227, 1955.

11. S. Russell 'Typical light alloy aircraft joints S-N curves for a range of mean stresses' British Aircraft Ltd. Technical Office Report No. 139, February 1961.

12. R.J. Wyse, G.D. Sellers 'Environmental test summary' British Aircraft Corporation Report No. SST/B74S-5/TA/2.4.11 Report No. 5, Issue 2. 15 November 1968.

13. R.J. Wyse, G.D. Sellers 'Thermal fatigue tests on deep box specimens' British Aircraft Corporation Report No. SST/B74S-5/TA/12.2, Section 1, Report No. 2, March 1970.

APPENDIX I

Literature Survey carried out in September, 1965

Thermal Stress Fatigue and Mechanical Strain Fatigue at Elevated Temperatures

PART 1

1. INTRODUCTION

This literature survey lists most of the readily available reports in English published between 1954 and 1963, but due to the time lag between publication and inclusion in reference indices very little information is more recent than 1961.

Two previous literature surveys on this topic are listed, one published in 1959, the other in 1961.

The reports are divided into five sections:

1. Comparison between thermal stress fatigue and mechanical fatigue.
2. Pulsating thermal stress cycling.
3. Thermal stress fatigue
4. Constant strain amplitude fatigue at elevated temperatures.
5. Reports held by the Structures Development Group, B.A.C. Filton.

Constant stress amplitude fatigue was not included due to the vast quantity of literature now published.

The reports in Section One are reviewed briefly in Part 2 to

indicate current thought in the most interesting of the sections listed above.

2. SOURCES OF INFORMATION

1. Applied Mechanics Reviews 1954-1965.
2. Scientific and Technical Aerospace Reports (STAR) 1964, V3, N1-7 1965.
3. International Aerospace Abstracts 1963.
4. B.A.C. Technical Reports Classification Index.
5. Thermal Stress - Benham & Hayle.
6. Thermal Stress - Gatewood.

3. LITERATURE SURVEY

3.1 COMPARISON OF THERMAL STRESS FATIGUE AND MECHANICAL FATIGUE

1. Majors, H. Jr. 'Comparison of thermal fatigue with mechanical fatigue cycling' Bureau of Engineering Research, University of Alabama, 1957.

2. Coffin, L.F.Jr. 'Thermal stresses and thermal stress fatigue' Proc. Society for Experimental Stress Analysis, Vol. XV, No. 2, 1958.

3. Taira, S.,Minata, H., Shiraisi, T., Ohnami, M. 'Thermal fatigue and cyclic mechanical fatigue at elevated temperatures of 18-8 Cb stainless steel and 2.25 Cr - 1 Mo steel' J.S.M.E. Bulletin, Vol. 6, May 1963.

4. Coffin, L.F.Jr. 'Problem of thermal stress fatigue in austenitic steels at elevated temperatures' A.S.T.M. S.T.P. 165, 1954.

5. Coffin, L.F. Jr. 'Strain cycling and thermal stress fatigue' 4th Sagamore Ordnance Materials Research Conference, August 1957.

3.2 PULSATING THERMAL STRESS CYCLING

6. Taira, S., Ohnami, M., Kyogoku, T. 'Thermal fatigue under pulsating thermal stress cycling' J.S.M.E. Bulletin, Vol. 6, May 1963.

3.3 THERMAL STRESS FATIGUE

7. Glenny, E. 'Thermal fatigue - a literature survey' Metallurgical Reviews, Vol. 6, No. 24, 1961.

8. Yen, T.C. 'Thermal fatigue - a critical review' Welding Research Council Bulletin, No. 72, 1959.

9. Majors, H. Jr. 'Thermal shock and fatigue - a literature survey' University of Alabama. Bureau of Engineering Research Bulletin No. 4, 1956.

10. Manson, S.S. 'Thermal stresses in design - part 5' Machine Design, September 1958.

11. Glenny, E., Taylor, T.A. 'A study of the thermal fatigue behaviour of metals' Journal of Institute of Metals, 88, Part II, 1959.

12. Baron, H.G., Bloomfield, B.S. 'Resistance to thermal stress fatigue of some steels, heat resisting alloys and cast irons' Journal of Iron and Steel Institute, London. Vol. 197, No. 3, March 1961.

13. Lardge, H.E. 'Thermal fatigue testing of sheet metal' A.S.T.M. S.T.P. 174, 1956.

14. Clauss, F.J., Freeman, J.W. 'Thermal fatigue of ductile materials. Parts I and II' NACA TN.4160 and NACA TN.4165

15. Clauss, F.J. 'Thermal fatigue of ductile materials' 4th Sagamore Ordnance Materials Conference, August 1957.

16. Clauss, F.J. 'Thermal fatigue of ductile materials. Part III' NASA TND-69.

17. Coffin, L.F.Jr. 'A study of the effects of cyclic thermal stresses in a ductile metal' Trans. A.S.M.E.76, 1954.

18. Mehringer, F.J., Felgar, R.P. 'Low cycle fatigue of two nickel-base alloys by thermal stress cycling' Trans. A.S.M.E. Series D Journal of Basic Engineering, September 1960.

19. Thorkildsen, R.L. 'Creep and fatigue criteria for high temperature turbo-compressor loop materials' STAR V3 N2 N65-11335.

20. Horton, K.E. 'Investigation of the thermal stress fatigue behaviour of stainless steels' ATL-A-135. EURAEC - 632, 1963.

21. Quarterly Progress Reports: Investigation of the thermal stress fatigue behaviour of stainless steels. ATL-A-134 EURAEC-555 Reports 3 and 4.

22. Pultsin, N.M., Samoylov, N.S., Pokrovskaya, V.B. 'Thermal fatigue of certain titanic alloys' STAR V3 N1 N65-10737.

23. Freudenthal, A.M. 'Aspects of thermal fatigue damage at elevated temperatures' Acta. Metallurgica, Vol. 11, No. 7, July 1963.

24. Carden, A.E., Sodergren, J.H. 'The failure of 304 stainless steel by thermal stress cycling at elevated temperature' A.S.M.E. Paper 61-WA-200, 1961.

25. Majors, H.Jr. 'Correlation of thermal stress fatigue with mean temperatures and the influence of combined stresses' Seattle University Report to U.S. Army Research Office Project No.2090, March 1962.

26. Fransson, A. 'Effect of simultaneous cyclic variation of stress and temperature on a high temperature material' IUTAM Colloquium on Fatigue, Stockholm, 1955.

27. Smith, R.W., Smith, G.T. 'Thermal fatigue crack growth characteristics and mechanical strain cycling behaviour of A-286, Discaloy and 16-25-6 austenitic steels' NASA THD-479

28. Weiss, V., Saule, A., Schaeffer, G. 'Strength properties of aluminium alloy X-2020-T6 under thermal cycling' Syracuse University. REFS. INST. MET. ENG. DEPT. MET. 598-599-TR2, 1959.

29. Manson, S.S., Sachs, G., Brown, W.F.Jr. 'The effect of cyclic heating and loading on creep, stress- rupture and fatigue properties of metals at elevated temperatures' Joint A.S.T.M. - A.S.M.E. Committee on the effects of temperature on properties of metals. New York, 1957.

30. Miller, J. 'Effect of temperature cycling on rupture strength of some high temperature alloys' A.S.T.M. S.T.P.165, 1954.

31. Moon, D.P., Vanecho, J.A., Simmons, W.F., Barker, J.F. 'Structural damage in thermally cycled Rone '41 and Astraloy sheet materials' DMIC Report 126, 1960.

32. Padlog, J., Schnitt, A. 'A study of creep, creep-fatigue and thermal stress fatigue in airframes subjected to aerodynamic heating' WADC-TR-58-294, 1950.

33. Majors, H.Jr. 'Thermal and mechanical fatigue of nickel and titanium' Trans. A.S.M. 51, 1959.

34. Robinson, A.T., Ramsdell, J.D. 'Effect of high temperature rapid thermal cycling load' U.S. Naval Ordnance Test Station Inyokern NOTS - TM. No.1620, 1954.

35. Serensen, S.V., Kotov, P.I. 'Tests with cyclic thermal stresses of varying severity in the investigation of thermal fatigue' Industrial Lab. 25-10 August, 1960.

3.4 CONSTANT STRAIN AMPLITUDE FATIGUE AT ELEVATED TEMPERATURES

36. Johnsson, A. 'Fatigue of steels at constant strain amplitudes and elevated temperatures' IUTAM Colloquium on Fatigue, Stockholm, 1955.

37. 'Effect of compressive loads on structural fatigue at elevated temperatures' ASD-TDR-488. Douglas Aircraft Co. Contract AF 33 (616)-8130, 1962.

38. Smith, R.W., Hirschberg, M.H., Manson, S.S. 'Fatigue behaviour of materials under strain cycling in low and intermediate life range' NASA TND-1574, 1963.

39. Ronay, M., Reiman, W.H., Wood, W.A. 'Mechanism of fatigue deformation at elevated temperatures' Columbia University, New York Advanced Research Projects Agency. Technical Report No. 07 NR 064-470, 1956.

40. Vitovec, Lazan 'Creep rupture and notch-sensitivity properties of S-816 Alloy up to 1650°F under fatigue and static stress' A.S.T.M. S.T.P. 174, 1956.

41. 'Aspects of reliability under conditions of elevated temperature creep and fatigue' ASD-TDR-63-267, 1963.

42. Tapsell, H.J. 'Fatigue at high temperatures. Symposium on high temperature steels and alloys for gas turbines. Iron and Steel Institutes, London, 1950.

43. 'Symposium on the effect of cyclic heating and stressing of metals at elevated temperatures' A.S.T.M. S.T.P. 165, 1954.

44. 'Co-operative investigation of the relationship between static and fatigue properties of wrought N-155 alloy at elevated temperatures' N.A.C.A. TN.3216, 1955.

45. Hoff, N.J. 'High temperature effects in aircraft structures' AGARD No. 28, Permagon Press, New York.

46. 'Cyclic strain fatigue studies on AlSl type 347 stainless steel' A.S.T.M. Preprint No. 64, 1957.

47. Coffin, L.F.Jr. 'The stability of metals under cyclic plastic strain' A.S.M.E. Trans. 82D (Journal of Basic Engineering) 3, 1963.

3.5 REPORTS HELD BY STRUCTURES DEVELOPMENT GROUP, B.A.C. FILTON

48. Stephenson, N. 'A review of the literature on the effect of frequency on the fatigue properties of metals and alloys' N.G.T.E. Memorandum M320, 1958.

49. Heath-Smith, J., Kite, R.J. 'Symposium on fatigue and creep of structures at elevated temperatures. Fatigue strength at elevated temperature of aluminium alloy specimens and structure' R.A.E. Preprint SFC/4, 1963.

50. 'Thermal or mechanical cycling, with or without creep' Joint International Conference on Creep. Session 3. 1963.

51. Kawamoto, M., Tanaka, T., Nakajima, H. 'Thermal fatigue behaviour of steels subjected to cyclic mechanical strain independently' Japan Congress of Testing Materials - Proc. J.S.M.E. October, 1962.

52. Taira, S., Ohnami, M., Shiraishi, T. 'Thermal fatigue combined with fully reversed mechanical stresses' J.S.M.E. October 1962.

53. Taira, S., Ohnami, M., Shiraishi, T. 'Thermal fatigue under multiaxial thermal stresses' J.S.M.E. October 1962.

54. Miki, H., Sugimori, M. 'On the behaviour of metals in thermal fatigue' J.S.M.E. October 1962.

55. Taira, S., Koterazawa, R. 'Dynamic creep of metallic materials at elevated temperature compressive varying stress' J.S.M.E. October 1962.

PART 2

Comparison between Thermal Stress Fatigue and Mechanical Strain Fatigue at Elevated Temperatures

1. MAJORS, H. Jr.

Comparison of thermal fatigue with mechanical fatigue cycling

Lui et al. and Coffin carried out fatigue tests on 24ST duralumin and AlSl type 347 stainless steel, their results being represented by:

$$N^K \Delta\varepsilon_p = C.$$

where N = no. of cycles to failure

$\Delta\varepsilon_p$ = plastic strain change in one half cycle

K & C = material constants

Tests on type Ti - 75A titanium and type A nickel were carried out in the same type of rig as used by Coffin, using constant amplitude of strain rather than load.

Results: A: Ti - 75A titanium

Figure A1.1 shows the effect of temperature range about a mean temperature of 575°F and comparing it with Figure A1.2, a normal fatigue curve of stress versus log cycles to rupture, the degree of scatter appears quite small.

Figure A1.3 shows strain range and plastic strain range against stress cycles to failure. Titanium shows very little plastic strain prior to rupture, possibly due to its crystalline structure - close packed hexagonal.

Results: B: A type nickel

The results are plotted in Figures A1.4 - A1.6 in the same manner as Figures A1.1 - A1.3. Greater scatter is accounted for by varying grain size and degree of constraint during testing. Type A

nickel can absorb much more plastic strain before rupture (having a face centred cubic crystal structure).

Load fatigue tests were carried out on the two materials; titanium at 575°F and nickel at 525°F. The results are shown in Figures A1.7 - A1.10.

Figures A1.7 and A1.9 are the usual plots of stress range v log cycles to rupture and it is evident that the life to rupture under thermal cycling is very much less than under load cycling. (For titanium, under thermal cycling conditions a stress amplitude of 25,000 p.s.i. will cause failure in 200,000 cycles, while under load cycling a stress amplitude of 35,000 p.s.i. no failure would occur at 575°F.)

Figures A1.8 and A1.10 are plots of plastic strain v log cycles to rupture. For titanium, a fivefold decrease in plastic strain amplitude occurs under thermal cycling conditions from those amplitudes under load cycling; nickel can withstand even more plastic strain amplitude than titanium.

More thermal cycling data is required to make extrapolation from load cycling to thermal cycling legitimate.

The data in Figures A1.8 and A1.10 may be expressed as:

$N^{0.48}\Delta\varepsilon_p = 0.23$ (load cycling, 575°F mean temp.)
$N^{0.51}\Delta\varepsilon_p = 0.052$ (thermal cycling, 575°F mean temp.) } titanium

$N^{0.35}\Delta\varepsilon_p = 0.087$ (load cycling, 525°F mean temp.)
$N^{0.35}\Delta\varepsilon_p = 0.043$ (thermal cycling, 525°F mean temp.) } nickel

Tests of thermal cycling under constant load were compared with thermal cycling under constant strain range and load cycling under constant temperature and strain range. The mean temperature was 525°F; the range of temperature was allowed to oscillate about the mean under a constant stress. Although the mean strain varied as cycling progressed, the range of strain was constant as was the temperature range.

Titanium: Some difficulty was experienced in thermal cycling under constant load and the results are extremely sensitive to any variation in starting conditions, especially upper temperature. Figure A1.11 illustrates a typical relationship of mean strain to number of cycles: the plot is similar to a typical creep curve showing secondary and tertiary regions, but the secondary region under thermal cycling consists of elastic and thermal strains until the onset of massive plastic flow.

Kurg and other investigators have shown that there is a marked increase in strength when increased heating rates are used.

Nickel: Curves are given in Figure A1.12; the secondary region is similar for the four specimens but the onset of massive plastic flow does not occur at the same number of cycles. More tests are required to determine the influence of rates of heating, hold times at temperature and initial mechanical strain on the onset of the tertiary region.

Figure A1.13 shows that grain size appears to have very little effect on life to rupture; Baldwin made this point from tests on A1S2 type 347 stainless steel.

Comparison of load cycling fatigue (constant temperature) with thermal cycling fatigue (constant strain range)

The comparison is made on the basis of permanent deformation; total plastic strain is defined as $2\Delta\varepsilon_p N$,

$\Delta\varepsilon_p$ = plastic strain determined from hysteresis stress-strain loop at zero stress

N = number of cycles of stress reversed to rupture

$2\Delta\varepsilon_p N$ = total plastic strain absorbed to failure.

The effect of total plastic strain on cycles to rupture is plotted in Figures A1.14 and A1.15 for titanium and nickel respectively.

The range of plastic strain computed for the case $N = \frac{1}{4}$, which should have some relation to the fracture ductility of a tension test is tabulated in Figure A1.16. This shows that only one value of

extrapolated plastic strain at $\frac{1}{4}$ cycle is similar to the fracture ductility in a tension test. More data is required to relate static tension strains to thermal and load fatigue strains.

The data in Figures A1.14 and A1.15 were approximated with linear relationships on logarithmic coordinate axes, and the load cycling curves appear to be parallel to the thermal cycling curves. It is evident that the total plastic strain sustained under thermal cycling conditions is very much less than for load cycling conditions on both nickel and titanium.

For the same life to rupture and mean temperature, type 'A' nickel under load cycling can absorb 21 times the total plastic strain under thermal cycling conditions, and type Ti-75A titanium under load cycling can absorb 5.5 times the total plastic strain under thermal cycling. Figure A1.17 shows the test results obtained on type 347 stainless steel rod in which a load cycling test can absorb 2.3 times the total plastic strain of a thermal cycling test.

Figures A1.18 and A1.19 provide a comparison with other data. Values of C vary widely with temperature whereas values of K vary from 0.35 to 0.82.

2. COFFIN, L.F. Jr.

Thermal stresses and thermal stress fatigue

The effect of cold work in thermal stress fatigue resistance has been investigated for AISI type 347 stainless steel specimens. It is found that prior cold work can be advantageous for low strain levels but deleterious at high mechanical strain levels. Plotting this data in terms of stress range, it is found that increasing cold work uniformly increases the stress required to produce failure in a given number of cycles. Figures A1.20 and A1.21 point out very strongly the important difference between conventional fatigue behaviour where stress is the independent variable, and thermal stress fatigue where temperature and hence mechanical strain is the independent variable.

Thus techniques which are often used to raise the fatigue strength under applied loads, such as shot peening, case hardening and other surface treatments, can be deleterious in thermal stress fatigue applications.

The stress range obtained after 1000 cycles was plotted against mechanical strain range, for the various strain ranges examined, in Figure A1.22. The diagram shows that strain hardening does not play an important role for the strain levels encountered as it is evident that the stress range for the initially annealed material is less than the corresponding stress range for the static tensile test. This is contrary to common belief and to some theories on fatigue.

The number of cycles to failure decreases as the mean temperature increases, all other parameters being held constant. This can be explained on the basis of an increase in the plastic portion of the mechanical strain range with increasing mean temperature for a particular thermal strain range.

Increasing cycle time (longer periods hot and cold) also decreases the number of cycles to failure.

Total plastic strain ($2N\,\Delta\varepsilon_p$) is suggested as an important parameter in assessing fatigue damage and life, and a relationship of the form:

$$N^K \Delta\varepsilon_p = C$$

is found to exist. K & C have been evaluated for several materials and test conditions in Figure A1.23.

3. TAIRA, S. ET AL,

Thermal fatigue and cyclic mechanical strain fatigue at elevated temperatures of 18-8Cb stainless steel and 2.25Cr-1Mo steel

For comparison purposes, a concept of an equivalent steady temperature for thermal fatigue, such that the thermal fatigue resistance is equivalent to a mechanical strain fatigue of the same strain amplitude at a steady temperature is introduced. The comparison is made on the basis of the accumulated fatigue damage reaching a finite

value, which is a material constant independent of test conditions. Fatigue damage is considered to be a function of the square of the plastic strain amplitude in one half cycle.

accumulated damage = $2N\lambda(T)\ (\Delta\varepsilon_p)^2$

N = number of cycles

$\lambda(T)$ = temperature dependent constant

$\Delta\varepsilon_p$ = plastic strain amplitude in one half cycle

This analysis is applied to an idealised hysteresis loop to derive the value of the equivalent temperature in terms of the upper and lower cycle temperatures.

Using test equipment similar to that used by Coffin, it was found in cyclic strain tests that little difference in life to fracture resulted from temperatures between 400°C and 600°C for AISI type 347 stainless steel but with 2.25 Cl-1Mo steel the results were considerably more temperature sensitive, the higher temperatures producing shorter lives.

From these results $\lambda(T)$ was evaluated relative to a reference $\lambda(To)$ enabling the equivalent steady temperature to be evaluated for thermal cycling.

Comparing the life to fracture under strain cycling and thermal cycling, the life was considerably reduced for thermal cycling at high strain amplitudes but slightly increased at low strain amplitudes. Tests at 300°C and 610°C showed a general reduction in life, however.

A mathematical allowance for strain localization due to uneven temperature distribution along the specimen under thermal cycling was made to correct the results.

Increasing the frequency of cycling lengthened the fatigue life by shortening the hold time at temperature and prohibiting plastic deformation and metallurgical changes.

4. COFFIN, L.F. Jr.

Problems of thermal stress fatigue in austenitic steels at elevated temperatures

Tests using strain localization techniques were compared under thermal cycling and constant strain cycling to predict the failures from analysis and simple laboratory experiments.

Type 347 stainless steel specimens were thermally cycled with total strain kept constant and Figure A1.24 shows the relationship between stress change and cycles of strain to failure. The amount of strain hardening was slight, increasing with increased strain amplitude, but it was found that with previously cold worked materials, strain softening occurred. Increasing the cyclic temperature (and hence the elastic and plastic strain change) decreases the number of cycles to failure, as in Figure A1.25. Fatigue failure from cyclic thermal conditions was found to depend on the total accummulated plastic strain absorbed by the specimen. The expression

$$N^{0.5}\Delta\varepsilon_p = 0.36$$

was found to fit the results fairly well.

Prior cold work had the effect of reducing the constant term on the right hand side.

Stress concentration factors were then imparted to the test specimens and the tests repeated and the results compared with those of "normal" tests. Figure A1.26 shows the results of a specimen having a .040" dia. hole drilled through the specimen compared with normal results. Both curves have the same slope, the one with the stress concentration giving shorter lives.

A second series of tests were carried out using a specially designed specimen having sections of cold worked and annealed material within the test length. The length of the annealed portion was variable, and the results of strain cycling tests at 1% strain at a constant temperature of 350°C are shown in Figure A1.27. Fatigue failure occurred as expected in the annealed region and as this length was

decreased, a drastic reduction in life occurred.

Comparison of thermal cycling and strain cycling

Identical cyclic strains were used in both tests, with the mean temperature being 350°C. Figure A1.28 shows the stress change against cycles of strain for the two cycling methods in both the annealed and cold worked states. In the annealed state, both types of cycling produced the same ultimate stress change, but the strain hardening characteristics differ; with thermal cycling the initial stress change is initially lower and the strain hardening is more marked. For prior cold worked specimens, thermal cycling produces a stress change somewhat lower than strain cycling. The strain softening is also less pronounced; thus the plastic strain change is larger for the thermally cycled specimen.

Figure A1.29 shows that there is approximately a four fold decrease in life under thermal cycling from the life under strain cycling; this is true of both material conditions.

From the results in Figure A1.30, an expression of the form

$$N^{K}\Delta\varepsilon_{p} = C$$

may be written as:

$$N^{0.43}\Delta\varepsilon_{p} = 0.28$$

5. COFFIN, L.F. Jr.

Strain cycling and thermal stress fatigue

Experimental results of constant temperature cyclic strain tests

The work on Johansson, Low, Baldwin,Sokol and Coffin and Stout is presented in the form of plots of plastic strain range against cycles to failure to illustrate the validity of the empirical expression.

$$N^{0.5}\Delta\varepsilon_{p} = C$$

in describing strain cycling life at constant temperature. The validity of the expression for $N = \frac{1}{4}$, i.e. the static test, is also demonstrated. Materials tested ranged from chromium steels, AlSl type 347 stainless steels to aluminium alloys.

Comparison of cyclic temperature and constant temperature strain cycling experiments. Coffin's work on AlSl type 347 stainless steel is used.

In Figure A1.31 constant temperature and cyclic temperature tests are compared using the representation of the plastic strain range versus cycles to failure. It is clear that the cyclic temperature data fall considerably below that obtained under constant temperature conditions, even below the 600°C constant temperature data. It is noted that in the cyclic temperature tests, the upper temperature never exceeded 600°C and yet the life is reduced. Possible reasons for this reduction, including surface finish, surface area, non-uniform temperature distributions and the methods of measuring strains are discussed.

Metallurgical effects of temperature cycling without external stresses are discussed.

APPENDIX 2

STRUCTURAL ANALYSIS OF THE FATIGUE TESTING MACHINE

A2.1 INTRODUCTION

The fatigue testing machine, idealised into a line diagram indicating the approximate neutral axes of the machine frame as shown in Figure 2.7, was divided into two systems: a basic system of a single channel containing mechanism loads only, and a redundant system of three channels containing the redundant loads at the common centre joint, as indicated in Figure 2.8. The displacement analysis was based on the compatability of the relative displacements of the centre joint under the two systems of loading. Referring to Figure 2.8 and denoting:

δ as the relative displacement of F

δ_{10} as the relative displacement of F_1 for unit specimen load

δ_{11} as the relative displacement of F_2 for unit redundant load

then $\delta = \delta_{10} + X\delta_{11} = 0$

where $X =$ magnitude of the redundant load for unit specimen load.

Applying the unit load theorem to each system in turn:

$$\delta_{10} = \int \frac{M\bar{M}}{EI} ds + \int \frac{P\bar{P}}{AE} ds = \int \frac{M_o M_1}{EI} ds + \int \frac{P_o P_1}{AE} ds$$

$$\delta_{11} = \int \frac{M\bar{M}}{EI} ds + \int \frac{P\bar{P}}{AE} ds = \int \frac{M_1^2}{EI} ds + \int \frac{P_1^2}{AE} ds$$

where M_o and P_o are the moment and end load distributions in the basic system and M_1 and P_1 are the moment and end load distributions in the redundant system. Then from the compatability condition:

$$X = -\frac{\delta_{10}}{\delta_{11}}.$$

The complete moment and end load distributions for the complete

structure are then given by:

$$M = M_o + XM_1 ; \qquad P = P_o + XP_1$$

Reapplication of the unit load theorem to both the complete structure and the operating mechanism enabled the relative displacement of the testing machine between the specimen holders to be determined from:

$$\delta_m = \int \frac{M\bar{M}}{EI} ds + \int \frac{P\bar{P}}{AE} ds = \int \frac{M_o(M_o + XM_1)}{EI} ds + \int \frac{P_o(P_o + XP_1)}{AE} ds$$

Specimen displacement $\delta_s = \frac{Pl_s}{A_s E}$,

hence machine to specimen stiffness ratio $= \frac{\delta_s}{\delta_m}$,

and accuracy of specimen displacement $\alpha = \left(1 - \frac{\delta_s}{\delta_s + \delta_m}\right) \times 100\%$.

A2.2 DETERMINATION OF REDUNDANT LOADS

The design case selected was for a single loaded channel, giving the most severe asymmetric loading case, since with two or three loaded channels the combined loading is decreased by the out of phase loads of opposite sign in the other channels.

The redundant loads X_1, X_2 and X_3 in channels A, B and C shown in Figure 2.8 were simplified by consideration of the load equilibrium. From a consideration of the equilibrium of point F_2:

$$X_{1A} = X_{1B} = X_{1C},$$

$$X_{2A} = -2X_{2B} = -2X_{2C},$$

and $X_{3A} = X_{3B} = X_{3C}$.

From a consideration of the equilibrium of each individual channel,

$$X_2 = 0$$

and $X_3 = -aX_1$.

Hence the problem of the determination of the redundant loads is only concerned with the magnitude of X_1.

The moment and end load distributions caused by unit specimen load and unit redundant load are shown in Figures 2.9 and 2.10 respectively. The integrals $\int \frac{M_o M_1}{EI} ds$, $\int \frac{P_o P_1}{AE} ds$ etc., were evaluated by graphical integration, for which the variations in I and A around the structure were determined and are shown in Figure 2.11. Figure 2.12 lists the component contributions to δ_{10} and δ_{11} from which the magnitude of the redundant load X_1 was calculated,

$$\text{i.e. } X_1 = \frac{-\delta_{10}}{\delta_{11}} = \frac{-1.3801 \times 10^{-6}}{219.95 \times 10^{-6}}$$

$$\text{i.e. } X_1 = -0.00627$$

The final moment and end load distributions for the complete structure are therefore given by:

$$M = M_o + X_1 M_1 = M_o - 0.00627 M_1$$

$$P = P_o + X_1 P_1 = P_o - 0.00627 P_1$$

which are shown in Figure 2.13.

A2.3 DETERMINATION OF THE RELATIVE DISPLACEMENT BETWEEN THE SPECIMEN HOLDERS

With unit loads applied to the specimen holders, in the complete structure, the unit load theorem was applied in the previous manner to both the machine frame and the straining mechanism, the respective displacements being calculated from:

$\delta_{FRAME} = \int \frac{M_o M}{EI} ds + \int \frac{P_o P}{AE} ds$ where M and P are given in Figure 2.13.

$\delta_{MECH} = \int \frac{M_o^2}{EI} ds + \int \frac{P_o^2}{AE} ds$ since $M = M_o$ and $P = P_o$ for the mechanism.

The moment and end load distributions for the mechanism and the relevant variations in I and A are shown in Figure 2.14. The variations in the products $\frac{MM_o}{I}$, $\frac{PP_o}{A}$ etc. around the entire testing machine, which indicate those areas which contribute most significantly to the overall machine displacement, are shown in Figures 2.15 to 2.17, and Figure 2.18 lists the component displacements obtained by graphical integration of these curves.

Hence $\delta_{FRAME} = 0.261339 \times 10^{-6}$ ins.

$\delta_{MECH} = 0.261065 \times 10^{-6}$ ins.

$\therefore \delta_m = 0.52240 \times 10^{-6}$ ins.

Specimen displacement $\delta_s = 6.84 \times 10^{-6}$ ins.

Stiffness ratio = 13.10

Accuracy of specimen displacement $\alpha = 7.1\%$

APPENDIX 3

AN ANALYSIS OF THE BUCKLING BEHAVIOUR OF A SLENDER ENCASTRÉ STRUT UNDER DISPLACEMENT CONTROLLED CONDITIONS

A3.1 GEOMETRIC RELATIONSHIP

Under the action of an end displacement a strut with an initial curvature will assume a new curvature, the change in position of an element of which is shown in Figure 3.1. The contribution of this element to the end displacement Q is given by:

$$\delta Q = (\delta s - \delta x) - (\delta s_o - \delta x_o) + \delta e$$

where δe = the contribution to the compressive axial strain e under the action of the associated end load P

and suffix o indicates the original unloaded condition

Since $\delta e = \frac{P \delta x}{AE}$

and $(\delta s)^2 \simeq (\delta x)^2 + (\delta y)^2$

or $\delta s \simeq \left[1 + \left(\frac{\delta y}{\delta x}\right)^2\right]^{\frac{1}{2}} \delta x,$

the expression for δQ becomes:

$$\delta Q = \left[1 + \left(\frac{\delta y}{\delta x}\right)^2\right]^{\frac{1}{2}} \delta x - \delta x - \left[1 + \left(\frac{\delta y_o}{\delta x_o}\right)^2\right]^{\frac{1}{2}} \delta x_o - \delta x_o + \frac{P \delta x}{AE}$$

In the limit, as δx tends to zero, this may be written:

$$dQ = \left[1 + \left(\frac{dy}{dx}\right)^2\right]^{\frac{1}{2}} dx - dx - \left[1 + \left(\frac{dy_o}{dx_o}\right)^2\right]^{\frac{1}{2}} dx_o - dx_o + \frac{P dx}{AE}$$

Expanding the square root as a series gives:

$$dQ = \left[\frac{1}{2}\left(\frac{dy}{dx}\right)^2 - \frac{1}{8}\left(\frac{dy}{dx}\right)^4 + \frac{1}{16}\left(\frac{dy}{dx}\right)^6 - \ldots\right] dx - \left[\frac{1}{2}\left(\frac{dy_o}{dx_o}\right)^2 - \frac{1}{8}\left(\frac{dy_o}{dx_o}\right)^4 + \left(\frac{dy_o}{dx_o}\right)^6 - \ldots\right] dx_o + \frac{P dx}{AE}$$

The complete end displacement is obtained by integration over the length of the strut:

$$Q = \int_0^L \left[\frac{1}{2}\left(\frac{dy}{dx}\right)^2 - \frac{1}{8}\left(\frac{dy}{dx}\right)^4 + \frac{1}{16}\left(\frac{dy}{dx}\right)^6 - \cdots\right] dx - \int_0^{L_o} \left[\frac{1}{2}\left(\frac{dy_o}{dx_o}\right)^2 - \frac{1}{8}\left(\frac{dy_o}{dx_o}\right)^4 + \frac{1}{16}\left(\frac{dy_o}{dx_o}\right)^6 - \cdots\right] dx_o + \frac{P}{AE}\int_0^L dx.$$

This geometric relationship contains the unknown term of end load, which may be evaluated from a consideration of the bending moment conditions.

A3.2 DETERMINATION OF THE END LOAD

The end load may be determined by use of the engineer's bending theory expression relating bending moment and change of curvature, and the appropriate boundary conditions,

$$\text{i.e.} \quad M = -EI\left[\frac{d^2y}{dx^2} - \frac{d^2y_o}{dx_o^2}\right]$$

For an encastré strut with the assumed curvature shown in Figure 3.2, the bending moment at a distance x from one end is given by:

$$M = Py - M_E = -EI\left[\frac{d^2y}{dx^2} - \frac{d^2y_o}{dx_o^2}\right]$$

where M_E = the end fixing moment.

The shape of an encastré strut with initial curvature may be conveniently expressed in the form:

$$y_o = \frac{b_o}{2}\left(1 - \cos\frac{2\pi x}{L_o}\right)$$

which satisfies all the boundary conditions indicated in Figure 3.2, the suffix o indicating the unloaded condition. The selection of this particular form of expression rather than any of the alternatives

(e.g. parabola or circular arc for the central half of the strut) is justified by the simplification of the subsequent mathematical processes involved in this analysis. In addition it affords a direct correlation with the Euler solution to the buckling of a perfectly straight strut. Assuming that the form of the curved shape is preserved on loading, with only the coefficients changing in magnitude, the loaded curved shape may then be expressed as:

$$y = \frac{b}{2}\left(1 - \cos\frac{2\pi x}{L}\right)$$

where b and L are current values of the central lateral deflection and length respectively.

The curved shape of the loaded strut passes through a point of inflexion at $x = \frac{L}{4}$ so that:

$$\frac{d^2y}{dx^2} = 0 \text{ and } y = \frac{b}{2}.$$

For $L \simeq L_o$, $\frac{d^2y_o}{dx_o^2} \simeq 0$.

Thus $M = P.\frac{b}{2} - M_E = 0$

and $M_E = P.\frac{b}{2}$.

In the general expression for the bending moment:

$$M = Py - P\frac{b}{2} = -EI\left[\frac{d^2y}{dx^2} - \frac{d^2y_o}{dx_o^2}\right].$$

$$\text{Thus } P = \frac{-EI}{\left(y - \frac{b}{2}\right)}\left[\frac{d^2y}{dx^2} - \frac{d^2y_o}{dx_o^2}\right].$$

Hence both the end displacement and end load may be expressed in terms of the central deflection and the assumed shape of the deflected strut.

A3.3 ALIGNMENT ERRORS

Further errors in alignment of the ends of an encastré strut may be expressed by considering them to be made up of two separate types of deflection of the strut axis, as indicated in Figure 3.3. Misalignment due to the slope of the strut axis may be expressed simply as:

$$y = mx$$

and parallel relative displacement of the strut ends may be expressed as:

$$y = \frac{c}{2}\left(1 - \cos\frac{\pi x}{L}\right)$$

where c = parallel relative displacement of the strut ends. The final expression for the curved shape of the strut with all three sources of misalignment is then given by:

$$y_o = \frac{b_o}{2}\left(1 - \cos\frac{2\pi x}{L_o}\right) + \frac{c}{2}\left(1 - \cos\frac{\pi x}{L_o}\right) + mx.$$

It is assumed that the loaded shape can be similarly expressed by:

$$y = \frac{b}{2}\left(1 - \cos\frac{2\pi x}{L}\right) + \frac{c}{2}\left(1 - \cos\frac{\pi x}{L}\right) + mx$$

c and m being independent of the loaded condition of the strut.

Application of these two expressions to the general expression for the end displacement, taking only the first term of the expansion of the square root, yields:

$$Q = \frac{1}{2}\int_0^L\left[\frac{b\pi}{L}\sin\frac{2\pi x}{L} + \frac{C\pi}{2L}\sin\frac{\pi x}{L} + m\right]^2 dx - \frac{1}{2}\int_0^{L_o}\left[\frac{b_o\pi}{L_o}\sin\frac{2\pi x}{L_o} + \frac{C\pi}{2L_o}\sin\frac{\pi x}{L_o} + m\right]^2 dx + \int_0^L\frac{P dx}{AE}.$$

On integration and observing that $\frac{m^2}{2}\left[L_o - L\right] = \frac{m^2 Q}{2}$, this gives

$$Q = \left[\frac{1}{1 + \frac{m^2}{2}}\right]\left[\frac{\pi^2}{4}\left(\frac{b^2}{L} - \frac{b_o^2}{L_o}\right) + \frac{c^2\pi^2}{16}\left(\frac{1}{L} - \frac{1}{L_o}\right) + \frac{PL}{AE}\right].$$

The inclusion of alignment errors also modifies the expression for the end load. Considering the strut shape shown in Figure 3.3c, the point of inflexion is where the bending moment is zero:

$$\text{i.e. where } M = -EI\left[\frac{d^2y}{dx^2} - \frac{d^2y_o}{dx^2}\right] = 0$$

$$\text{i.e. where } \frac{d^2y}{dx^2} - \frac{d^2y_o}{dx^2} = 0$$

$$\text{i.e.} \left(\frac{2\pi^2 b}{L^2}\cos\frac{2\pi x}{L} + \frac{c\pi^2}{2L^2}\cos\frac{\pi x}{L}\right) - \left(\frac{2\pi^2 b_o}{L_o^2}\cos\frac{2\pi x}{L_o} + \frac{c\pi^2}{2L_o^2}\cos\frac{\pi x}{L_o}\right) = 0$$

Since L and L_o differ only very slightly in practical cases, the assumption can be made that:

$$\cos\frac{2\pi x}{L} = \cos\frac{2\pi x}{L_o} \quad \text{and} \quad \cos\frac{\pi x}{L} = \cos\frac{\pi x}{L_o}$$

$$\text{Then } 2\pi^2\left[\frac{b}{L^2} - \frac{b_o}{L_o^2}\right]\cos\frac{2\pi x}{L} + \frac{c\pi^2}{2}\left[\frac{1}{L^2} - \frac{1}{L_o^2}\right]\cos\frac{\pi x}{L} = 0$$

Writing $\cos\frac{2\pi x}{L}$ as $2\cos^2\frac{\pi x}{L} - 1$, the expression becomes

$$2\pi^2\left[\frac{b}{L^2} - \frac{b_o}{L_o^2}\right]\left[2\cos^2\frac{\pi x}{L} - 1\right] + \frac{c\pi^2}{2}\left[\frac{1}{L^2} - \frac{1}{L_o^2}\right]\cos\frac{\pi x}{L} = 0$$

from which

$$\cos\frac{\pi x}{L} = \frac{-\frac{c\pi^2}{2}\left[\frac{1}{L^2} - \frac{1}{L_o^2}\right] \pm \sqrt{32\pi^4\left[\frac{b}{L^2} - \frac{b_o}{L_o^2}\right] + \frac{c^2\pi^4}{4}\left[\frac{1}{L^2} - \frac{1}{L_o^2}\right]^2}}{8\pi^2\left[\frac{b}{L^2} - \frac{b_o}{L_o^2}\right]}.$$

Considering firstly the expression under the square root.

With the strut slightly buckled $b > b_o$ and hence

$$\left[\frac{b}{L^2} - \frac{b_o}{L_o^2}\right]^2 > \left[\frac{1}{L^2} - \frac{1}{L_o^2}\right]^2.$$

In addition, for $b > c$

$$32\pi^4\left[\frac{b}{L^2} - \frac{b_o}{L_o^2}\right]^2 \gg \frac{c^2\pi^4}{4}\left[\frac{1}{L^2} - \frac{1}{L_o^2}\right]^2$$

and as b increases, the first term dominates the square root.

Thus the expression for $\cos\frac{\pi x}{L}$ may be reduced to:

$$\cos\frac{\pi x}{L} = \frac{-\frac{c\pi^2}{2}\left[\frac{1}{L^2} - \frac{1}{L_o^2}\right] \pm 4\pi^2\sqrt{2}\left[\frac{b}{L^2} - \frac{b_o}{L_o^2}\right]}{8\pi^2\left[\frac{b}{L^2} - \frac{b_o}{L_o^2}\right]}.$$

By a similar argument, as b increases, the influence of the first term diminishes and the expression may be further reduced to:

$$\cos\frac{\pi x}{L} = \frac{\pm 4\pi^2\sqrt{2}\left[\frac{b}{L^2} - \frac{b_o}{L_o^2}\right]}{8\pi^2\left[\frac{b}{L^2} - \frac{b_o}{L_o^2}\right]}$$

$$\text{i.e.} \quad \cos\frac{\pi x}{L} = \pm\frac{1}{\sqrt{2}}$$

$$\text{and} \quad x = \frac{L}{4}.$$

Thus the inclusion of alignment errors has negligible effect on the position of the point of inflexion of the curved shape of the loaded strut. The error caused by the simplifying assumptions is greatest with small displacements, but diminishes rapidly as the displacements increase as the following example illustrates.

Example:

With the values: $L_o = 10''$, $b_o = 0.01''$ and $c = 0.1''$

and $L = 9.95''$, $b = 0.11''$

then $\left[\frac{b}{L^2} - \frac{b_o}{L_o^2}\right]^2 = 1.02 \times 10^{-6}$; $\left[\frac{1}{L^2} - \frac{1}{L_o^2}\right] = 1.02 \times 10^{-8}$.

$32\pi^4\left[\frac{b}{L^2} - \frac{b_o}{L_o^2}\right]^2 \simeq 3.2 \times 10^{-3}$; $\frac{c^2\pi^4}{4}\left[\frac{1}{L^2} - \frac{1}{L_o^2}\right] \simeq 2.5 \times 10^{-9}$.

$4\pi^2\sqrt{2}\left[\frac{b}{L^2} - \frac{b_o}{L_o^2}\right] \simeq 5.6 \times 10^{-2}$; $\frac{c\pi^2}{2}\left[\frac{1}{L^2} - \frac{1}{L_o^2}\right] \simeq 5.05 \times 10^{-4}$.

Since $y = \frac{b}{2}\left(1 - \cos\frac{2\pi x}{L}\right) + \frac{c}{2}\left(1 - \cos\frac{\pi x}{L}\right) + mx$

at $x = \frac{L}{4}$, $y = \frac{b}{2} + \frac{c}{2}\left(1 - \cos\frac{\pi}{4}\right) + \frac{mL}{4}$.

The bending moment at the point of inflexion at $x = \frac{L}{4}$ is given by:

$$M = Py - M_E = 0$$

i.e. $$M_E = P\left[\frac{b}{2} + \frac{c}{2}\left(1 - \cos\frac{\pi}{4}\right) + \frac{mL}{4}\right].$$

Therefore, in the general expression for the bending moment:

$$M = Py - M_E = P\left[\frac{b}{2}\left(1 - \cos\frac{2\pi x}{L}\right) + \frac{c}{2}\left(1 - \cos\frac{\pi x}{L}\right) + mx\right] - P\left[\frac{b}{2} + \frac{c}{2}\left(1 - \cos\frac{\pi}{4}\right) + \frac{mL}{4}\right]$$

i.e. $$M = P\left[m\left(x - \frac{L}{4}\right) + \frac{c}{2}\left(\cos\frac{\pi}{4} - \cos\frac{\pi x}{L}\right) - \frac{b}{2}\cos\frac{2\pi x}{L}\right].$$

$$\text{Since } M = -EI\left[\frac{d^2y}{dx^2} - \frac{d^2y_o}{dx^2}\right]$$

$$P\left[m\left(x - \frac{L}{4}\right) + \frac{c}{2}\left(\cos\frac{\pi}{4} - \cos\frac{\pi x}{L}\right) - \frac{b}{2}\cos\frac{2\pi x}{L}\right] = -EI\left[2\pi^2\left(\frac{b}{L^2} - \frac{b_o}{L_o^2}\right)\cos\frac{2\pi x}{L} + \frac{c\pi^2}{2}\left(\frac{1}{L^2} - \frac{1}{L_o^2}\right)\cos\frac{\pi x}{L}\right]$$

i.e. $$P = \frac{-EI\left[2\pi^2\left(\frac{b}{L^2} - \frac{b_o}{L_o^2}\right)\cos\frac{2\pi x}{L} + \frac{c\pi^2}{2}\left(\frac{1}{L^2} - \frac{1}{L_o^2}\right)\cos\frac{\pi x}{L}\right]}{\left[m\left(x - \frac{L}{4}\right) + \frac{c}{2}\left(\cos\frac{\pi}{4} - \cos\frac{\pi x}{L}\right) - \frac{b}{2}\cos\frac{2\pi x}{L}\right]}$$

at $x = \frac{L}{2}$ the expression reduces to:

$$P = \frac{P_E\left[\frac{L_o^2}{L^2} - \frac{b_o}{b}\right]}{\left[1 + \frac{c}{b}\cos\frac{\pi}{4} + \frac{mL}{2b}\right]}$$

where $P_E = \frac{4\pi^2 EI}{L_o^2}$, the Euler load for an encastré strut.

From this expression, it may be seen that the inclusion of errors of alignment reduces the value of the load at the centre of the buckled strut.

A3.4 SURFACE STRESSES

The surface stress on either face of the buckled strut at mid length is given by:

$$\sigma = -\frac{P}{A} \pm \frac{Mh}{I}$$

where h = half the thickness of the strut.

Hence $\sigma = P\left[-\frac{1}{A} \pm \frac{h}{2I}\left(b + c\cos\frac{\pi}{4} + \frac{mL}{2}\right)\right]$

i.e. $\sigma = P_E\left[\frac{L_o^2}{L^2} - \frac{b_o}{b}\right]\left[\pm \frac{hb}{2I} - \frac{1}{A\left(1 + \frac{c}{b}\cos\frac{\pi}{4} + \frac{mL}{2b}\right)}\right]$

FIGURE 1.1

TYPICAL TEMPERATURE VARIATION DURING FLIGHT

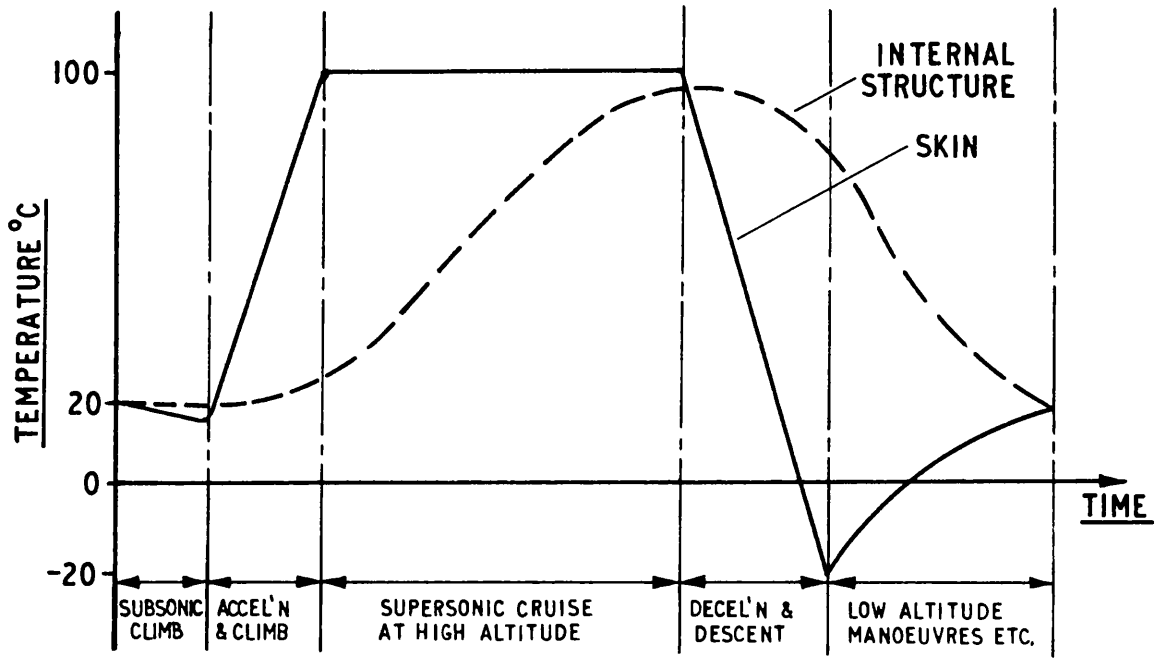

FIGURE 1.2

TYPICAL THERMAL STRESS VARIATION DURING FLIGHT

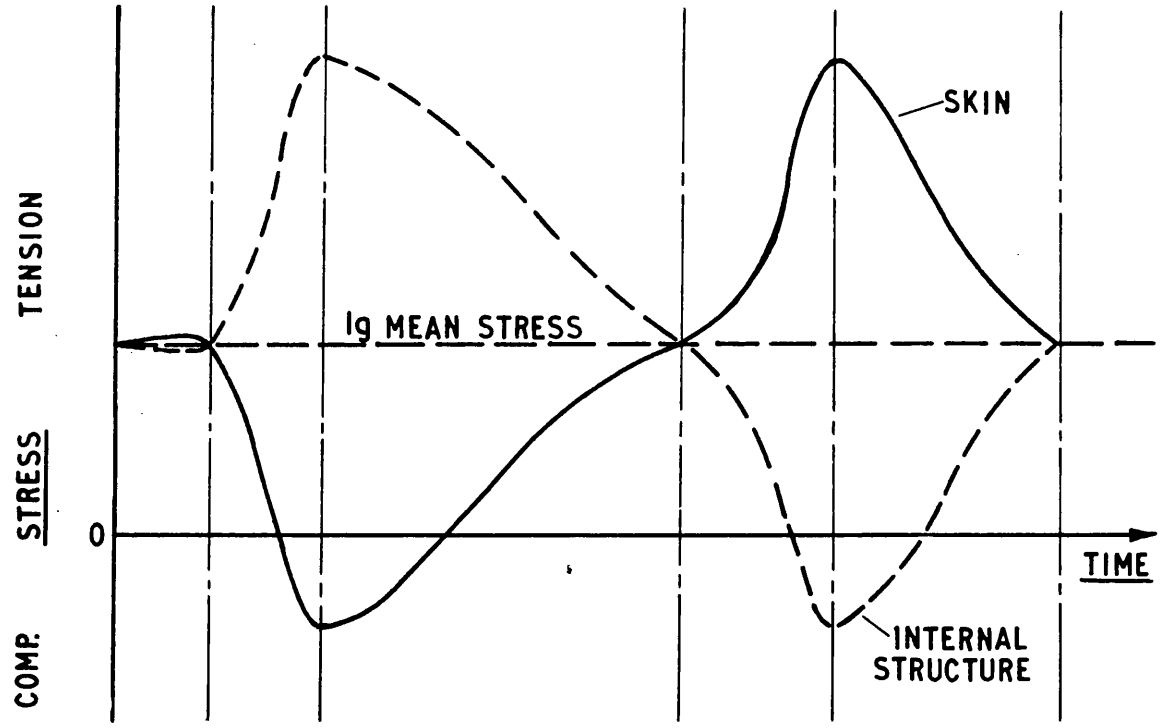

FIGURE 1.3

SECTION OF AIRCRAFT STRUCTURE INDICATING AREAS WHERE THERMAL STRESSES ARE MOST SIGNIFICANT

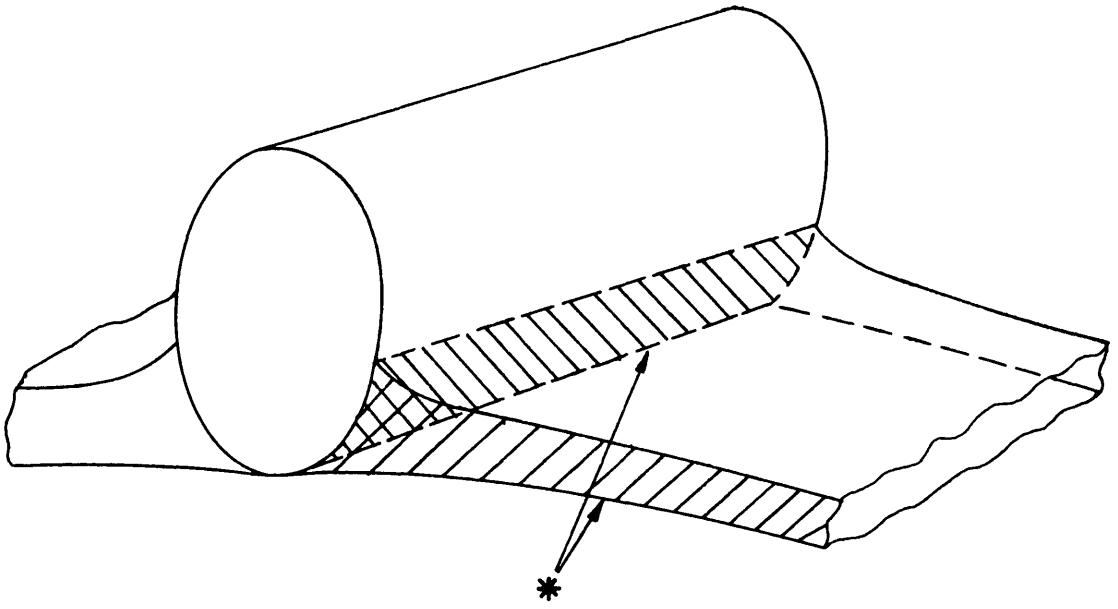

FIGURE 1.4

STRESS VARIATION OF AN UNSTABLE ELEMENT OF THE INTERNAL STRUCTURE

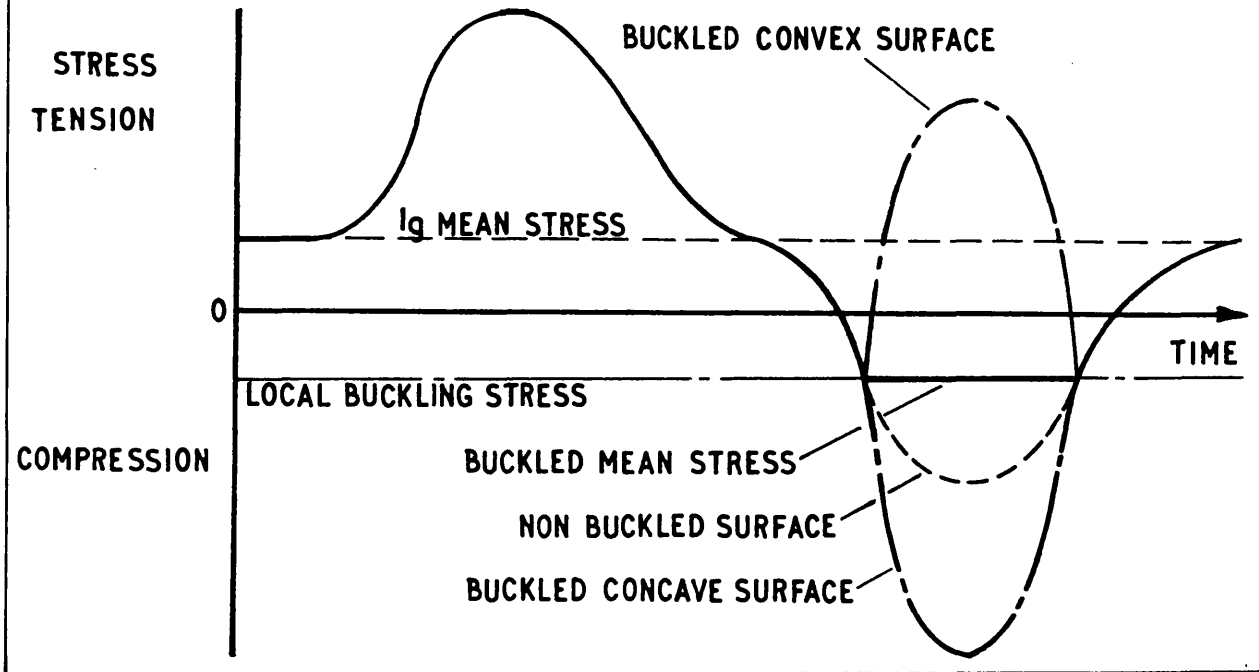

FIGURE 1.5

IDEALISATION OF WING WEB STRUCTURE INTO A SIMPLE I SECTION BEAM

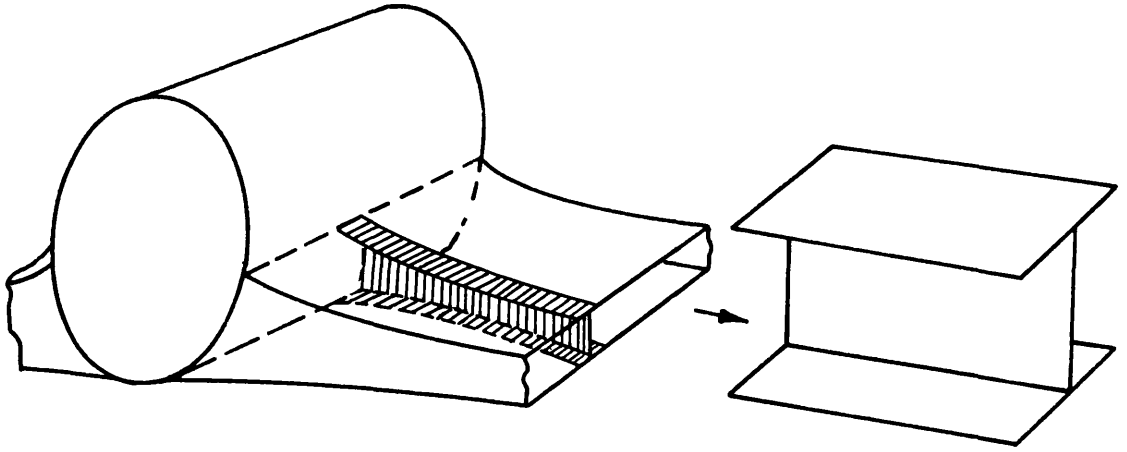

FIGURE 1.6

IDEALISATION OF WING MASKED SECTION OF FUSELAGE INTO A SIMPLE 3 BAY PANEL

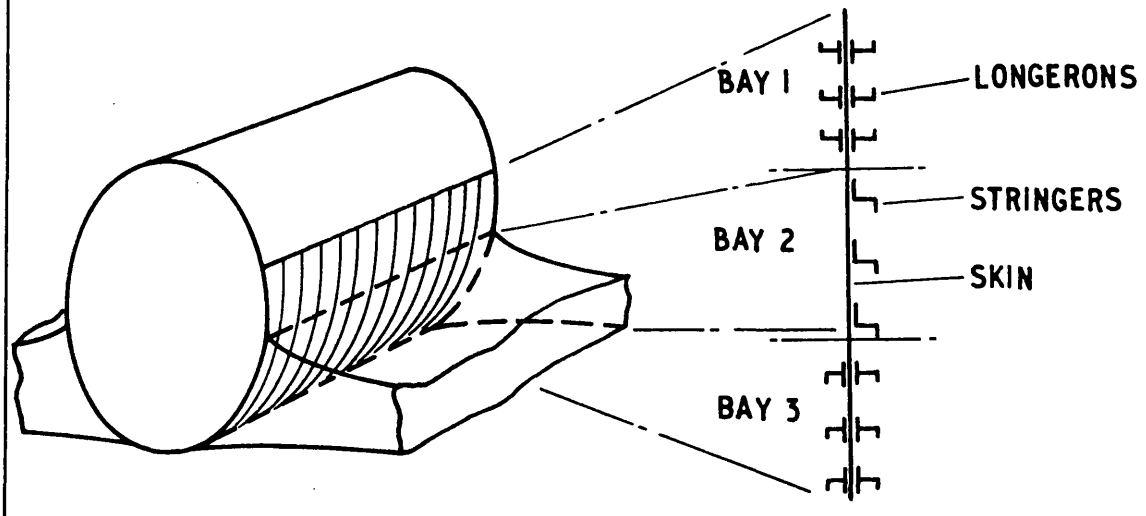

FIGURE 1.7

BLOCK DIAGRAM INDICATING THE RELATIONSHIP OF THE SECTIONS OF THIS REPORT

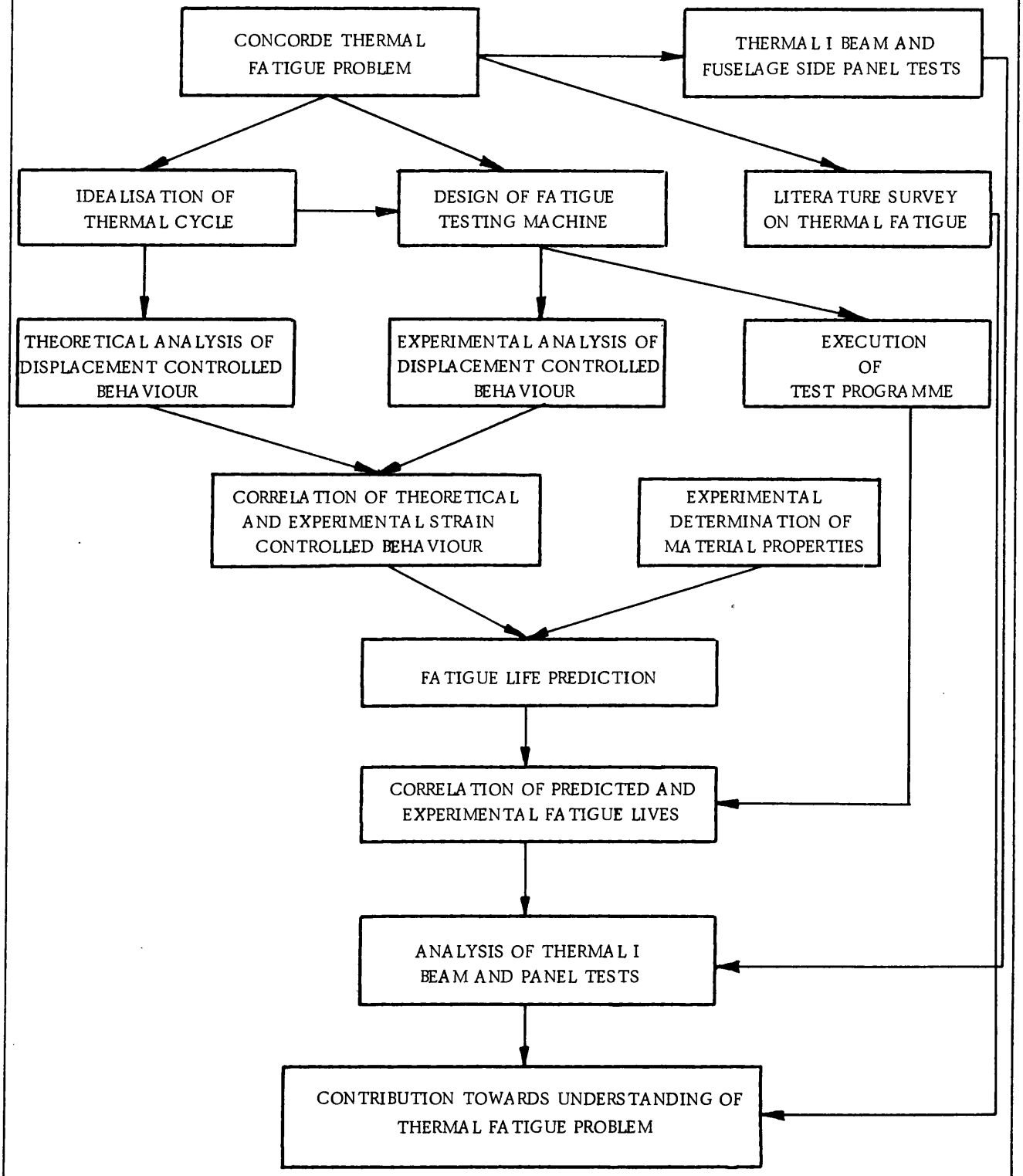

FIGURE 2.1

AN IDEALISED DEAD WEIGHT LOADING SYSTEM

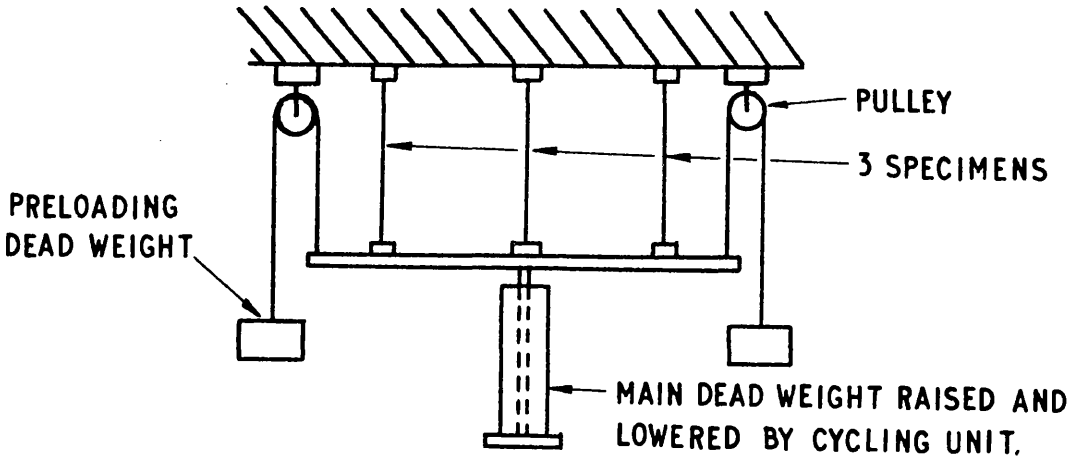

FIGURE 2.2

AN IDEALISED COILED SPRING LOADING SYSTEM

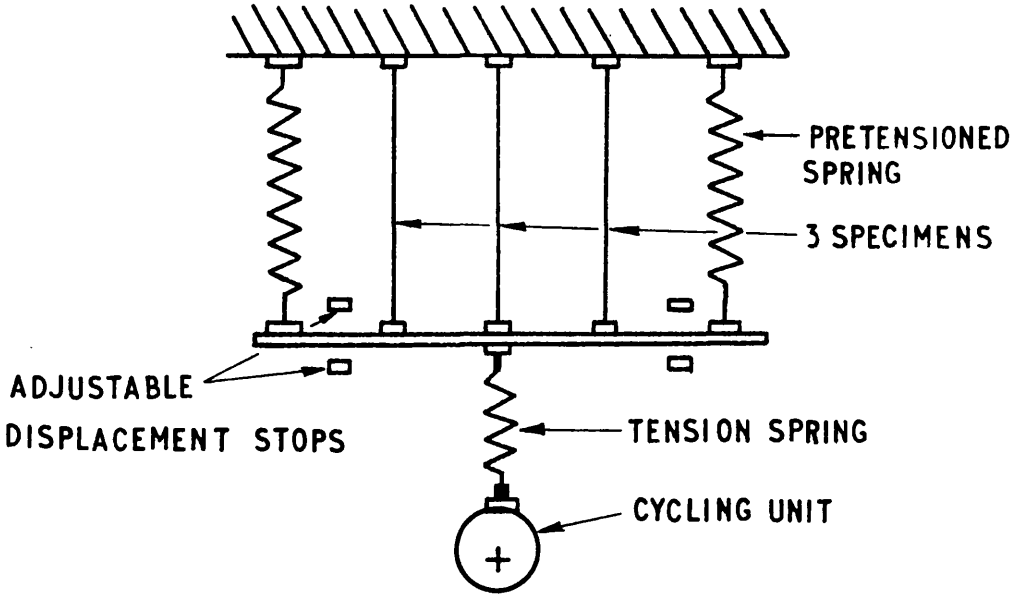

FIGURE 2.3

AN IDEALISED DISPLACEMENT CONTROLLED TESTING MACHINE

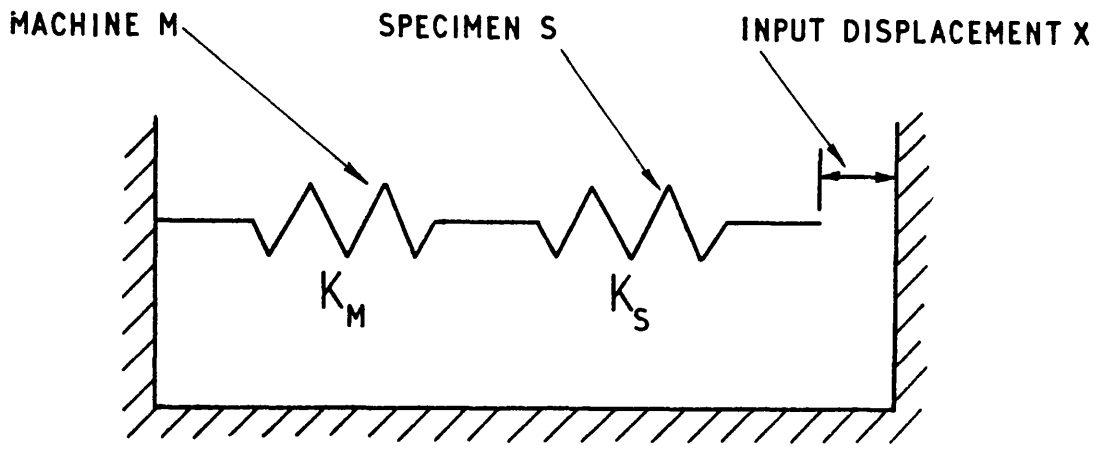

FIGURE 2.4

SIMPLE ARRANGEMENT OF AN IDEALISED DISPLACEMENT CONTROLLED TESTING MACHINE

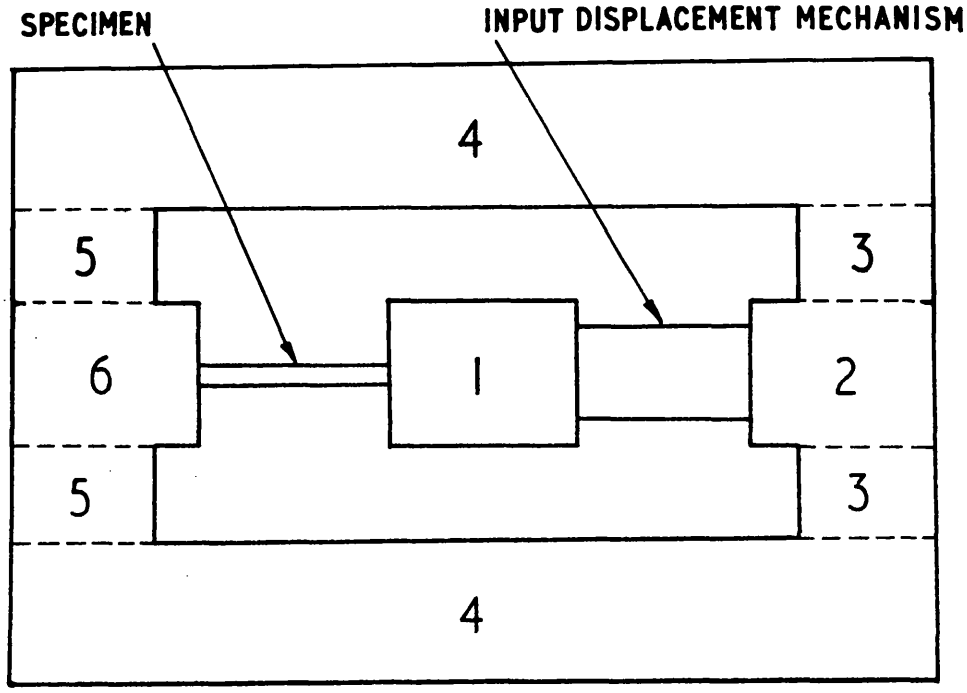

FIGURES 2.5,6

GENERAL ARRANGEMENT OF THE FATIGUE TESTING MACHINE

FIGURE 2.5A

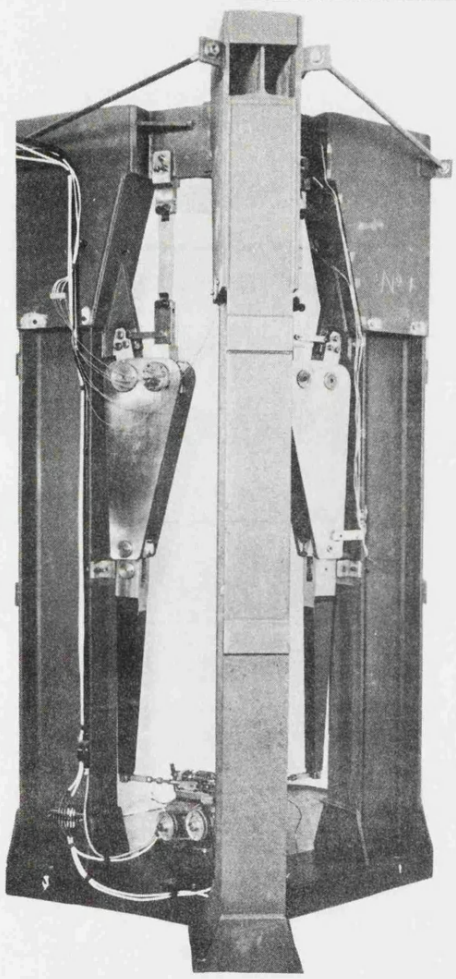

FIGURE 2.6

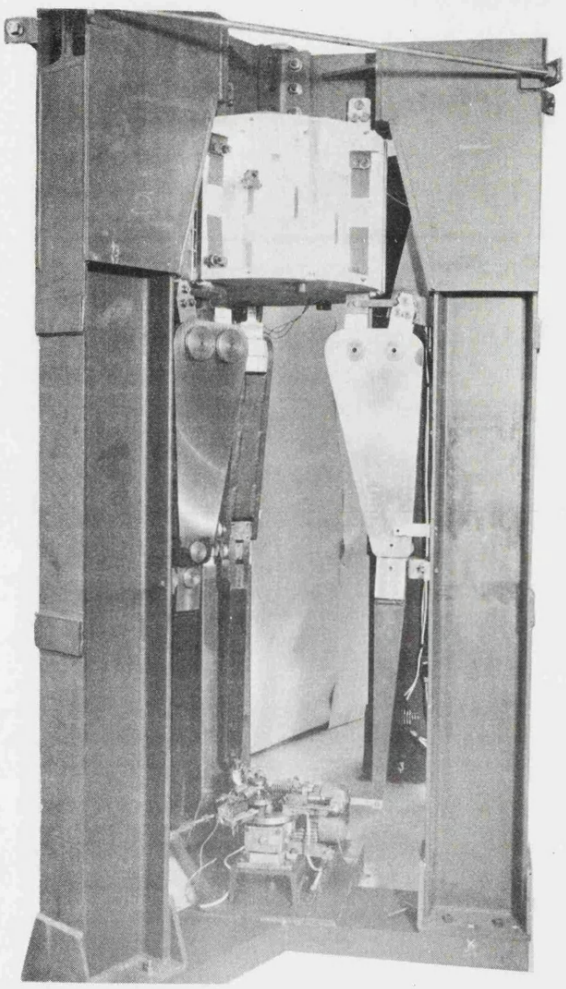

FIGURE 2.5B

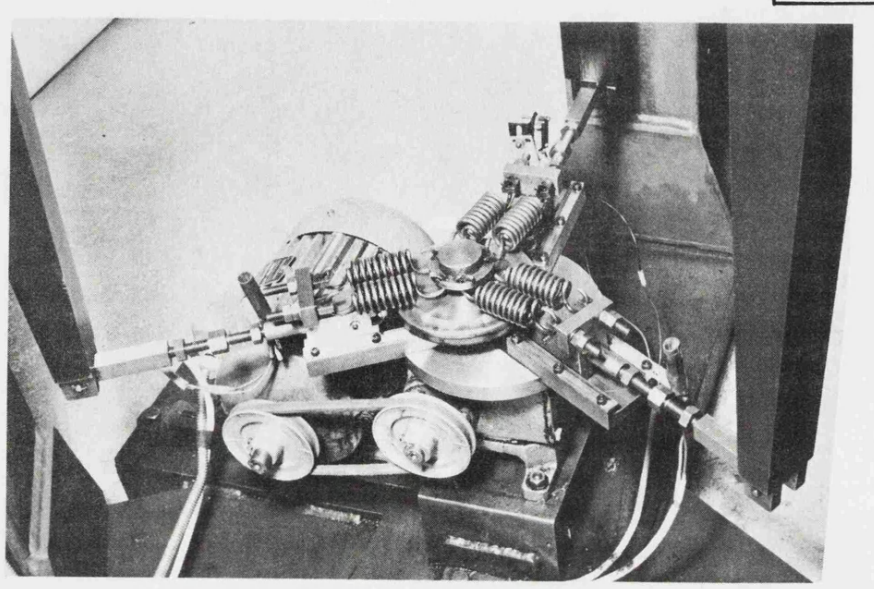

FIGURE 2.7

IDEALISATION OF TESTING MACHINE INTO FRAME AND MECHANISM: IDEALISED FRAME REPRESENTED BY CHAIN DOTTED LINES

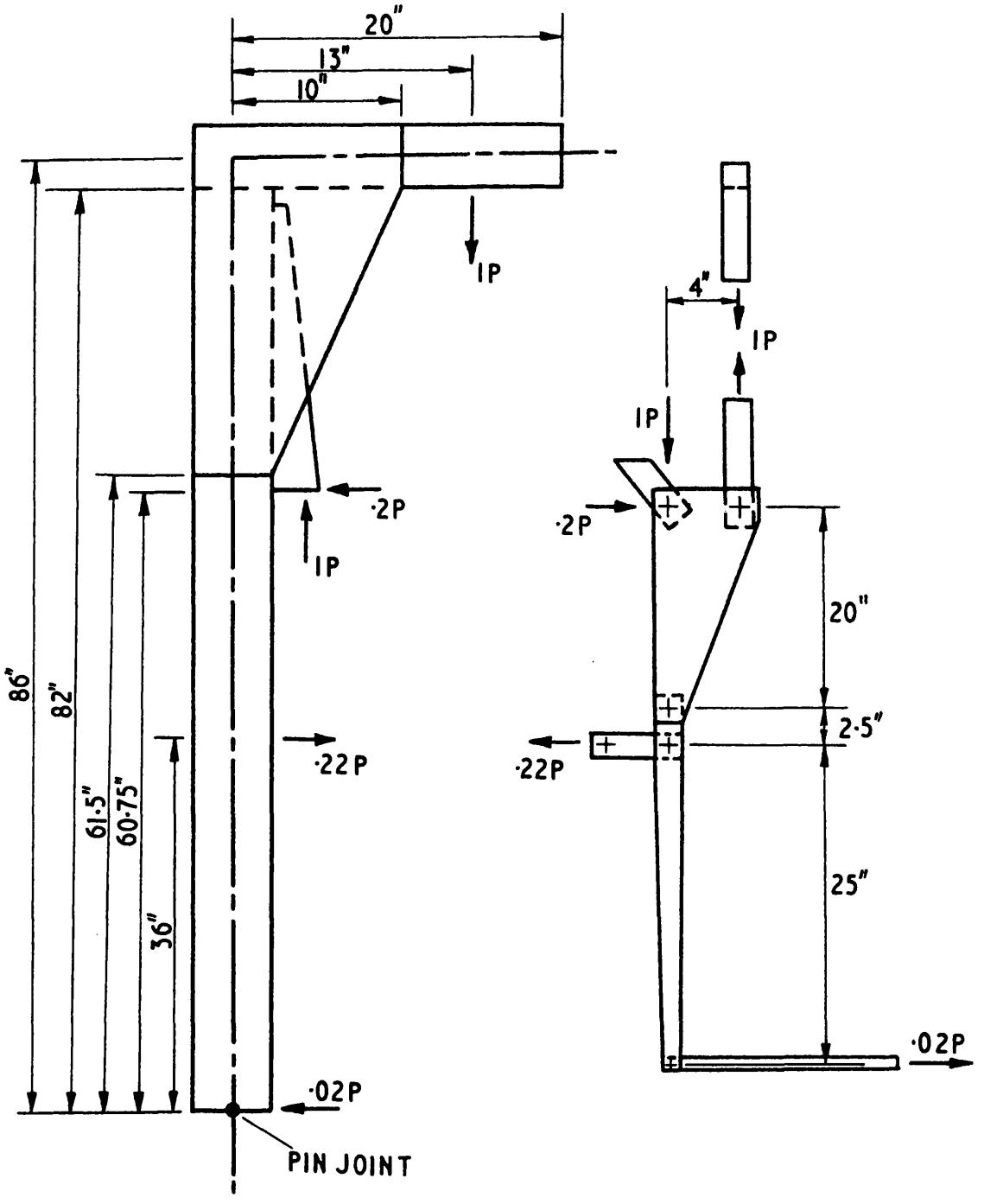

TESTING MACHINE IDEALISED FOR STRUCTURAL ANALYSIS

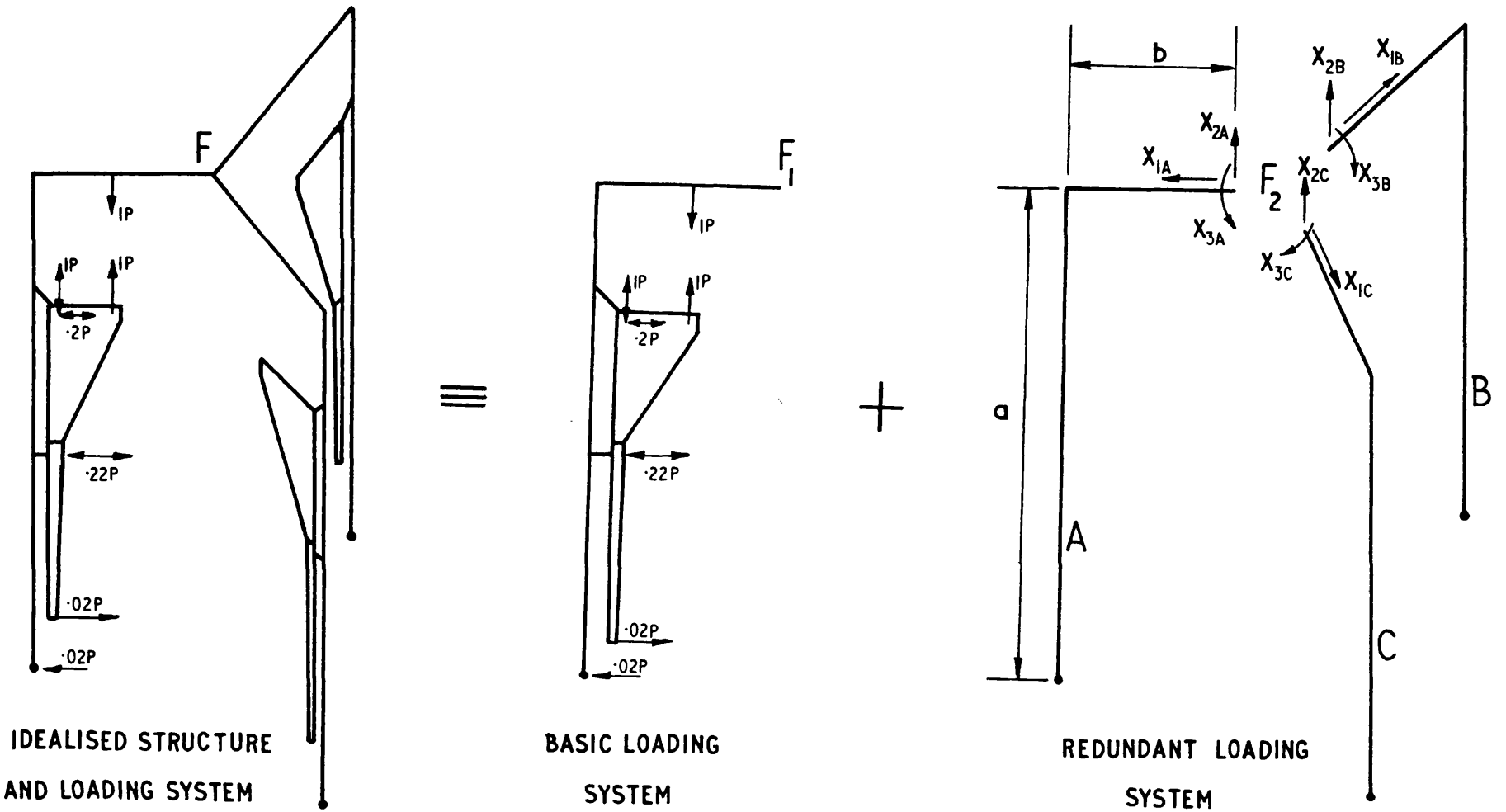

IDEALISED STRUCTURE AND LOADING SYSTEM

BASIC LOADING SYSTEM

REDUNDANT LOADING SYSTEM

FIGURE 2.8

FIGURE 2.9

LOADING, BENDING MOMENT AND END LOAD DISTRIBUTIONS FOR UNIT SPECIMEN LOAD

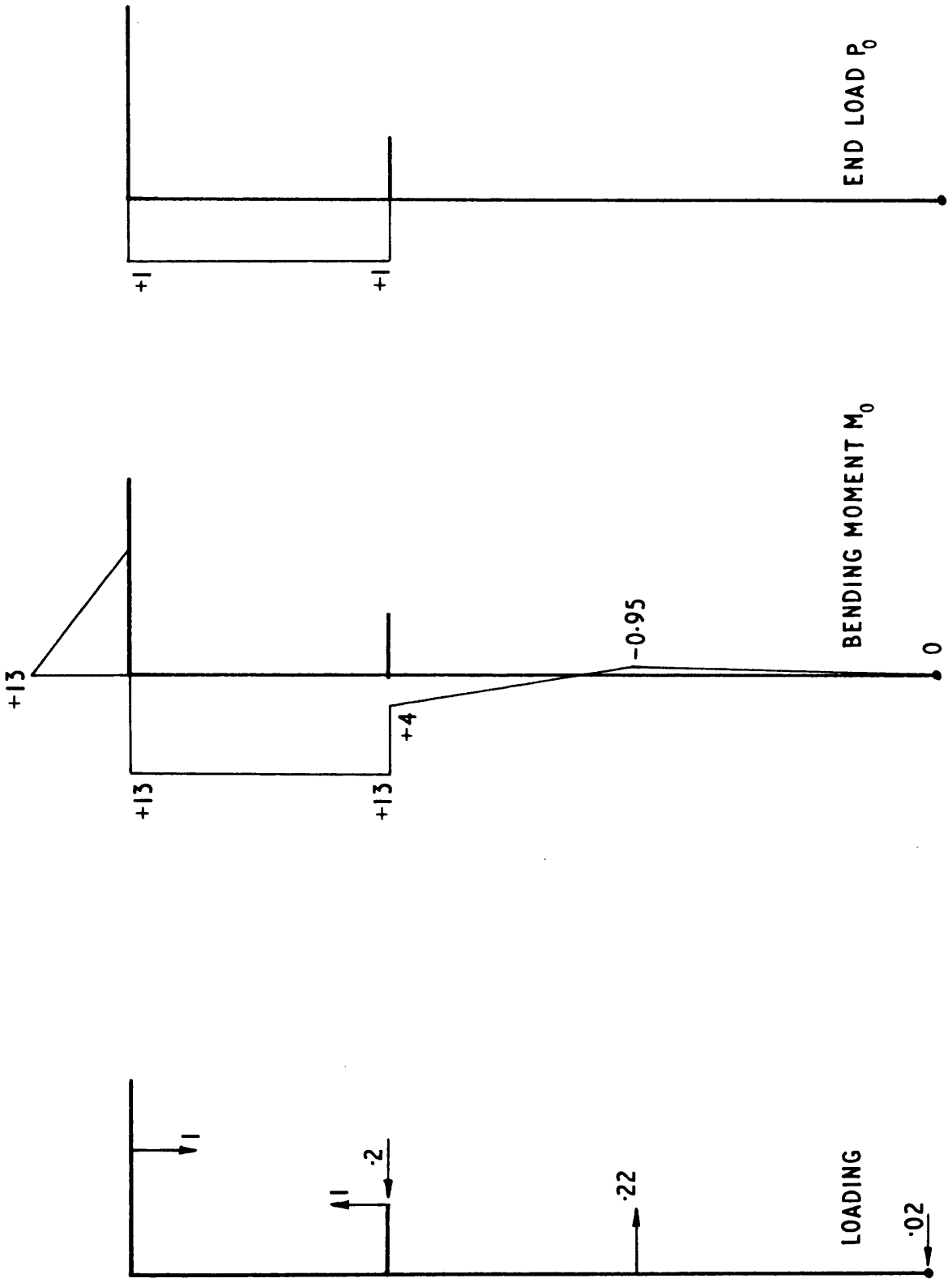

FIGURE 2.10

LOADING, BENDING MOMENT AND END LOAD DISTRIBUTIONS FOR UNIT REDUNDANT LOAD

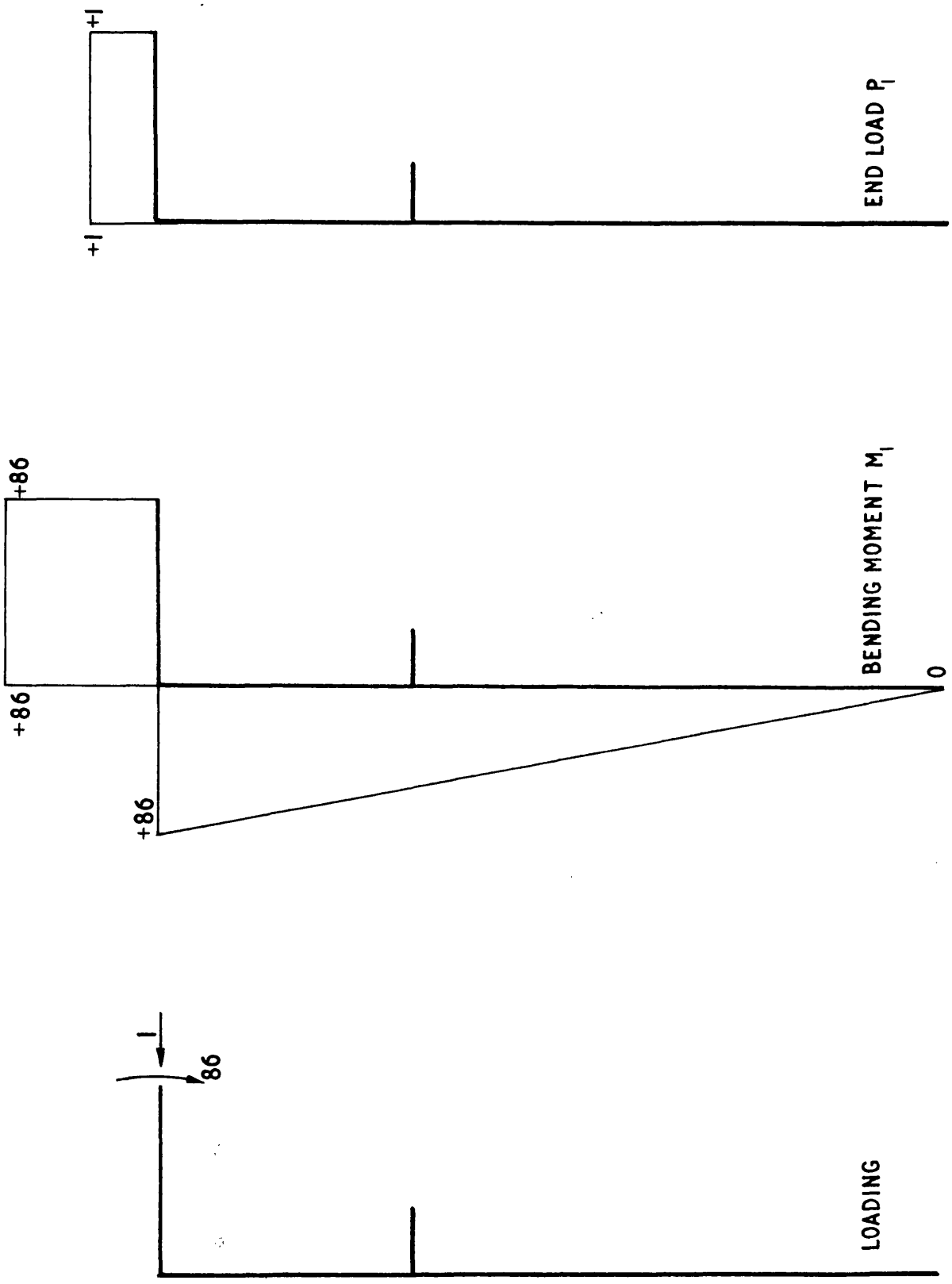

FIGURE 2.11

VARIATIONS OF I AND A, AND OF $\bar{M}^2$ AND $\bar{P}^2$ FOR UNIT SPECIMEN LOAD, AROUND THE MACHINE FRAME

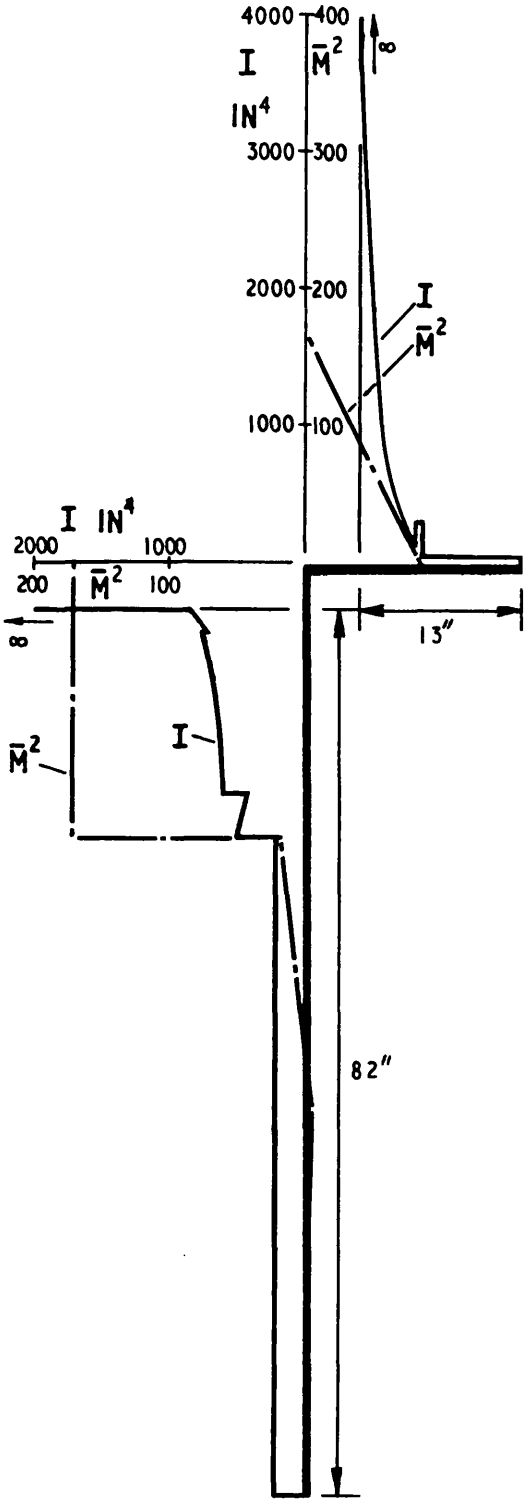

VARIATION OF I AND $\bar{M}^2$

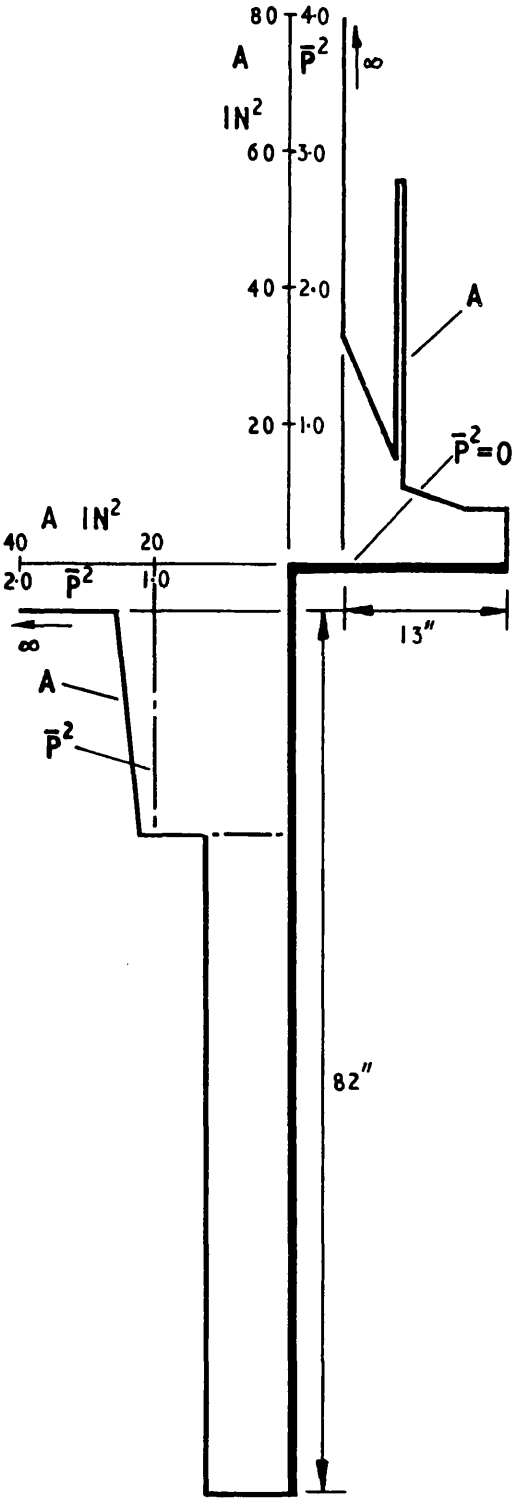

VARIATION OF A AND $\bar{P}^2$

FIGURE 2.12

COMPONENT CONTRIBUTIONS TO δ_{10} AND δ_{11}.

BASIC SYSTEM

COMPONENT	LOADING ACTION	DISPLACEMENT
FRAME TOP MEMBER	MOMENT $M_0 M_1$	$.3013 \times 10^{-6}$ INS.
	END LOAD $P_0 P_1$	0
FRAME SIDE MEMBER	MOMENT $M_0 M_1$	1.0788×10^{-6} INS.
	END LOAD $P_0 P_1$	0
TOTAL DISPLACEMENT δ_{10}		1.3801×10^{-6} INS.

REDUNDANT SYSTEM

COMPONENT	CHANNEL	LOADING ACTION	DISPLACEMENT
FRAME TOP MEMBER	A	MOMENT M_1^2	55.01×10^{-6} INS.
	B		55.01×10^{-6} INS.
	C		55.01×10^{-6} INS.
	A	END LOAD P_1^2	0.0439×10^{-6} INS.
	B		0.0439×10^{-6} INS.
	C		0.0439×10^{-6} INS.
FRAME SIDE MEMBER	A	MOMENT M_1^2	18.269×10^{-6} INS.
	B		18.269×10^{-6} INS.
	C		18.269×10^{-6} INS.
		END LOAD P_1^2	0
TOTAL DISPLACEMENT δ_{11}			219.950×10^{-6} INS.

FINAL BENDING MOMENT AND END LOAD DISTRIBUTIONS

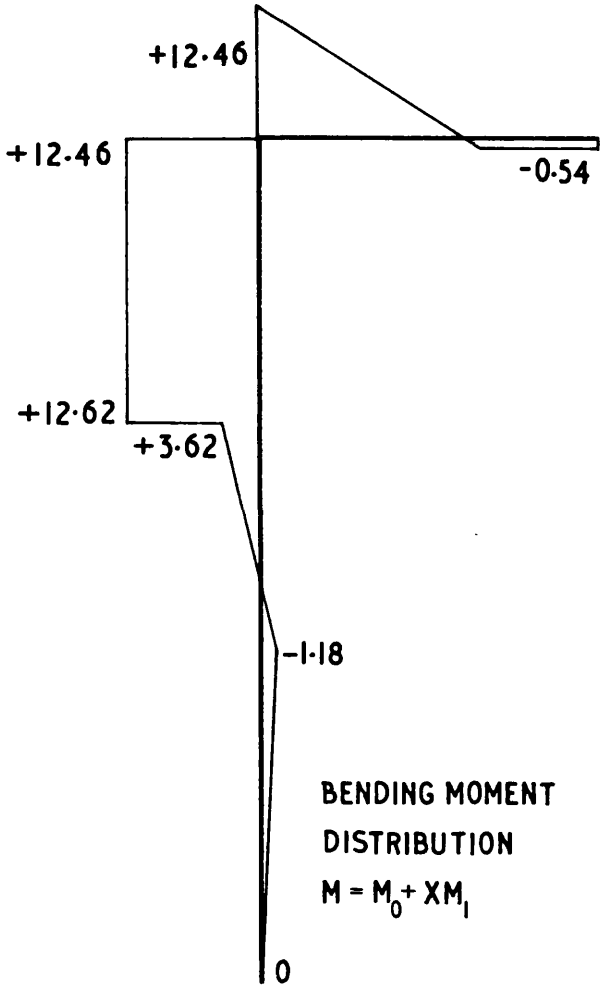

BENDING MOMENT
DISTRIBUTION
$M = M_0 + XM_1$

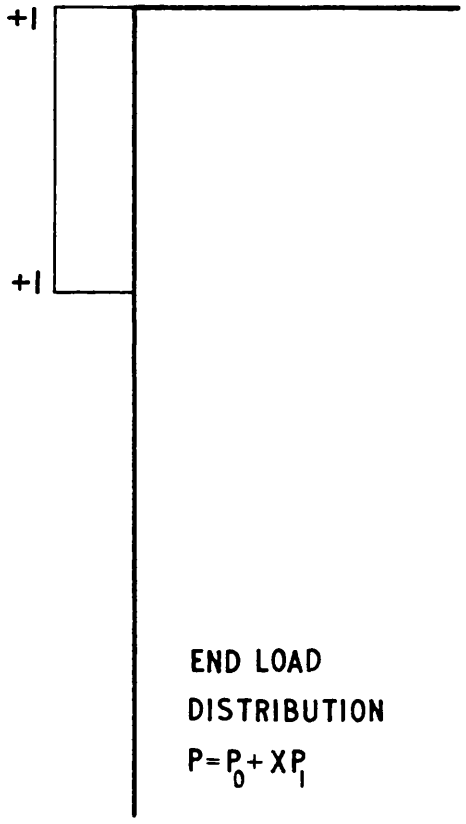

END LOAD
DISTRIBUTION
$P = P_0 + XP_1$

FIGURE 2.13

FIGURE 2.14

VARIATIONS OF I AND A, AND OF $\bar{M}^2$ AND $\bar{P}^2$ FOR UNIT SPECIMEN LOAD, AROUND THE MECHANISM

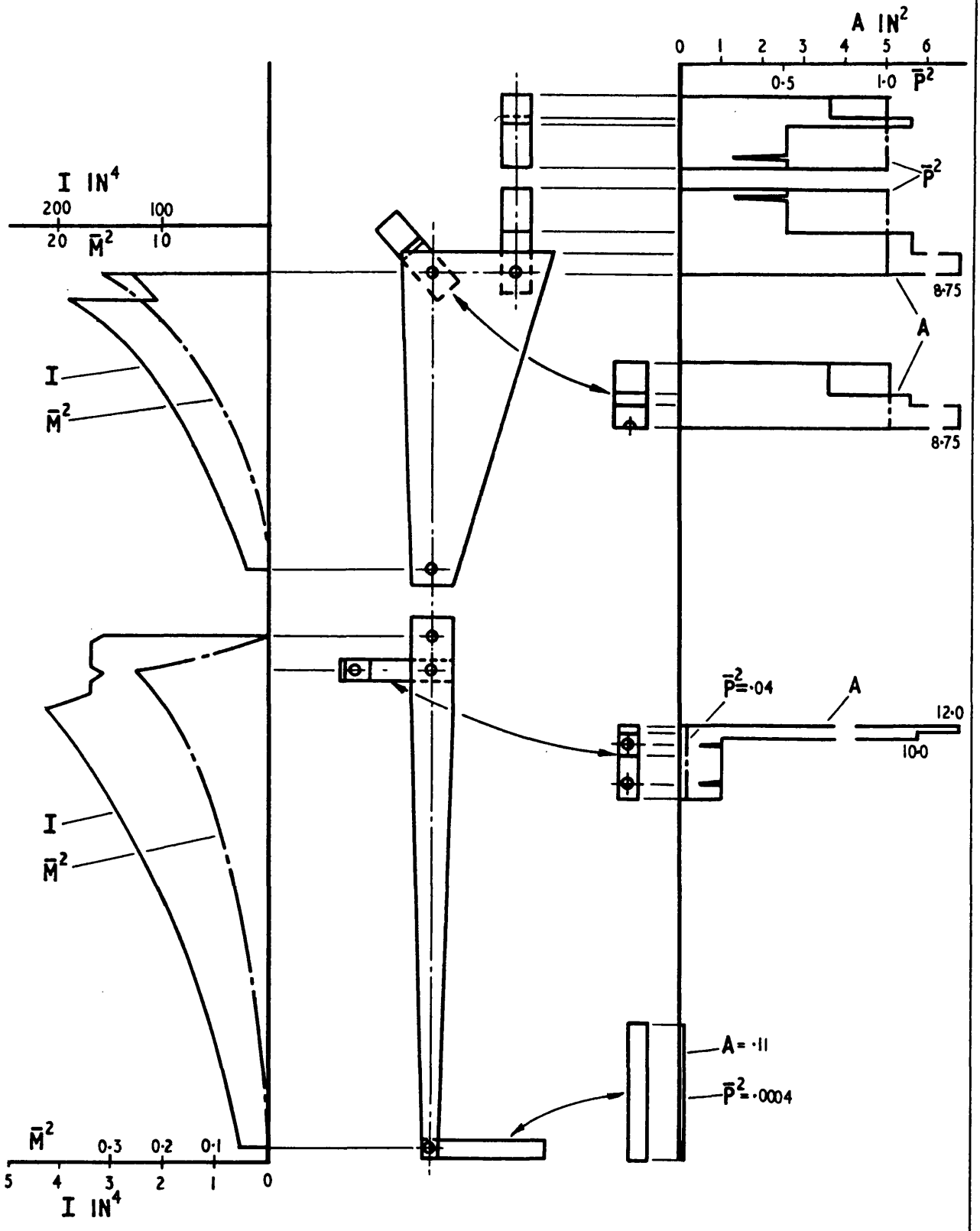

VARIATIONS OF I AND $\bar{M}^2$

VARIATIONS OF A AND $\bar{P}^2$

FIGURE 2.15

VARIATIONS OF $\frac{MM_o}{I}$ AND $\frac{PP_o}{A}$ AROUND THE MACHINE FRAME

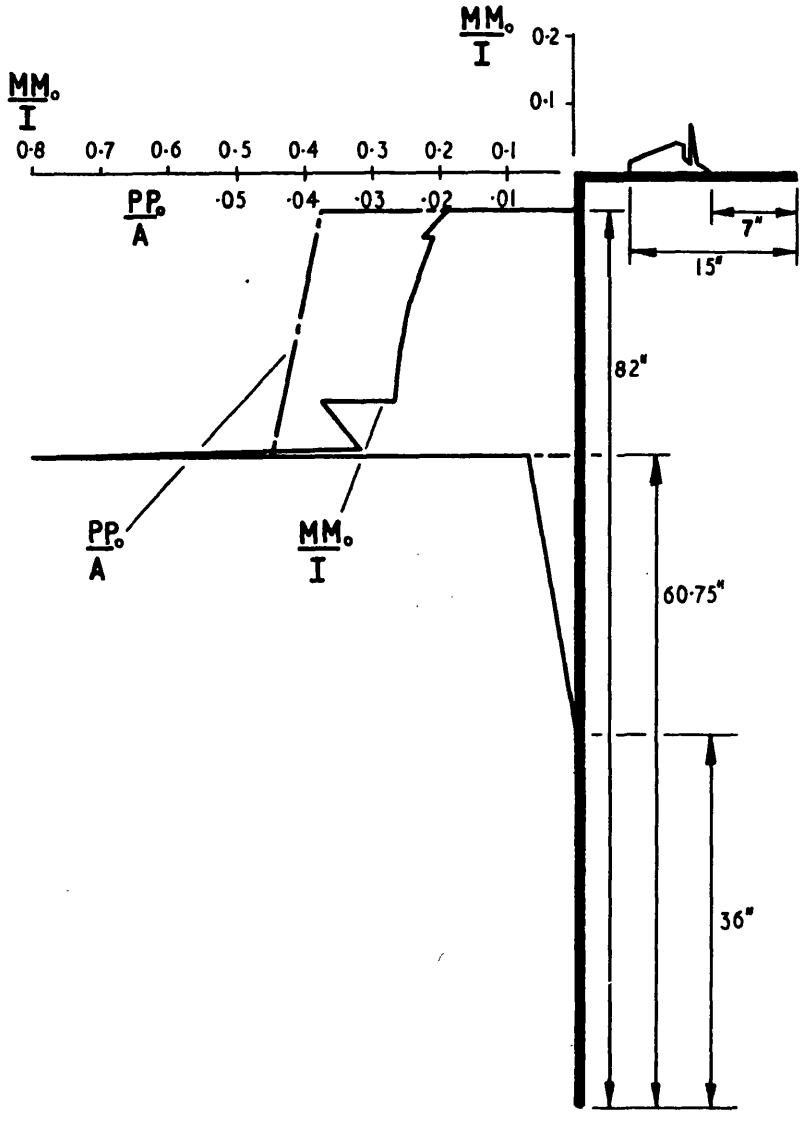

FIGURE 2.16

VARIATION OF $\frac{M_o^2}{I}$ ALONG THE LEVERS

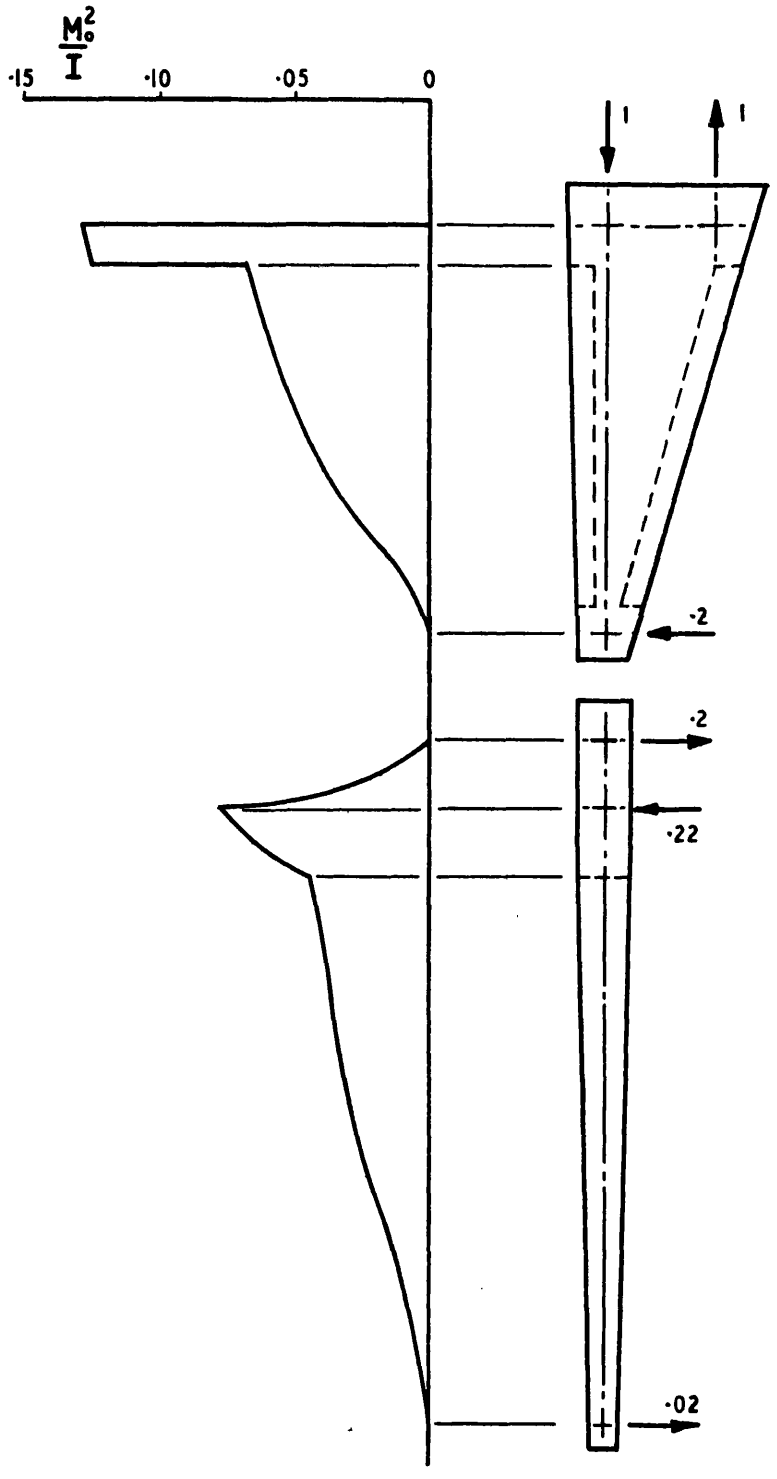

FIGURE 2.17

VARIATION OF $\frac{P_0^2}{A}$ IN THE END LOADED COMPONENTS OF THE MECHANISM

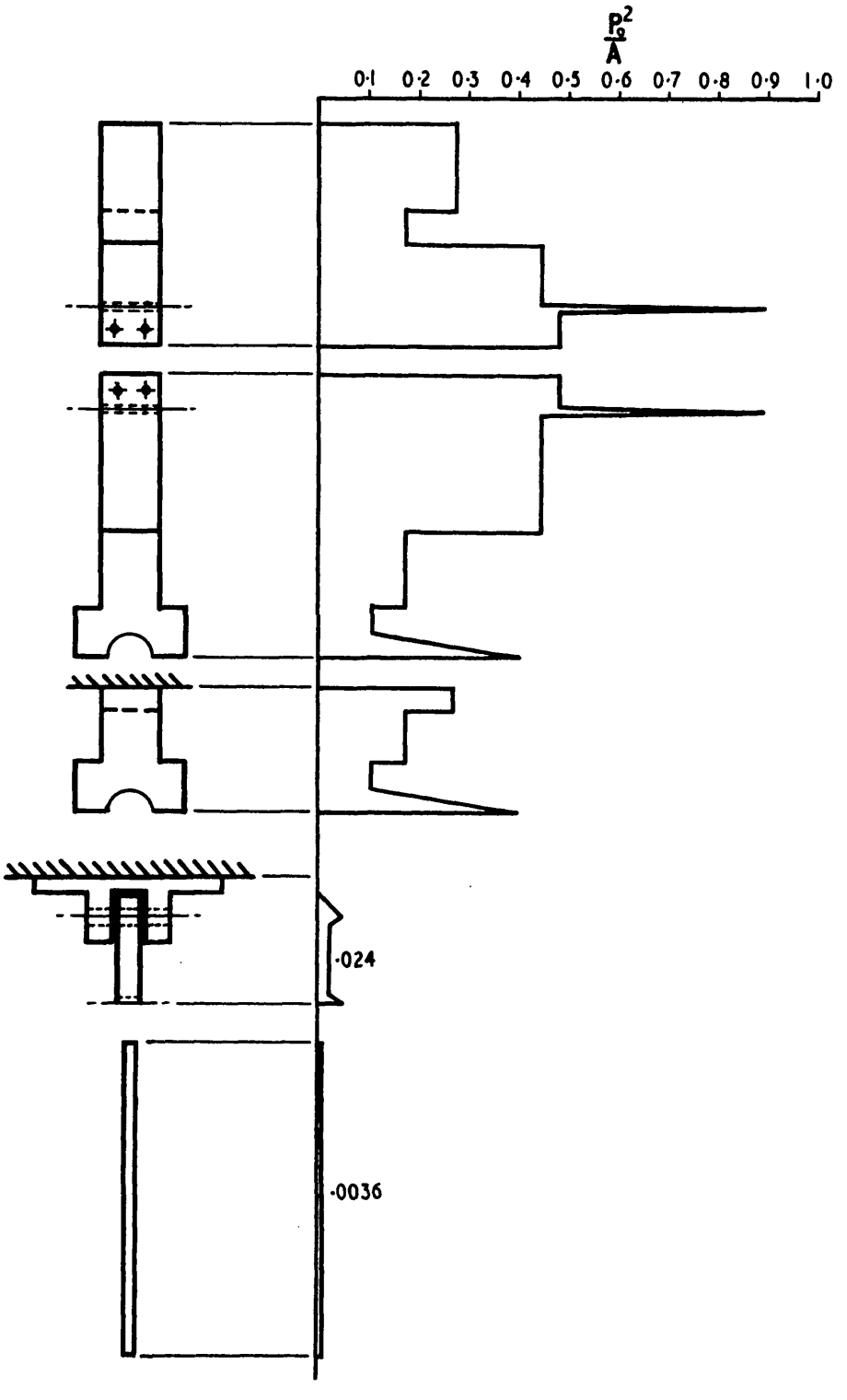

FIGURE 2.18

MACHINE COMPONENT DISPLACEMENTS.

COMPONENT	LOADING ACTION	DISPLACEMENT
FRAME TOP MEMBER	MOMENT	$.007119 \times 10^{-6}$ INS
	END LOAD	0
FRAME SIDE MEMBER	MOMENT	$.22488 \times 10^{-6}$ INS
	END LOAD	$.02934 \times 10^{-6}$ INS
TOTAL FRAME CONTRIBUTION		$.261339 \times 10^{-6}$ INS
UPPER SPECIMEN HOLDER	END LOAD	$.06610 \times 10^{-6}$ INS
LOWER SPECIMEN HOLDER	END LOAD	$.1055 \times 10^{-6}$ INS
MAIN BEARING SUPPORT	END LOAD	$.0266 \times 10^{-6}$ INS
BELL CRANK LEVER	MOMENT	$.03101 \times 10^{-6}$ INS
LOWER LEVER	MOMENT	$.027489 \times 10^{-6}$ INS
LOWER LEVER PIVOT LINK	END LOAD	$.00336 \times 10^{-6}$ INS
CAM FOLLOWER LINK	END LOAD	$.001205 \times 10^{-6}$ INS
TOTAL MECHANISM CONTRIBUTION		$.261065 \times 10^{-6}$ INS
TOTAL MACHINE DISPLACEMENT		$.522404 \times 10^{-6}$ INS

FIGURE 2.19

EXPERIMENTAL TORQUE-TENSION CURVES FOR THE SPECIAL BEARING HOUSING BOLTS

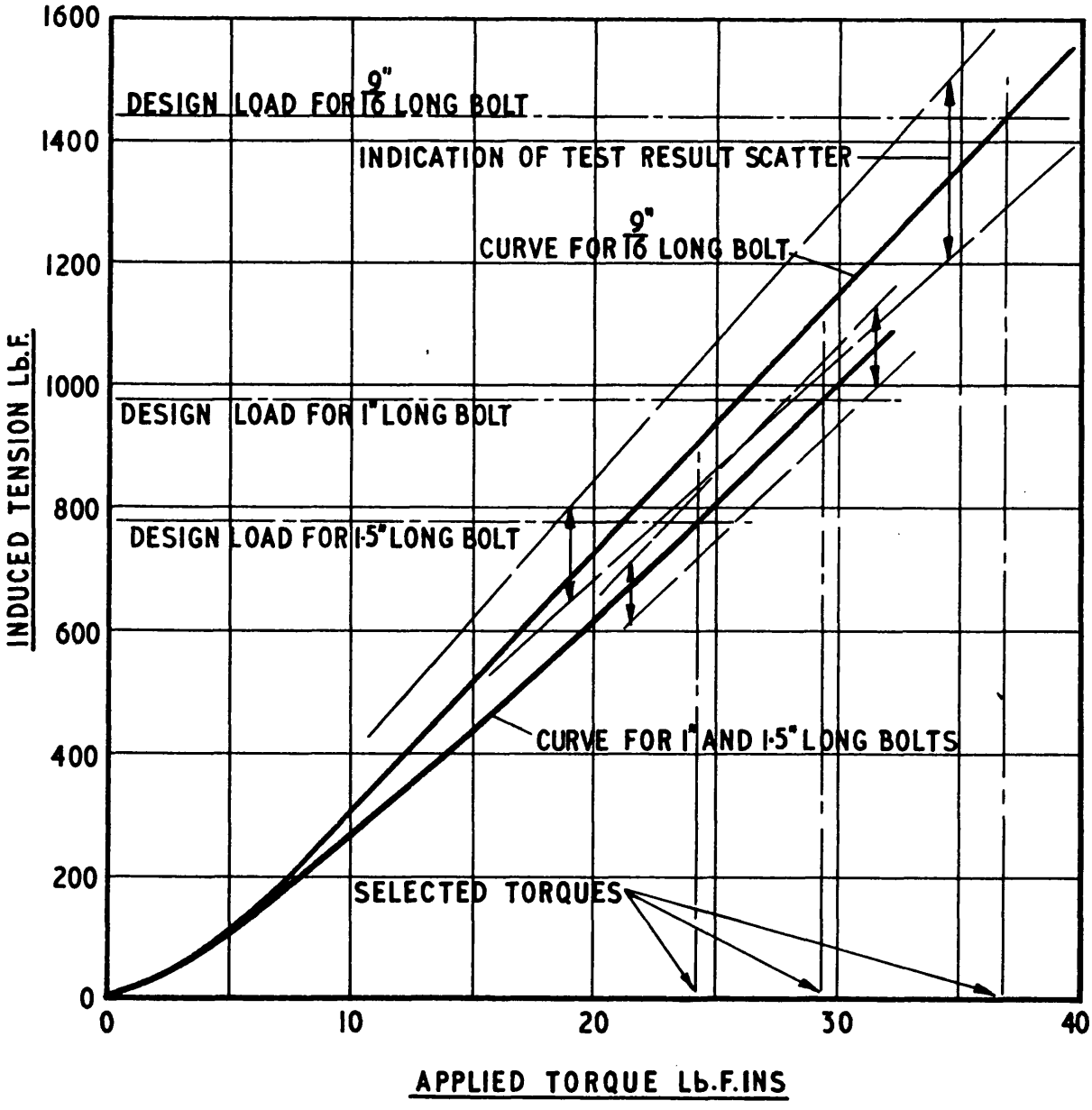

GENERAL ARRANGEMENT OF TESTING MACHINE

FIGURE 2.20

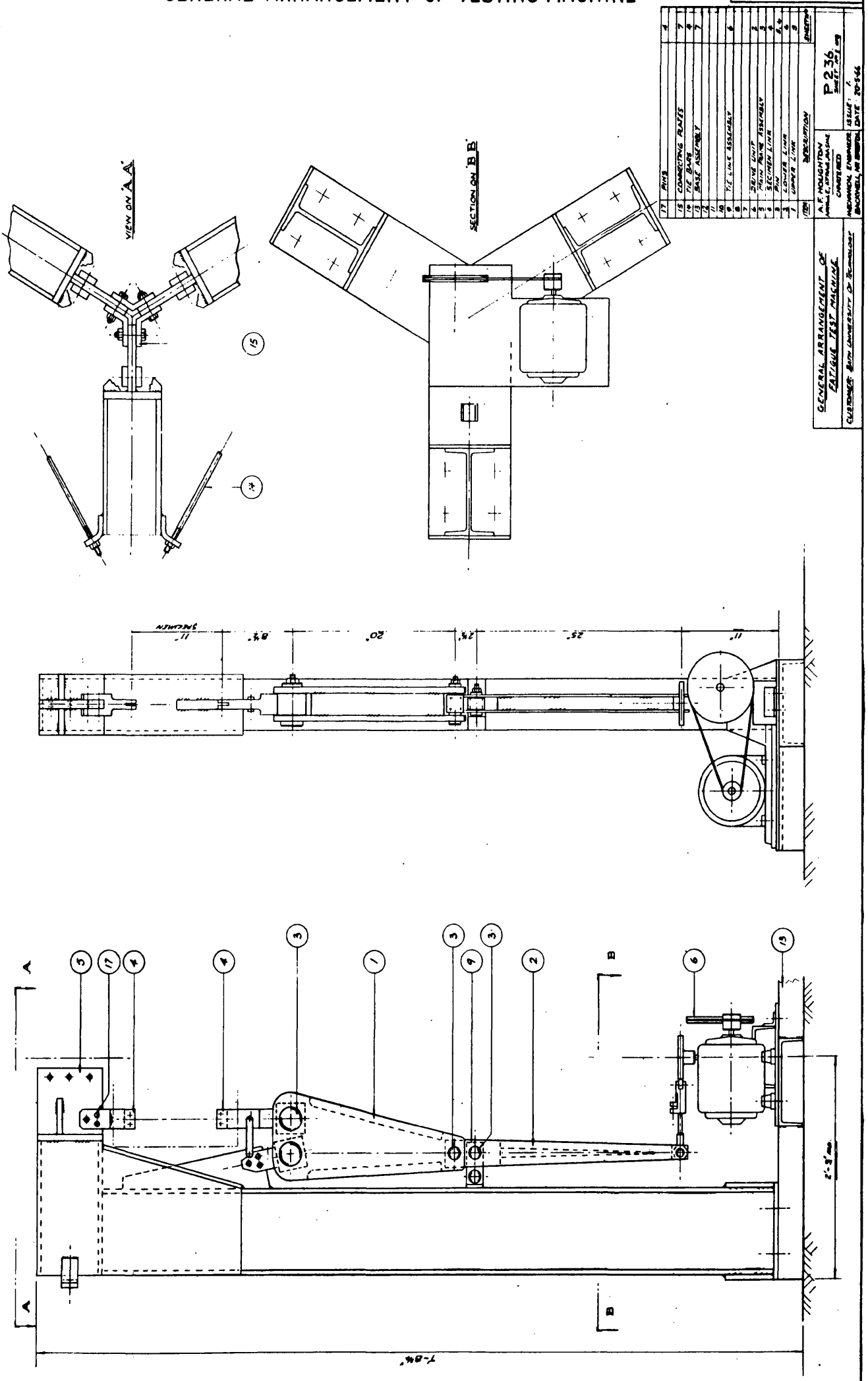

GENERAL ARRANGEMENT OF DRIVE UNIT.

FIGURE 2.21

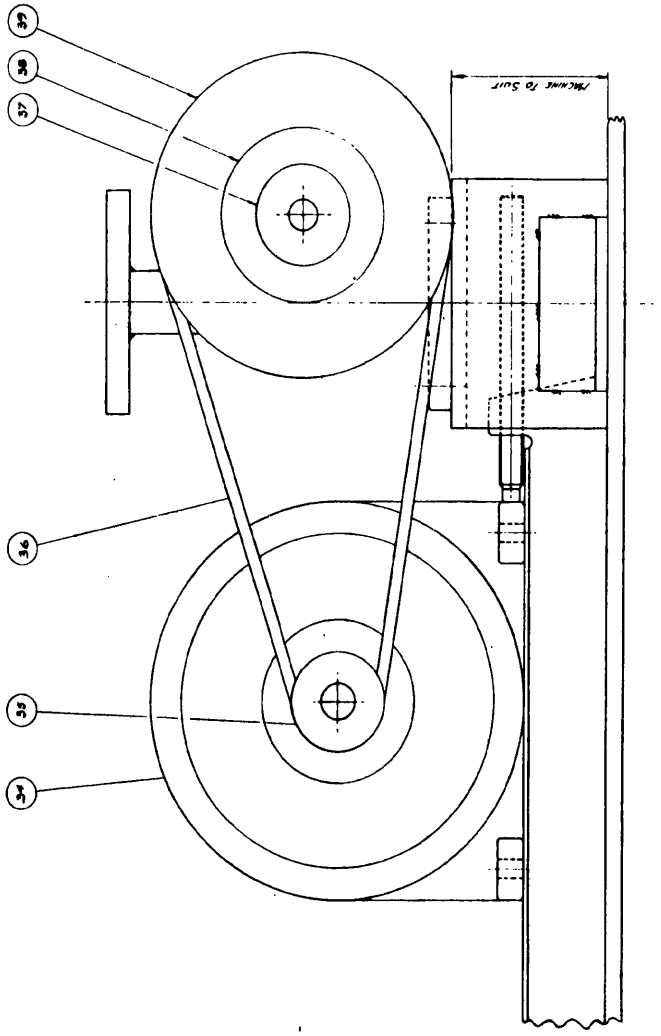

ITEM	DESCRIPTION	SIZE OR No.	MATERIAL	QTY
42	BEARING SKF 6200-2RS			1
41	SPACER DU BUSHING ¾ DIA SHAFT		DU	3
40	¾" DIA CAM FOLLOWER NASF-12-6			3
39	6" PCD PULLEY		AL	1
38	3" ---- ----		-"-	1
37	15" ---- ----		-"-	1
36	GRAYDON & KNIGHT 17 SECT. V/BELT		-"-	1
35	15" P.C.D. PULLEY		AL	1
34	MOTOR 1½HP, 960 RPM, 3 PHASE, B56 CAST FRAME			1
33	MOTOR END PLATE SUPPORT		MS.	2
32	GEAR BOX SUPPORT			1
31	MODIFIED REDUCTION UNIT RPM 1/30 T. RATIO		MS.	1
30	GUIDE SUPPORT 3"x3½" 6½ CHANNEL			1
29	CAM FOLLOWER BLOCK GUIDE	8	MS.	3
28	CAM	8	As Above	3
27	RETAINING SPRING BEARING CAP	8	MS.	1
26	'RETAILO' SPRING AR-M12M	8	-"-	1
25	CAM FOLLOWER BLOCK	8	-"-	6
24	PARALLEL LINK ¾" BSF R/HAND	8	MS.	3
23	LOCK NUT	8	-"-	3
22	LINK SCREW ADJUSTER ¾"B.S.F L/HR HAND	8	-"-	6
21	PARALLEL LINK ¾" BSF L/HAND	8	-"-	3
ITEM	DESCRIPTION	SIZE OR No.	MATERIAL	QTY

FATIGUE TEST MACHINE — BLOCK MECHANISM

SCHOOL OF MECHANICAL & PRODUCTION ENGINEERING

BATH UNIVERSITY OF TECHNOLOGY

P230 SHEET 2 OF 8

ISSUE 1 — 25-5-1966

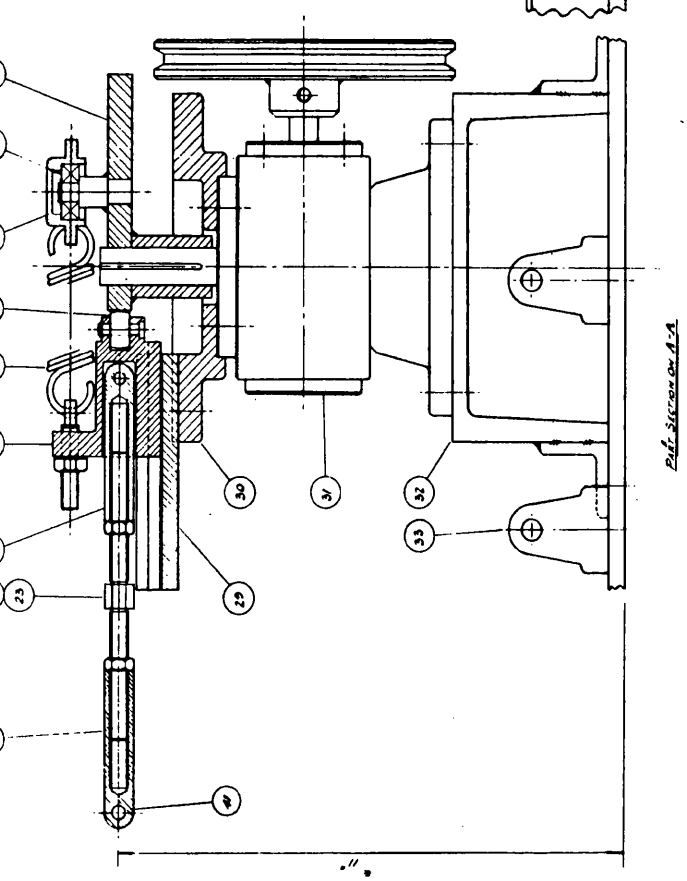

PART SECTION ON A-A

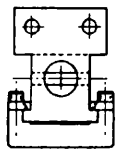

BLOCK = SLIDE

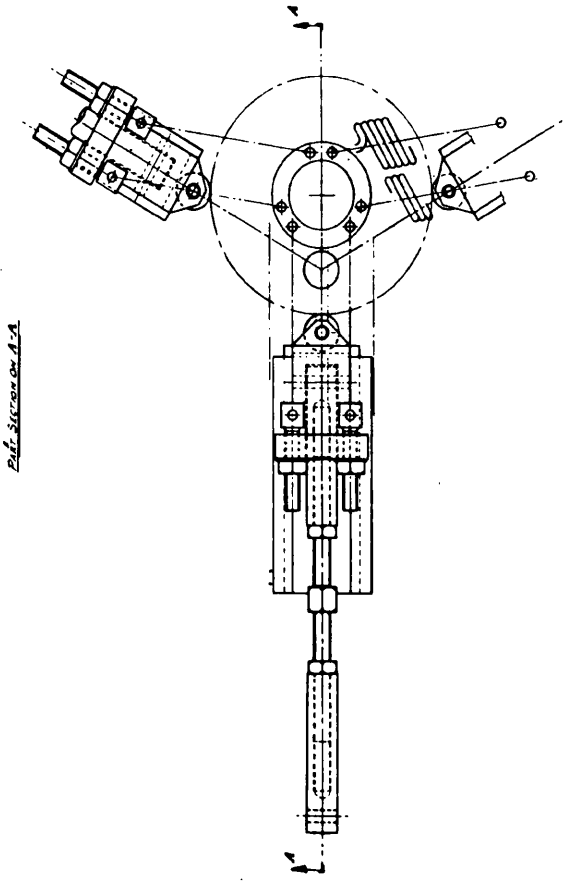

DETAILS OF MACHINE FRAME.

FIGURE 2.22

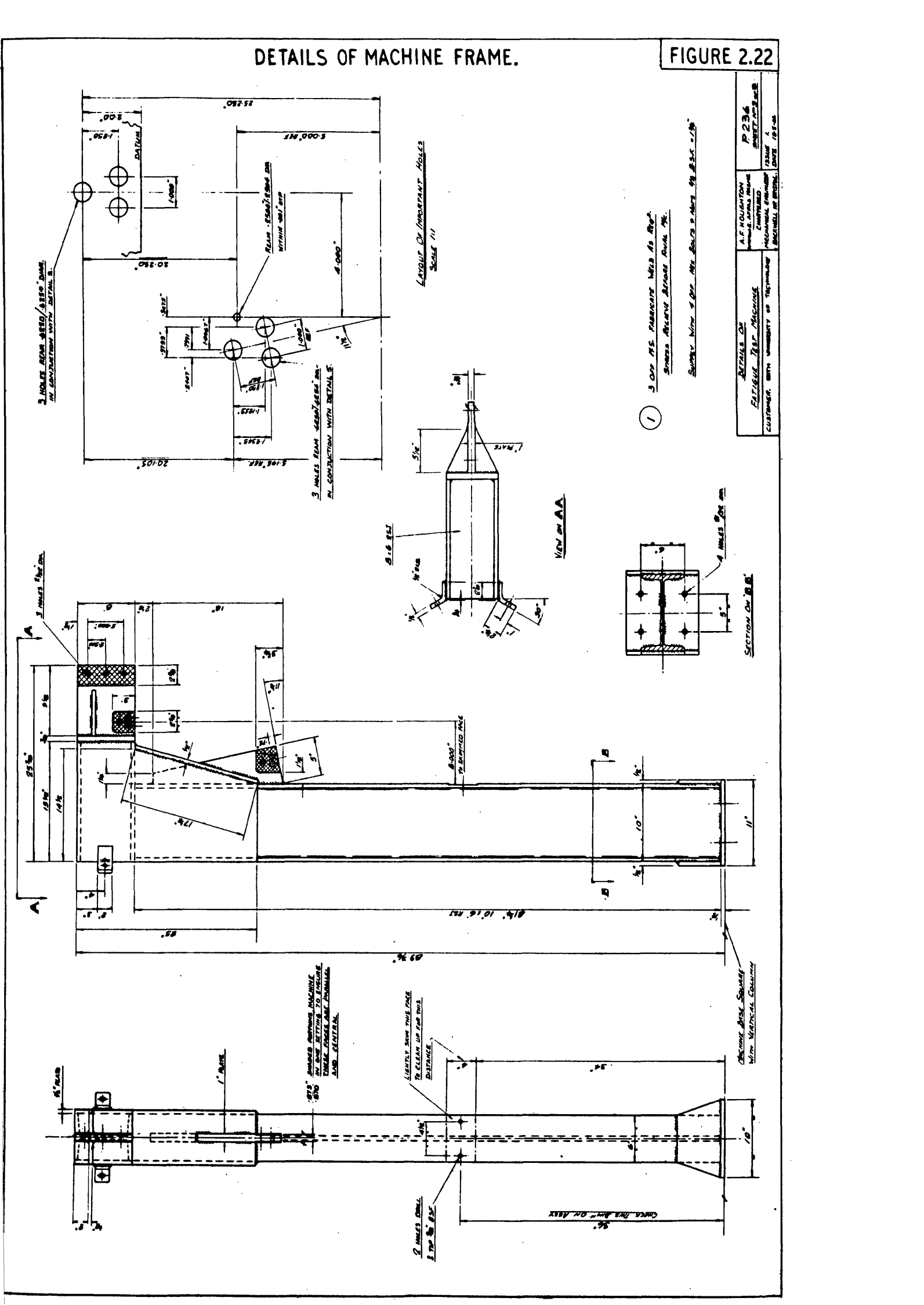

DETAILS OF SPECIMEN HOLDERS AND MAIN BEARING HOUSINGS.

FIGURE 2.23

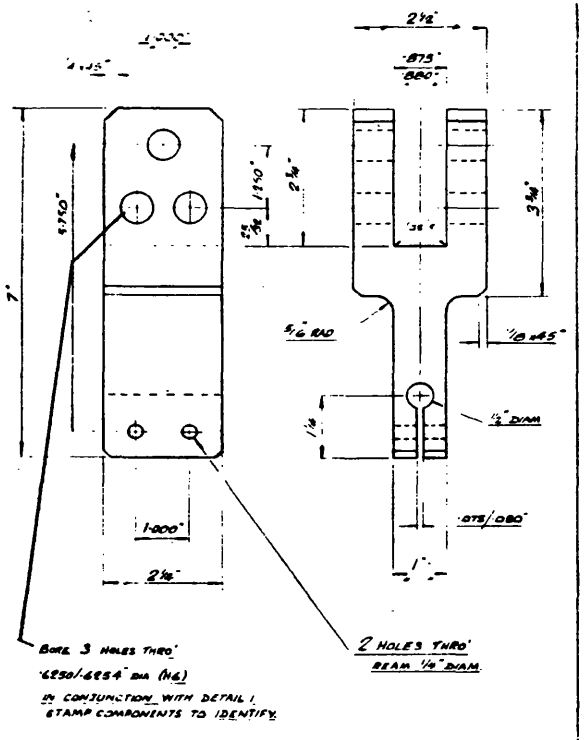

(2) 3. OFF M.S.

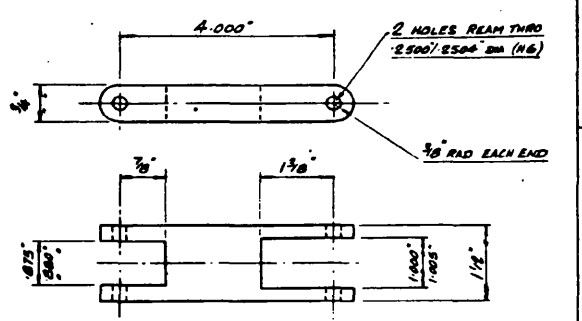

(4) 3. OFF B M S
SUPPLY WITH 2 PINS
¼" DIA DRIVE FIT x 1¾" LG

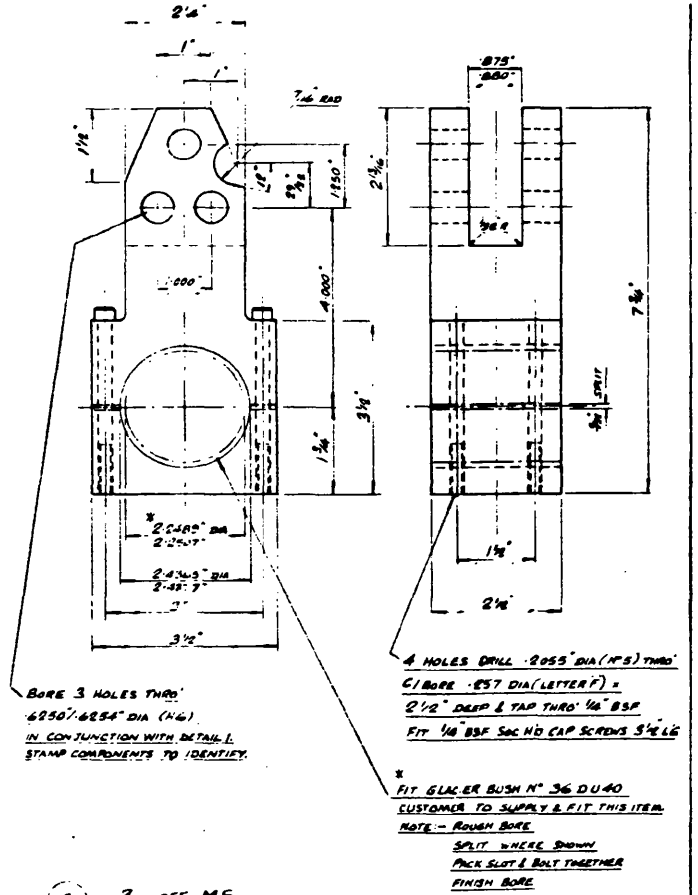

(5) 3. OFF M.S.

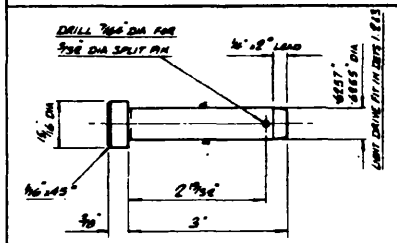

(17) 18 OFF UBAS C/HDN & ERD
SUPPLY WITH SPLIT PIN 3/32" DIA x 1¼" LG

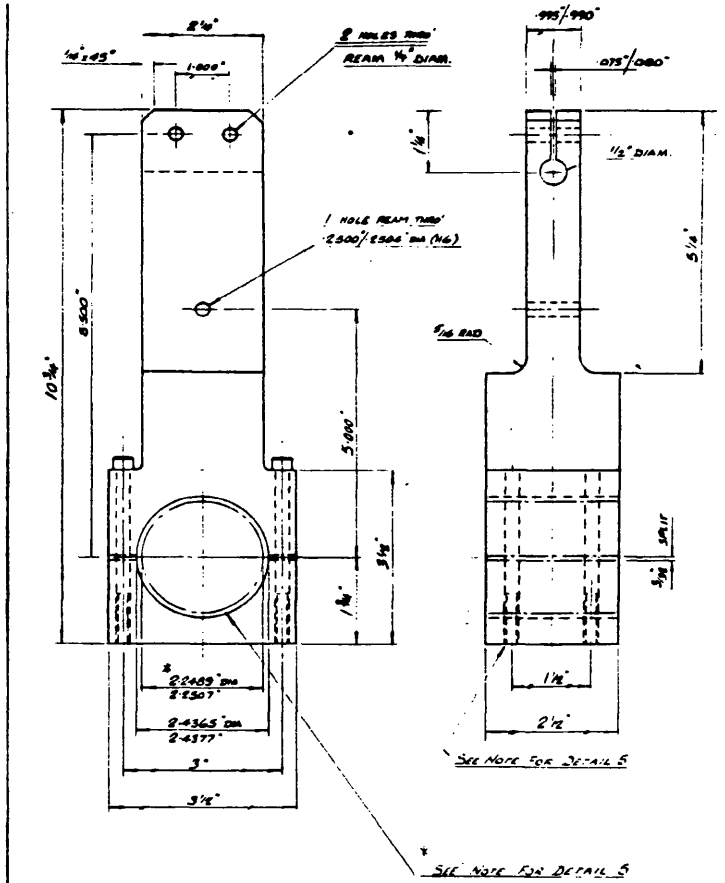

(3) 3. OFF M.S.

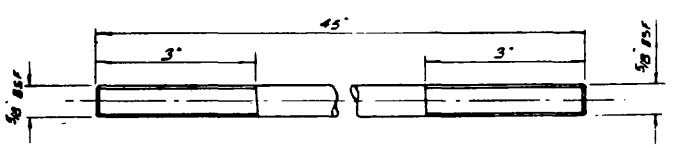

(14) 3. OFF B M S SUPPLY WITH 2 HEX NUTS

DETAILS OF FATIGUE TEST MACHINE CUSTOMER. BATH UNIVERSITY OF TECHNOLOGY	A. F. HOUGHTON. AMIMECHE, AFRAS, MASME CHARTERED MECHANICAL ENGINEER BACKWELL NR BRISTOL	P. 236 SHEET N° 41 OF ISSUE 1. DATE 18-5-66

DETAILS OF BELL CRANK LEVER AND BEARING JOURNALS.

FIGURE 2.24

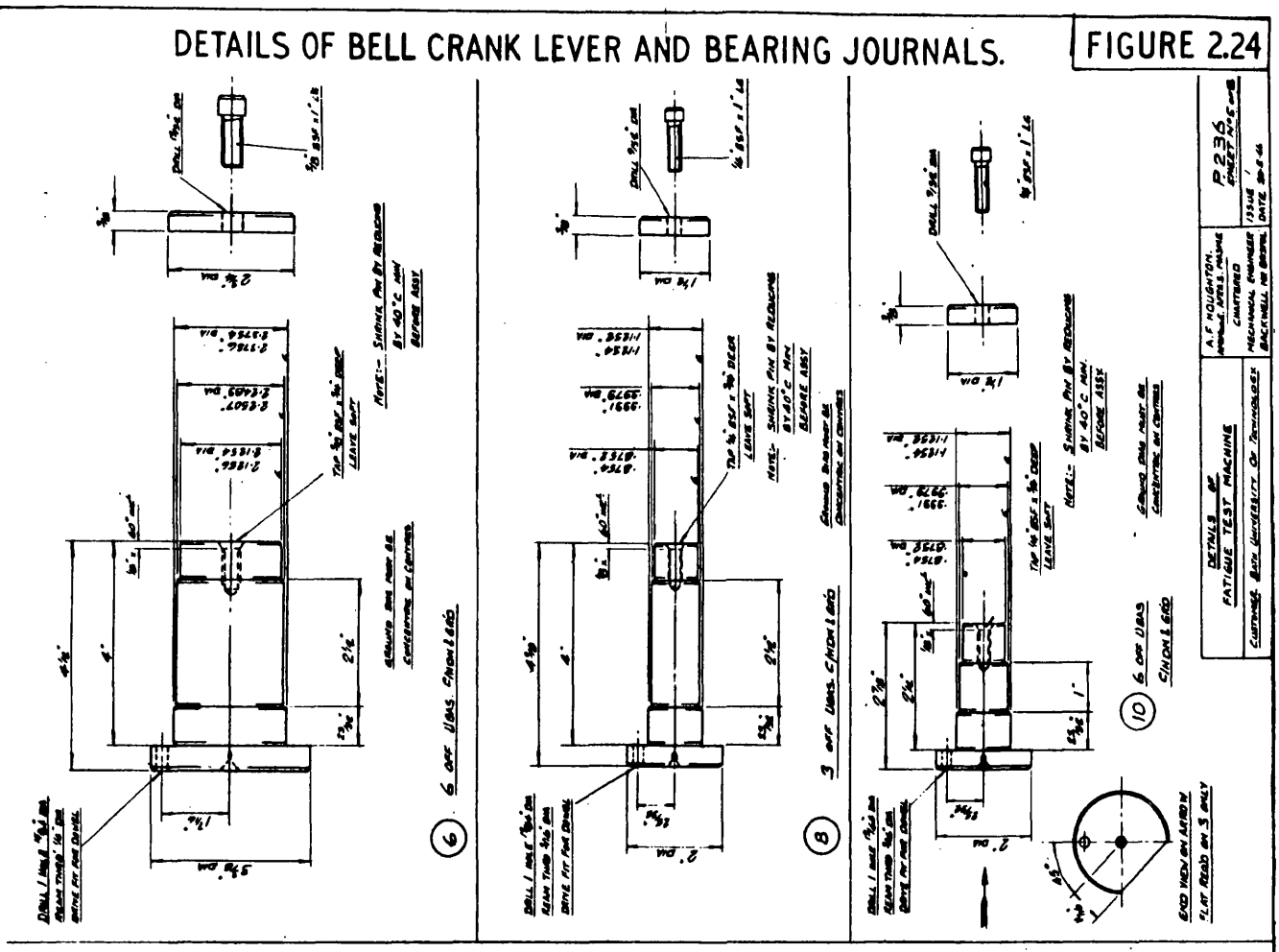

DETAILS OF LOWER LEVER AND LOWER LEVER PIVOT LINK.

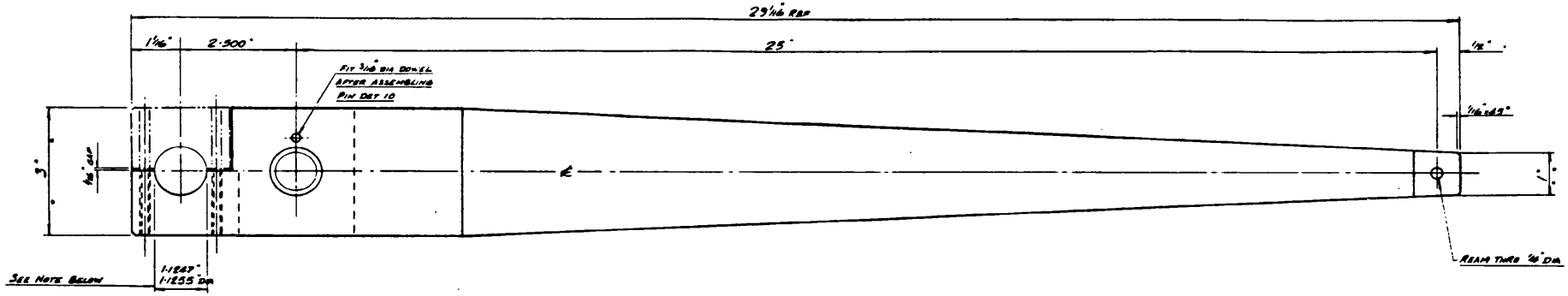

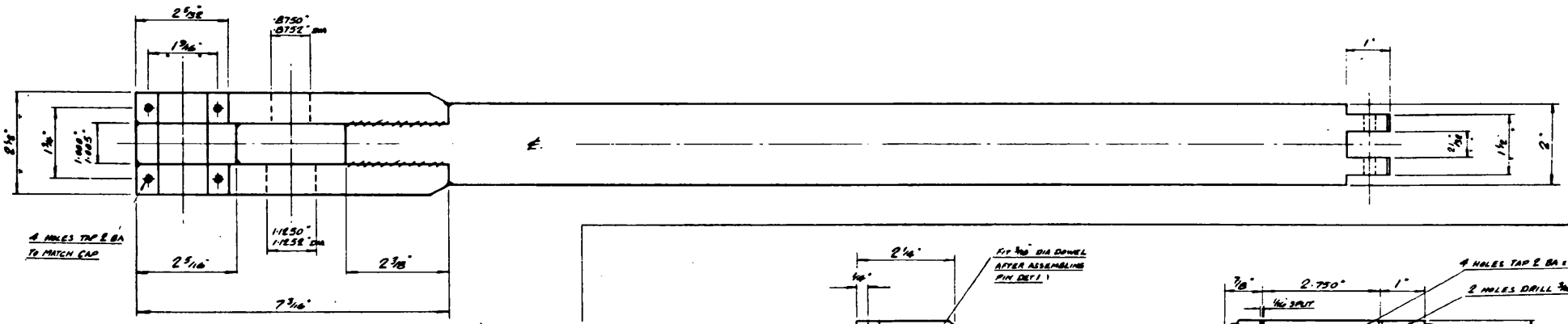

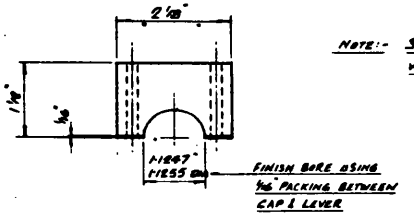

NOTE:- 3 BORES MUST BE SQUARE WITH ℄ OF LEVER ARM

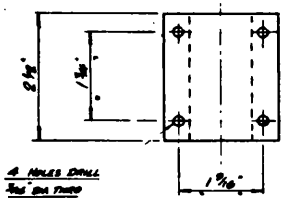

FIT GLACIER BUSH N° 16 DU 16
CUSTOMER TO SUPPLY & FIT THIS ITEM

(11) 3 OFF MS. FABRICATED
WELD AS REQ'D
STRESS RELIEVE BEFORE
FINAL MACHINING

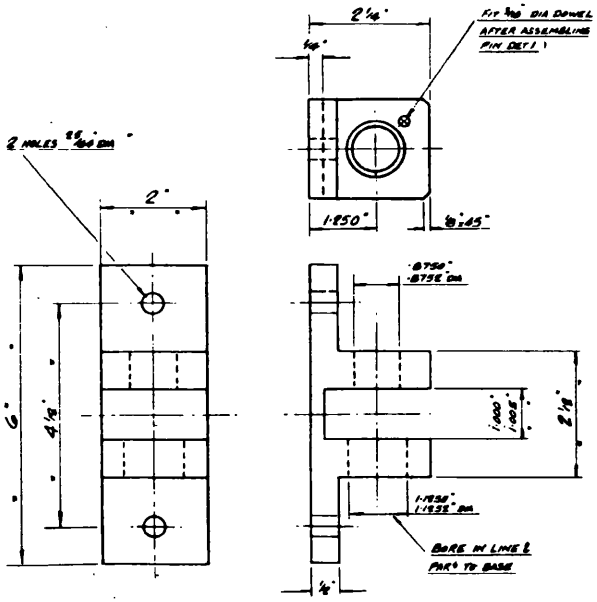

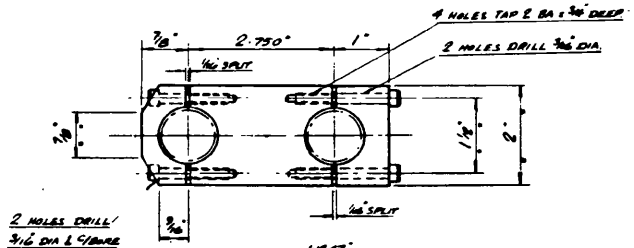

FIT GLACIER BUSH N° 16 DU 16.
CUSTOMER TO SUPPLY & FIT THIS ITEM.

NOTE:- ROUGH BORE
SPLIT WHERE SHOWN
PACK SLOT & BOLT TOGETHER
FINISH BORE. (2 BORES)

(9) 3 OFF MS.

DETAILS OF FATIGUE TEST MACHINE	A F HOUGHTON ARCHITECTURAL METAL WORK CHARTERED MECHANICAL ENGINEERS BACKWELL, NR BRISTOL	P.236 SHEET No 4 of 8
CUSTOMER: BATH UNIVERSITY OF TECHNOLOGY		ISSUE 1. DATE 20-5-66

FIGURE 2.25

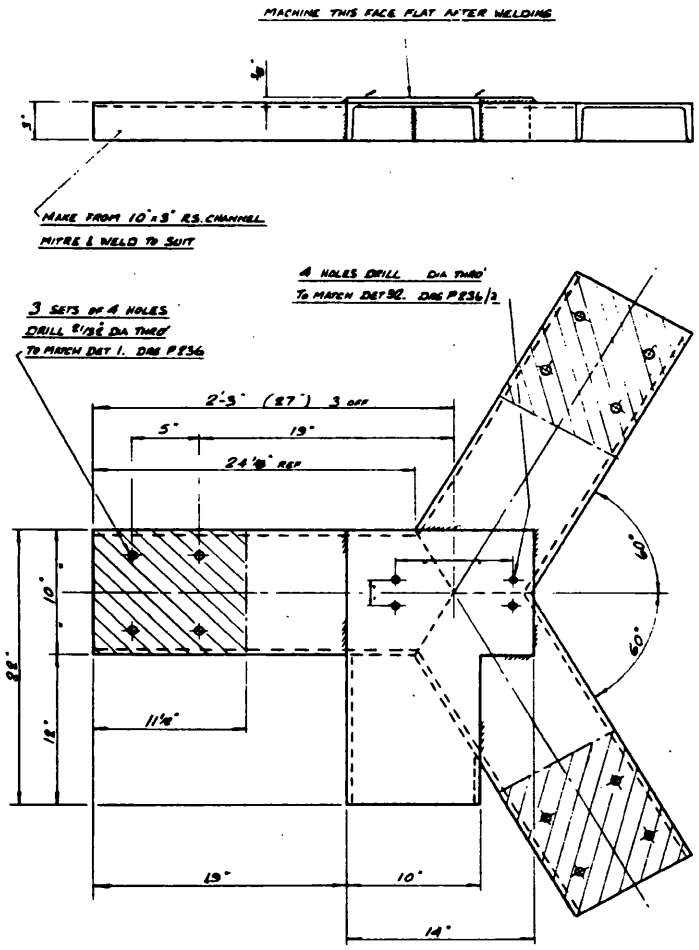

(13) 1 OFF M.S. FABRICATE
LIGHTLY M/C SHADED FACES TO BE ALL IN THE SAME PLANE
& PARALLEL TO M/C'D FACE OF PLATE
STRESS RELIEVE AFTER WELDING & BEFORE FINAL M/C'G

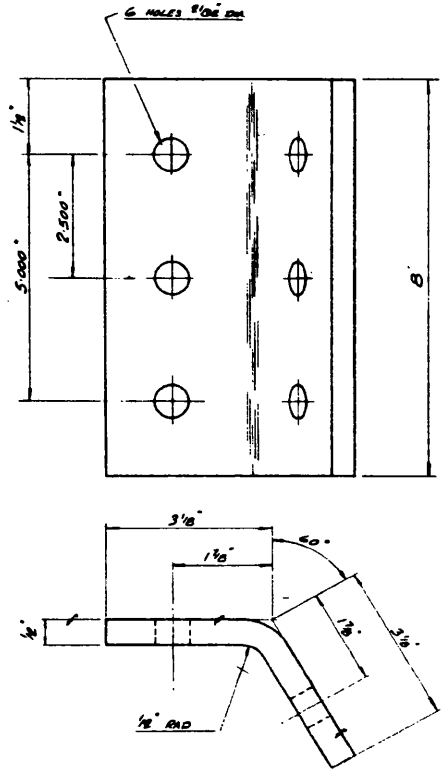

(15) 3 OFF M.S. MACHINE FLAT AT ℄
SUPPLY WITH 3 HEX BOLTS & NUTS 5/8" BSF x 2 3/16"

DETAILS OF MACHINE BASE

DETAILS OF FATIGUE TEST MACHINE	A F HOUGHTON MANUFACTURING ENGINEERS LIMITED	P236 SHEET No 7 of 8
CUSTOMER BATH UNIVERSITY OF TECHNOLOGY	MECHANICAL ENGINEER BACKWELL NR BRISTOL	ISSUE 1. DATE 20.5.66

FIGURE 2.26

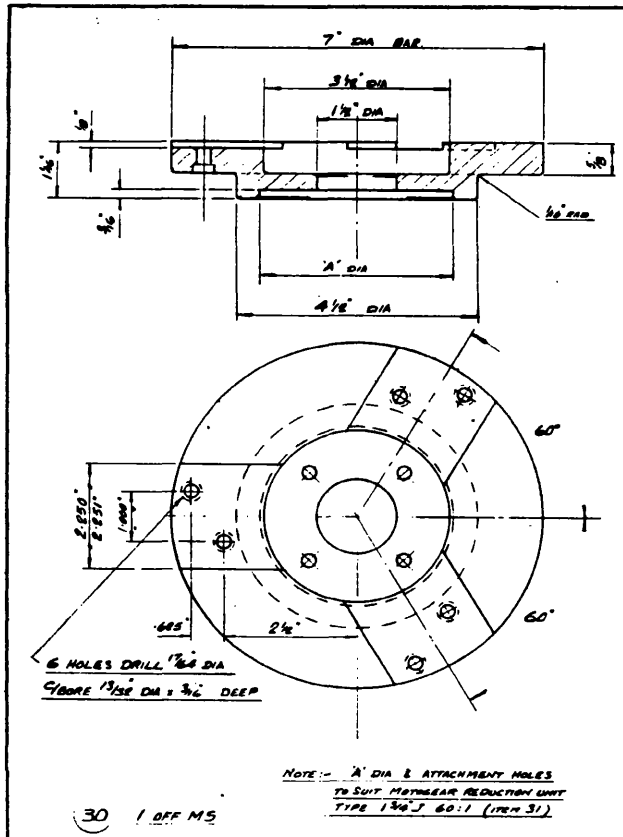

NOTE:- 'A' DIA & ATTACHMENT HOLES TO SUIT MOTOGEAR REDUCTION UNIT TYPE 1 3/16 J 60:1 (ITEM 31)

(30) 1 OFF MS

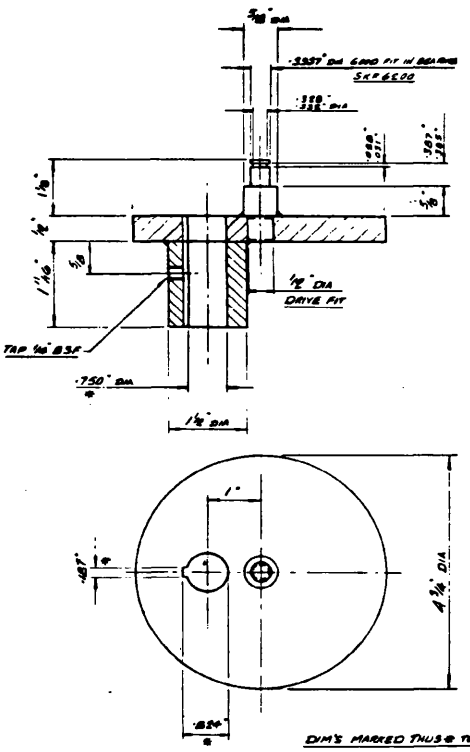

DIM'S MARKED THUS @ TO SUIT SHAFT OF WORM GEAR REDUCTION UNIT "MOTOGEAR 1 3/16 J"

(28) 1. OFF MS

SUPPLY WITH CIRCLIP SALTER Nº 6138
" " SOC GRUB SCREW 1/4 BSF x 1/4"
" " KEY 3/16" SQ TO SUIT

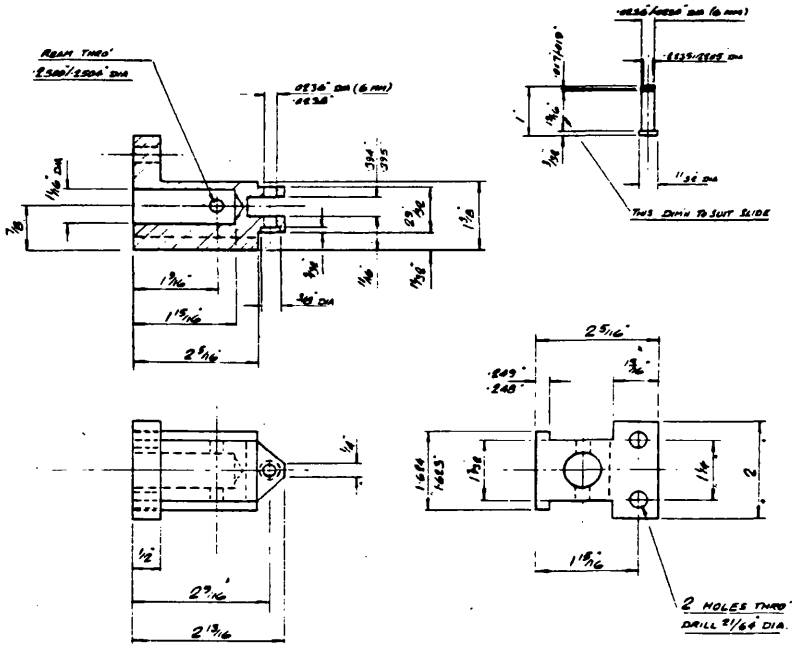

(25) 3. OFF MS (SLIDE)
3 OFF 31L 3FL (PH) SUPPLY WITH CIRCLIP SALTER Nº 5/23.

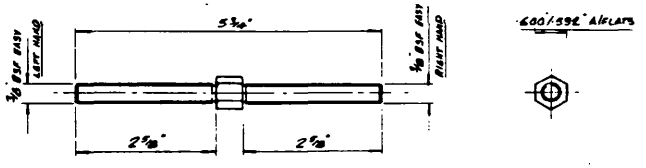

(23) 3. OFF BMS SUPPLY WITH HEX LOCK NUTS 1 OFF RH. 1 OFF LH.

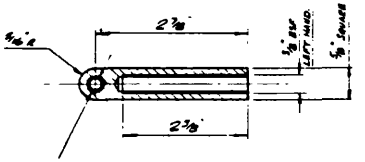

(21) 3 OFF BMS

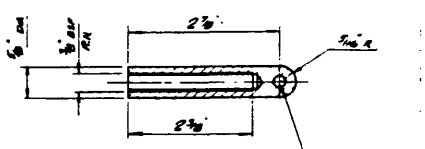

(24) 3 OFF BMS

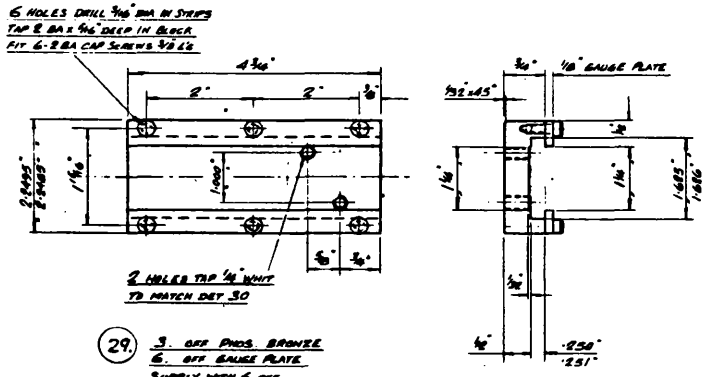

(29) 3. OFF PHOS. BRONZE
6. OFF GAUGE PLATE
SUPPLY WITH 6 OFF 1/4" BSF x 3/8" LG CAP SCREWS

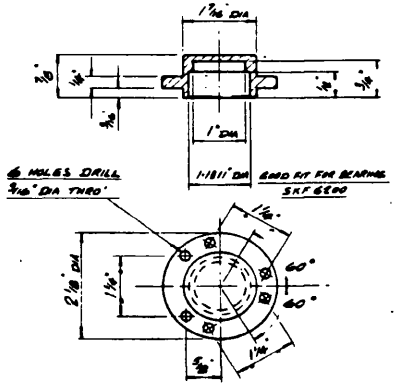

(27) 1. OFF MS

DETAILS OF DRIVE UNIT.

FIGURE 2.27

DETAILS OF FATIGUE TEST MACHINE	A.F. HOUGHTON ASSOC.M.A.F.R.A.S. M.I.Mech.E. CHARTERED MECHANICAL ENGINEER BACKWELL NR BRISTOL	P.236 SHEET Nº 8 OF 8.
CUSTOMER: BATH UNIVERSITY OF TECHNOLOGY		ISSUE 1 DATE 20.5.66

FIGURE 2.28

DETAILS OF FURNACE.

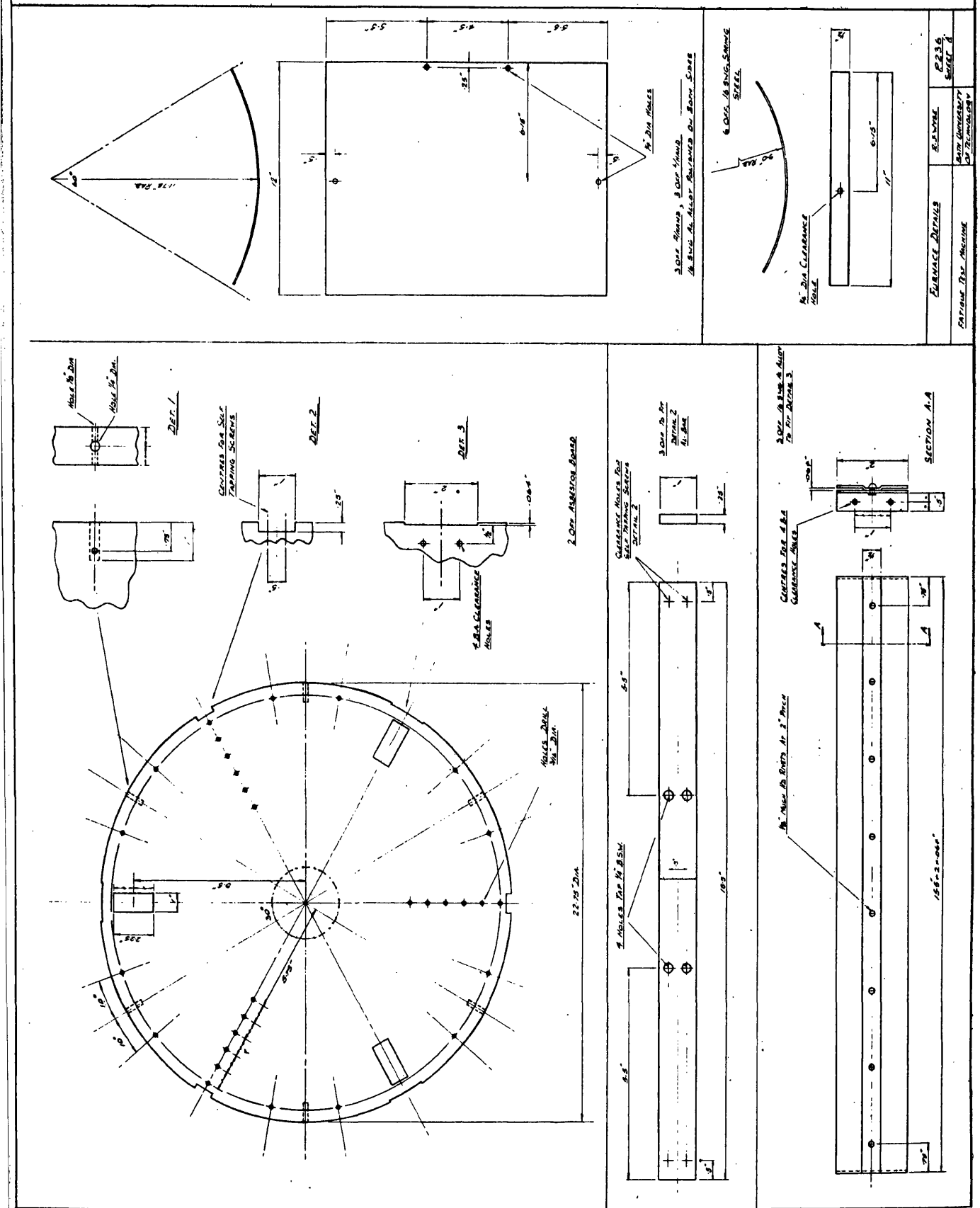

FIGURE 2.29

SKETCH OF THE SPECIMEN DRILLING JIG

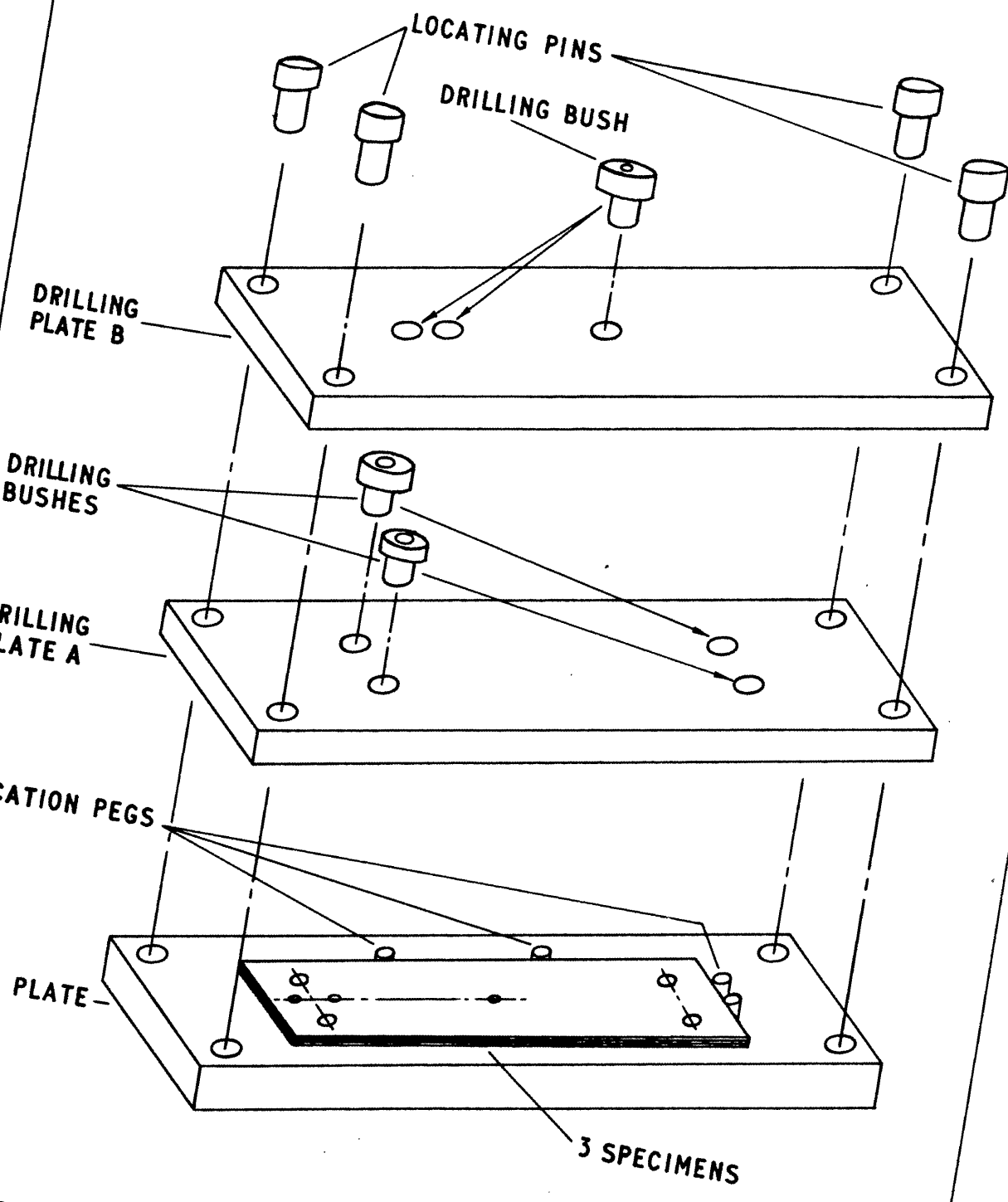

FIGURE 2.30

INPUT DISPLACEMENT CYCLE CALIBRATION

A: CIRCULAR PROFILE CAM WAVE COMPARED WITH A SINE WAVE ON A ROTATION BASIS

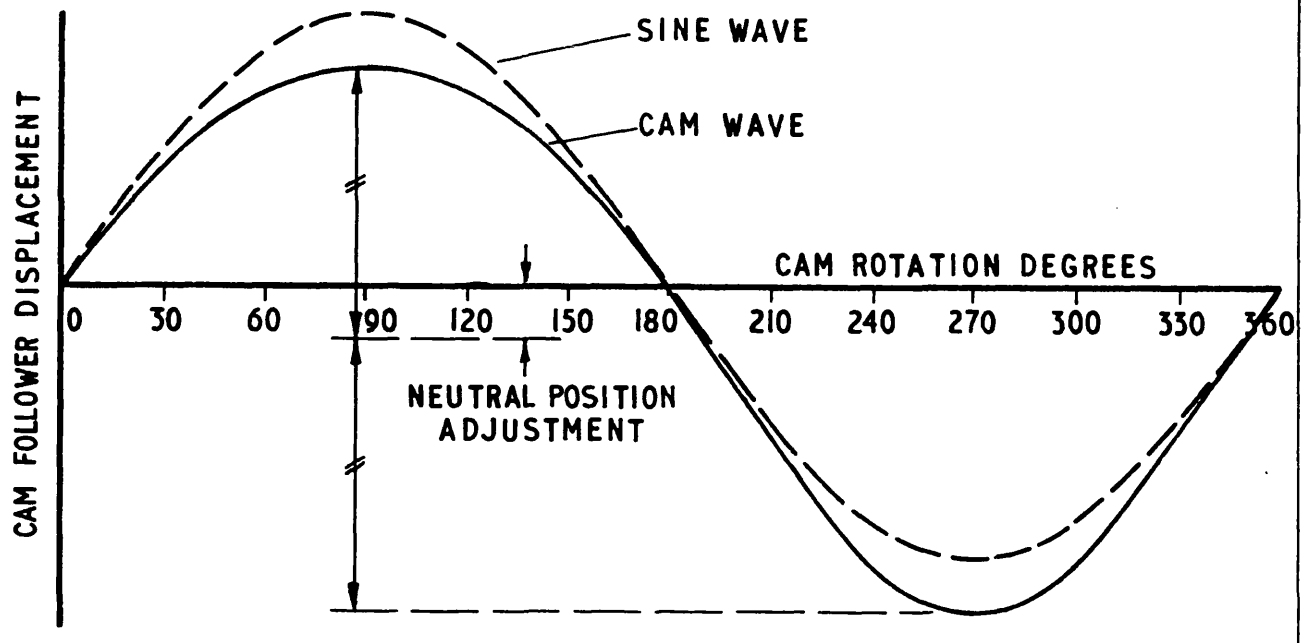

B: CIRCULAR PROFILE CAM WAVE ADJUSTED TO GIVE CORRECT AMPLITUDE COMPARED WITH A SINE WAVE

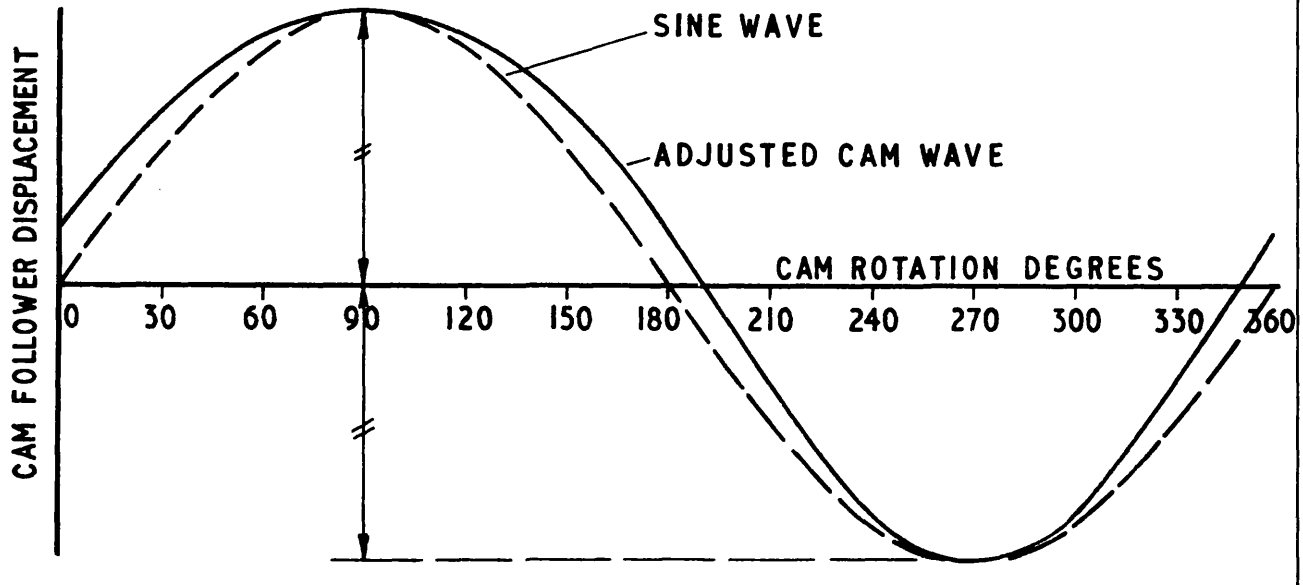

FIGURE 2.31

TYPICAL CHANNEL CALIBRATION CURVES

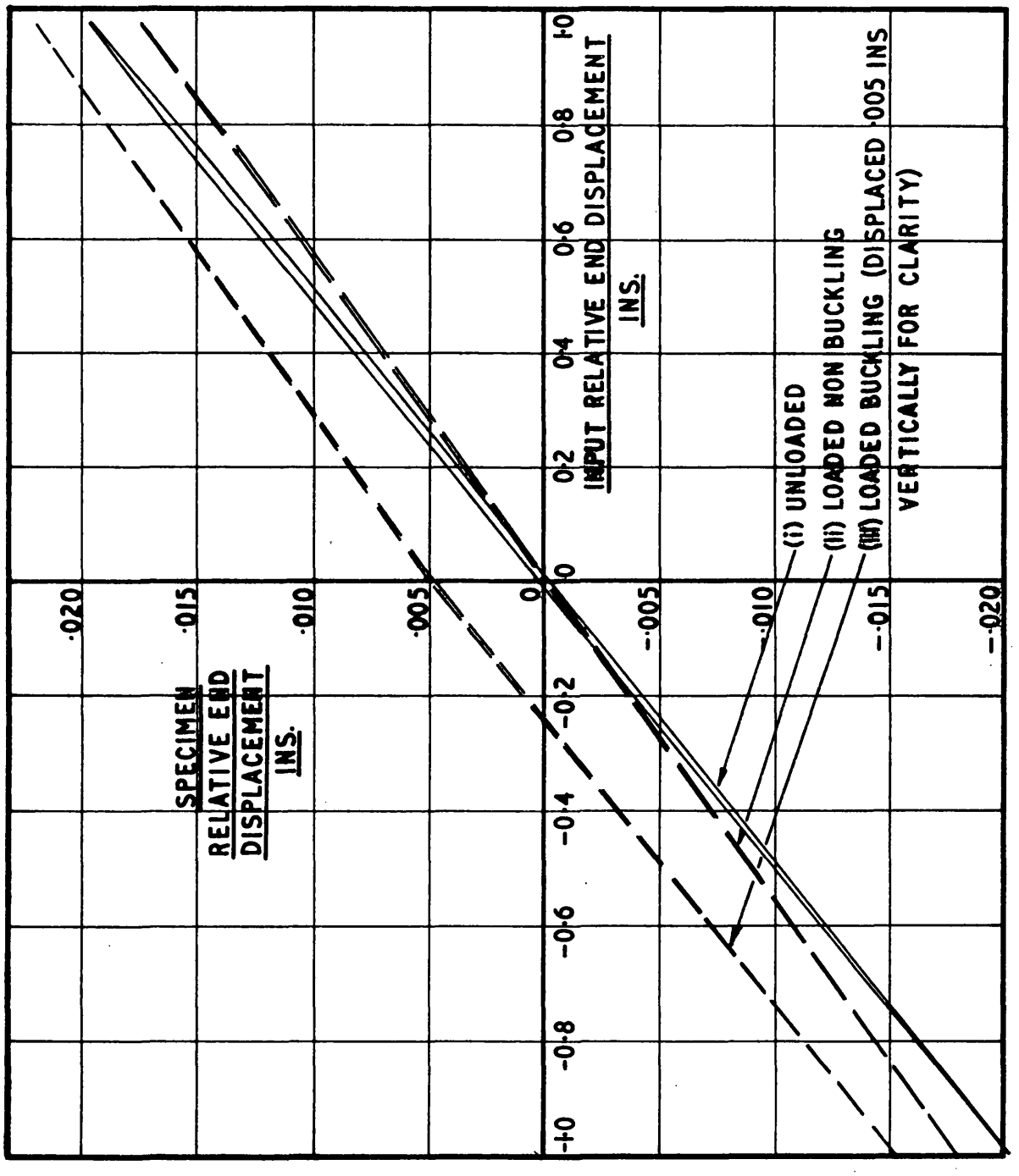

FIGURE 2.32

SUMMARY OF MACHINE CALIBRATION TESTS.

CHANNEL NO.	CALIBRATION SLOPES				STIFFNESS RATIOS			DISPLACEMENT ACCURACY		
	WITHOUT SPECIMEN	NON-BUCKLING	BUCKLING		NON-BUCKLING	BUCKLING		NON-BUCKLING	BUCKLING	
			TENSION	COMP.		TENSION	COMP.		TENSION	COMP.
1	.018665	.01814	.01736	.01921	34.6	13.30		2.7%	6.99%	0.0%
2	.02007	.01783	.01750	.02009	7.96	6.81		11.16%	12.80%	0.0%
3	.01993	.01828	.01820	.01990	11.08	10.52	663	8.28%	8.68%	0.15%
4	.02003	.01904	.01843	.01982	19.23	11.73	94.3	4.94%	7.99%	1.03%
5	.01981	.01799	.01762	.01981	9.88	8.05		9.19%	11.05%	0.0%
6	.02022	.01796	.01810	.02014	7.95	8.54	252	11.18%	10.47%	0.39%

FIGURE 2.33

TYPICAL TEMPERATURE VARIATIONS ABOUT 150°C ALONG THE LENGTH OF A STRAIGHT SPECIMEN

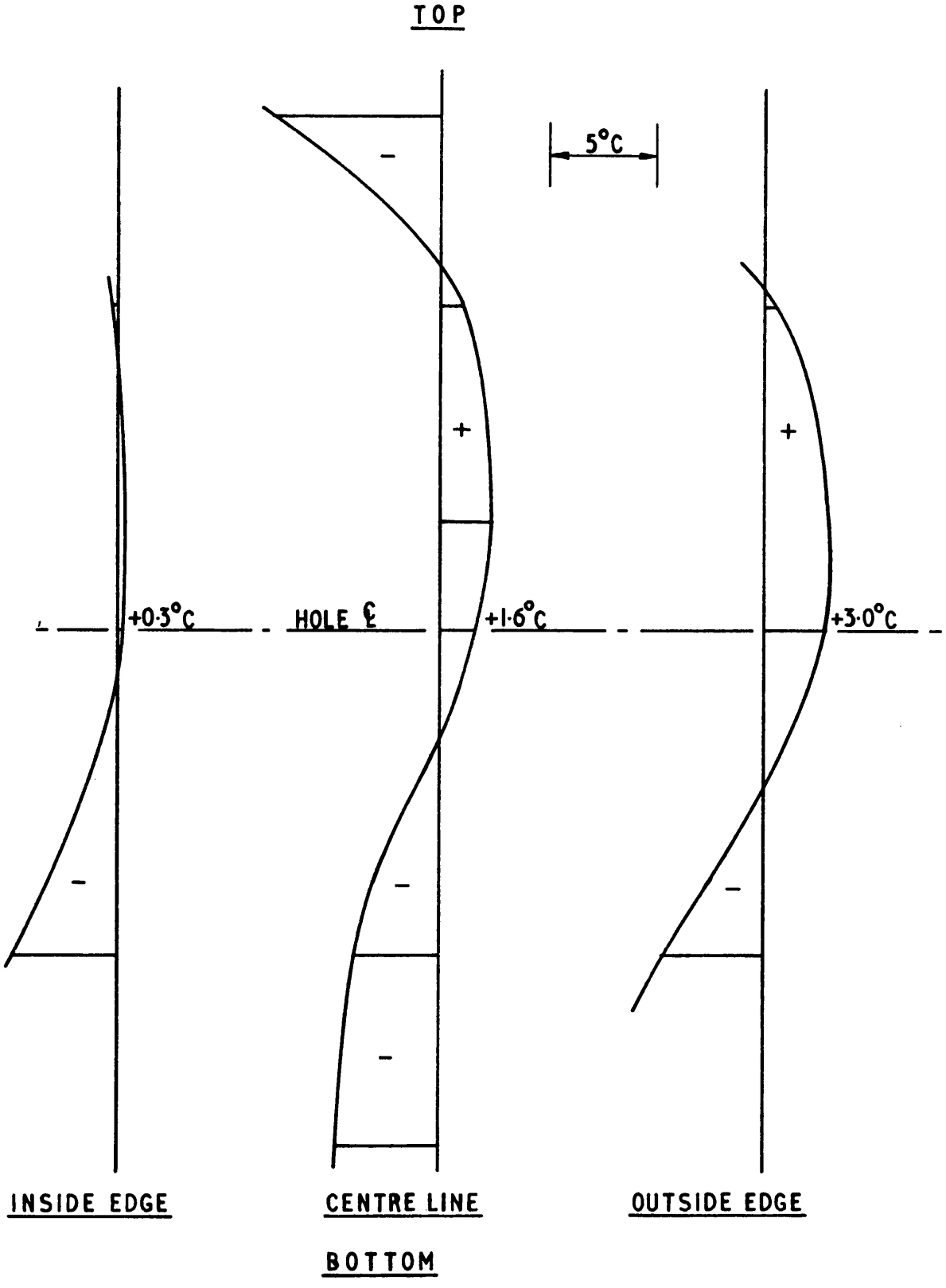

FIGURE 2.34

FURNACE CONFIGURATION FOR OPTIMUM TEMPERATURE CONDITIONS

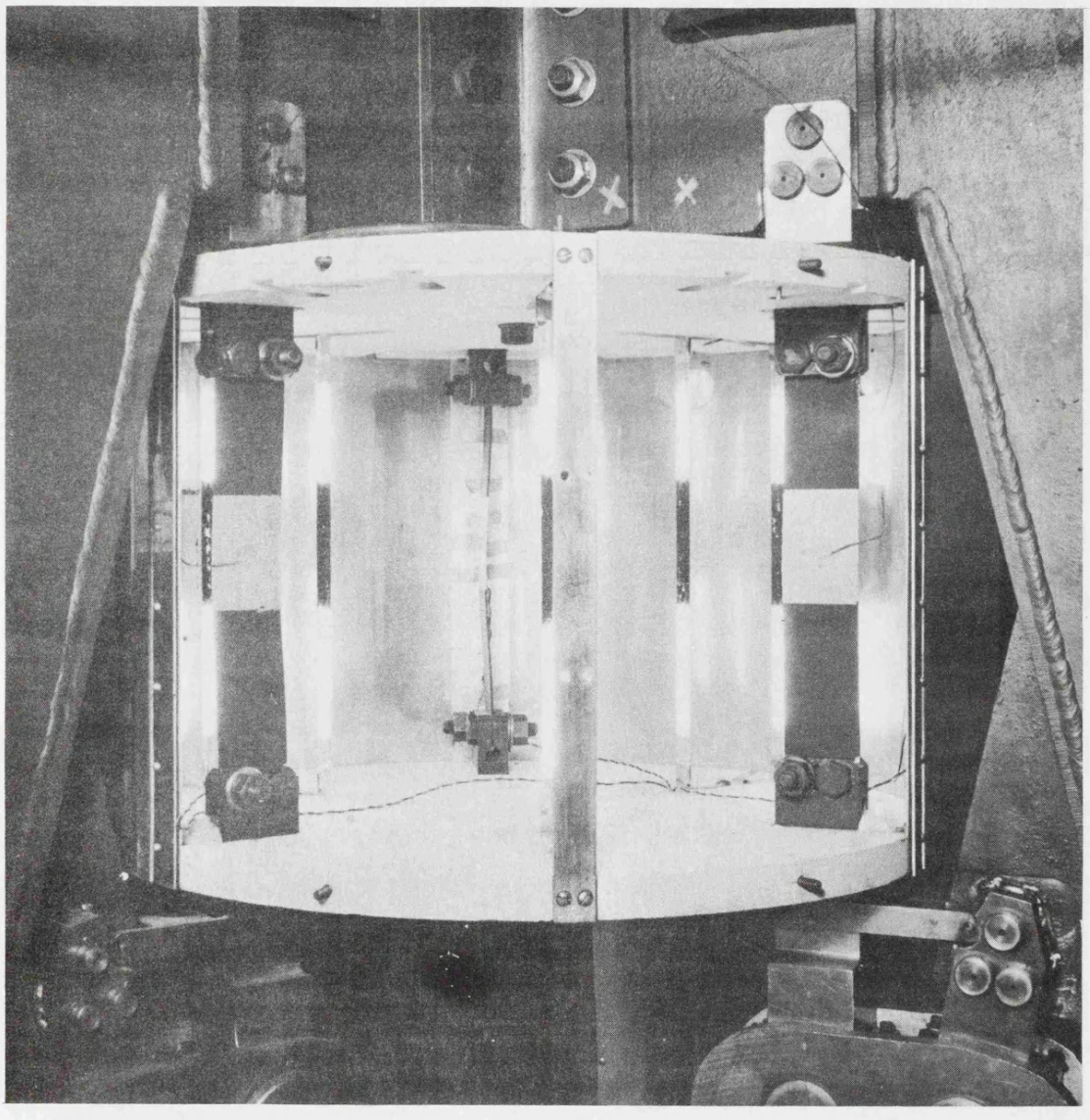

FIGURE 2.35

CURCUIT FOR CYCLE COUNTING AND AUTOMATIC FAILURE INDICATION

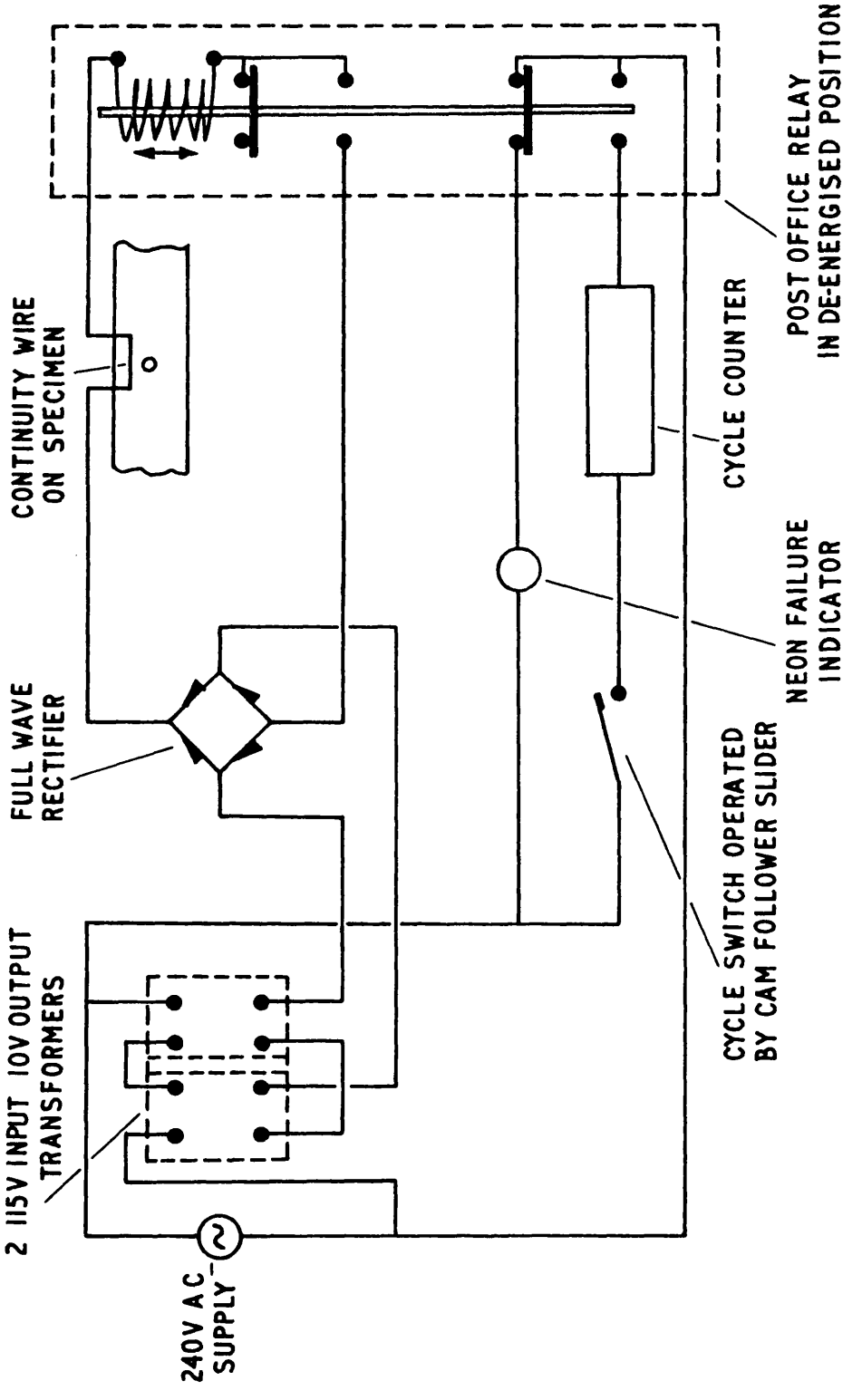

FIGURE 2.36

DIAGRAM OF INSTRUMENTATION USED TO DETERMINE STRUT BUCKLING BEHAVIOUR

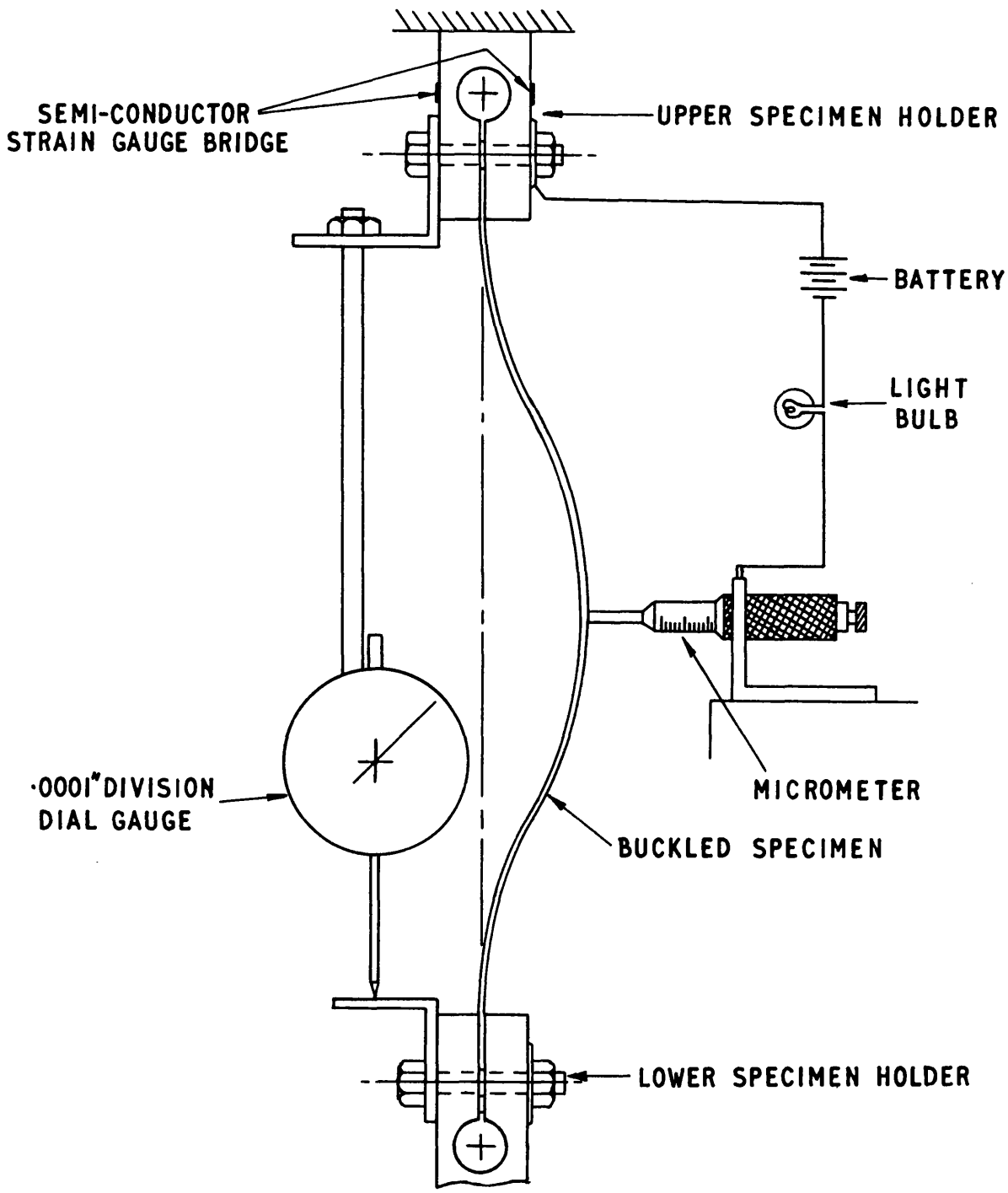

FIGURE 2.37

EFFECT OF CYCLIC CREEP STRAIN ON DISPLACEMENT CONTROLLED CYCLING

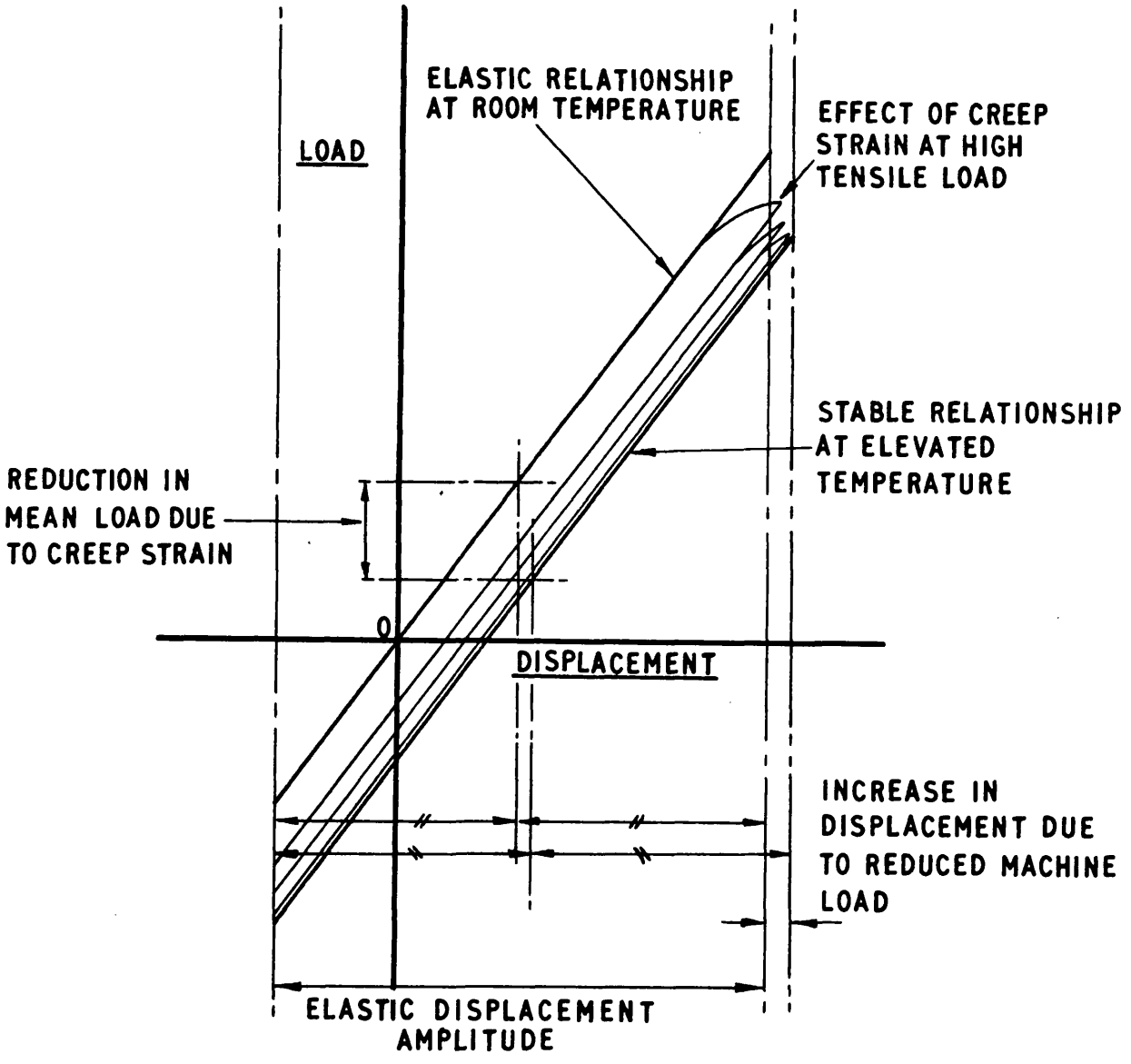

FIGURE 3.1

CHANGE OF POSITION OF AN ELEMENT OF A STRUT WITH INITIAL CURVATURE UNDER THE ACTION OF AN END DISPLACEMENT

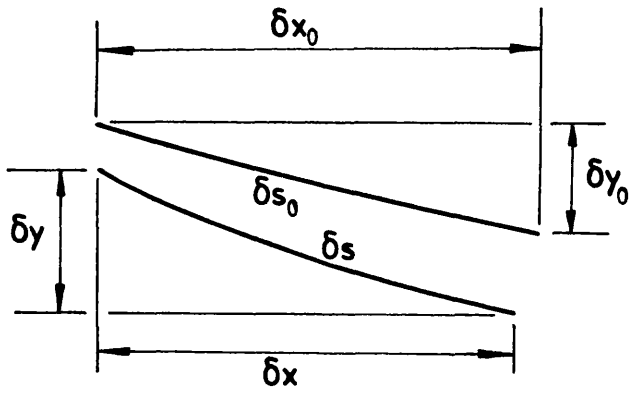

SUFFIX 0 INDICATES THE ORIGINAL POSITION

FIGURE 3.2

AN ECASTRÉ STRUT WITH A CENTRAL LATERAL DEFLECTION b_0

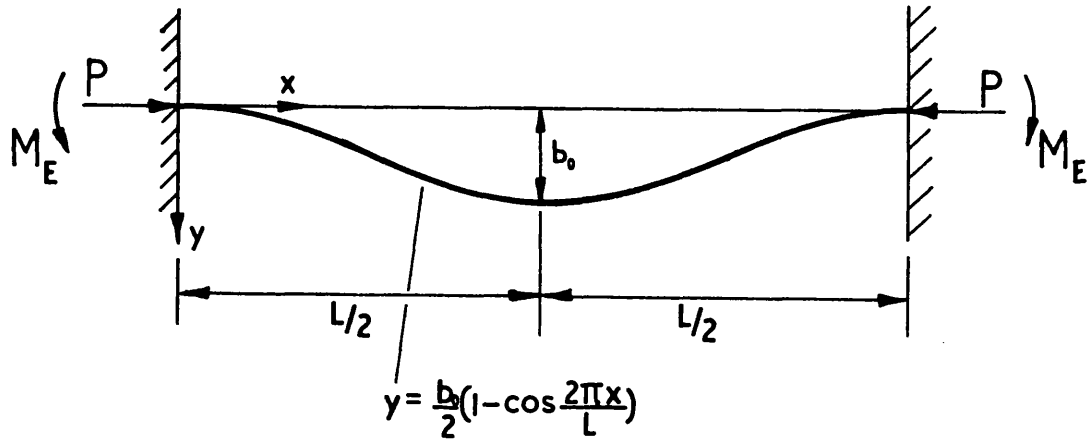

FIGURE 3.3

EXPRESSIONS FOR AN ENCASTRÉ STRUT WITH INITIAL CURVATURE AND ALIGNMENT ERRORS

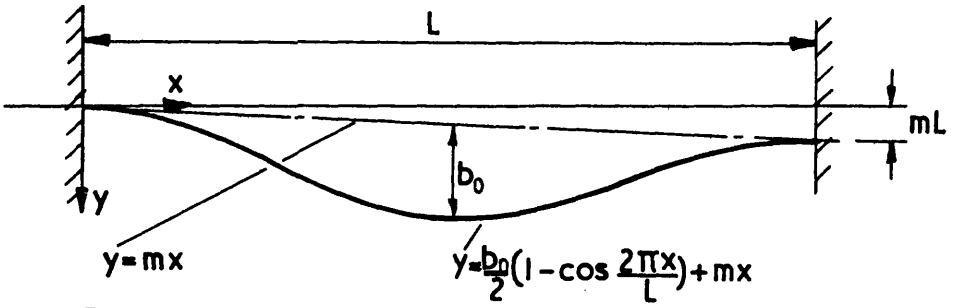

FIGURE 3.3A MISALIGNMENT DUE TO SLOPE OF STRUT AXIS

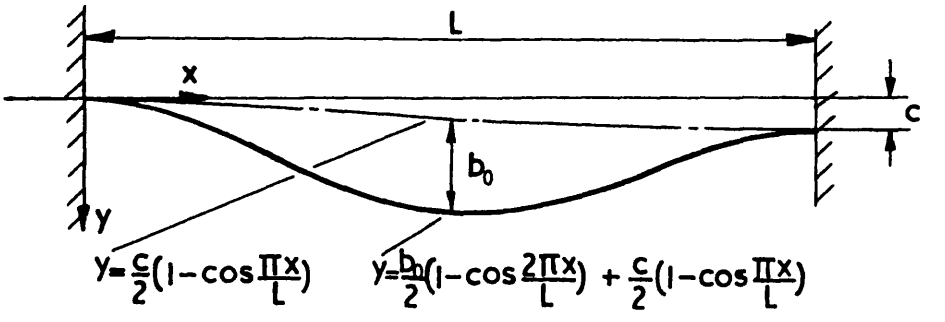

FIGURE 3.3B MISALIGNMENT DUE TO PARALLEL RELATIVE DISPLACEMENT OF THE STRUT ENDS

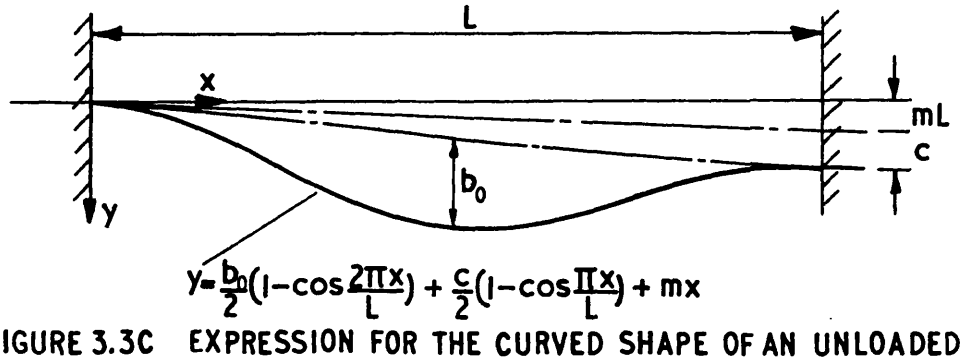

FIGURE 3.3C EXPRESSION FOR THE CURVED SHAPE OF AN UNLOADED ENCASTRÉ STRUT WITH INITIAL CURVATURE AND ALIGNMENT ERRORS

FIGURE 3.4

VARIATION OF END LOAD AND APPARENT CENTRAL DEFLECTION WITH END DISPLACEMENT FOR 10" STRUT WITH INITIAL CURVATURE b_0

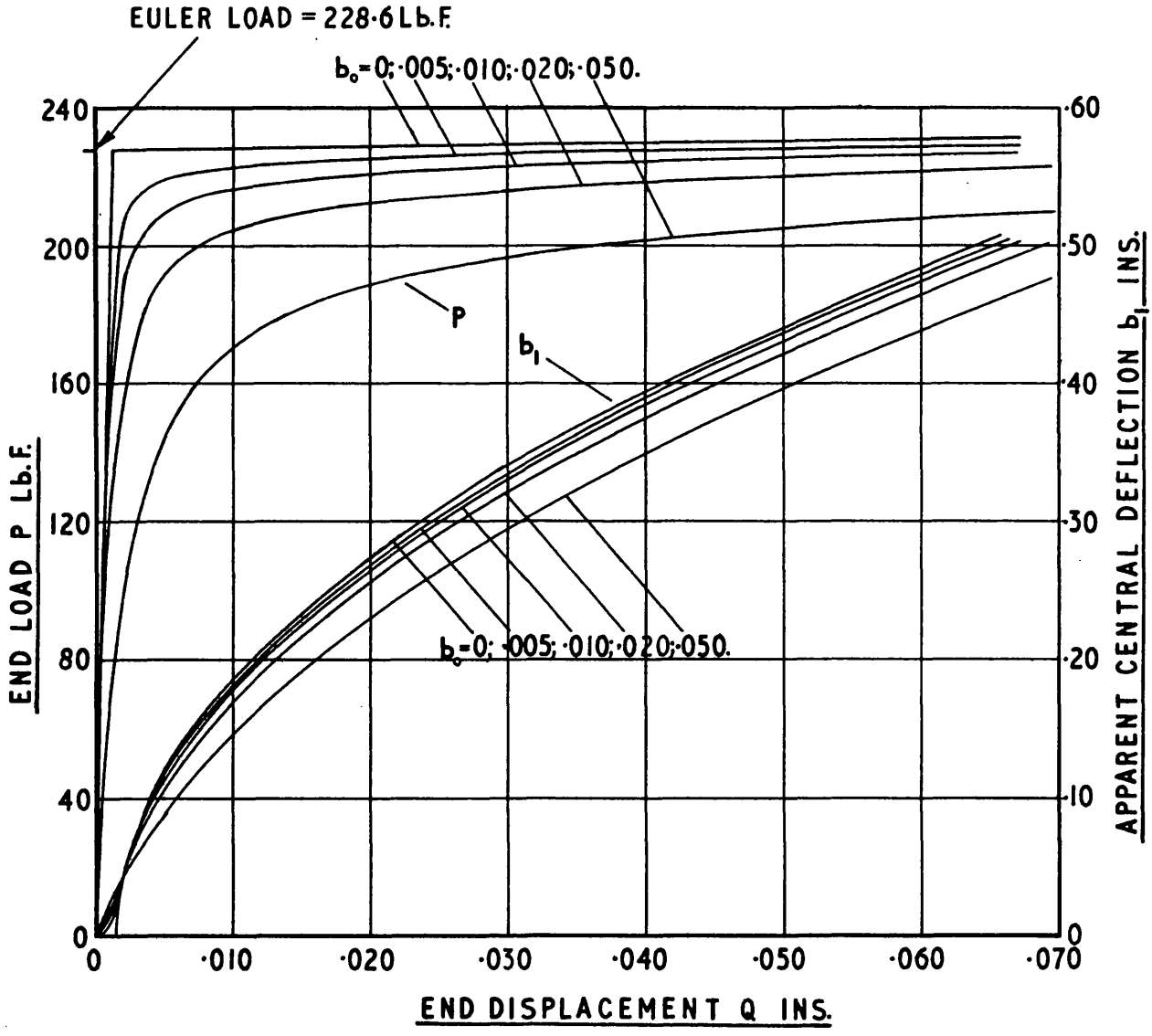

FIGURE 3.5

VARIATION OF END LOAD AND APPARENT CENTRAL DEFLECTION WITH END DISPLACEMENT FOR 10" STRUT WITH SLOPE M ON THE STRUT AXIS

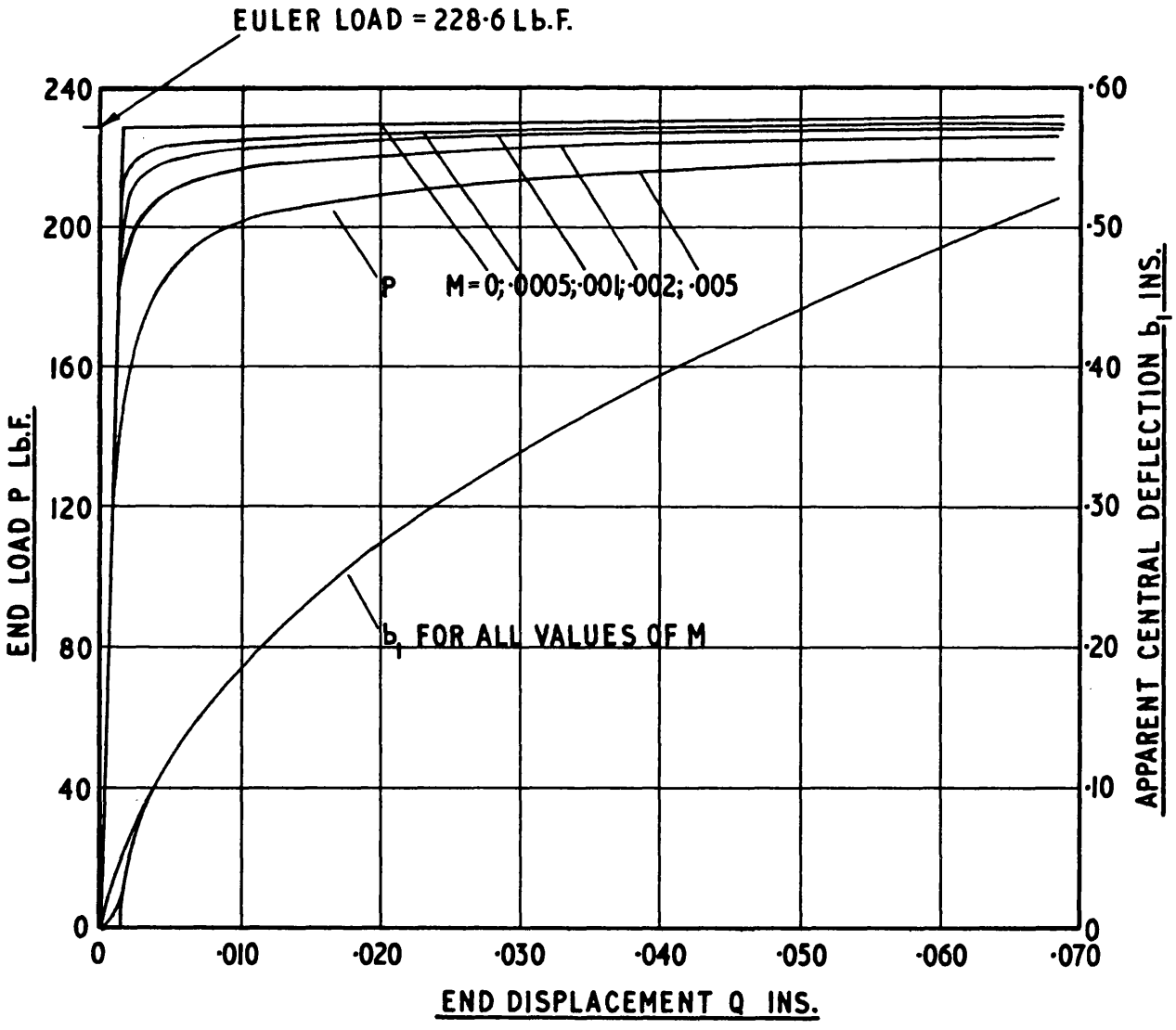

FIGURE 3.6

VARIATION OF END LOAD AND APPARENT CENTRAL DEFLECTION WITH END DISPLACEMENT FOR 10" STRUT WITH PARALLEL END DISPLACEMENT C

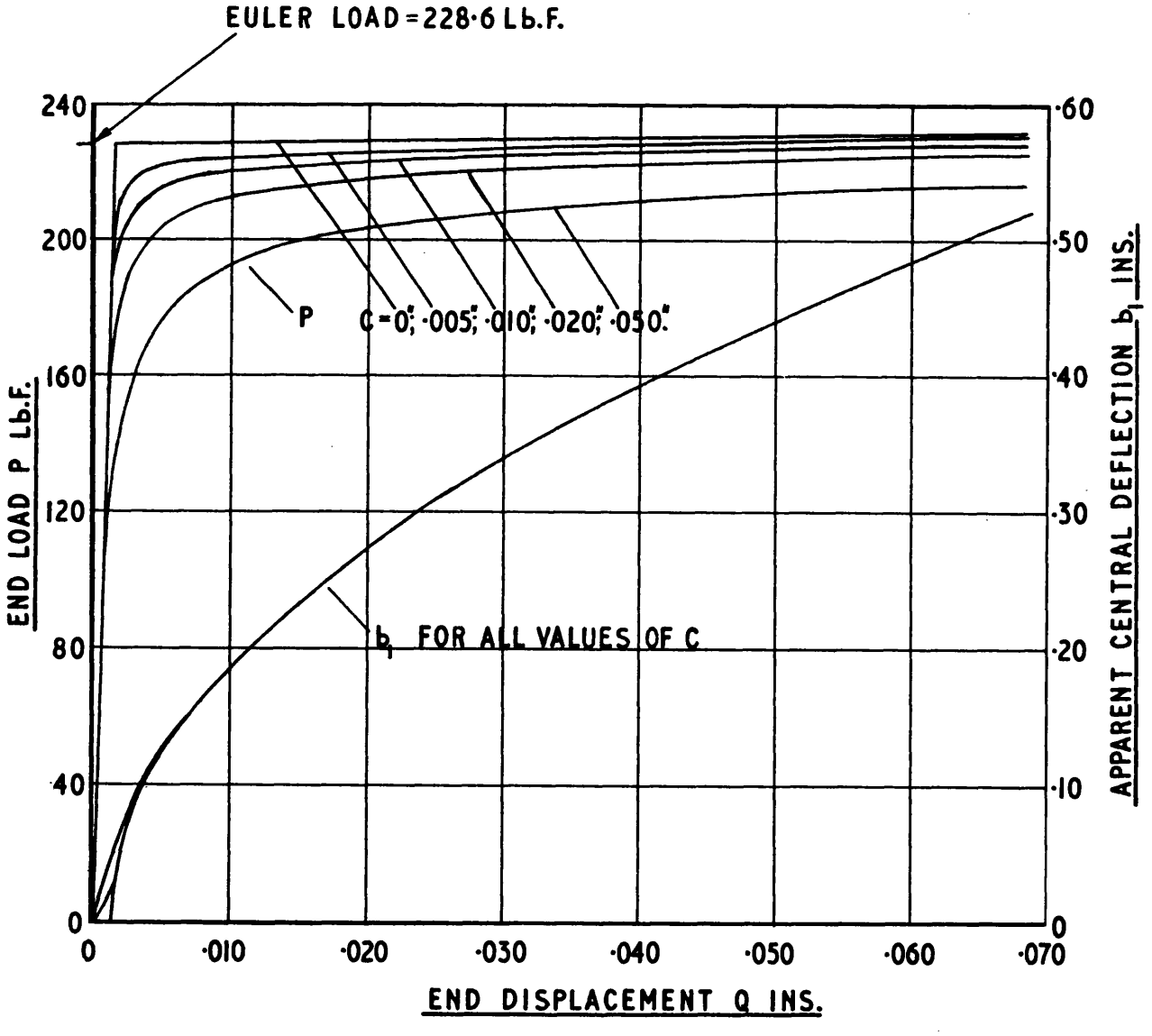

FIGURE 3.7

VARIATION OF SURFACE STRESS WITH END DISPLACEMENT FOR A 10" LONG ENCASTRÉ STRUT

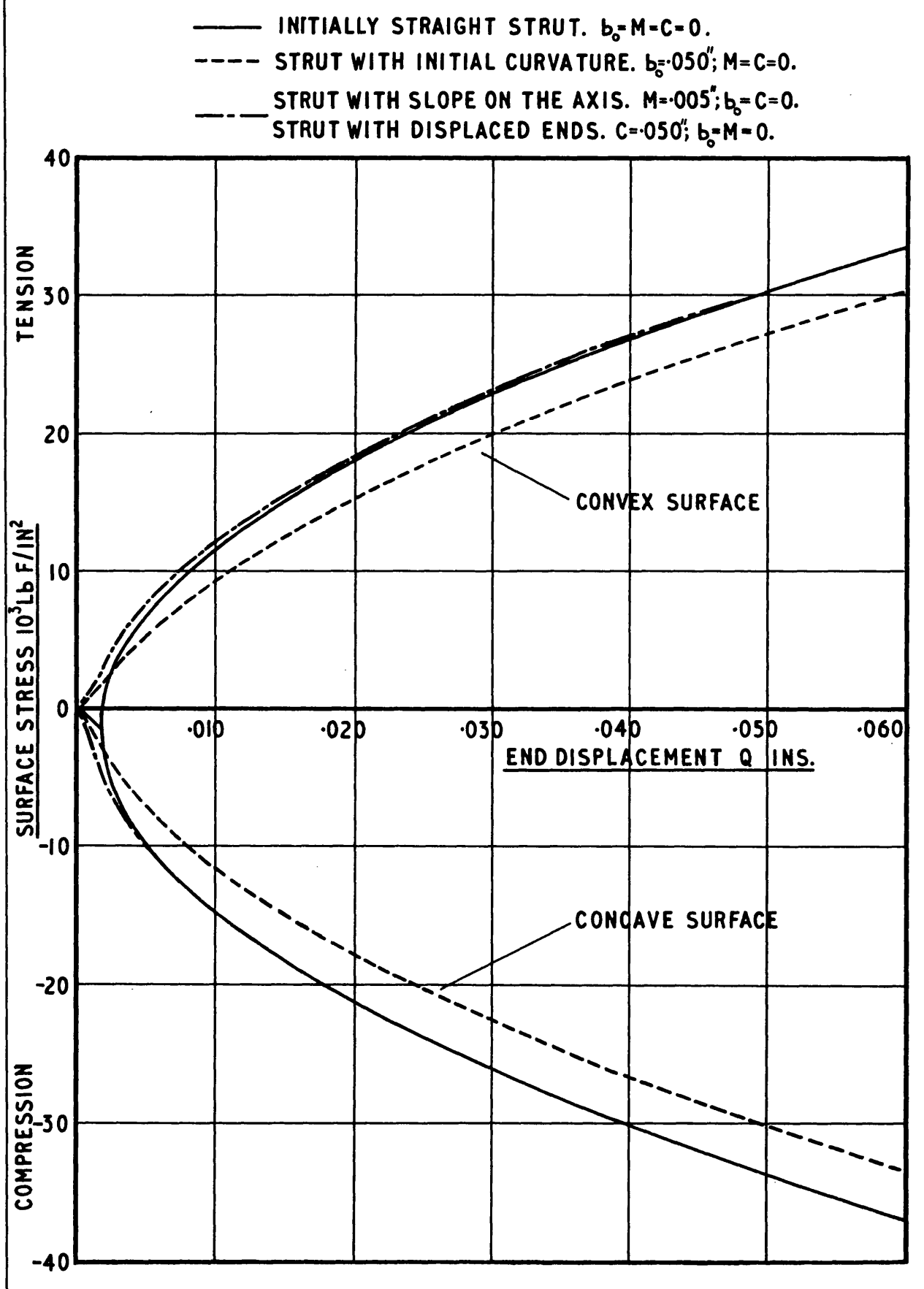

FIGURE 3.8

VARIATION OF END LOAD AND APPARENT CENTRAL DEFLECTION WITH END DISPLACEMENT FOR 10" STRUT WITH COMBINATIONS OF ALIGNMENT ERRORS

CASE				
	A	$b_o = 0"$	$M = 0"$	$C = 0"$
	B	$b_o = -.050"$	$M = -.005"$	$C = -.050"$
	C	$b_o = -.050"$	$M = -.005"$	$C = 0"$
	D	$b_o = -.050"$	$M = 0"$	$C = -.050"$
	E	$b_o = -.050"$	$M = -.005"$	$C = -.050"$

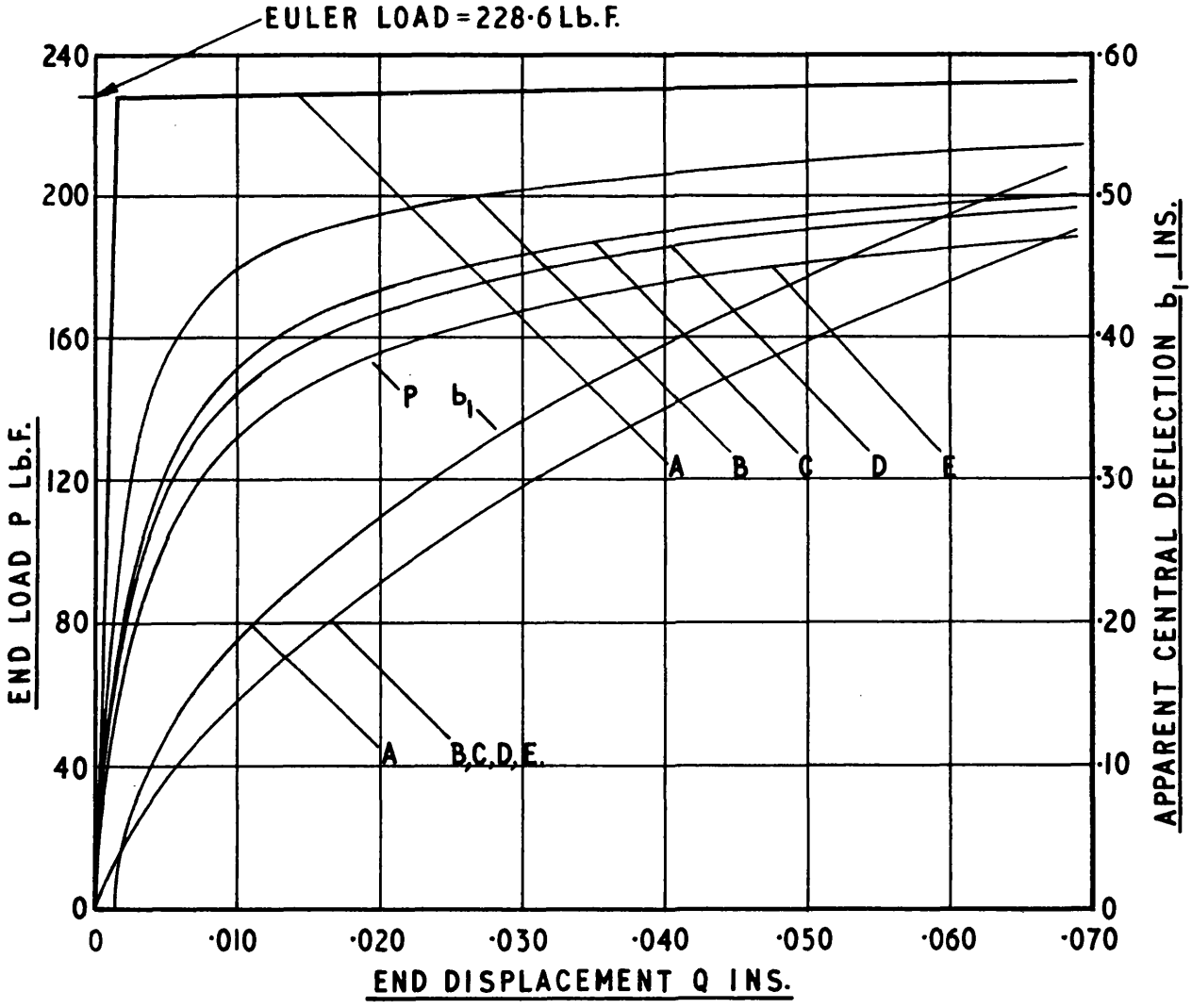

FIGURE 3.9

COMPARISON OF THE ELASTICA AND COSINE SOLUTIONS TO THE BUCKLING OF AN INITIALLY STRAIGHT 10" LONG ENCASTRÉ STRUT. VARIATIONS OF END LOAD AND CENTRAL DEFLECTION WITH END DISPLACEMENT

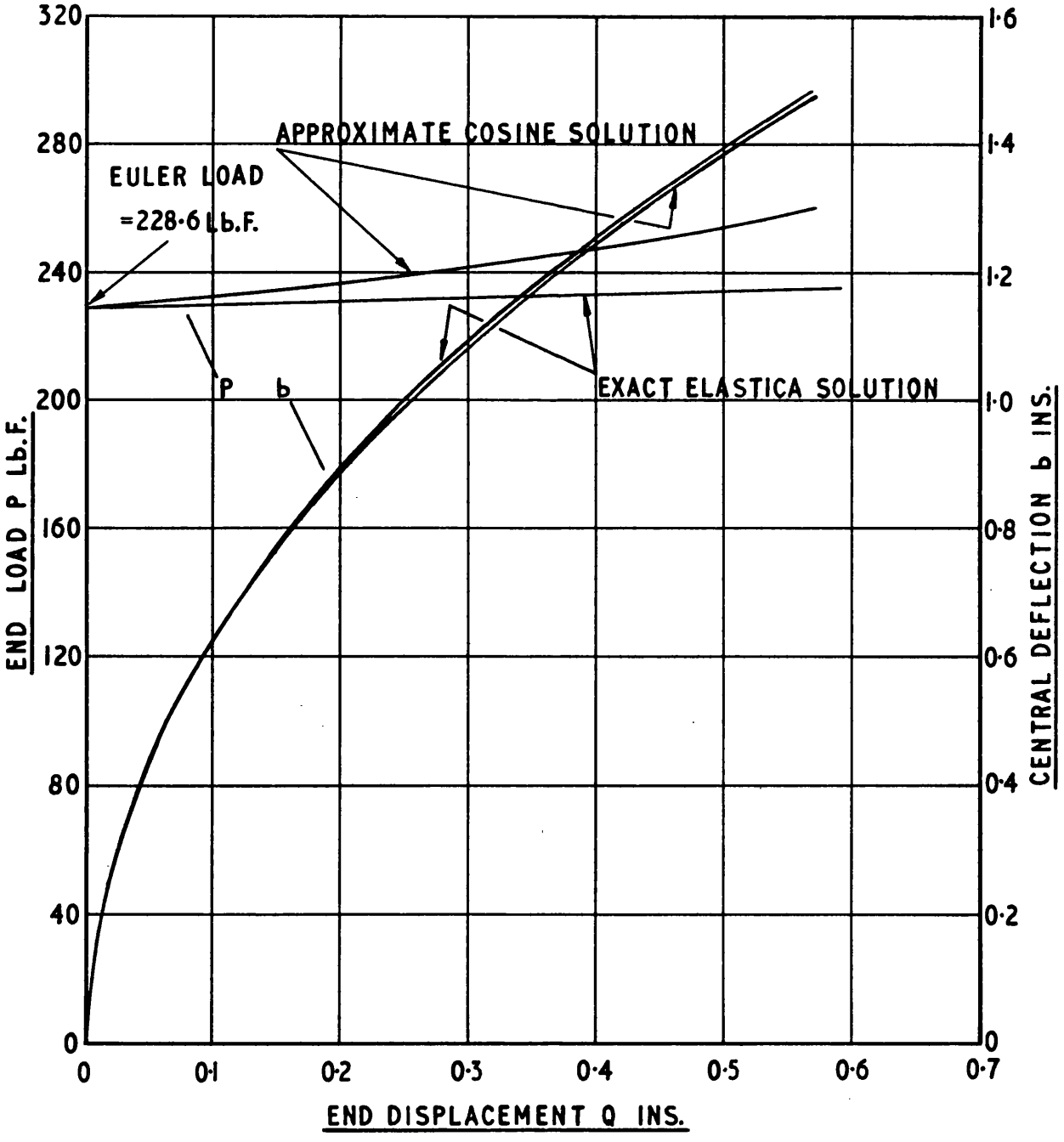

FIGURE 3.10

COMPARISON OF THE ELASTICA AND COSINE SOLUTIONS TO THE BUCKLING OF AN INITIALLY STRAIGHT 10" LONG ENCASTRÉ STRUT. VARIATION OF SURFACE STRESS WITH END DISPLACEMENT

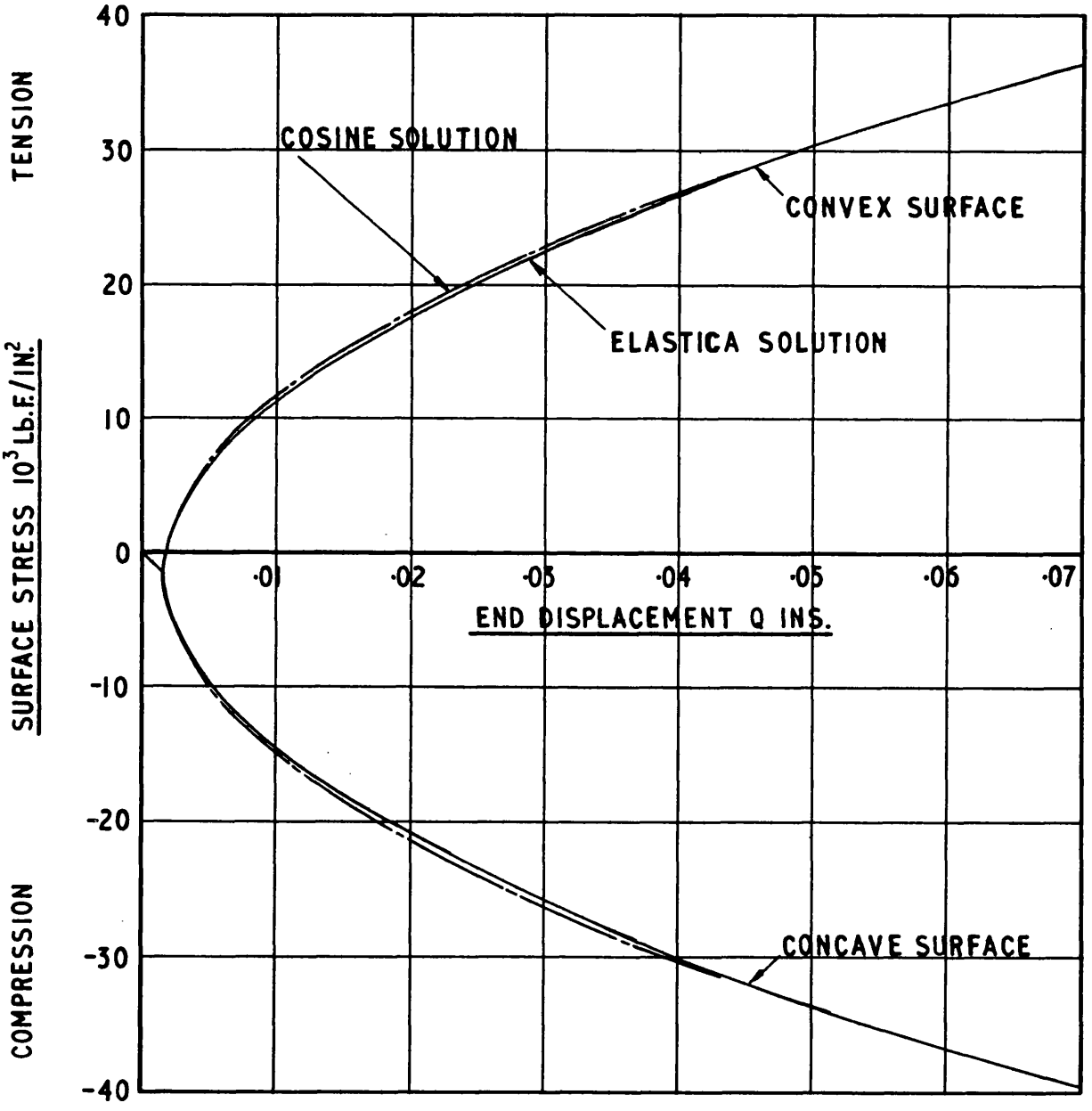

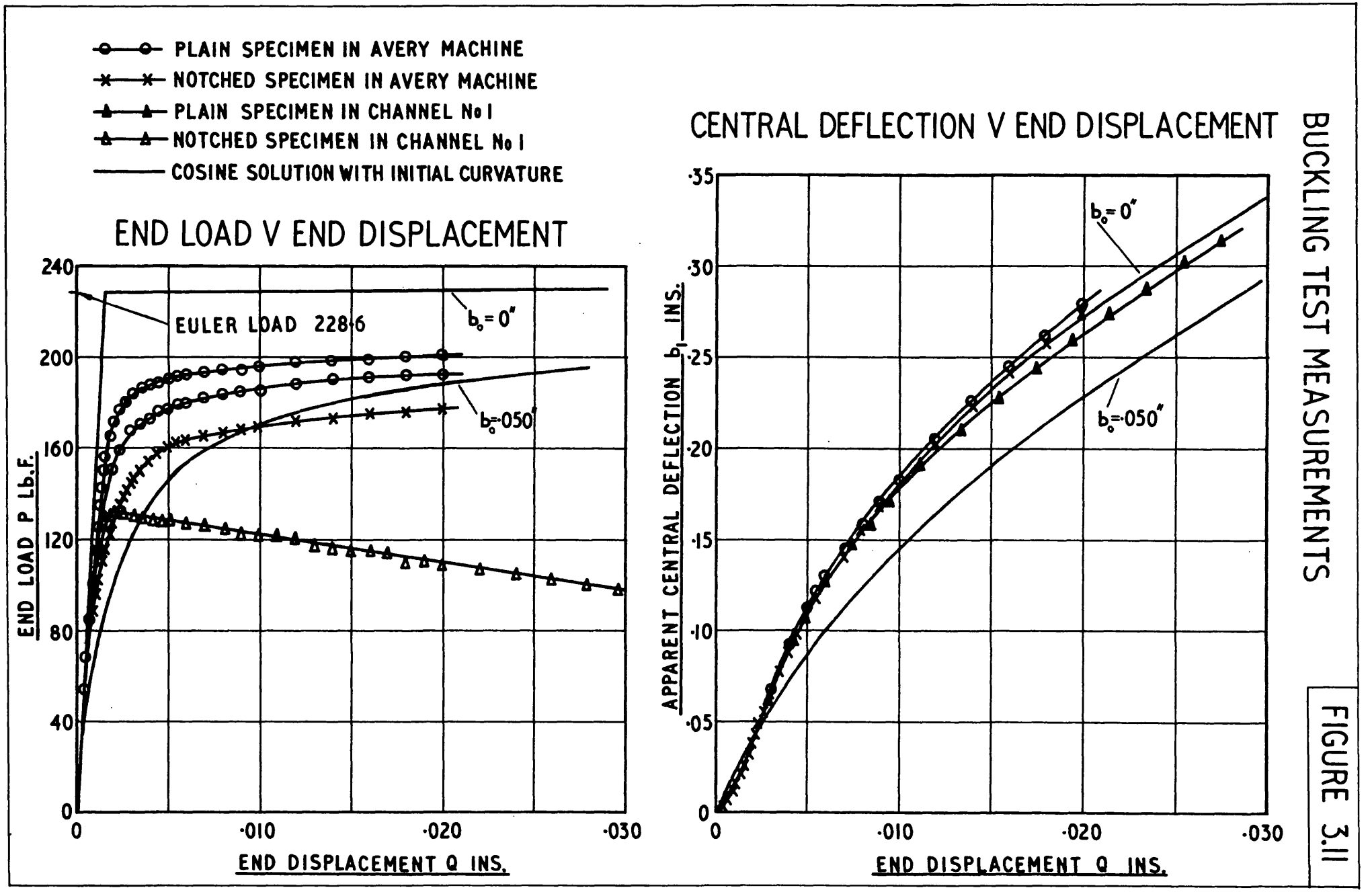
PLAIN SPECIMEN IN AVERY MACHINE
NOTCHED SPECIMEN IN AVERY MACHINE
PLAIN SPECIMEN IN CHANNEL No I
NOTCHED SPECIMEN IN CHANNEL No I
COSINE SOLUTION WITH INITIAL CURVATURE
END LOAD V END DISPLACEMENT
EULER LOAD 228·6
b_o= 0"
b_o=·050"
END LOAD P Lb.F.
240
200
160
120
80
40
0
0
·010
·020
·030
END DISPLACEMENT Q INS.
CENTRAL DEFLECTION V END DISPLACEMENT
APPARENT CENTRAL DEFLECTION b_1 INS.
·35
·30
·25
·20
·15
·10
·05
0
b_o= 0"
b_o=·050"
0
·010
·020
·030
END DISPLACEMENT Q INS.
BUCKLING TEST MEASUREMENTS
FIGURE 3.11

FIGURE 3.12

CORRELATION OF THEORETICAL AND TEST VALUES OF SURFACE STRESS FOR A BUCKLING STRUT

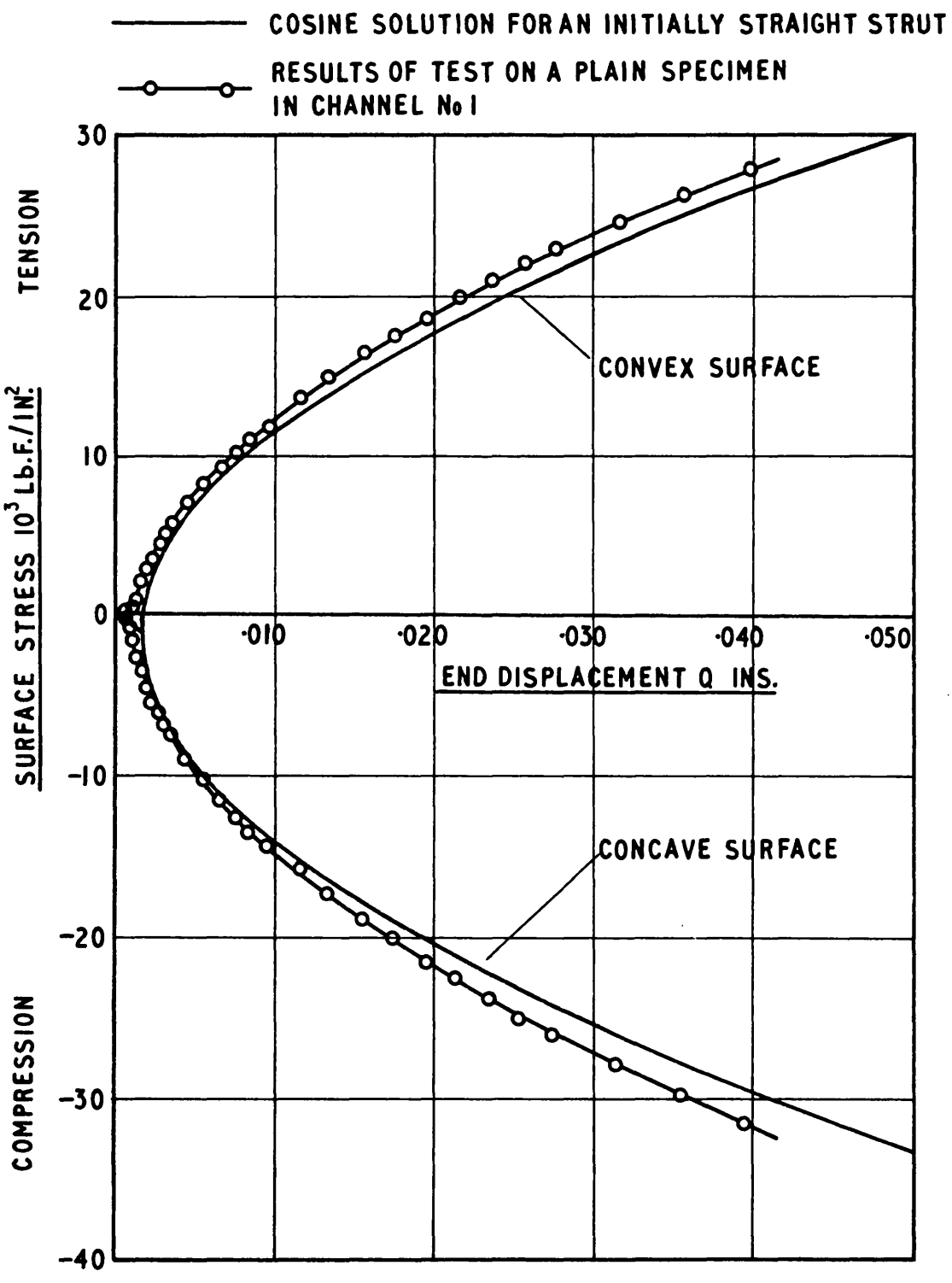

FIGURE 3.13

SEMI-CONDUCTOR STRAIN GAUGE BRIDGE ON UPPER SPECIMEN HOLDER IN CHANNEL No.1

STRAIN GAUGES: KYOWA TYPE KSP-3-F2-11
RESISTANCE: 116Ω±2%
GAUGE FACTOR: 223±3%
SENSE: P: POSITIVE
N: NEGATIVE

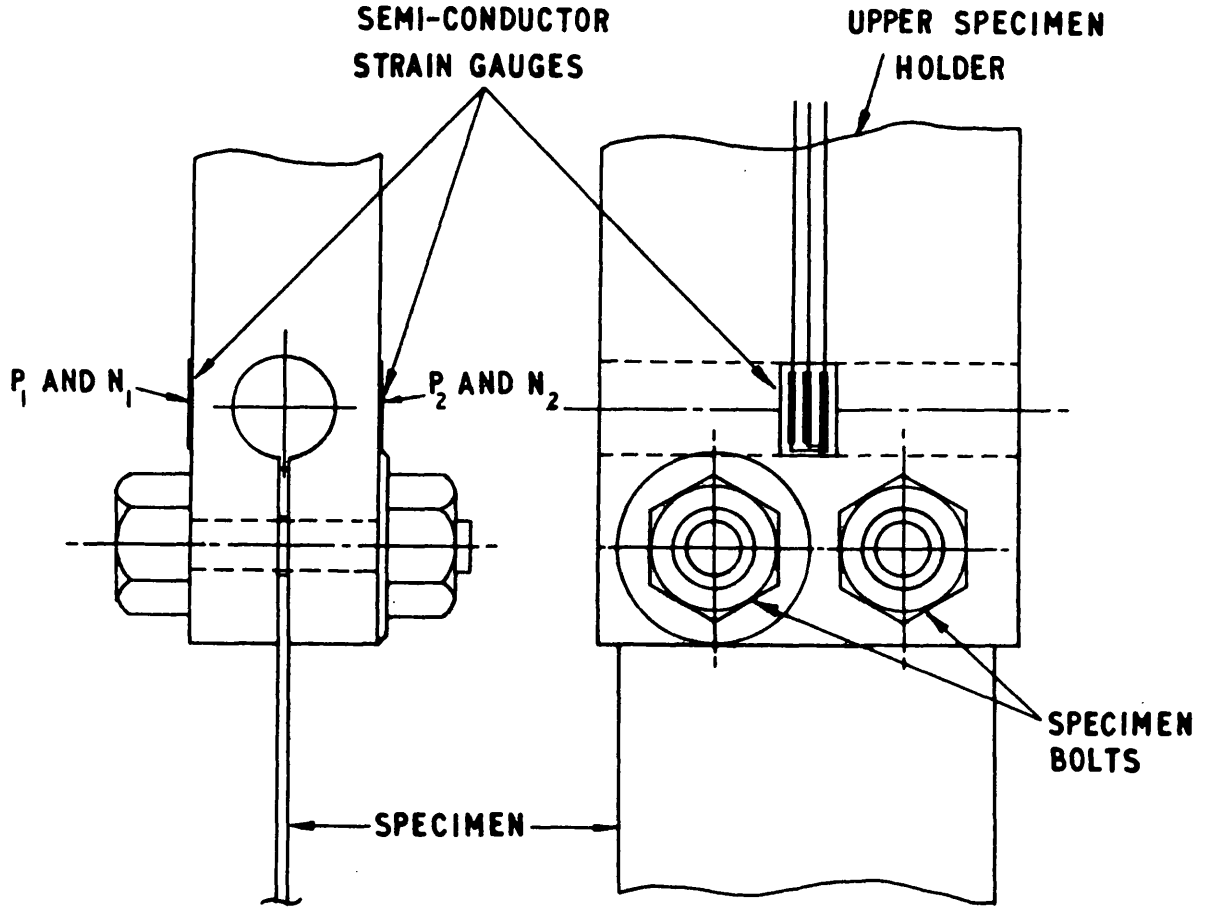

STRAIN MEASUREMENT CIRCUIT

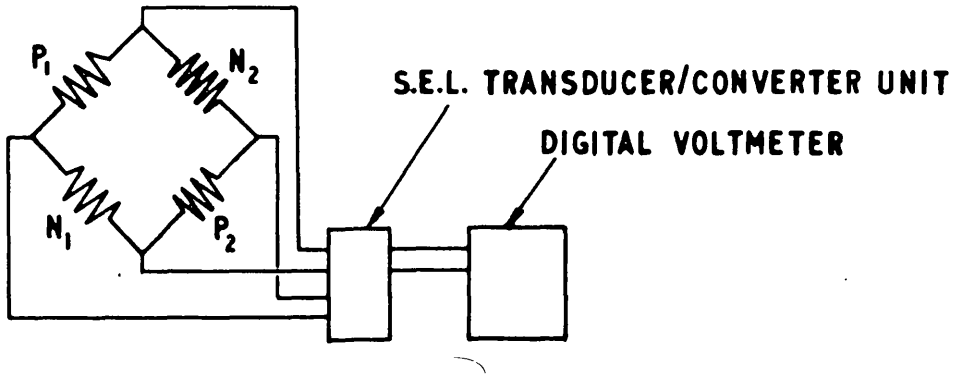

FIGURE 4.1

DETAILS OF TEST SPECIMENS.

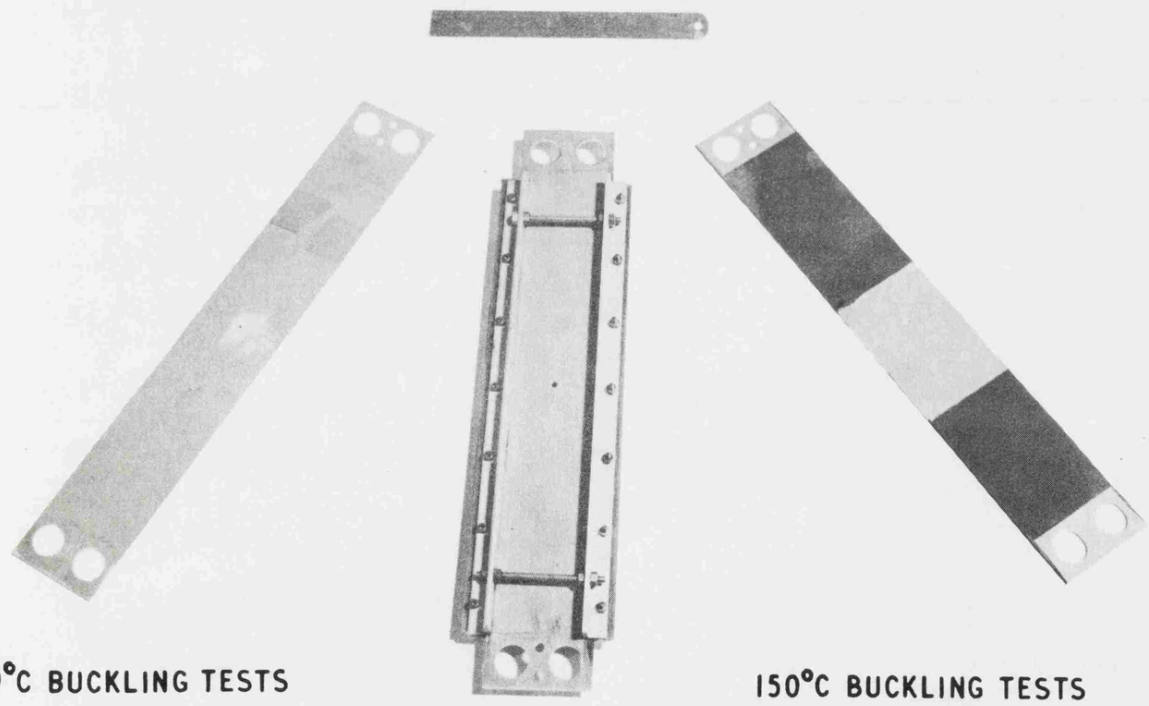

20°C BUCKLING TESTS

NON BUCKLING TESTS

150°C BUCKLING TESTS

FIGURE 4.2

SPECIFICATION OF CM001/ID ALUMINIUM ALLOY

ELEMENT	CORE		CLADDING	
	MIN. %	MAX. %	MIN. %	MAX. %
COPPER	1.8	2.7	-	-
MAGNESIUM	1.2	1.8	-	-
SILICON	0.15	0.25	-	-
IRON	0.9	1.4	-	-
MANGANESE	-	0.2	-	-
NICKEL	0.8	1.4	-	-
ZINC	-	0.1	0.8	1.2
LEAD	-	0.05	-	-
TIN	-	0.05	-	-
TITANIUM	-	0.2	-	-
ALUMINIUM	-	REMAINDER	-	REMAINDER

HEAT TREATMENT

Material delivered in fully heat treated condition (T6) having been cold rolled, solution treated at $530^{\circ}C \pm 5^{\circ}C$ and water quenched, pre-aged at $150^{\circ}C \pm 10^{\circ}C$ for 30 ± 10 min. and quenched, flattened and precipitated at $190^{\circ}C \pm 5^{\circ}C$ for 19.5 ± 0.5 hours.

MINIMUM TENSILE PROPERTIES

0.2% proof stress : 21.0 tons/in.^{2}

tensile strength : 25.5 tons/in.^{2}

elongation % : 6 on 2"

ACCEPTANCE CREEP TEST

Total plastic strain $< 0.1\%$ after 93 hours at 175° at 10.16 tons f./in.^{2}

MEASURED STATIC TENSILE STRENGTH

Plain specimen : 60,900 lb.f./in.^{2}

Notched specimen: 60,000 lb.f./in.^{2}

FIGURE 4.3

TYPICAL STRESS-STRAIN CURVE FOR CM001 ALUMINIUM ALLOY IN THE FULLY HEAT TREATED CONDITION

U.T.S.= 60,900 Lb. F./IN.^{2}

0·1% PROOF STRESS = 56,000 Lb.F./IN.^{2}

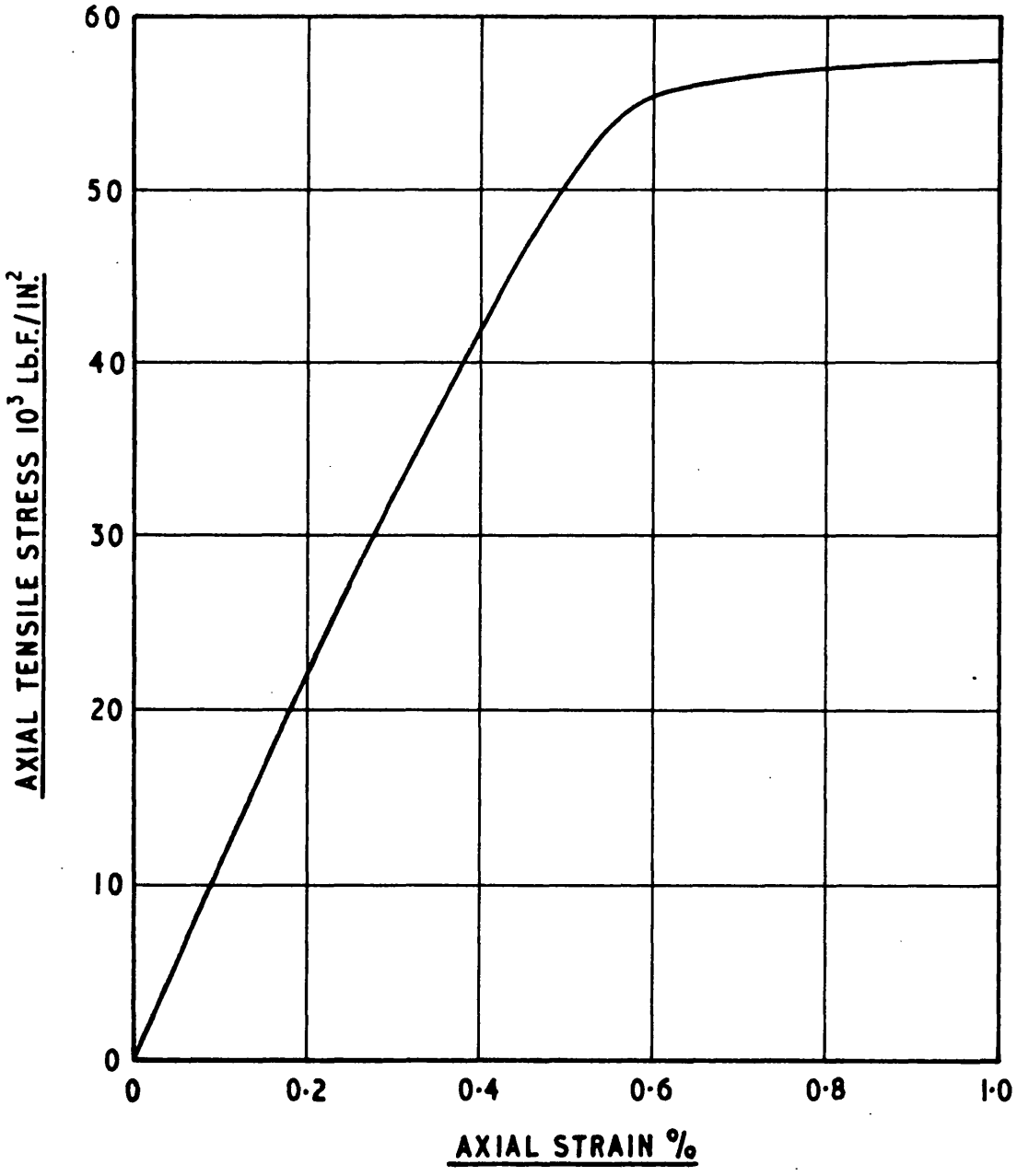

TEST SERIES	TYPE OF TEST	NOMINAL MEAN DISPLACE-MENT	TEST TEMP. °C.	CHANNEL NO.	ACTUAL MEAN DISPLACE-MENT	ACTUAL DISPLACE - MENT AMPLITUDE	FATIGUE LIFE CYCLES	COMMENTS
A 1	FLUCTUATING TENSION	+ .020"	20°C	1	+ .02226"	± .01611"	8,646	
				2	+ .0212"	± .0173"	8,282	
				3	+ .0222"	± .01617"	7,379	
	FLUCTUATING TENSION	+ .020"	150°C	4	+ .0204"	± .01805"	5,454	APPRECIABLE BUCKLING DUE TO CREEP ELONGATION DURING LOADING
				5	+ .0203"	± .0186"	6,630	
				6	+ .0201	± .01895"	7,318	
B 1	TENSION-COMPRESSION WITHOUT BUCKLING	+ .015	20°C	4	+ .0168"	± .0173"	11,181	
				5	+ .0169"	± .01705"	8,949	
				6	+ .0164"	± .01725"	11,555	
	TENSION COMPRESSION NOMINALLY WITHOUT BUCKLING	+ .015"	150°C	4	+ .0154"	± .01805	7,725	APPRECIABLE BUCKLING DUE TO CREEP ELONGATION DURING LOADING
				5	+ .0150"	± .0189"	8,472	
				6	+ .0152"	± .0190"	6,460	
C1B	BUCKLING TEST	+ .010"	20°C	1	+ .0124"	± .01625	15,521	
				2	+ .0123"	± .0147"	14,721	
				1	+ .0109"	± .01685"	14,920	REPEAT TEST
		+ .010"	150°C	4	+ .0103"	± .01825"	12,584	CONTINUITY WIRE DID NOT BREAK
				5	+ .0103"	± .01895"	11,764	
				6	+ .0101"	± .0191"	11,897	
C1NB	NON-BUCKLING TEST	+ .010"	20°C	1	+ .0111"	± .01695"	13,483	
				2	+ .0108"	± .01775"	11,496	
				3	+ .0106"	± .01755"	10,896	
C 2B	BUCKLING TEST	+ .005"	20°C	4	+ .0061"	± .0163"	-	CYCLE COUNTER BECAME UNSERVICABLE
				5	+ .0063"	± .01725"	18,467	
				6	+ .0132"	± .0173"	-	DRIVE LINK BECAME DISCONNECTED
	BUCKLING TEST	+ .005"	150°C	4	+ .0047"	± .01835"	19,492	
				5	+ .0050"	± .0193	16,309	
				6	+ .0047"	± .0193"	16,014	

TEST PROGRAMME AND RESULTS

FIGURE 4.4

TEST PROGRAMME AND RESULTS CONT'D

FIGURE 4.5

TEST SERIES	TYPE OF TEST	NOMINAL MEAN DISPLACE - MENT	TEST TEMP. °C	CHANNEL NO.	ACTUAL MEAN DISPLACE - MENT	ACTUAL DISPLACE - MENT AMPLITUDE	FATIGUE LIFE CYCLES	COMMENTS
C2NB	NON-BUCKLING TEST	+ .005"	20°C	1	+ .0065"	± .0160"	17,275	
				2	+ .0059"	± .0169"	19,304	
				3	+ .0057"	± .0176"	15,179	
C3B	BUCKLING TEST	.000"	20°C	4	+ .0004"	± .0181"	33,112	
				5	+ .0010"	± .01775"	35,329	
				6	+ .0004"	± .0172"	31,085	
	BUCKLING TEST	.000"	150°C	4	.000"	± .0189"	33,022	
				5	.000"	± .0193"	34,146	
				6	.000"	± .0193"	35,839	
C3NB	NON-BUCKLING TEST	.000"	20°C	1	+ .0001"	± .0177"	)	ESTIMATED LIVES, AS CONTINUITY WIRES DID NOT BREAK
				2	+ .0002"	± .01745"	) 24,635	
				3	+ .0017"	± .0172"	)	
C4B	BUCKLING TEST	- .005"	20°C	1	- .0054"	± .01855"	95,616	
				2	- .0056"	± .0191"	98,396	
				3	- .0089"	± .01875"	79,037	
	BUCKLING TEST	- .005"	150°C	4	- .0054"	± .0189"	74,064	
				5	- .0053"	± .0187"	66,024	
				6	- .0049"	± .01915"	68,330	
REPEAT C4B	BUCKLING TEST	- .005"	20°C	1	- .0063"	± .01665"	131,292	
				2	- .0058"	± .01865"	87,398	
				3	- .0055"	± .0188"	100,935	
C4NB	NON-BUCKLING TEST	- .005"	20°C	1	- .0042"	± .01685"	35,046	
				2	- .0047"	± .01735"	39,963	
				3	- .0051"	± .01735"	43,412	

TEST PROGRAMME AND RESULTS CONT'D

TEST SERIES	TYPE OF TEST	NOMINAL MEAN DISPLACE-MENT	TEST TEMP. °C	CHANNEL NO.	ACTUAL MEAN DISPLACE-MENT	ACTUAL DISPLACE-MENT AMPLITUDE	FATIGUE LIFE CYCLES	COMMENTS
C5B	BUCKLING TEST	-.010"	20°C	4	-.0121"	±.01785"	386,687	) SPECIMENS FAILED AT JAW
				5	-.0129"	±.01775"	386,687	) EDGES
				6	-.0128"	±.01770"	382,846"	
	BUCKLING TEST	-.010"	150°C	4	-.0105"	±.0185"	214,507	
				5	-.0098"	±.01935"	117,069	
				6	-.0109"	±.01940	201,941	
REPEAT C5B	BUCKLING TEST	-.010"	20°C	1	-.0104"	±.0187"	177,979	
				2	-.0106"	±.0186"	245,331	
				3	-.0101"	±.0189"	295,820	
C5NB	NON-BUCKLING TEST	-.010"	20°C	1	-.0092	±.01710"	86,390	) ESTIMATED FATIGUE LIVES AS
				2	-.0097"	±.01785"	79,380	) CONTINUITY WIRES FAILED
				3	-.0100"	±.01755"	96,593	) BEFORE SPECIMEN FAILURE.
C6B	BUCKLING TEST	-.015"	20°C	1	-.0176"	±.01755"	310,343	FAILED AT BOTTOM JAW EDGE
				2	-.0148"	±.01765"	452,557	
				3	-.0176"	±.01720"	325,642	
C6NB	NON-BUCKLING TEST	-.015"	20°C	1	-.0145"	±.01690"	229,424	ALSO CRACKED AT BOTTOM JAW EDGE
				2	-.0157"	±.01575"	186,199	
				3	-.0163"	±.01675	63,095	FAILED TOP JAW EDGE
D1B	COMPLETELY BUCKLED TEST	-.020"	20°C	1	-.0205"	±.01885"	338,640	
				2	-.0209"	±.01820"	373,697	
				3	-.0225"	±.01720"	721,661	UNBROKEN.

FIGURE 4.6

FIGURE 4.7

RESULTS OF FATIGUE TEST PROGRAMME.
MEAN DISPLACEMENT V CYCLES TO FAILURE

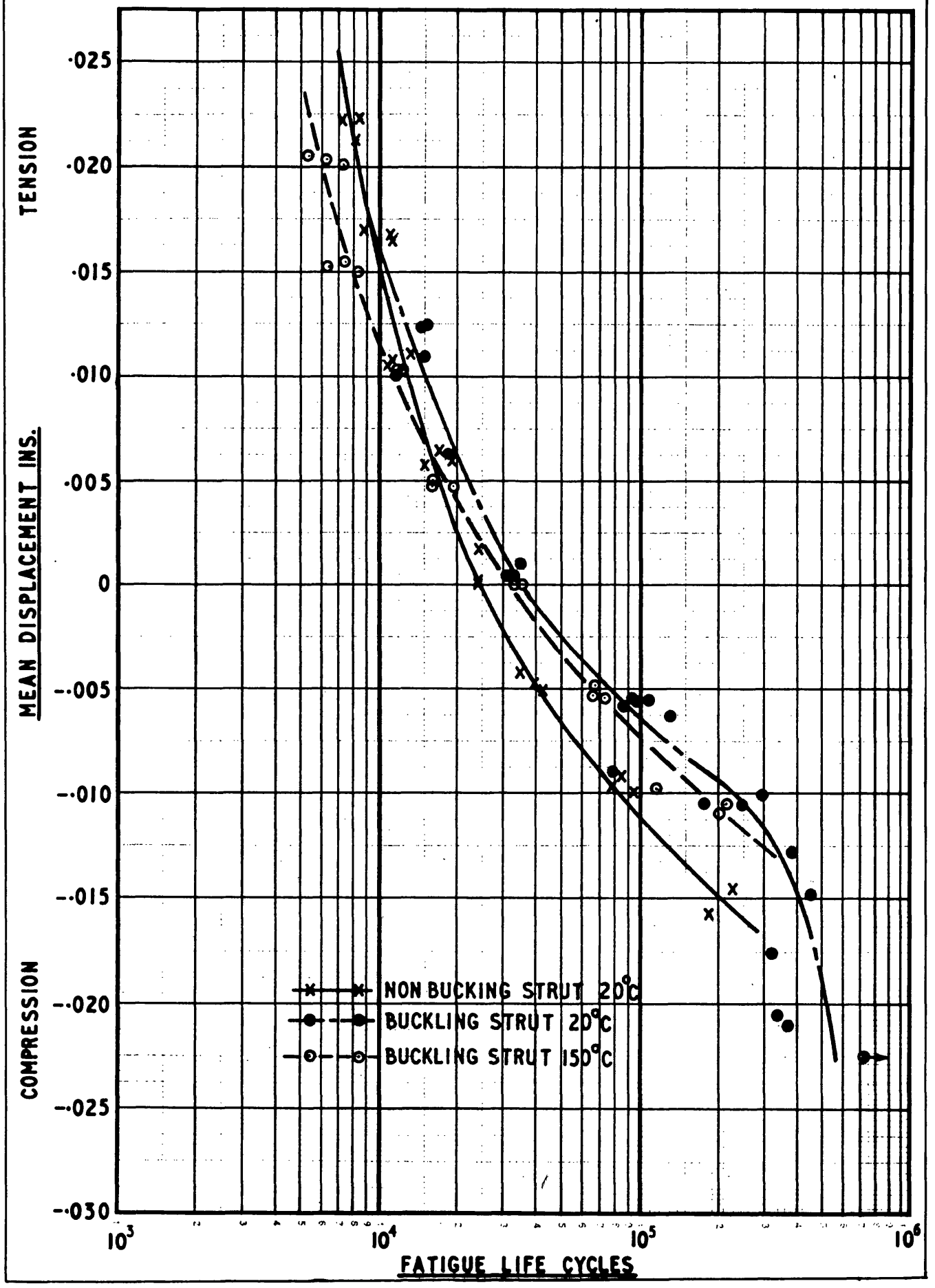

FIGURE 4.8

VARIATIONS IN APPEARANCE OF FRACTURE SURFACES OF SPECIMENS FROM 20°C BUCKLING TESTS

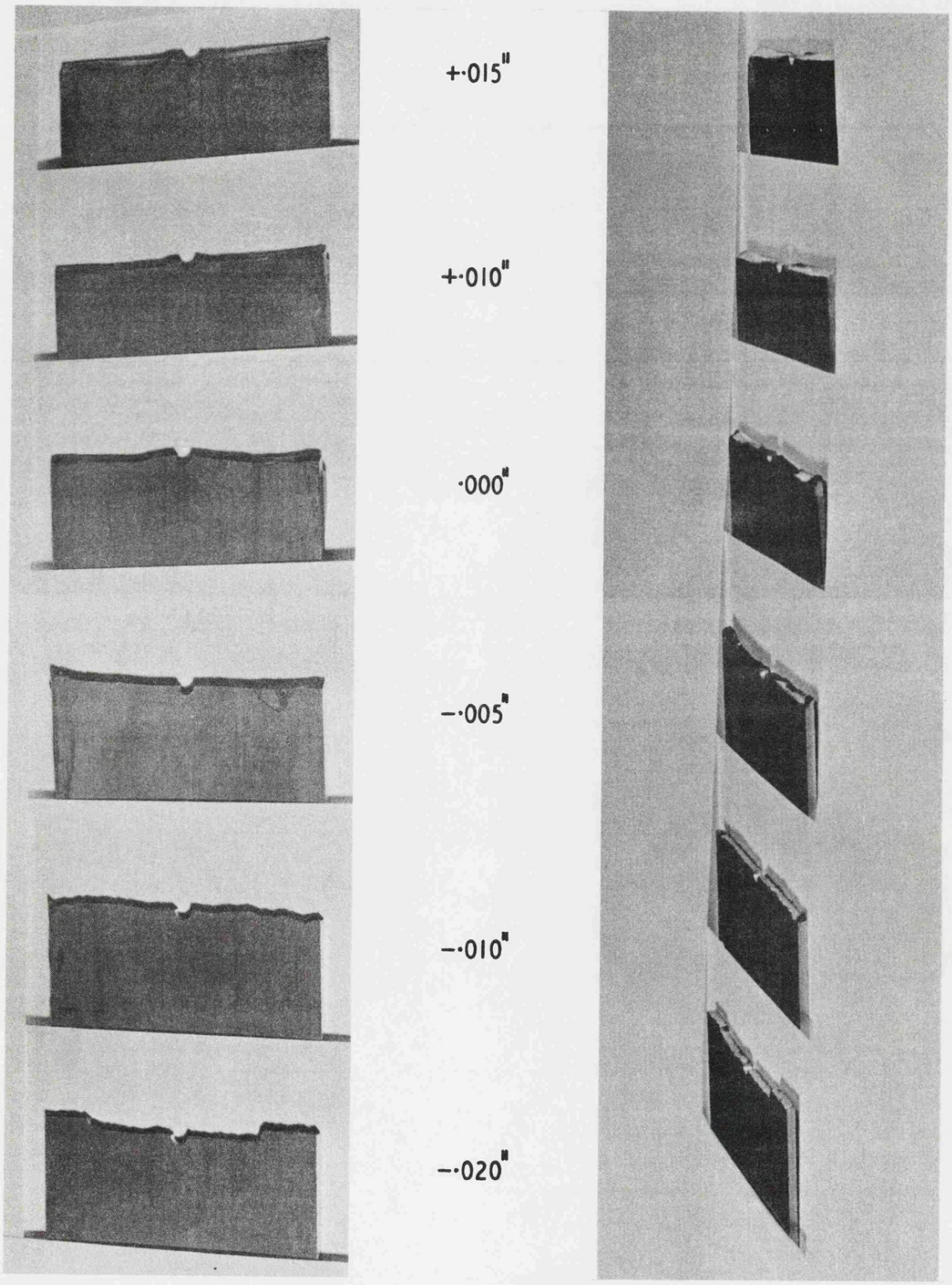

FIGURE 4.9

CRACK PROPAGATION CURVES FOR BUCKLING SPECIMEN TESTS

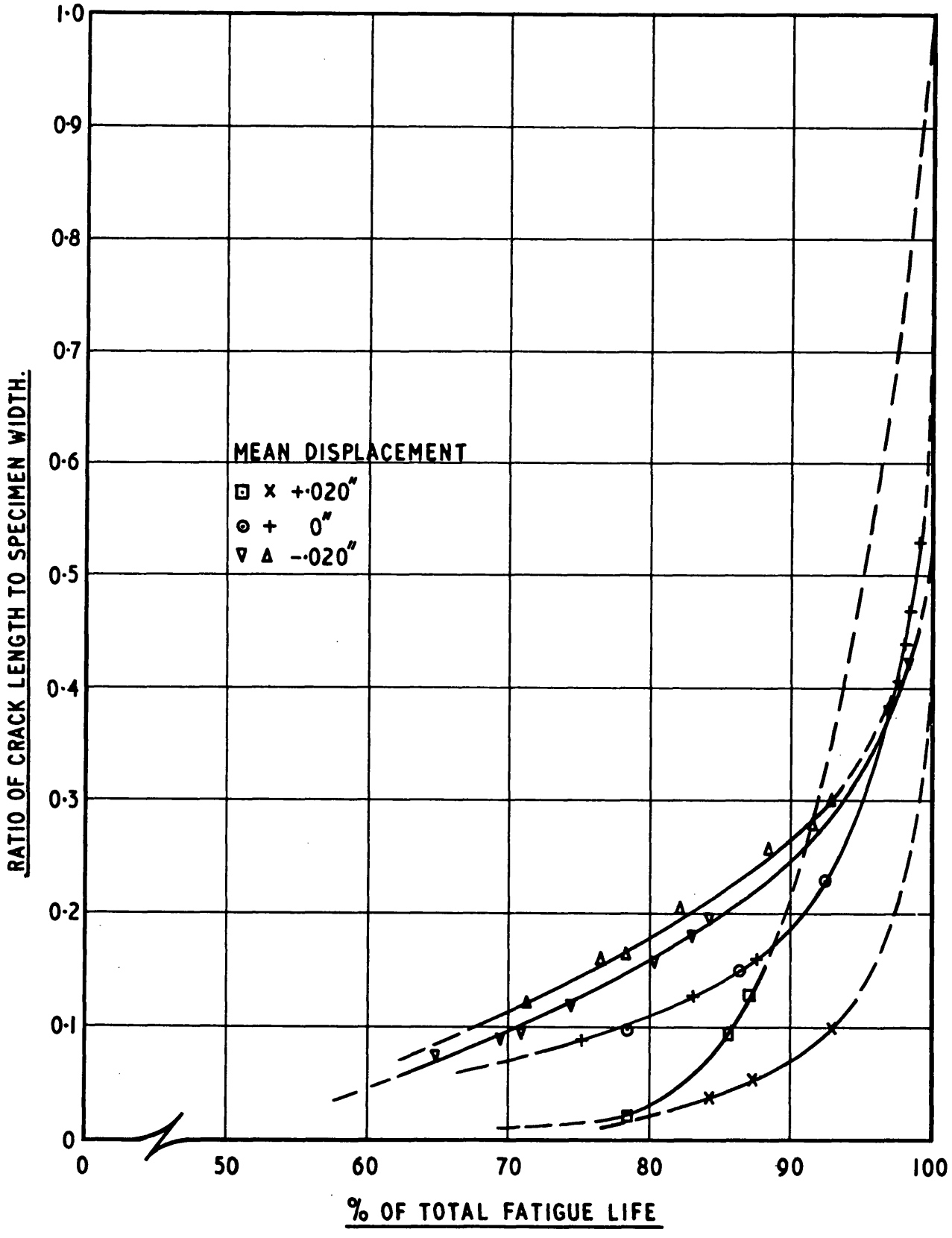

FIGURE 4.10

VARIATION OF DISPLACEMENT AMPLITUDE WITH MEAN DISPLACEMENT FROM TEST PROGRAMME MEASUREMENTS

OPEN POINTS: BUCKLING TESTS; CLOSED POINTS: NON BUCKLING TESTS.

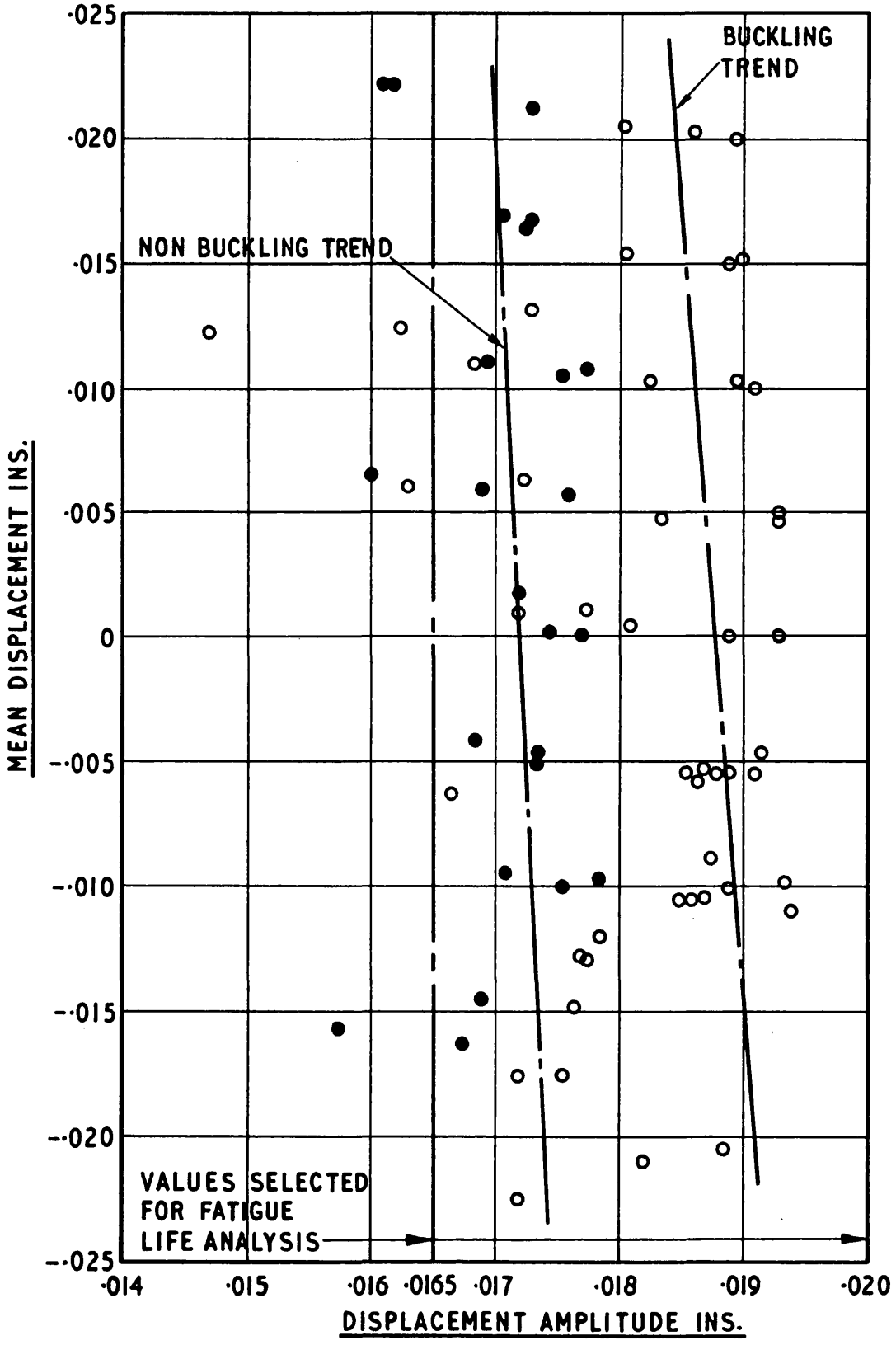

FIGURE 4.11

VARIATION OF SURFACE STRESS WITH END DISPLACEMENT FOR BUCKLING AND NON-BUCKLING STRUTS

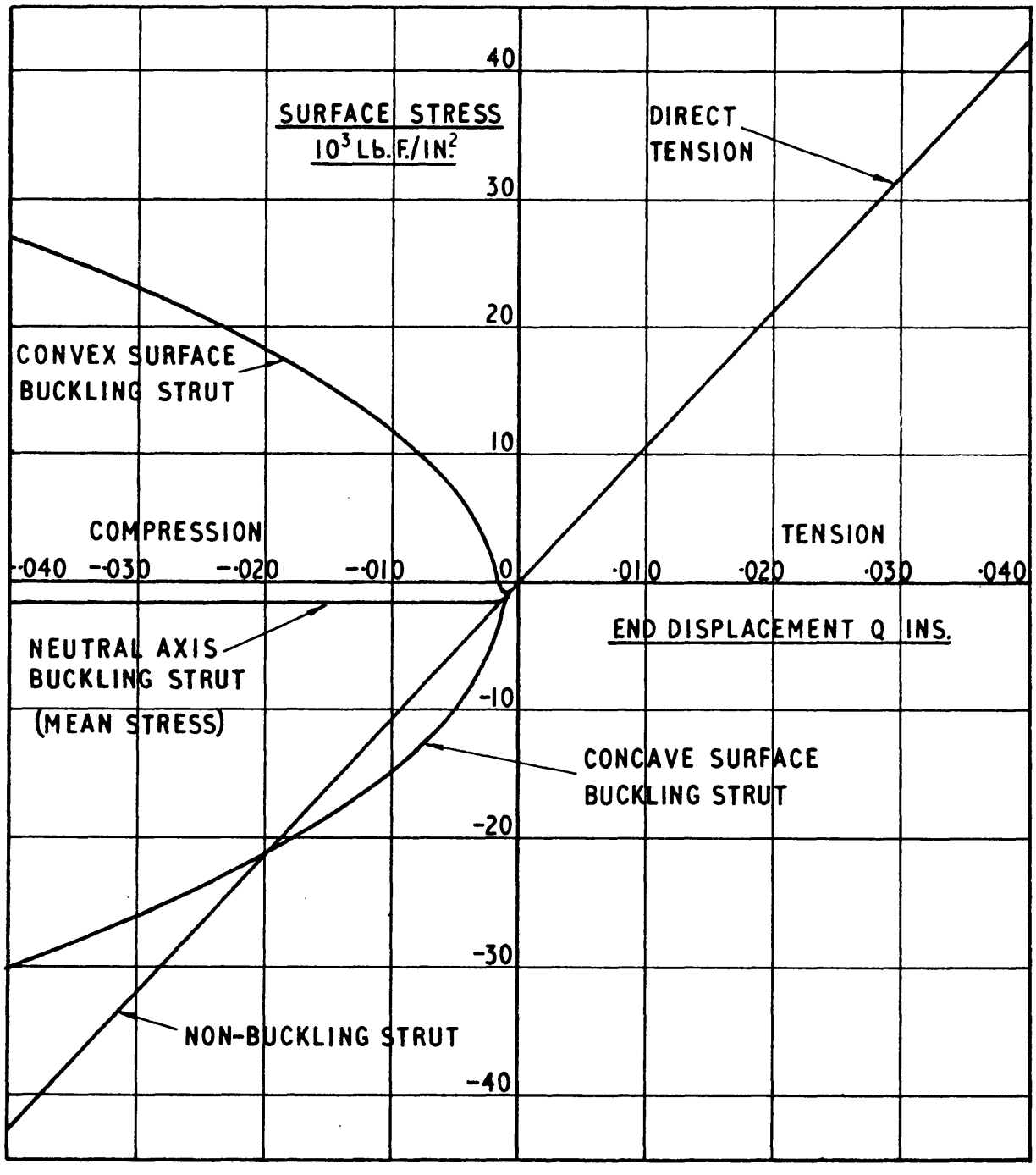

VARIATION OF MEAN STRESS WITH MEAN END DISPLACEMENT FOR BUCKLING AND NON BUCKLING STRUTS FOR A DISPLACEMENT AMPLITUDE OF ±·020"

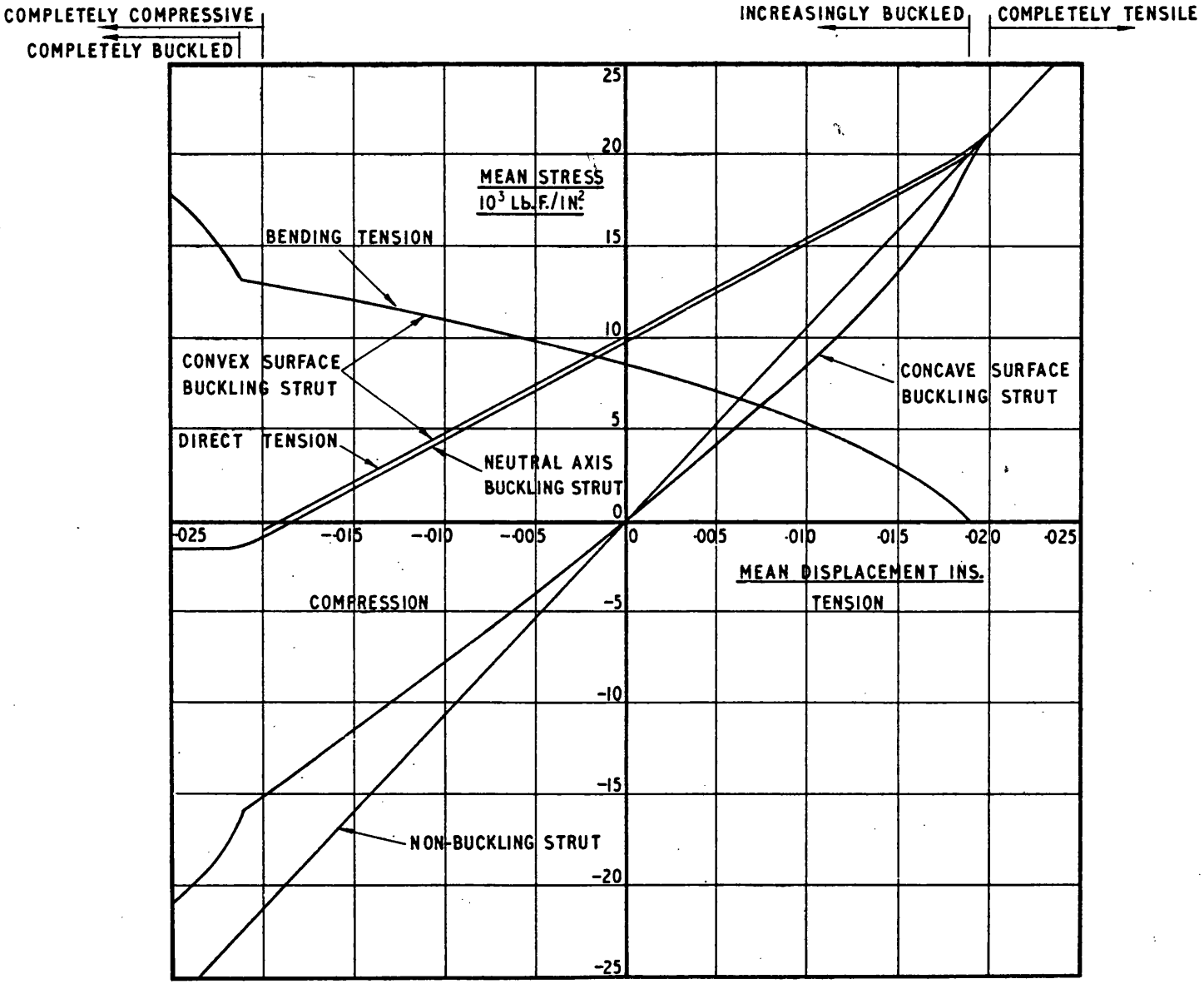

FIGURE 4.12

VARIATION OF ALTERNATING STRESS WITH MEAN END DISPLACEMENT FOR BUCKLING AND NON BUCKLING STRUTS FOR A DISPLACEMENT AMPLITUDE OF ±·020"

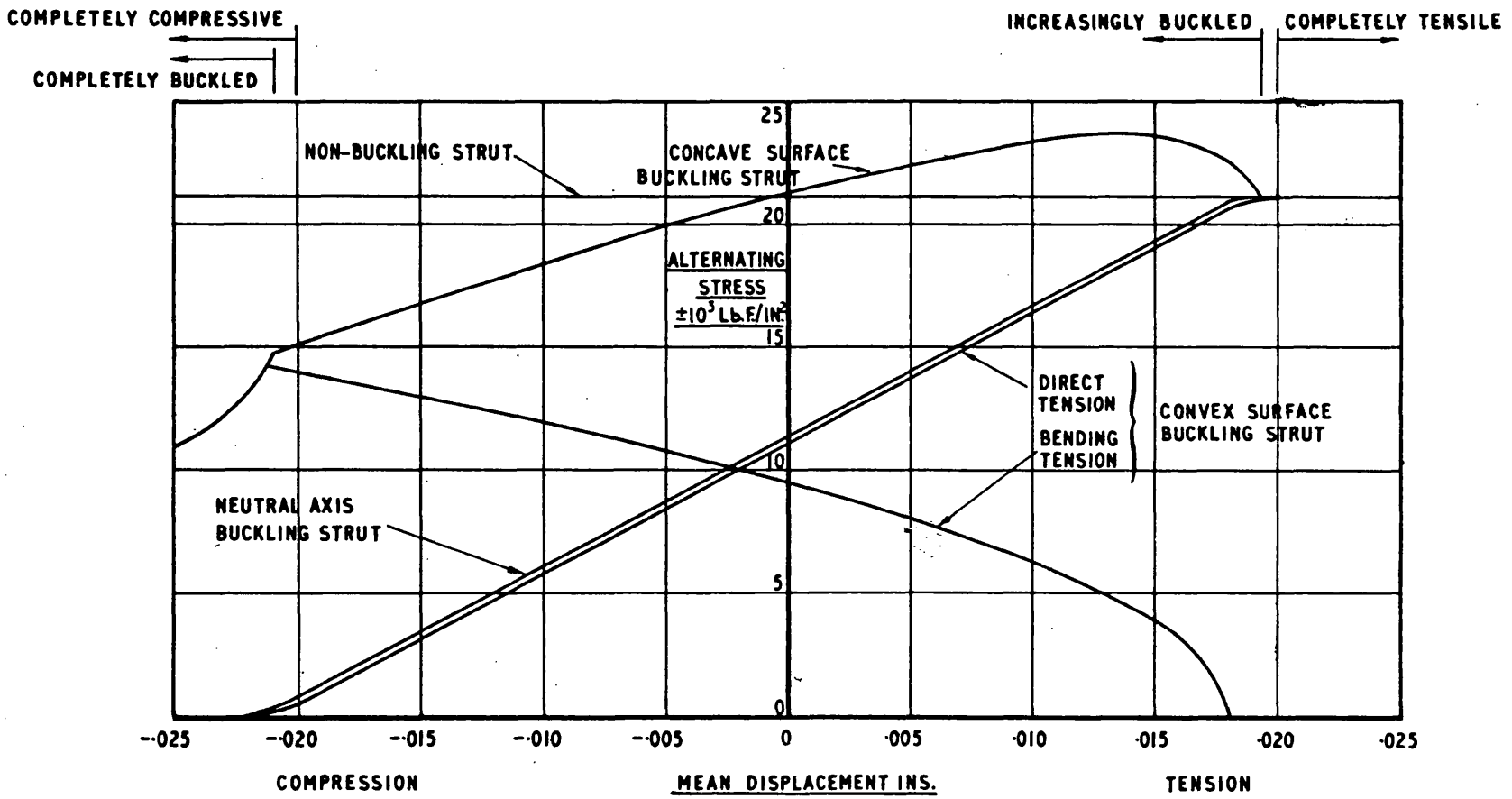

FIGURE 4.13

FIGURE 4.14

EXTRAPOLATED B.A.C. FATIGUE DATA FOR UNLOADED HOLES IN LIGHT ALLOY SHEET BASED ON NETT AREA STRESSES

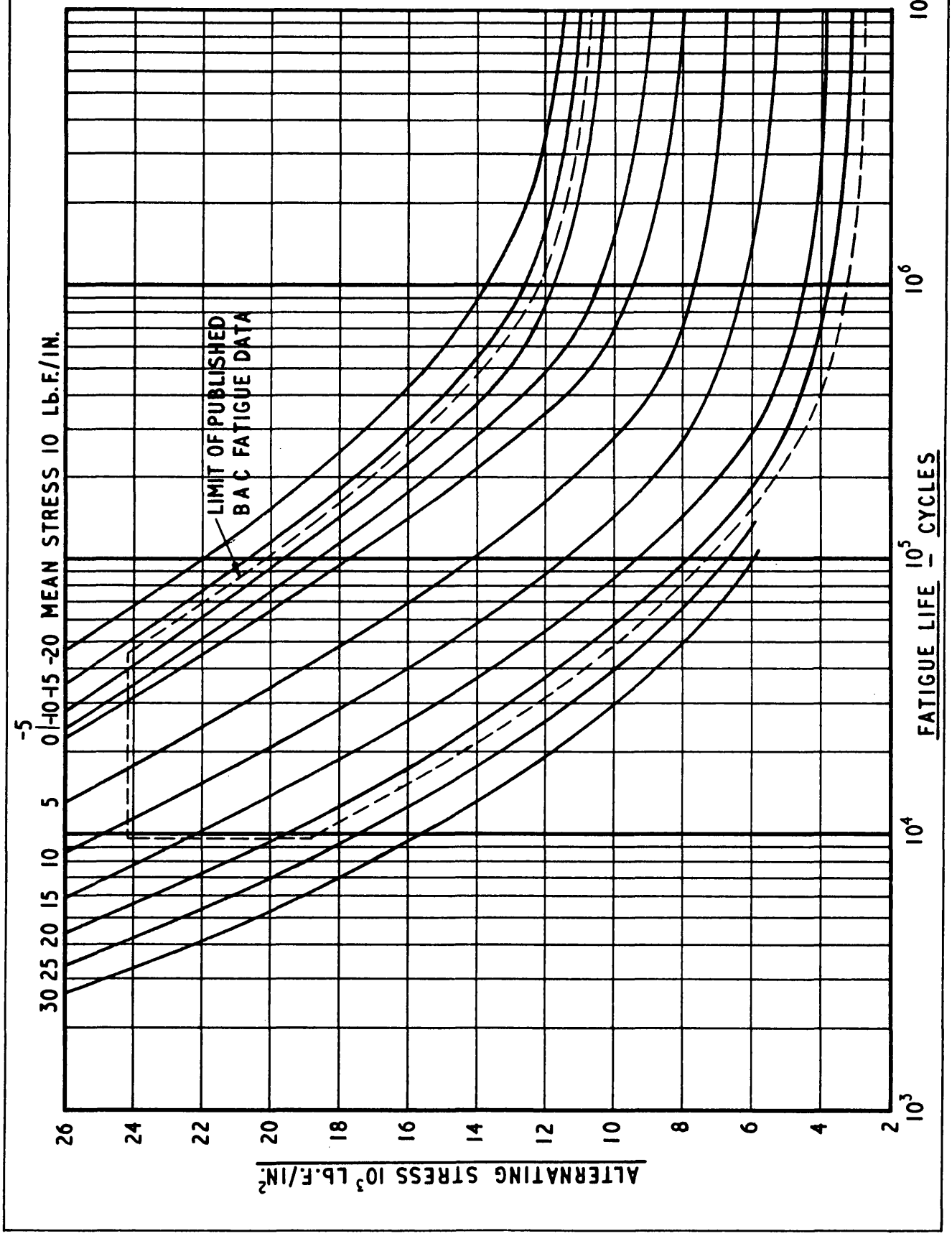

RESULTS OF B.A.C. FATIGUE PREDICTIONS FOR ±.020" DISPLACEMENT AMPLITUDE

FIGURE 4.15

MEAN DISP.	NON-BUCKLING STRUT			BUCKLING STRUT						CONVEX SURFACE				
				CONCAVE SURFACE			NEUTRAL AXIS			DIRECT TENSION		BENDING TENSION		
	MEAN STRESS	ALT. STRESS	LIFE CYCLES	MEAN STRESS	ALT. STRESS	LIFE CYCLES	MEAN STRESS	ALT. STRESS	LIFE CYCLES	MEAN STRESS	ALT. STRESS	MEAN STRESS	ALT. STRESS	LIFE CYCLES
INS.	P.S.I.	P.S.I.		P.S.I.	P.S.I.		P.S.I.	P.S.I.		P.S.I.	P.S.I.	P.S.I.	P.S.I.	
.026	29330	22550	3.9×10^3	29500	22550	3.9×10^3	29500	22550	3.9×10^3	29500	22550	-	-	3.9×10^3
.024	27050		4.4×10^3	27150	22550	4.4×10^3	27150	22550	4.4×10^3	27150	22550	-	-	4.4×10^3
.022	24830		5.1×10^3	24850	22550	5.1×10^3	24850	22550	5.1×10^3	24850	22550	-	-	5.1×10^3
.020	22550		5.7×10^3	22600	22600	5.7×10^3	22600	22600	5.7×10^3	22600	22600	-	-	5.7×10^3
.018	20300		6.7×10^3	18930	24000	6.0×10^3	20600	22350	6.7×10^3	20950	22000	1330	266	6.8×10^3
.016	18045		7.7×10^3	15680	25000	6.5×10^3	19470	21200	8.6×10^3	19800	20850	2450	3520	8.8×10^3
.014	15770		9.0×10^3	13200	25200	7.3×10^3	18380	20050	1.08×10^4	18700	19750	3700	4770	1.1×10^4
.012	13540		1.06×10^4	11040	25150	8.8×10^3	17220	18920	1.31×10^4	17550	18600	4745	5800	1.35×10^4
.010	11010		1.3×10^4	9040	24850	1.1×10^4	16100	17820	1.7×10^4	16400	17500	5675	6745	1.75×10^4
.008	9040		1.5×10^4	7120	24600	1.3×10^4	14960	16700	2.3×10^4	15300	16350	6450	7510	2.27×10^4
.006	6760		1.85×10^4	5280	24150	1.7×10^4	13820	15600	3.1×10^4	14200	15250	7200	8250	2.89×10^4
.004	4515		2.35×10^4	3490	23700	2.2×10^4	12780	14450	4.1×10^4	13075	14125	7850	8925	3.6×10^4
.002	2250		3.0×10^4	1680	23200	3.0×10^4	11580	13320	5.9×10^4	11900	12950	8500	9560	4.7×10^4
.000	0		4.1×10^4	53	22700	3.9×10^4	10450	12200	8.6×10^4	10820	11870	9080	10150	5.35×10^4
-.002	- 2250		4.3×10^4	- 1760	22150	4.6×10^4	9300	11080	1.17×10^5	9650	10700	9660	10720	6.0×10^4
-.004	- 4515		4.6×10^4	- 3380	21500	5.8×10^4	8180	9960	1.68×10^5	8540	9590	10200	11250	6.57×10^4
-.006	- 6760		5.0×10^4	- 5010	20900	6.6×10^4	7060	8820	3.0×10^5	7410	8460	10700	11780	6.86×10^4
-.008	- 9040		5.4×10^4	- 6660	20250	7.8×10^4	5810	7680	7.2×10^5	6260	7325	11220	12300	6.95×10^4
-.010	-11010		5.9×10^4	- 8260	19620	9.4×10^4	4800	6560	$>10^7$	5150	6200	11650	12720	6.5×10^4
-.012	-13540		6.6×10^4	- 9860	19000	1.13×10^5	3680	5440	-	4020	5090	12100	13180	5.8×10^4
-.014	-15770		7.4×10^4	-11470	18300	1.4×10^5	2420	4300	-	2880	3945	12580	13620	5.0×10^4
-.016	-18045		8.3×10^4	-13000	17580	1.8×10^5	1402	3180	-	1760	2820	13000	14050	4.35×10^4
-.018	-20300		9.5×10^4	-14580	16900	2.3×10^5	256	2035	-	613	1680	13400	14480	3.85×10^4
-.020	-22550		-	-16100	16100	3.2×10^5	- 890	890	-	- 530	530	13800	14880	3.5×10^4
-.022	-24830		-	-19050	13950	8.0×10^5	-1750	43	-	-	-	15500	13900	3.5×10^4
-.024	-27050		-	-21750	12200	-	-1750	43	-	-	-	18080	12100	4.3×10^4
-.026	-29330		-	-23300	11200	-	-1760	32	-	-	-	19700	11230	4.5×10^4

RESULTS OF B.A.C. FATIGUE PREDICTIONS FOR ±.0165" DISPLACEMENT AMPLITUDE

FIGURE 4.16

MEAN DISP.	NON-BUCKLING STRUT			BUCKLING STRUT										
				CONCAVE SURFACE			NEUTRAL AXIS			CONVEX SURFACE				
										DIRECT TENSION		BENDING TENSION		
	MEAN STRESS	ALT. STRESS	LIFE CYCLES	MEAN STRESS	ALT. STRESS	LIFE CYCLES	MEAN STRESS	ALT. STRESS	LIFE CYCLES	MEAN STRESS	ALT. STRESS	MEAN STRESS	ALT. STRESS	LIFE CYCLES
INS.	P.S.I.	P.S.I.		P.S.I.	P.S.I.		P.S.I.	P.S.I.		P.S.I.	P.S.I.	P.S.I.	P.S.I.	
.026	29350	18600	6.6×10^3	29350	18619	6.6×10^3	29350	18619	6.6×10^3	29350	18619	-	-	6.6×10^3
.024	27100	↓	7.4×10^3	27147	18619	7.4×10^3	27147	18619	7.4×10^3	27147	18619	-	-	7.4×10^3
.022	24800		8.4×10^3	24907	18619	8.4×10^3	24907	18619	8.4×10^3	24907	18619	-	-	8.4×10^3
.020	22550		9.6×10^3	22674	18619	9.6×10^3	22674	18619	9.6×10^3	22674	18619	-	-	9.6×10^3
.018	20300		1.1×10^4	20380	18619	1.1×10^4	20380	18619	1.1×10^4	20380	18619	-	-	1.1×10^4
.016	17950		1.32×10^4	18122	18646	1.28×10^4	18112	18646	1.28×10^4	18112	18646	-	-	1.28×10^4
.014	15800		1.56×10^4	13978	20593	1.37×10^4	16432	18139	1.55×10^4	16432	18139	587	2294	1.55×10^4
.012	13520		1.87×10^4	11097	21233	1.5×10^4	15311	17019	2.1×10^4	15311	17019	2507	4215	2.1×10^4
.010	11275		2.3×10^4	8643	21340	1.9×10^4	14138	15845	2.85×10^4	14138	15845	3681	5288	2.85×10^4
.008	9015		2.8×10^4	6589	21153	2.45×10^4	13017	14725	3.75×10^4	13017	14725	4668	6375	3.75×10^4
.006	6775		3.55×10^4	4588	20860	3.1×10^4	11870	13577	5.5×10^4	11870	13677	5548	7255	5.3×10^4
.004	4510		4.5×10^4	2694	20513	4.2×10^4	10750	12457	7.6×10^4	10750	12457	6348	8056	6.6×10^4
.002	2255		6.2×10^4	827	20086	5.9×10^4	9603	11310	1.1×10^5	9603	11310	7042	8749	8.05×10^4
.000	0		8.7×10^4	- 960	19633	7.4×10^4	8483	10190	1.55×10^5	8483	10190	7709	9416	9.1×10^4
-.002	- 2255		9.3×10^5	- 2694	19126	8.5×10^5	7362	9069	2.55×10^5	7362	9069	8323	10030	9.85×10^5
-.004	- 4510		1.0×10^5	- 4455	18592	1.02×10^5	6215	7922	5.4×10^6	6215	7922	8936	10643	1.08×10^5
-.006	- 6775		1.08×10^5	- 6135	18032	1.2×10^5	5095	6802	3.0×10^6	5095	6802	9470	11177	1.12×10^5
-.008	- 9015		1.18×10^5	- 7762	19419	1.4×10^5	3975	5682	$>10^7$	3975	5682	10003	11710	9.6×10^4
-.010	-11275		1.3×10^5	- 9416	16778	1.75×10^5	2827	4535	-	2827	4535	10537	12244	8.3×10^4
-.012	-13520		1.45×10^5	-11043	16165	2.25×10^5	1707	3201	-	1707	3201	11017	12724	6.8×10^4
-.014	-15800		1.61×10^5	-12644	15525	2.9×10^5	587	2294	-	587	2294	11470	13177	6.1×10^4
-.016	-17950		1.84×10^5	-14244	14831	4.1×10^5	- 560	1147	-	- 560	1147	11924	13631	5.3×10^4
-.018	-20300		2.14×10^5	-16325	13658	7.4×10^7	0	0	-	0	0	12920	13510	5.0×10^4
-.020	-22550		-	-19659	11123	1.6×10^7	-	-	-	-	-	16200	11100	6.0×10^4
-.022	-24800		-	-21553	10083	-	-	-	-	-	-	18000	10100	6.5×10^4
-.024	-27100		-	-23047	9390	-	-	-	-	-	-	20825	8880	6.8×10^4
-.026	-29350		-	-24328	8909	-	-	-	-	-	-	19500	9380	6.8×10^4

COMPARISON OF B.A.C. AND HEYWOOD FATIGUE DATA PREDICTIONS FOR BUCKLING AND NON BUCKLING STRUTS FOR A DISPLACEMENT AMPLITUDE OF ±·020"

FIGURE 4.17

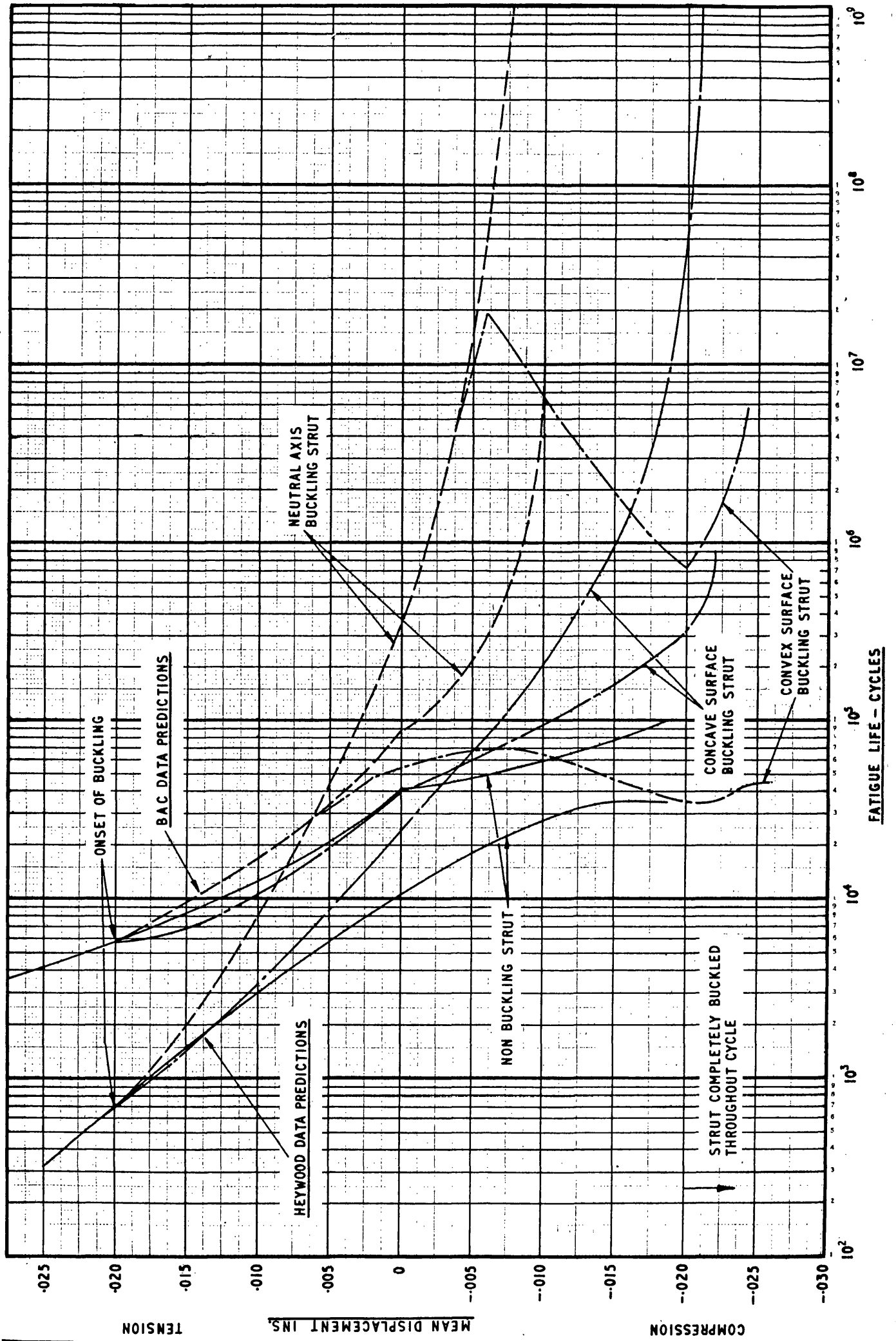

FIGURE 4.18

HEYWOOD'S BASIC FATIGUE DATA FOR PLAIN ALUMINIUM ALLOY SPECIMENS WITH AN ULTIMATE TENSILE STRENGTH OF 60,900Lb.F./IN.^{2}

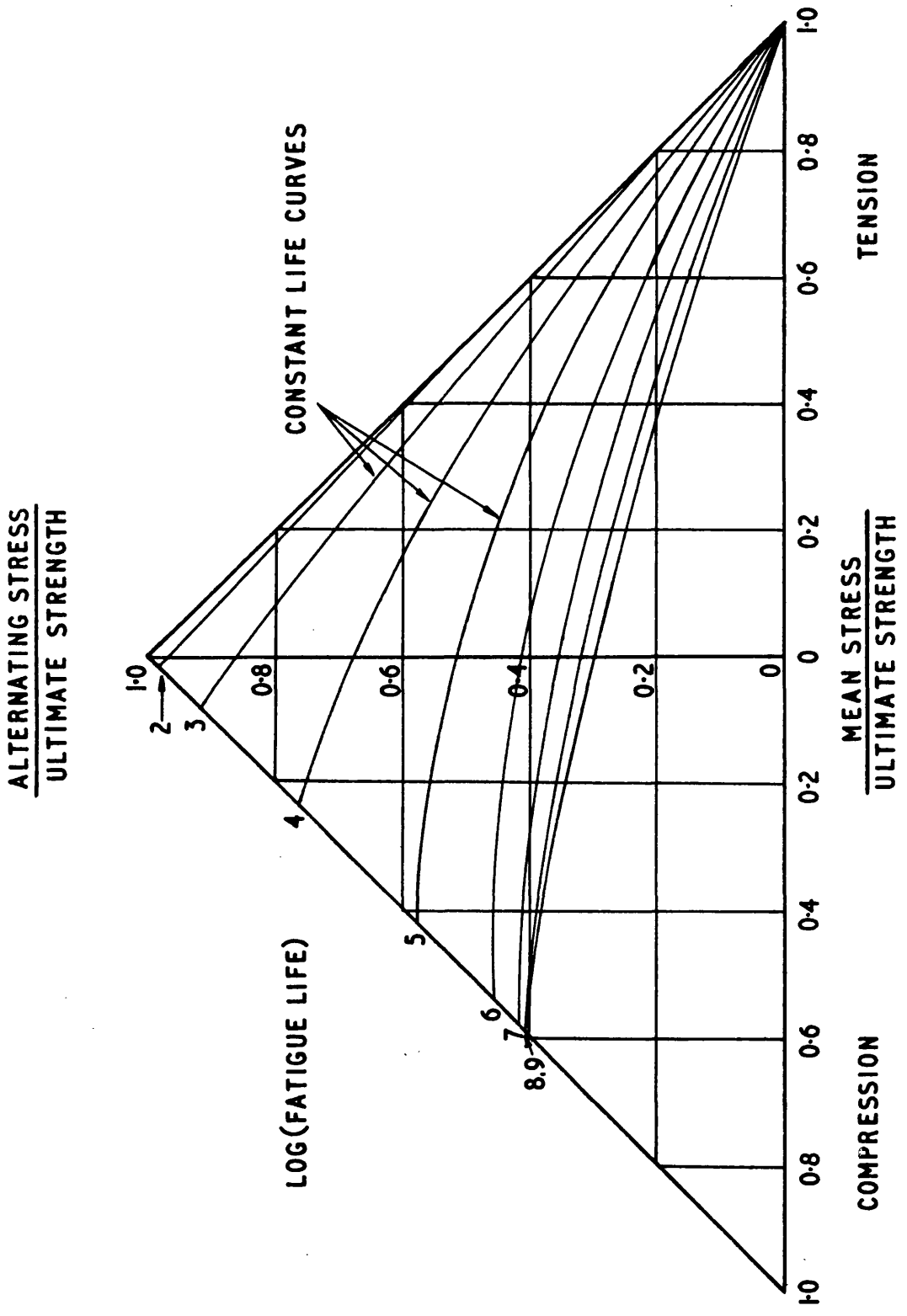

RESULTS OF HEYWOOD'S FATIGUE PREDICTIONS FOR ±.020" DISPLACEMENT AMPLITUDE

FIGURE 4.19

MEAN DISP.	NON-BUCKLING STRUT			BUCKLING STRUT										
				CONCAVE SURFACE			NEUTRAL AXIS			CONVEX SURFACE				
										DIRECT TENSION		BENDING TENSION		
	MEAN STRESS	ALT. STRESS	LIFE CYCLES	MEAN STRESS	ALT. STRESS	LIFE CYCLES	MEAN STRESS	ALT. STRESS	LIFE CYCLES	MEAN STRESS	ALT. STRESS	MEAN STRESS	ALT. STRESS	LIFE CYCLES
INS.	P.S.I.	P.S.I.		P.S.I.	P.S.I.		P.S.I.	P.S.I.		P.S.I.	P.S.I.	P.S.I.	P.S.I.	
.024	25380	21150	3.76×10^2	25450	21150	3.72×10^2	25450	21150	3.72×10^2	25450	21150	-	-	3.72×10^2
.022	23265		5.22×10^2	23300	21150	5.19×10^2	23300	21150	5.19×10^2	23300	21150	-	-	5.19×10^2
.020	21150		7.22×10^2	21200	21200	7.06×10^2	21200	21200	7.06×10^2	21200	21200	-	-	7.06×10^2
.018	19035		1.00×10^3	17750	22550	9.02×10^2	19350	20950	1.01×10^3	19350	20950	- 50	1550	1.58×10^3
.016	16920		1.32×10^3	14700	23450	1.21×10^3	18275	19875	1.573×10^3	18275	19875	2000	3600	1.58×10^2
.014	14805		1.73×10^3	12375	23675	1.66×10^3	17225	18825	2.54×10^3	17225	18825	3175	4775	2.54×10^3
.012	12690		2.27×10^3	10325	23575	2.36×10^3	16150	17750	4.40×10^3	16150	17750	4150	5750	4.40×10^3
.010	10575		2.99×10^3	8475	23325	3.39×10^3	15100	16700	8.00×10^4	15100	16700	5025	6625	8.01×10^3
.008	8460		3.92×10^3	6675	23025	4.92×10^3	14050	15650	1.52×10^4	14050	15650	5750	7350	1.52×10^4
.006	6345		5.10×10^3	4950	22650	7.25×10^3	13000	14600	3.00×10^4	13000	14600	6450	8050	3.00×10^4
.004	4230		6.63×10^3	3275	22225	1.07×10^4	11950	13550	6.13×10^4	11950	13550	7075	8675	6.13×10^4
.002	2115		8.40×10^3	1575	21775	1.61×10^4	10875	12475	1.41×10^5	10875	12475	7675	9275	1.41×10^5
.000	0		1.06×10^4	- 50	21300	2.44×10^4	9825	11425	3.80×10^6	9825	11425	8225	9825	3.80×10^5
-.002	- 2115		1.33×10^4	- 1650	20750	3.67×10^4	8750	10350	1.12×10^6	8750	10350	8775	10375	1.12×10^6
-.004	- 4230		1.65×10^4	- 3175	20175	5.47×10^4	7700	9300	5.50×10^7	7700	9300	9275	10875	5.13×10^7
-.006	- 6345		1.99×10^4	- 4700	19600	7.99×10^4	6650	8250	5.34×10^7	6650	8250	9750	11350	1.93×10^7
-.008	- 8460		2.36×10^4	- 6250	19000	1.24×10^5	5575	7175	$>10^9$	5575	7175	10225	11825	1.19×10^6
-.010	-10575		2.73×10^4	- 7750	18400	2.20×10^5	4525	6125	-	4525	6125	10650	12250	6.73×10^6
-.012	-12690		3.05×10^4	- 9250	17800	3.79×10^5	3475	5075	-	3475	5075	11075	12675	4.06×10^6
-.014	-14805		3.31×10^4	-10750	17150	6.68×10^6	2400	4000	-	2400	4000	11500	13100	2.46×10^6
-.016	-16920		3.49×10^4	-12175	16475	1.39×10^6	1350	2950	-	1350	2950	11900	13500	1.54×10^5
-.018	-19035		3.55×10^4	-13675	15825	4.65×10^7	275	1875	-	275	1875	12300	13900	9.76×10^5
-.020	-21150		3.50×10^4	-15100	15100	4.82×10^9	- 800	800	-	- 800	800	12675	14275	7.32×10^6
-.022	-23265		-	-17875	13075	10^9	-1600	0	-	-	-	14575	13075	1.35×10^6
-.024	-25380		-	-20200	11450	-	-	-	-	-	-	16975	11375	4.43×10^6
-.026	-27495		-	-21850	10500	-	-	-	-	-	-	18500	10550	-

RESULTS OF HEYWOOD'S FATIGUE PREDICTIONS FOR ±.0165" DISPLACEMENT AMPLITUDE

FIGURE 4.20

MEAN DISP.	NON-BUCKLING STRUT			BUCKLING STRUT										
				CONCAVE SURFACE			NEUTRAL AXIS			CONVEX SURFACE				
										DIRECT TENSION		BENDING TENSION		
	MEAN STRESS	ALT. STRESS	LIFE CYCLES	MEAN STRESS	ALT. STRESS	LIFE CYCLE	MEAN STRESS	ALT. STRESS	LIFE CYCLES	MEAN STRESS	ALT. STRESS	MEAN STRESS	ALT. STRESS	LIFE CYCLES
.024	25380	17450	1.19×10^3	25450	17450	1.19×10^3	25450	17450	1.19×10^3	25450	17450	-	-	1.19×10^3
.022	23265		1.65×10^3	23350	17450	1.63×10^3	23350	17450	1.63×10^3	23350	17450	-	-	1.63×10^3
.020	21150		2.30×10^3	21250	17450	2.27×10^3	21250	17450	2.27×10^3	21250	17450	-	-	2.27×10^3
.018	19035		3.18×10^3	19100	17450	3.09×10^3	19100	17500	3.09×10^3	19100	17500	-	-	3.09×10^3
.016	16920		4.39×10^3	16975	17475	4.31×10^3	16975	17474	4.31×10^3	16975	17475	-	-	4.31×10^3
.014	14805		6.09×10^3	13100	19300	4.89×10^3	15400	17000	6.70×10^4	15400	17000	550	2150	6.70×10^4
.012	12690		8.31×10^3	10400	19900	6.73×10^3	14350	15950	1.26×10^4	14350	15950	2350	3950	1.26×10^4
.010	10575		1.12×10^4	8100	20000	9.88×10^3	13250	14850	2.54×10^4	13250	14850	3450	5050	2.54×10^4
.008	8460		1.51×10^4	6175	19825	1.48×10^4	12200	13800	5.16×10^4	12200	13800	4375	5975	5.16×10^5
.006	6345		1.98×10^4	4300	19550	2.28×10^4	11125	12725	1.12×10^5	11125	12725	5200	6800	1.12×10^5
.004	4230		2.61×10^4	2525	19225	3.42×10^4	10075	11675	2.99×10^5	10075	11675	5950	7550	2.99×10^5
.002	2115		3.32×10^4	775	18825	5.21×10^4	9000	10600	8.43×10^6	9000	10600	6600	8200	8.43×10^6
.000	0		4.19×10^4	- 900	18400	7.73×10^5	7950	9550	3.74×10^7	7950	9550	7225	8825	3.74×10^7
-.002	- 2115		5.12×10^4	- 2525	17925	1.20×10^5	6900	8500	2.81×10^7	6900	8500	7800	9400	2.81×10^8
-.004	- 4230		6.13×10^4	- 4175	17425	2.16×10^5	5825	7425	$>10^9$	5825	7425	8375	9975	3.52×10^8
-.006	- 6345		7.10×10^4	- 5750	16900	3.76×10^5	4775	6375	-	4775	6375	8875	10475	2.32×10^7
-.008	- 8460		7.95×10^4	- 7275	16325	6.70×10^5	3725	5325	-	3725	5325	9375	10975	6.25×10^7
-.010	-10575		8.63×10^4	- 8825	15725	1.39×10^6	2650	4250	-	2650	4250	9875	11475	2.36×10^7
-.012	-12690		9.08×10^4	-10350	15150	4.30×10^6	1600	3200	-	1600	3200	10325	11925	9.99×10^6
-.014	-14805		9.22×10^4	-11850	14550	2.15×10^7	550	2150	-	550	2150	10750	12350	5.97×10^6
-.016	-16920		9.01×10^4	-13350	13900	$>10^9$	- 525	1075	-	- 525	1075	11175	12775	3.61×10^6
-.018	-19035		8.51×10^4	-15300	12800	-	-	-	-	-	-	12125	12675	3.28×10^7
-.020	-21150		7.78×10^4	-18425	10425	-	-	-	-	-	-	15200	10400	2.52×10^7
-.022	-23265		-	-20200	9450	-	-	-	-	-	-	16850	9450	7.10×10^7
-.024	-25380		-	-21600	8800	-	-	-	-	-	-	18300	8800	1.60×10^8
-.026	-27495		-	-22800	8350	-	-	-	-	-	-	19525	8325	3.20×10^8

FIGURE 4.21

CORRELATION OF EXPERIMENTAL FATIGUE LIVES WITH B.A.C. AND HEYWOOD FATIGUE DATA PREDICTIONS FOR A NON-BUCKLING STRUT AT 20°C

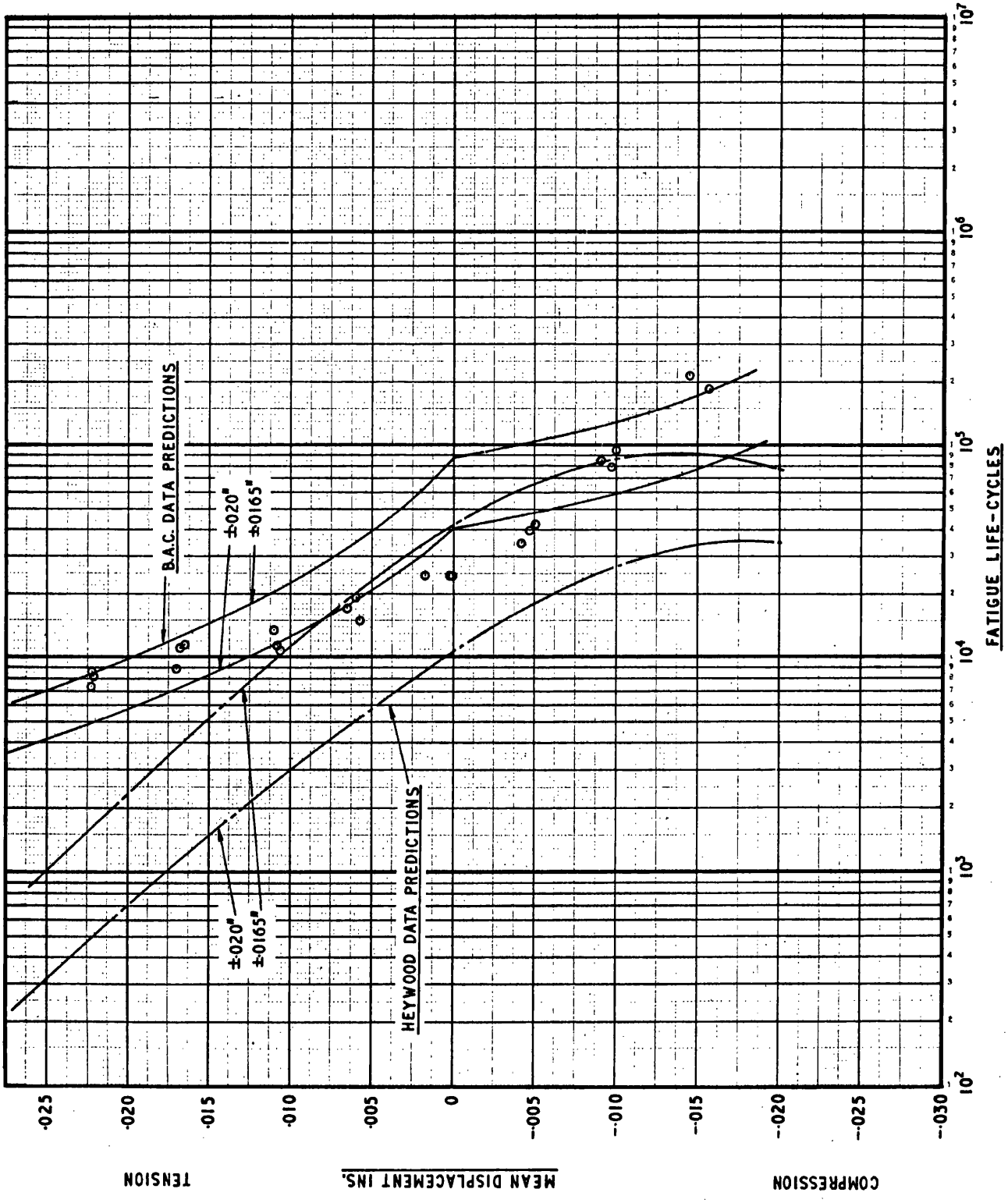

FIGURE 4.22

CORRELATION OF EXPERIMENTAL FATIGUE LIVES WITH B.A.C. AND HEYWOOD FATIGUE DATA PREDICTIONS FOR THE CONCAVE SURFACE OF A BUCKLING STRUT AT 20°C AND 150°C

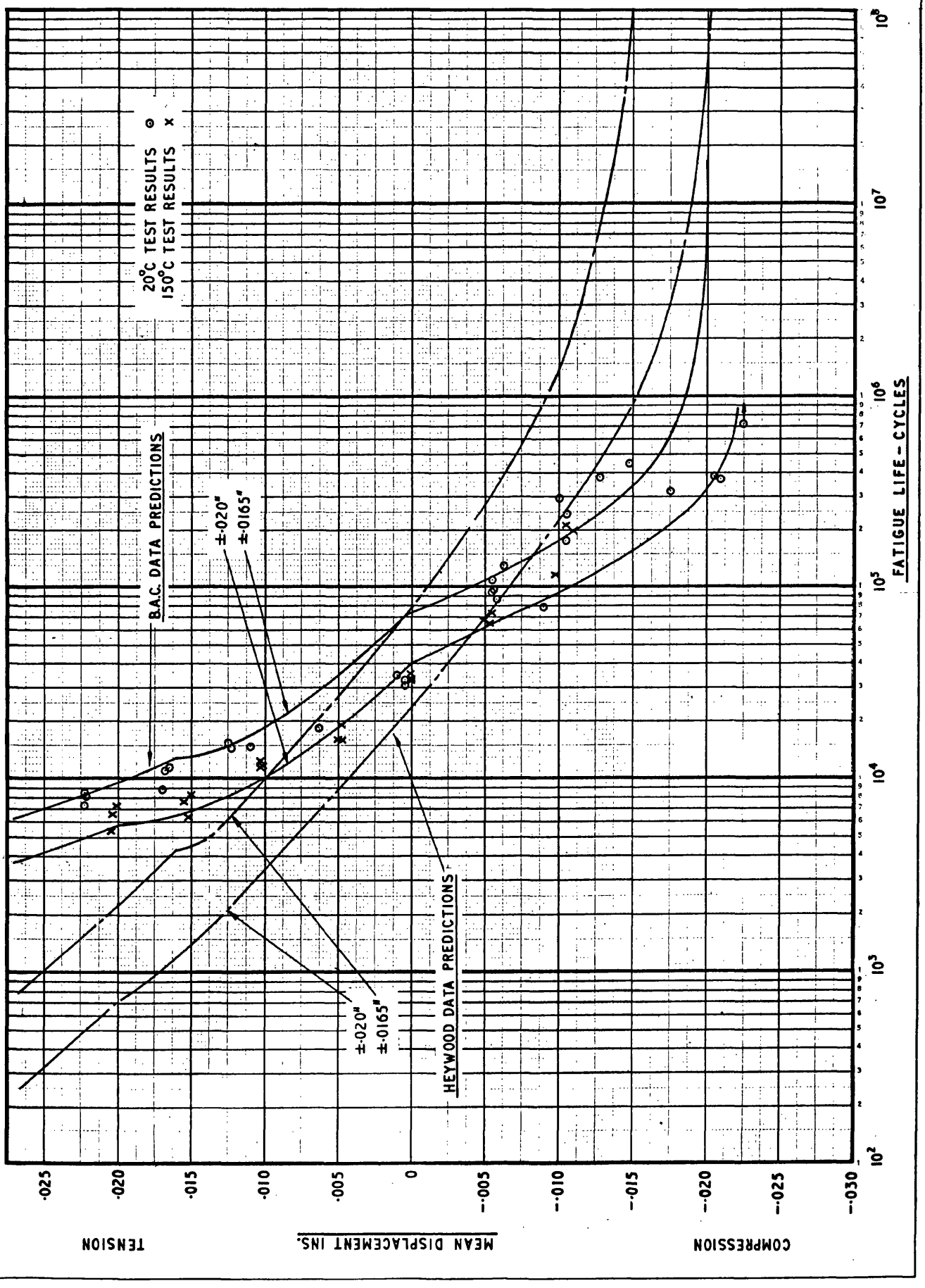

FIGURE 4.23

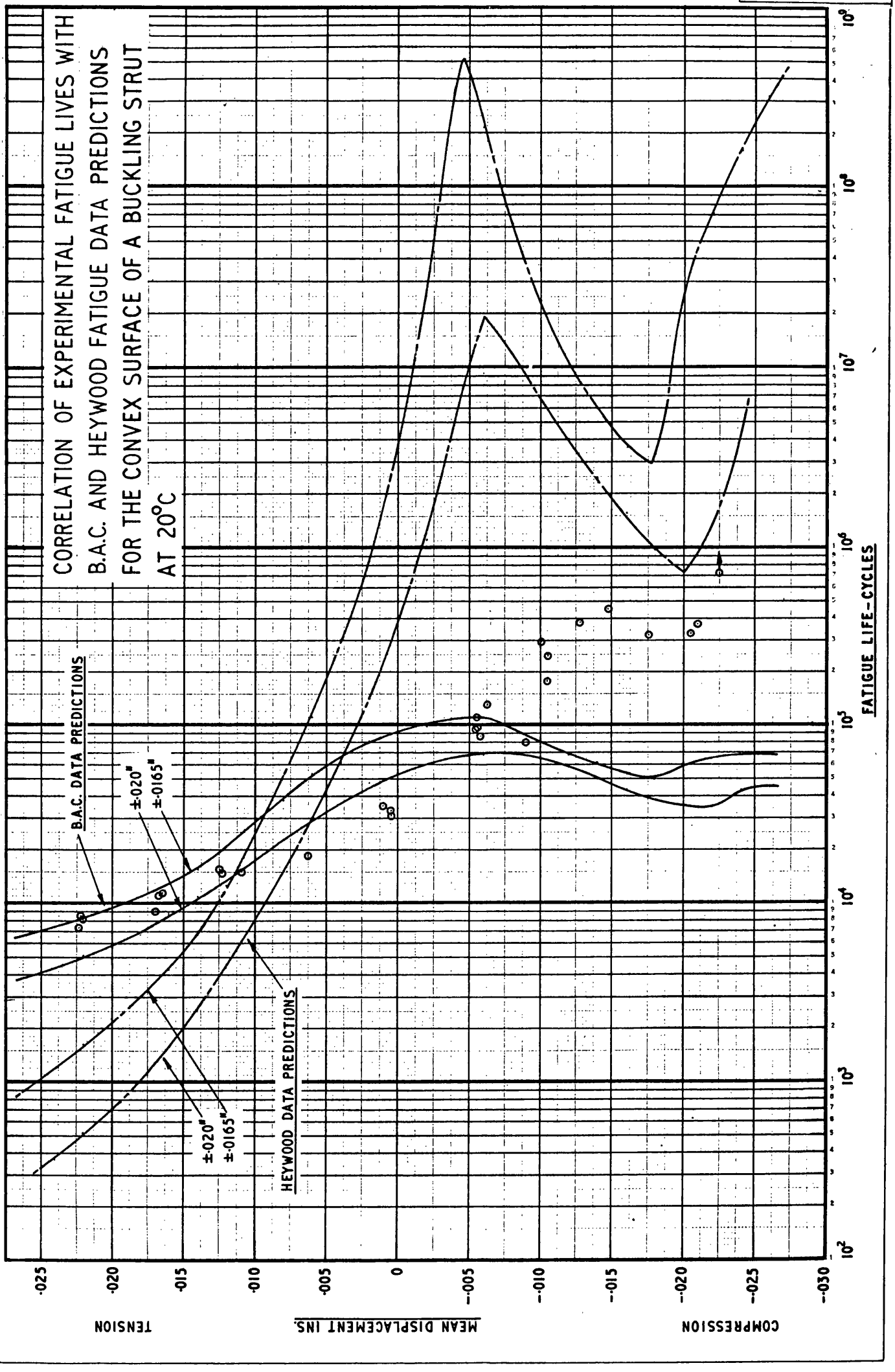
CORRELATION OF EXPERIMENTAL FATIGUE LIVES WITH B.A.C. AND HEYWOOD FATIGUE DATA PREDICTIONS FOR THE CONVEX SURFACE OF A BUCKLING STRUT AT 20°C
B.A.C. DATA PREDICTIONS
±·020"
±·0165"
HEYWOOD DATA PREDICTIONS
±·020"
±·0165"
FATIGUE LIFE-CYCLES
MEAN DISPLACEMENT INS.
TENSION
COMPRESSION
·025
·020
·015
·010
·005
0
-·005
-·010
-·015
-·020
-·025
-·030

FIGURE 4.24

CORRELATION OF 20°C BUCKLING TEST RESULTS WITH "MINIMUM LIFE CURVES" DERIVED FROM B.A.C. FATIGUE DATA FOR ±·0165" DISPLACEMENT AMP.

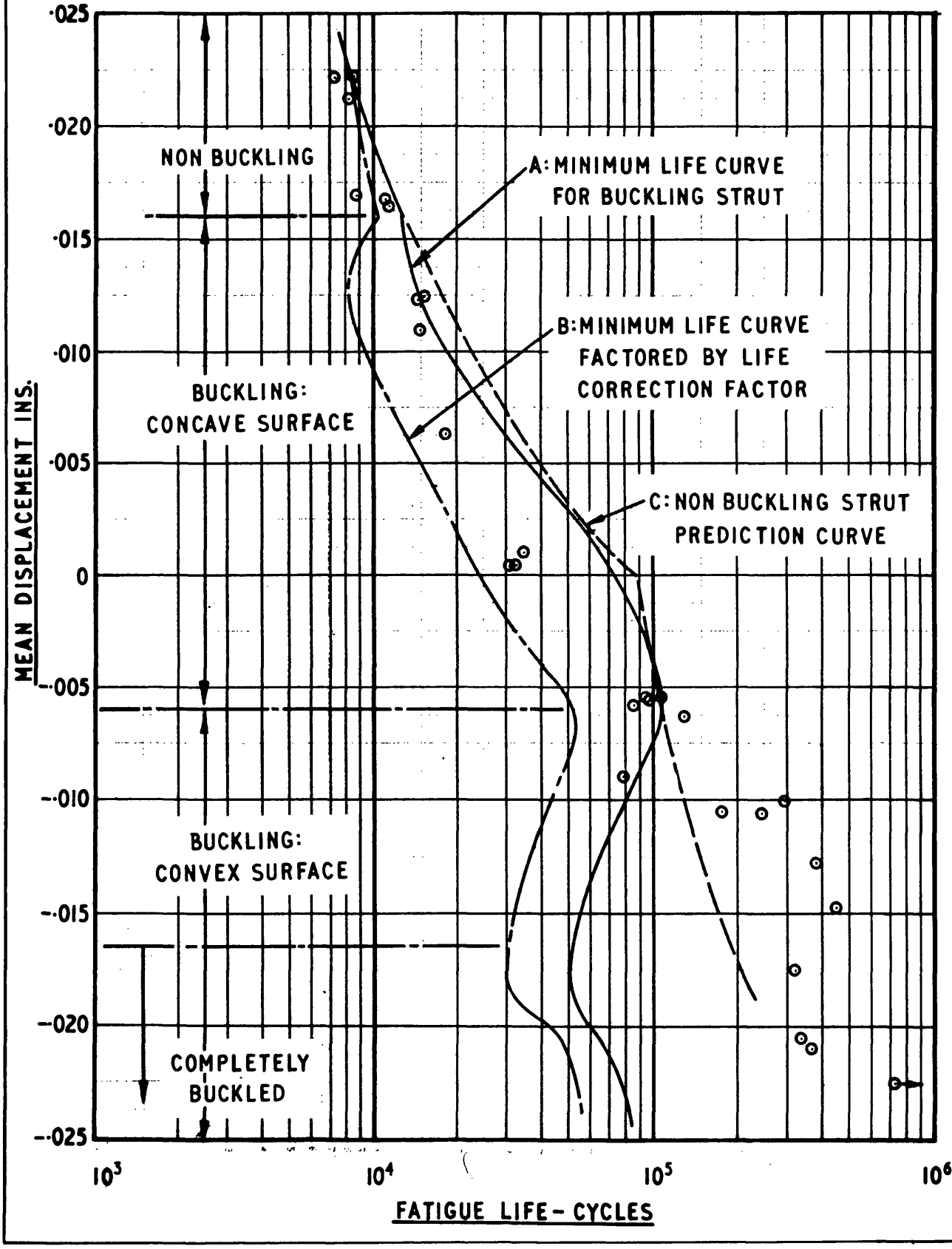

FIGURE 4.25

VARIATION OF LIFE CORRECTION FACTOR WITH MEAN STRESS, DERIVED FROM FIGURE 4.21 FOR A DISPLACEMENT AMPLITUDE OF ±·0165". ALTERNATING STRESS = ±18,600Lb.F./IN.^{2}

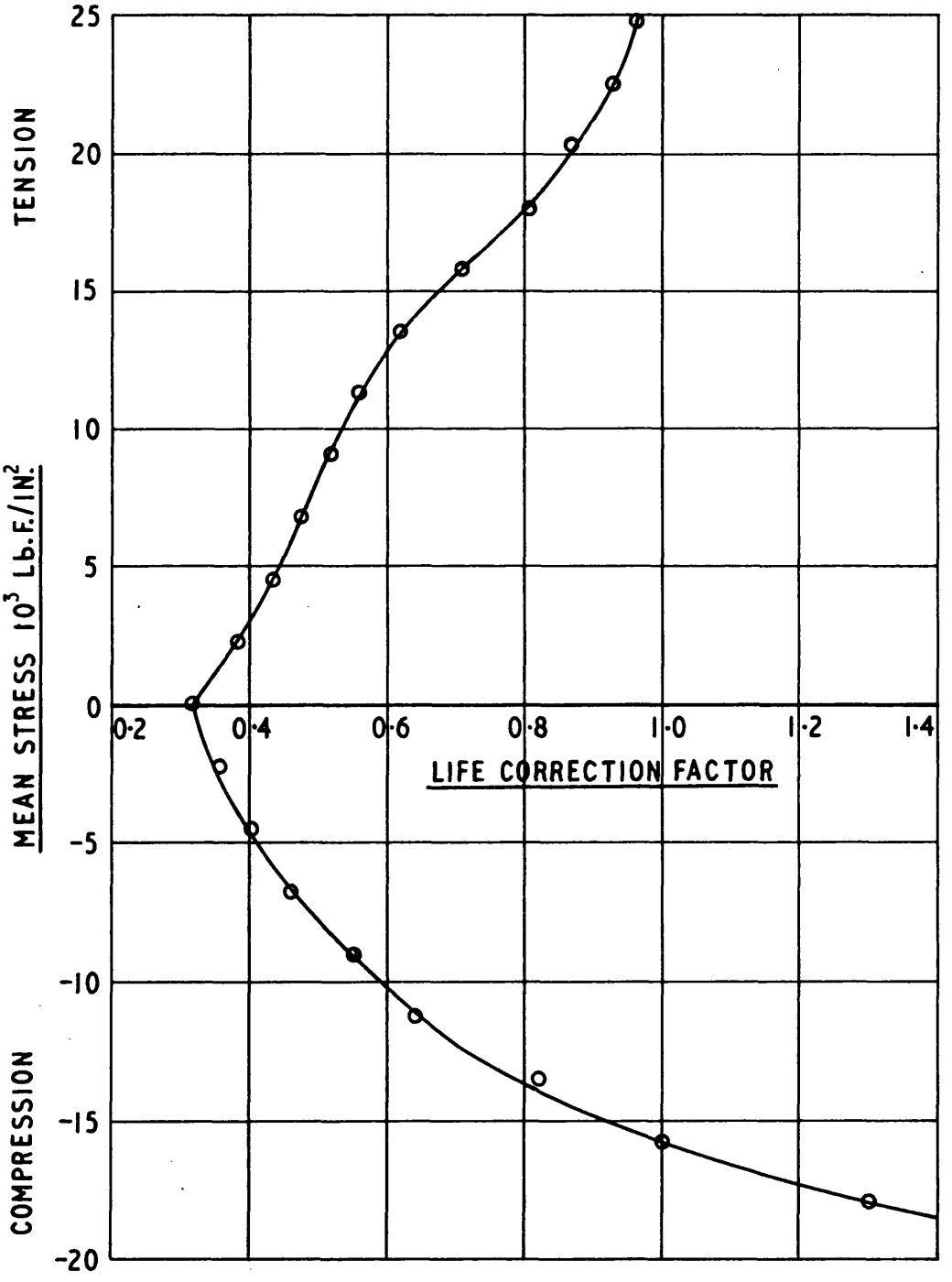

FIGURE 4.26

EFFECT OF VARIATIONS IN DISPLACEMENT AMPLITUDE ON MEAN AND ALTERNATING STRESS CHANGES, AND FATIGUE LIFE ESTIMATES, DUE TO BUCKLING

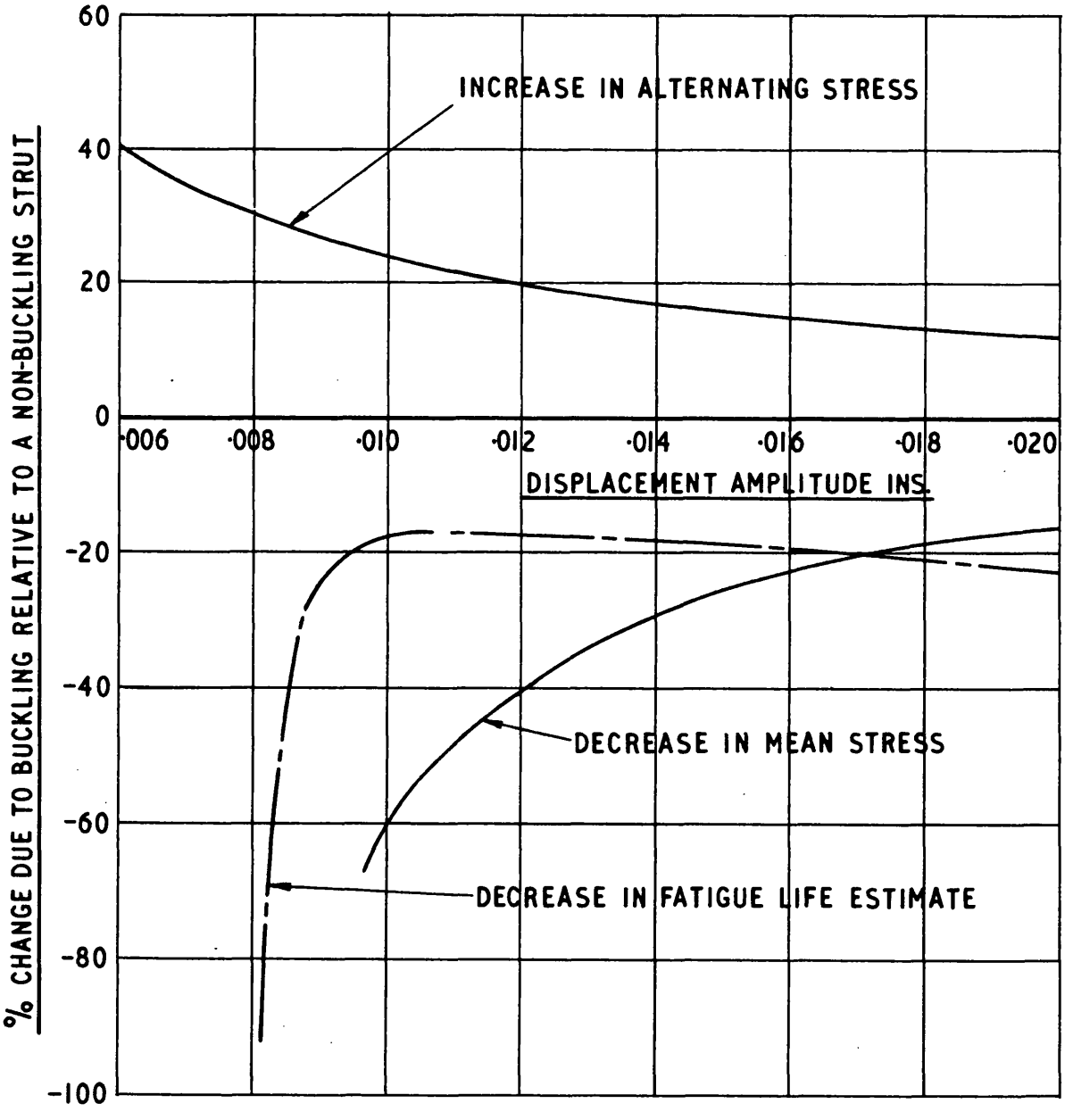

FIGURE 5.1

TYPICAL AVRO RIG TEST CYCLES

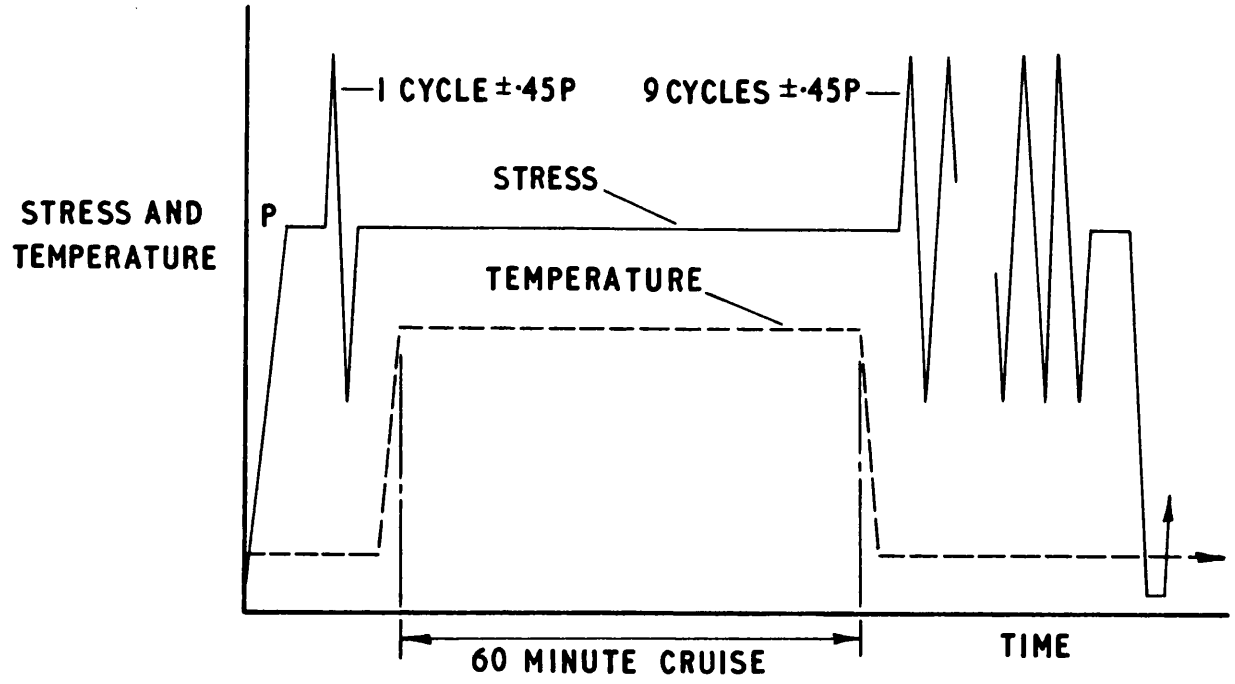

ONE INTERMITTENT CREEP TEST CYCLE

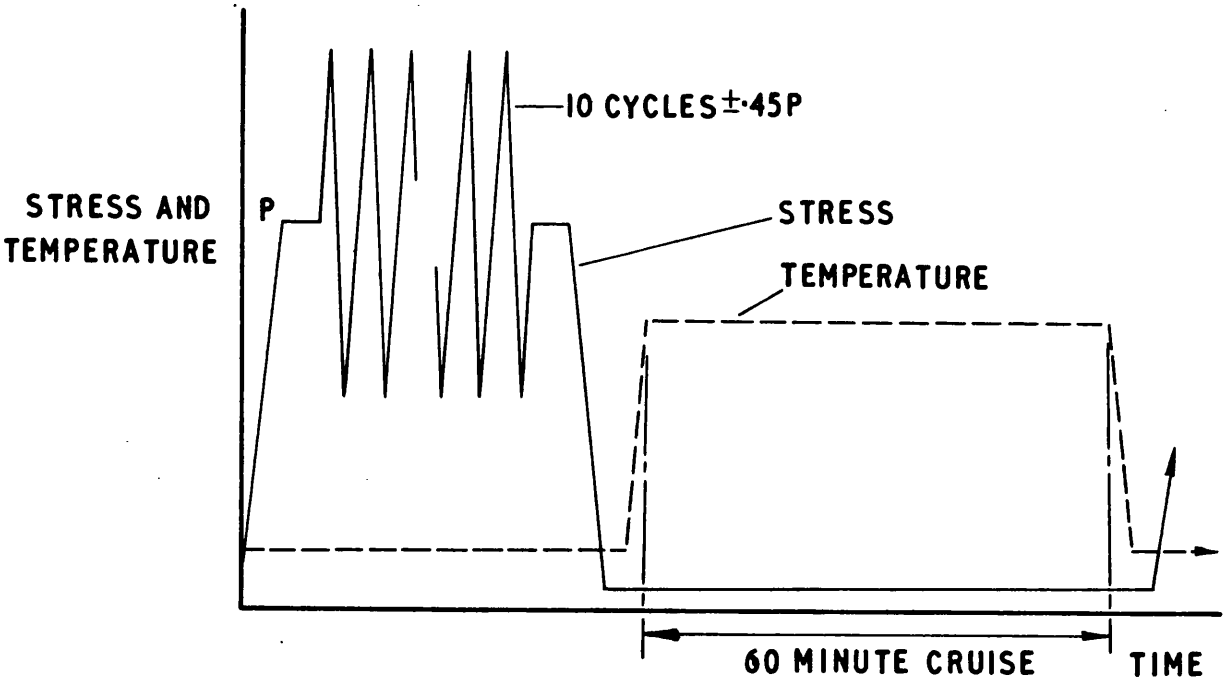

ONE INTERMITTENT HEATING TEST CYCLE

FIGURE 5.2

EFFECT OF TEMPERATURE CYCLING ON THE COLD FATIGUE LIFE OF CM001 NOTCHED SHEET COUPON AND RIVETED JOINT SPECIMENS TESTED IN THE AVRO RIG

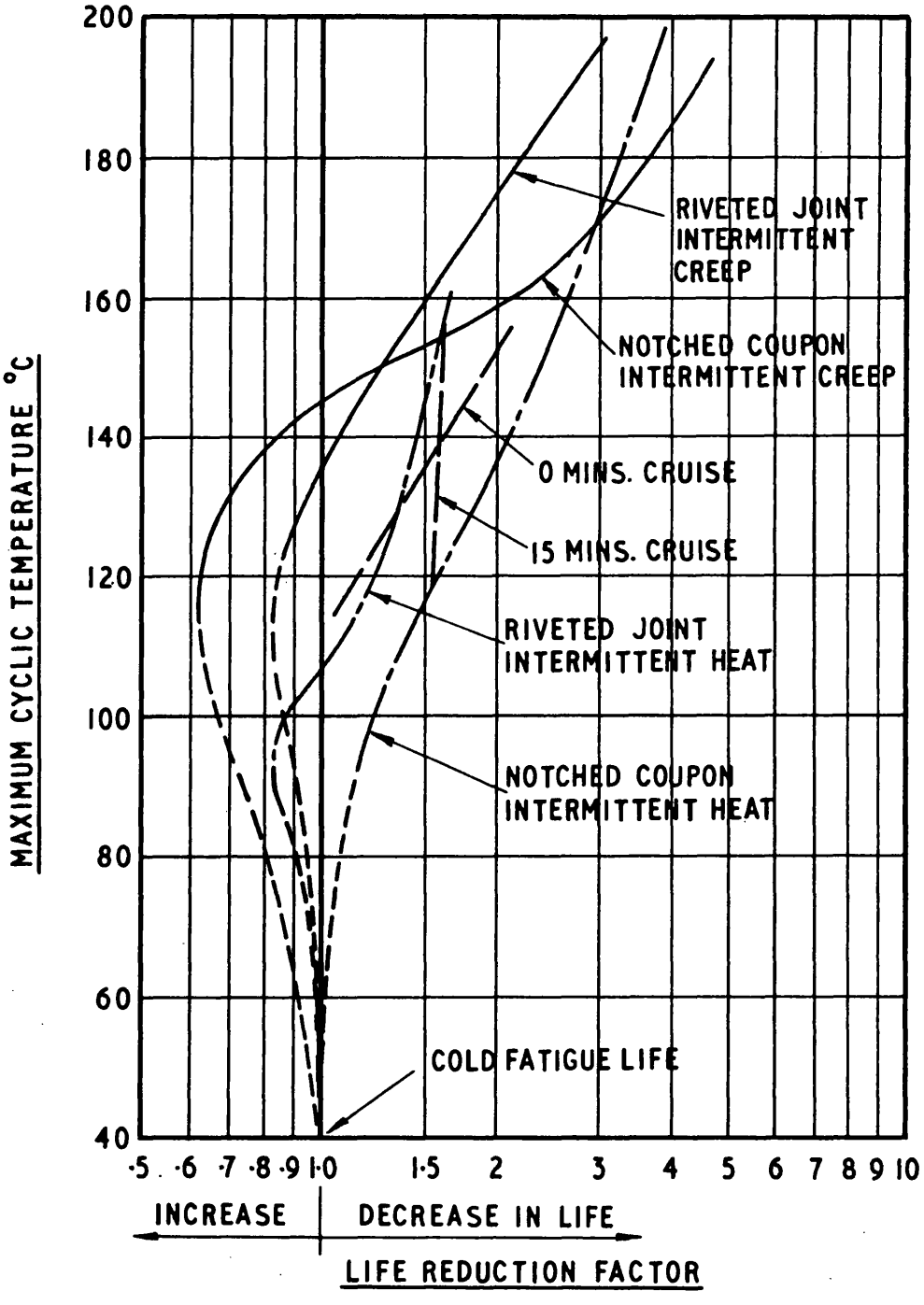

FIGURE 5.3

GENERAL ARRANGEMENT OF THE DEEP BOX THERMAL FATIGUE SPECIMEN

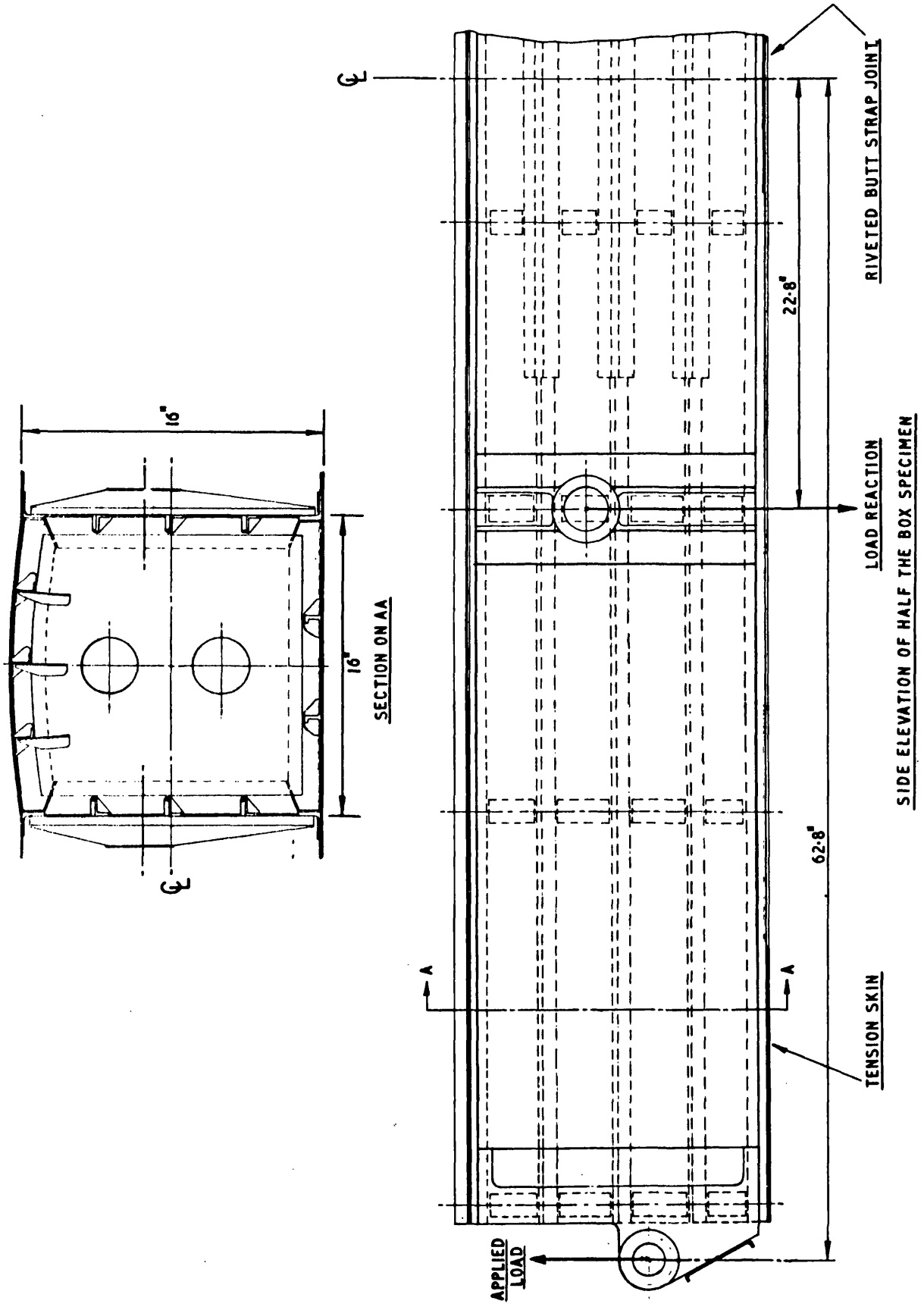

FIGURE 5.4

TYPICAL DEEP BOX TEST CYCLES

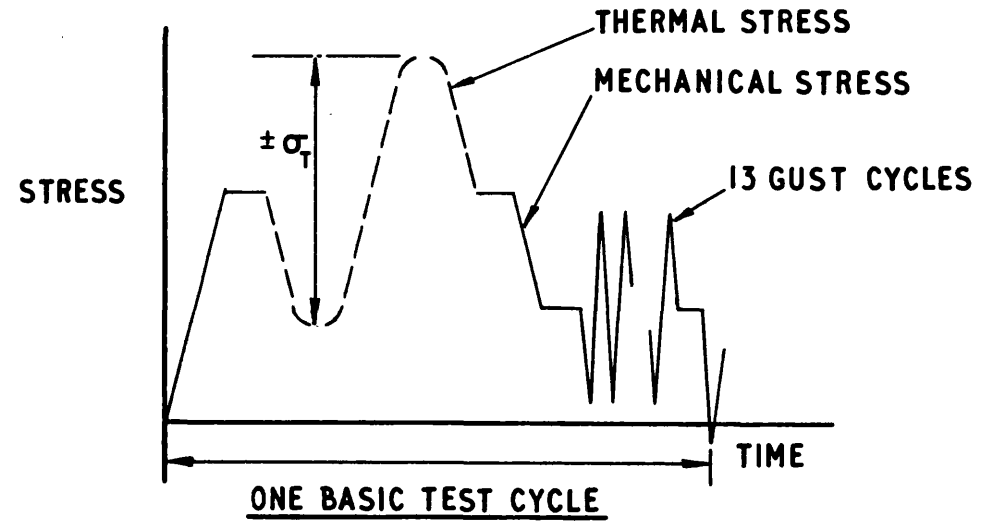

ONE BASIC TEST CYCLE

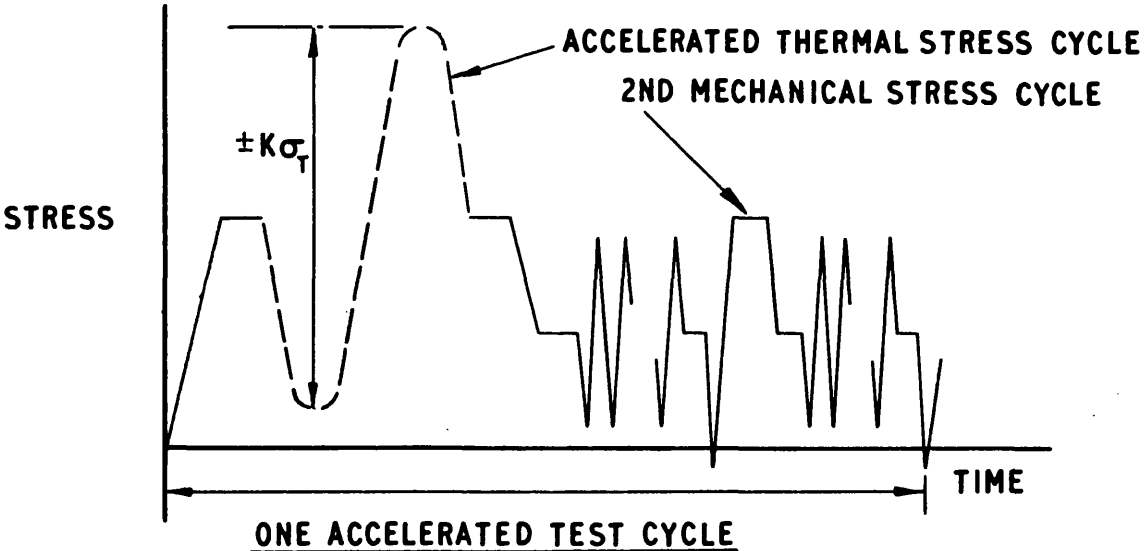

ONE ACCELERATED TEST CYCLE

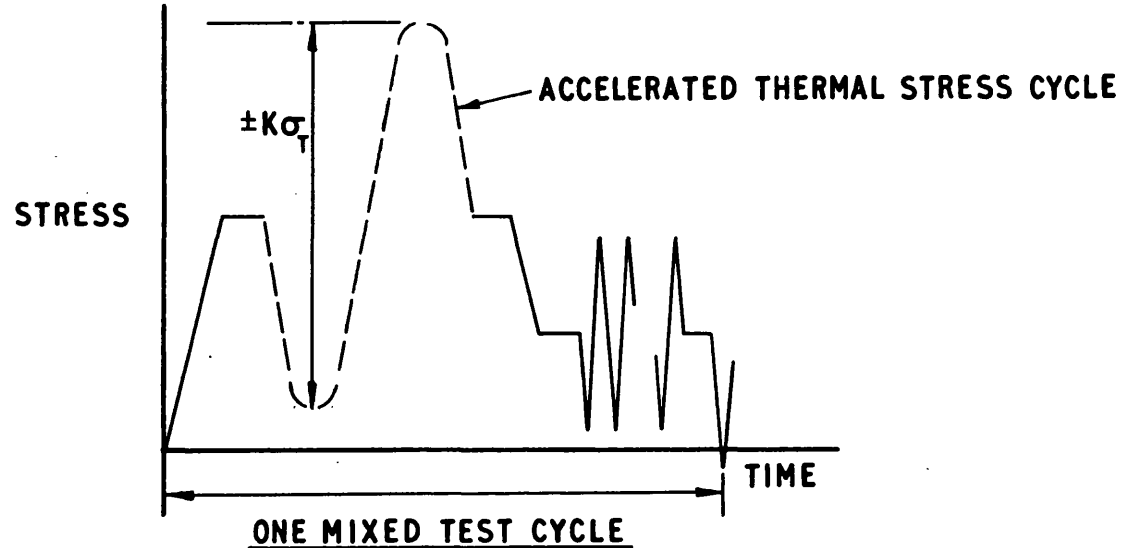

ONE MIXED TEST CYCLE

FIGURE 5.5

ANALYSIS OF THERMAL FATIGUE TESTS ON DEEP BOX SPECIMENS

TYPE OF TEST	TEMP. CYCLE	PREDICTED LIFE CYCLES	TEST LIFE CYCLES	PREDICTED THERMAL DAMAGE PER CYCLE	TEST THERMAL DAMAGE PER CYCLE	THERMAL DAMAGE RATIO $\frac{\text{TEST}}{\text{PREDICTION}}$
COLD MECHANICAL STRESS CYCLING	CONSTANT $20^{o}C$	33,450	28,150	-	-	-
BASIC THERMAL FATIGUE TEST	$110^{o}C$ TO $-12^{o}C$	13,170	7,427	$46.\times 10^{-6}$	99.15×10^{-6}	2.15
ACCELERATED THERMAL FATIGUE TEST	$135^{o}C$ TO $-30^{o}C$	4,880	3,841	145.6×10^{-6}	188.5×10^{-6}	1.30
MIXED THERMAL FATIGUE TEST	$135^{o}C$ TO $-30^{o}C$	5,700	3,752	145.6×10^{-6}	195.4×10^{-6}	1.34

NOTES:

1. Test lives are quoted in terms of the number of test cycles required to produce a crack in the riveted butt strap joint detectable by X-ray techniques.

2. Damage per cycle is defined as the reciprocal of fatigue life.

FIGURE 5.6

SUMMARY OF LIFE REDUCTION PHENOMENA

DAMAGING PHENOMENON	ORIGIN	MAGNITUDE	TREND WITH INCREASING TEMPERATURE
LIFE CORRECTION FACTOR	EXTRAPOLATION OF B.A.C. FATIGUE DATA	3 AT ZERO MEAN STRESS	–
EFFECT OF TEMP. ON RESIDUAL STRESS	BUCKLING TESTS AT 150°C	1.4 AT 150°C	PROBABLY INCREASING
EFFECT OF TEMP. CYCLING AT ZERO MEAN STRESS	AVRO RIG TEST RESULTS	1.55 AT 150°C RIVETED JOINTS; 2.4 AT 150°C FOR NOTCHED COUPONS	INCREASING
THERMAL STRESS CYCLING	DEEP BOX THERMAL FATIGUE TESTS	2.15 FOR $\Delta T = 122^{\circ}C$ 1.32 FOR $\Delta T = 165^{\circ}C$	DECREASING

FIGURE A1.1

EFFECT OF TEMPERATURE RANGE ON LIFE FOR Ti-75A TITANIUM. MEAN TEMPERATURE = 575°F.

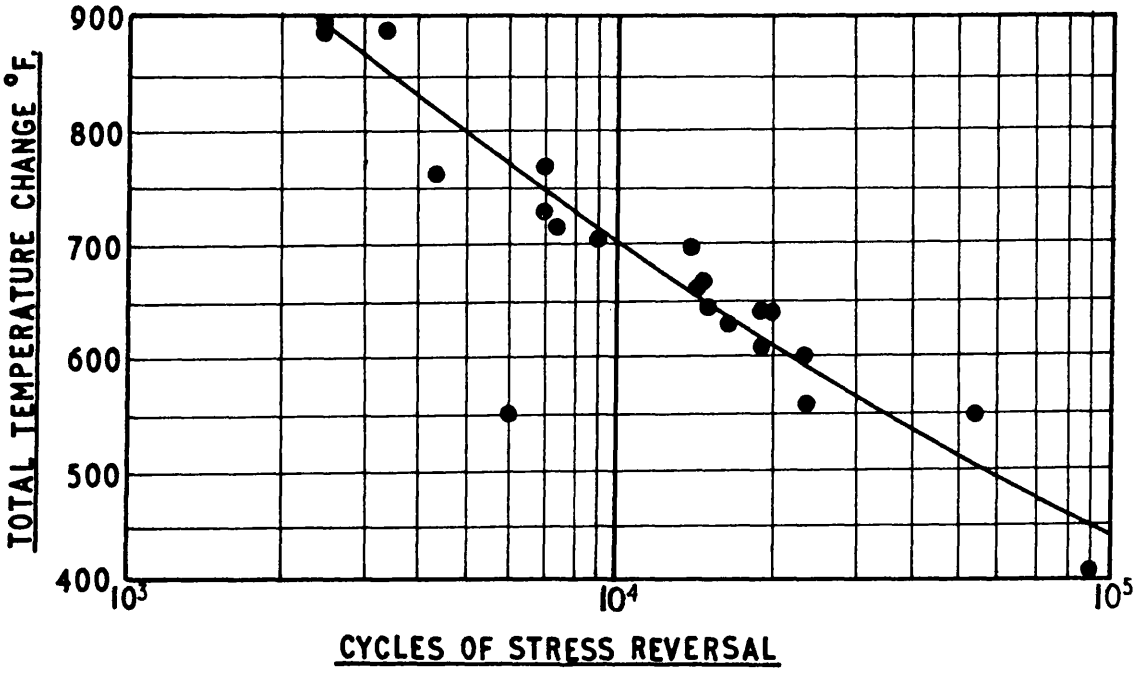

FIGURE A1.2

VARIATION OF LIFE WITH STRESS RANGE FOR Ti-75A TITANIUM. MEAN TEMPERATURE = 575°F.

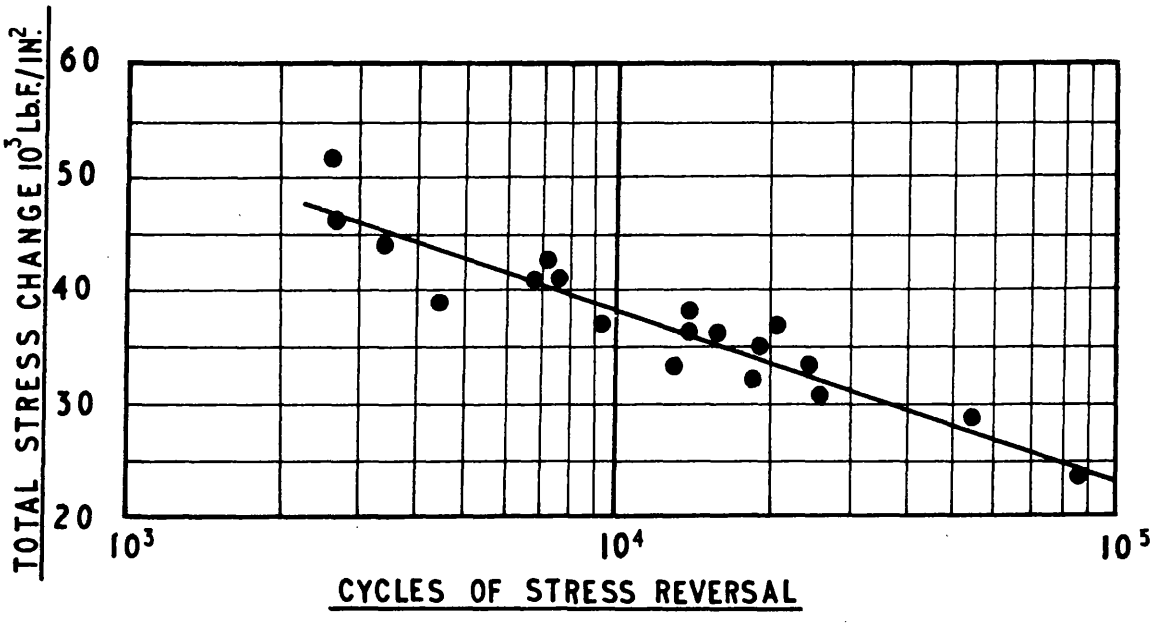

FIGURE A1.3

VARIATION OF LIFE WITH STRAIN RANGE FOR Ti-75A TITANIUM. MEAN TEMPERATURE = 575°F.

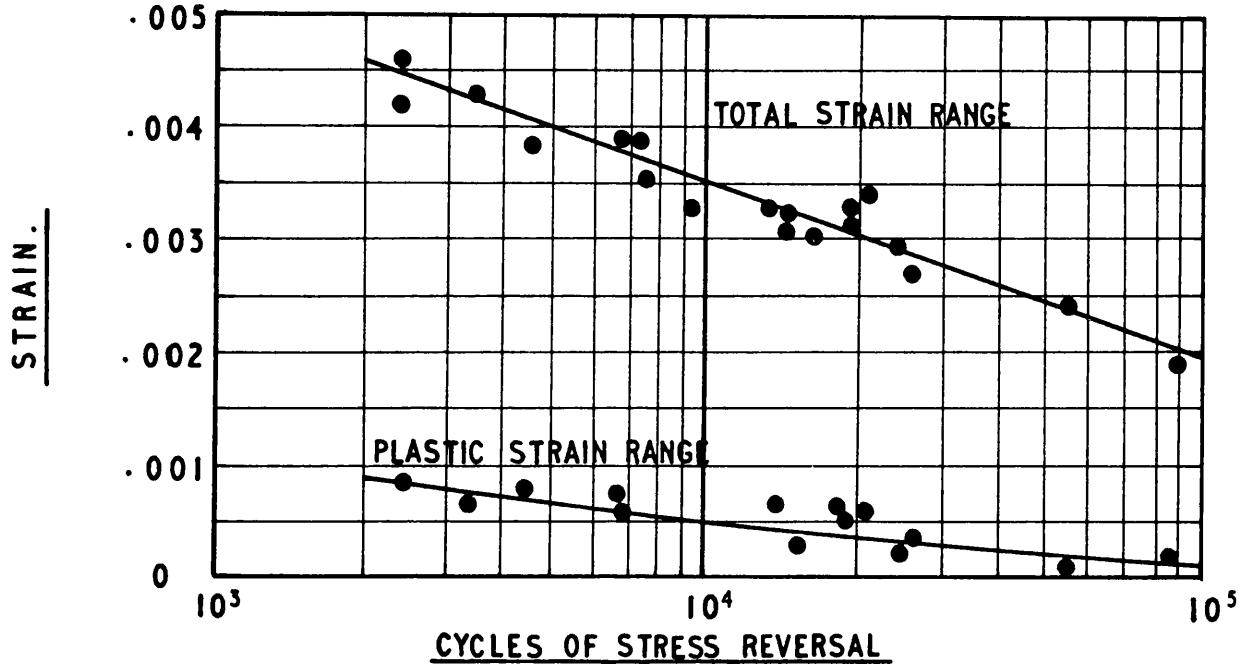

FIGURE A1.4

EFFECT OF TEMPERATURE RANGE ON LIFE FOR TYPE A NICKEL. MEAN TEMPERATURE = 525°F.

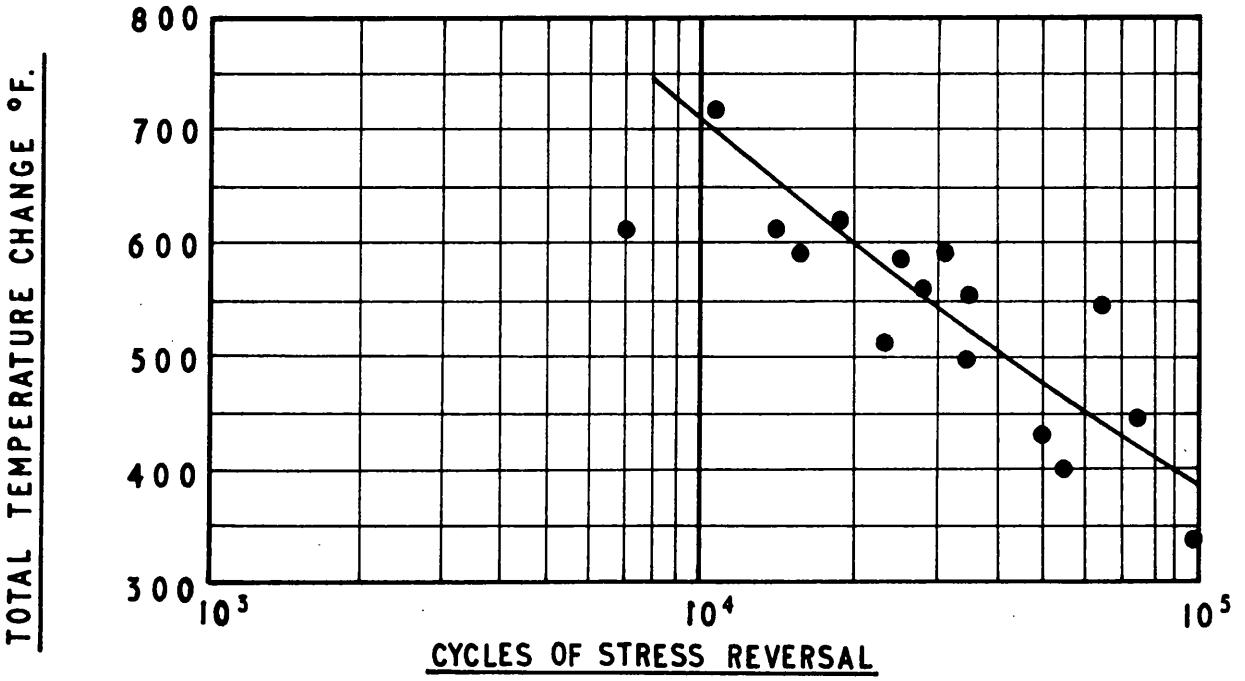

FIGURE A1.5

VARIATION OF LIFE WITH STRESS RANGE FOR TYPE A NICKEL. MEAN TEMPERATURE = 525°F.

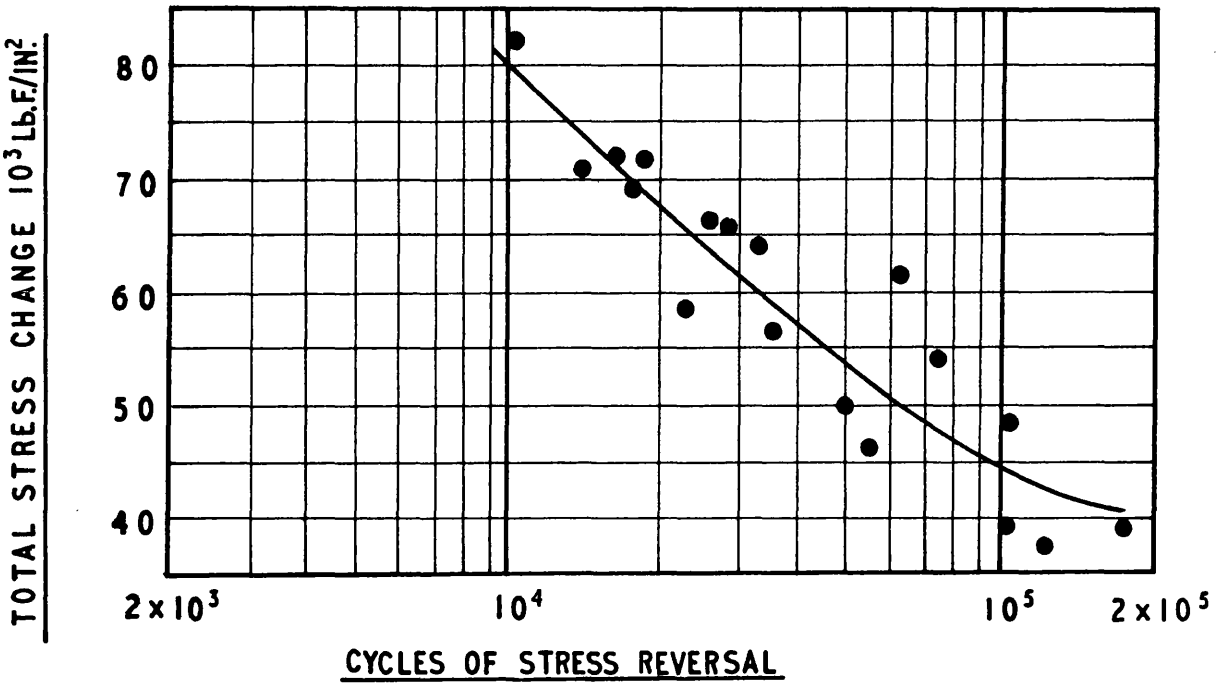

FIGURE A1.6

VARIATION OF LIFE WITH STRAIN RANGE FOR TYPE A NICKEL. MEAN TEMPERATURE = 525°F.

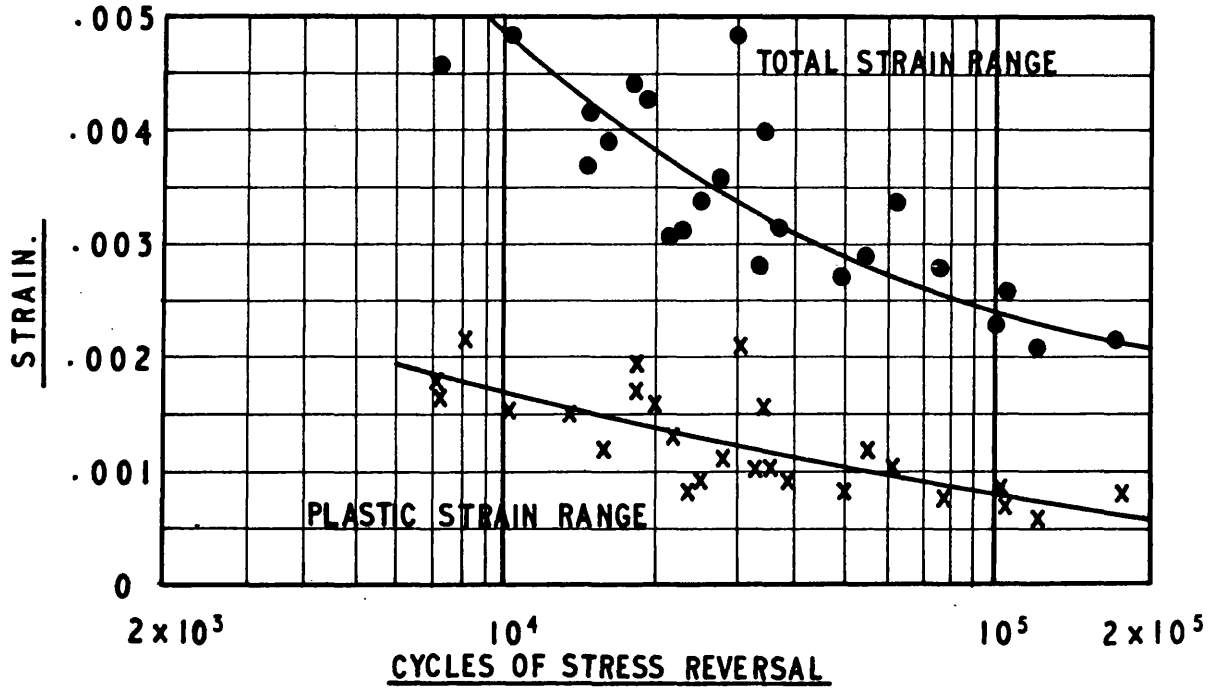

FIGURE A1.7

COMPARISON OF LOAD CYCLING AND THERMAL CYCLING ON Ti-75A TITANIUM. MEAN TEMP. 575°F. VARIATION OF LIFE WITH STRESS RANGE.

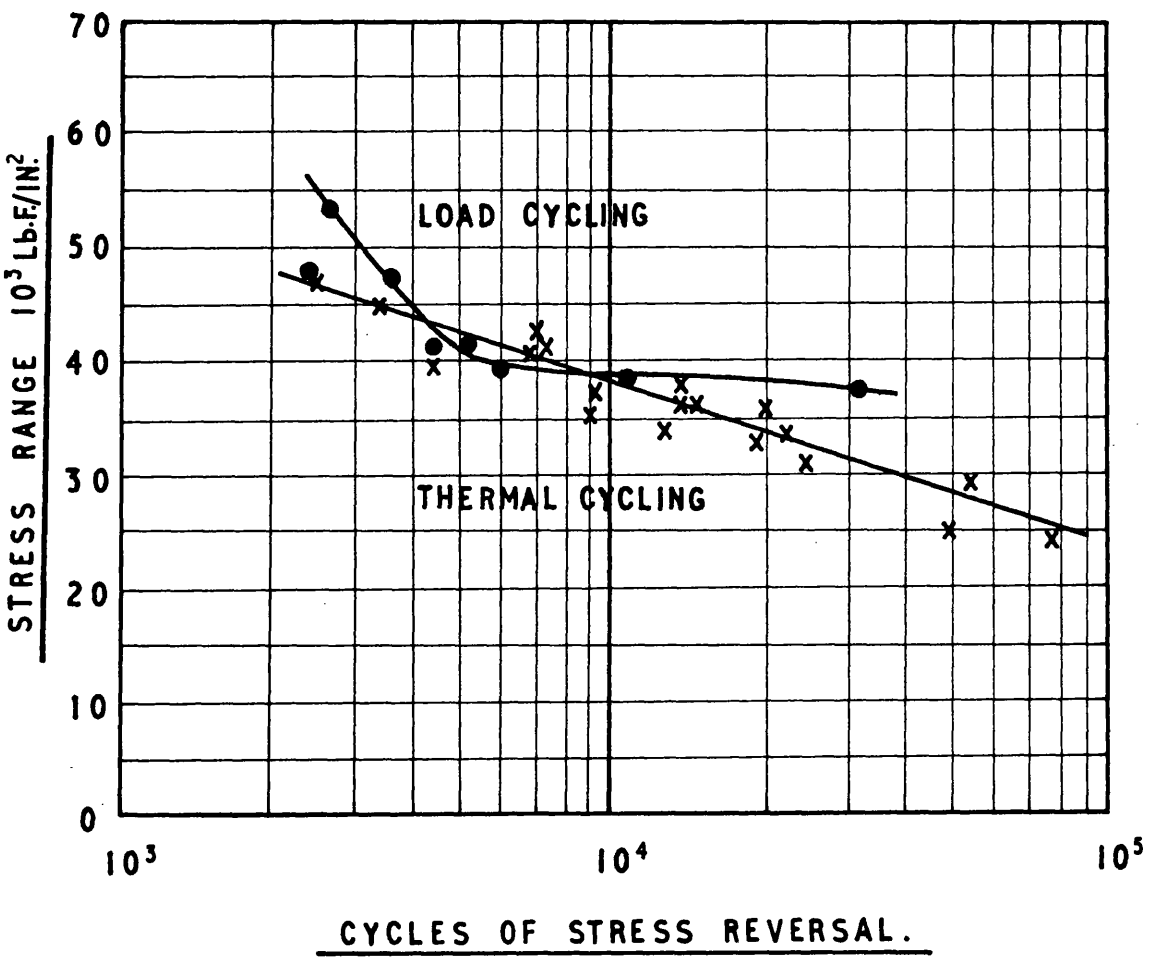

FIGURE A1.8

COMPARISON OF LOAD CYCLING AND THERMAL CYCLING ON Ti-75A TITANIUM. MEAN TEMP.= 575°F. VARIATION OF LIFE WITH PLASTIC STRAIN RANGE.

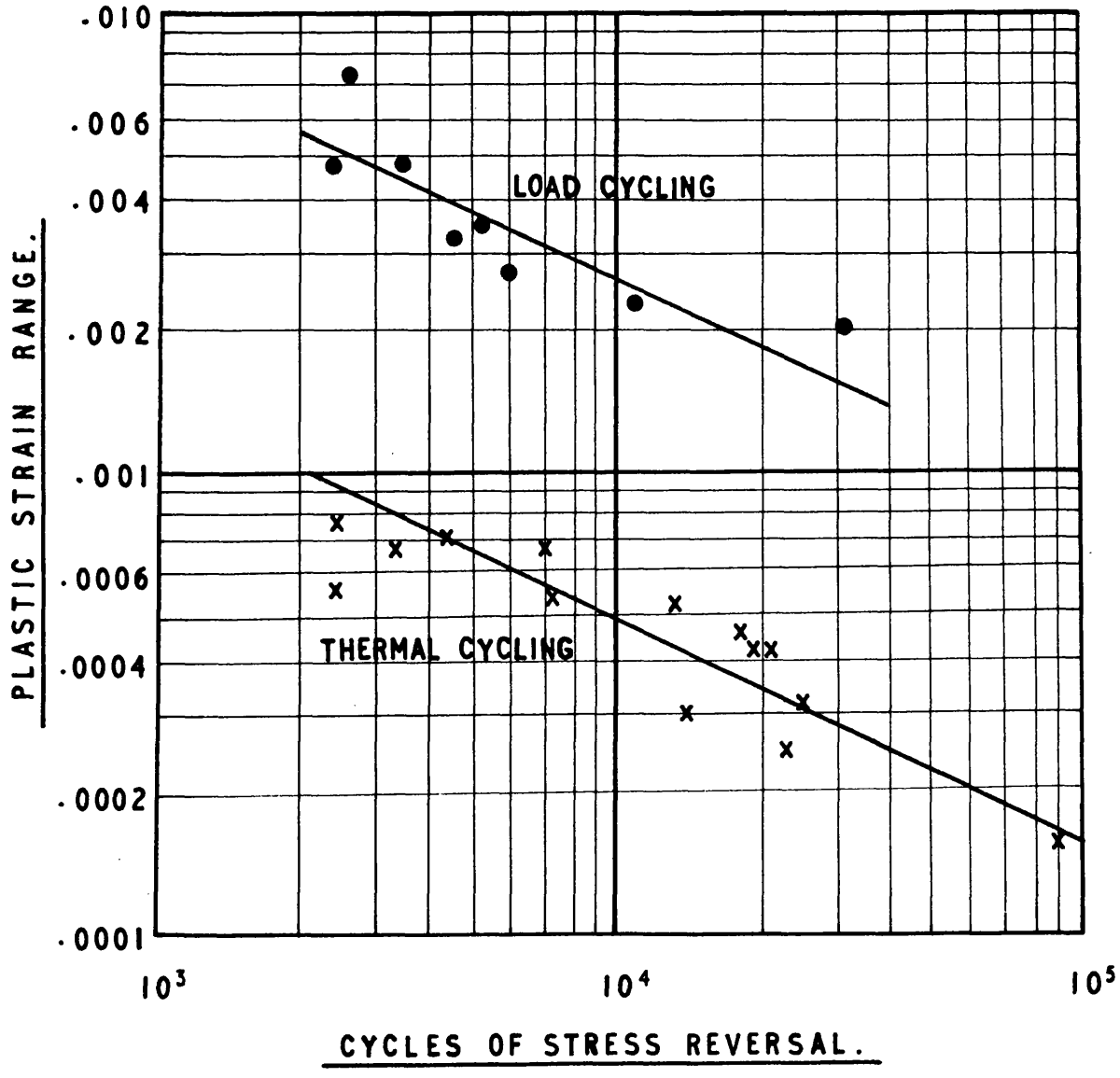

FIGURE A1.9

COMPARISON OF LOAD CYCLING AND THERMAL CYCLING ON TYPE A NICKEL. MEAN TEMP. = 525°F. VARIATION OF LIFE WITH STRESS RANGE.

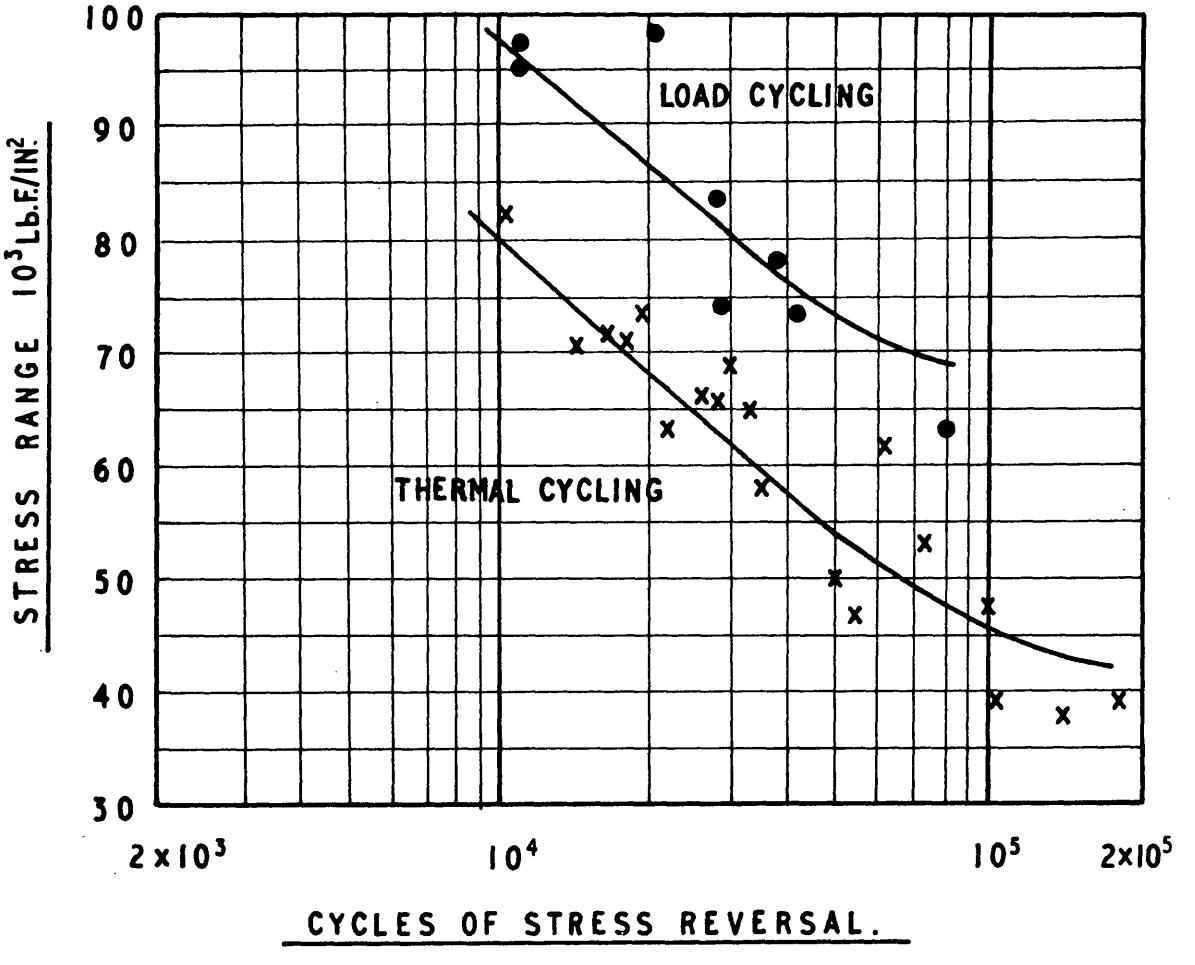

FIGURE A1.10

COMPARISON OF LOAD CYCLING AND THERMAL CYCLING ON TYPE A NICKEL. MEAN TEMP.=525°F. VARIATION OF LIFE WITH PLASTIC STRAIN RANGE.

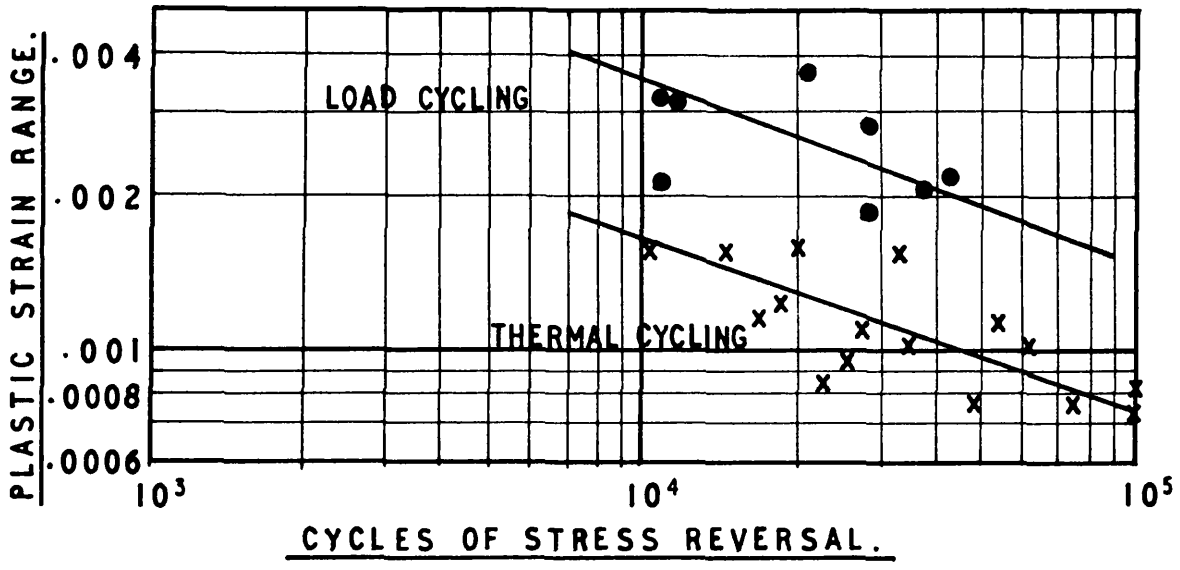

FIGURE A1.11

VARIATION OF MEAN STRAIN WITH NUMBER OF TEMPERATURE CYCLES FOR Ti-75A TITANIUM.

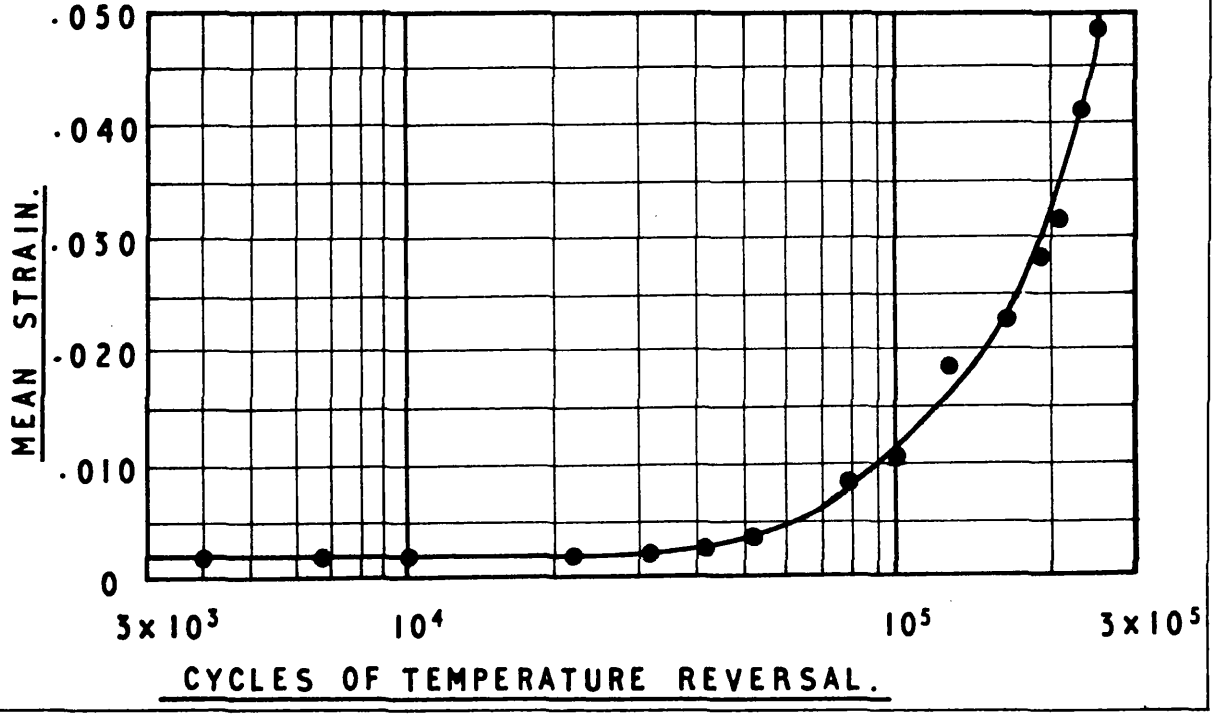

FIGURE A1.12

VARIATION OF MEAN STRAIN WITH NUMER OF TEMPERATURE CYCLES FOR TYPE A NICKEL.

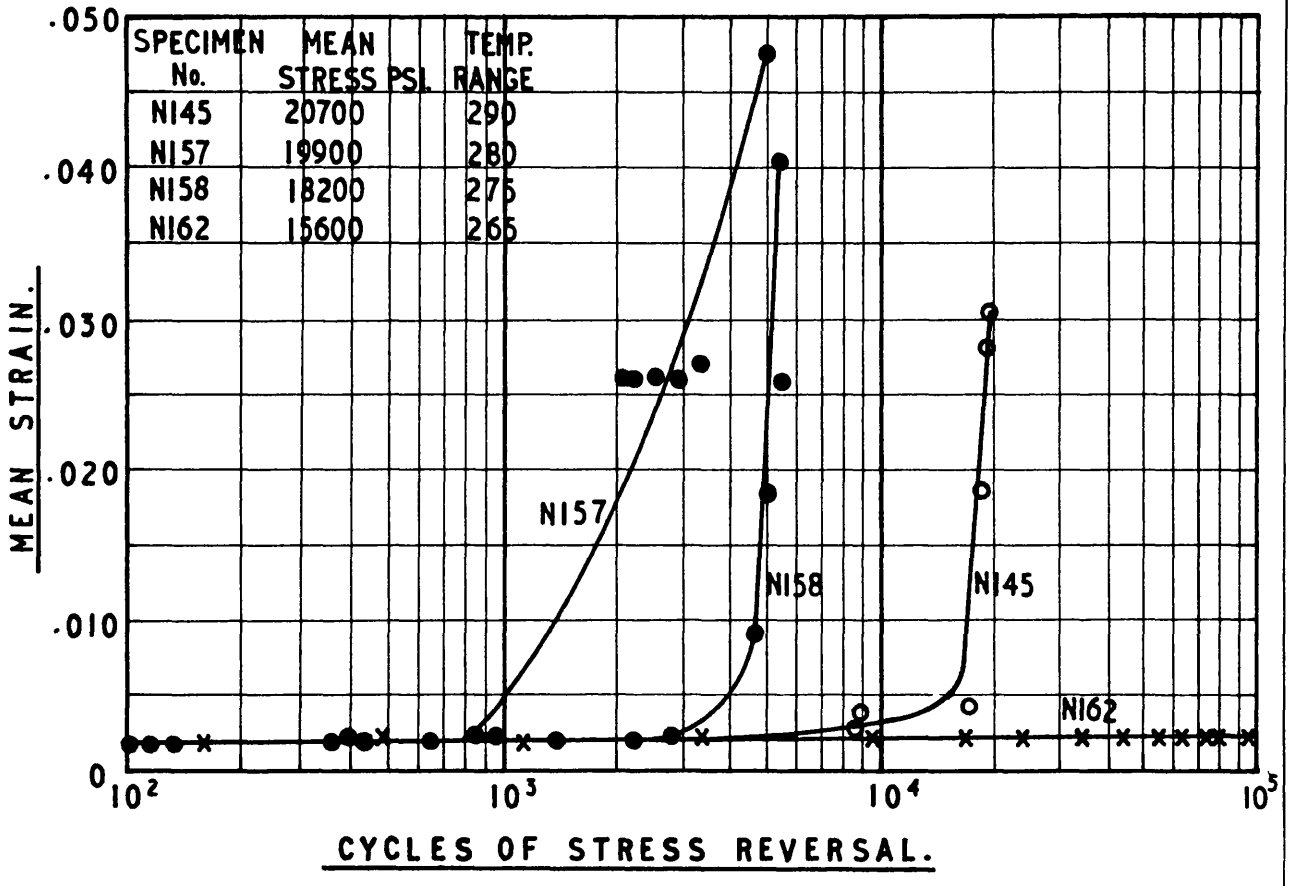

FIGURE A1.13

EFFECT OF GRAIN SIZE AND CONSTRAINT ON LIFE OF TYPE A NICKEL.

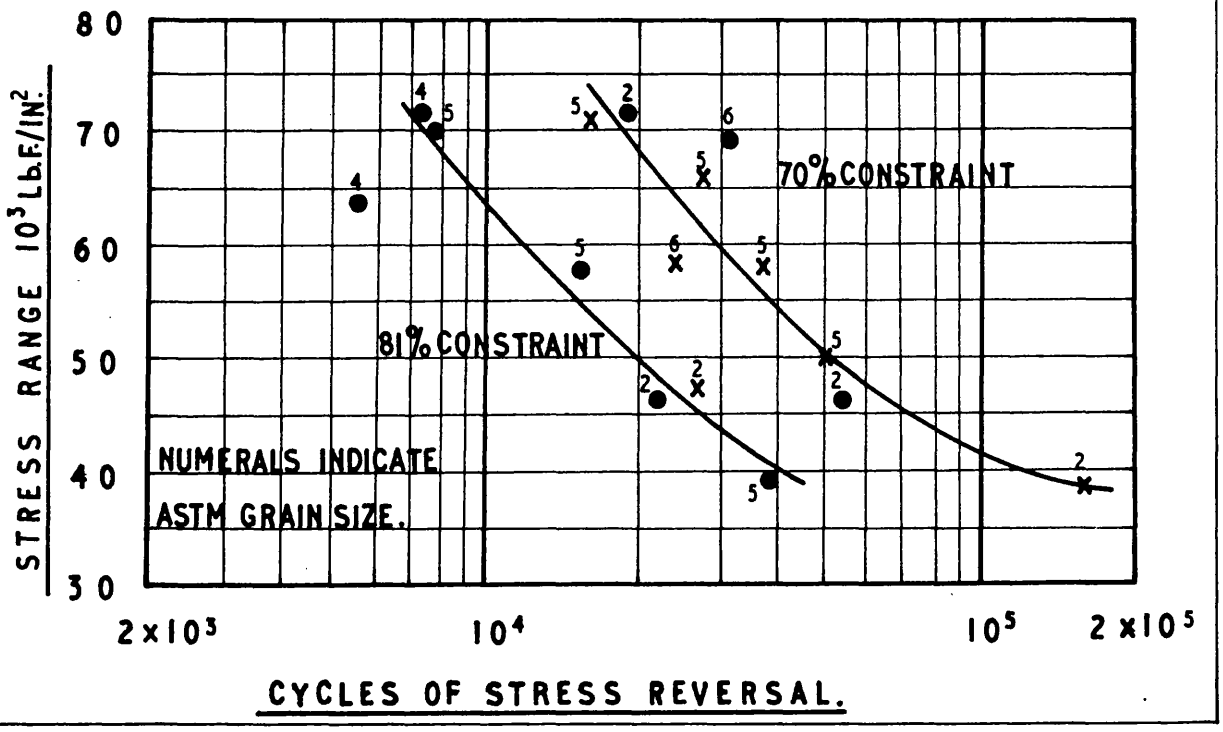

FIGURE A1.14

COMPARISON OF LOAD CYCLING AND THERMAL CYCLING: EFFECT OF TOTAL PLASTIC STRAIN ON LIFE OF Ti-75A TITANIUM.

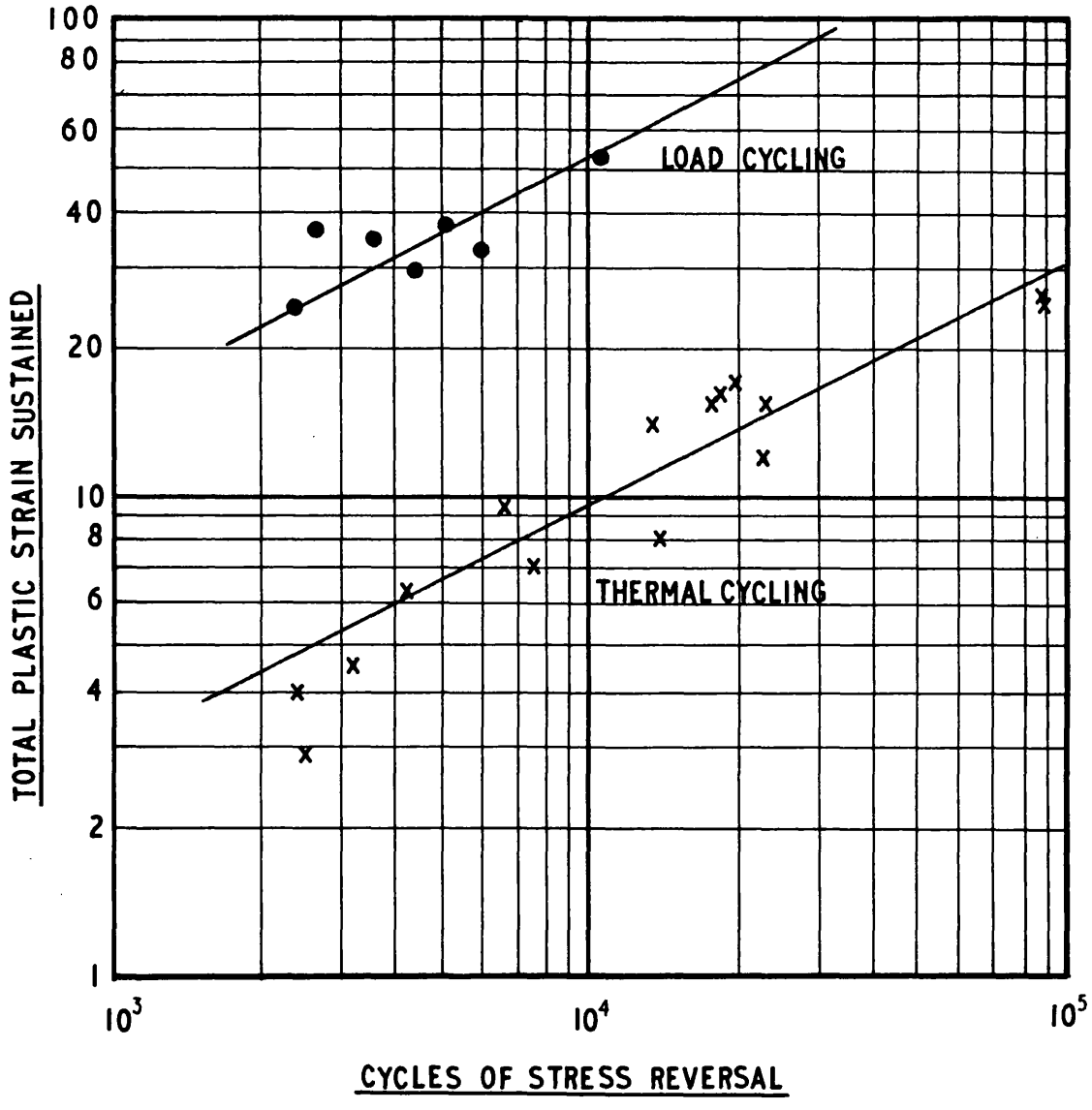

FIGURE A1.15

COMPARISON OF LOAD CYCLING AND THERMAL CYCLING: EFFECT OF TOTAL PLASTIC STRAIN ON LIFE OF TYPE A NICKEL.

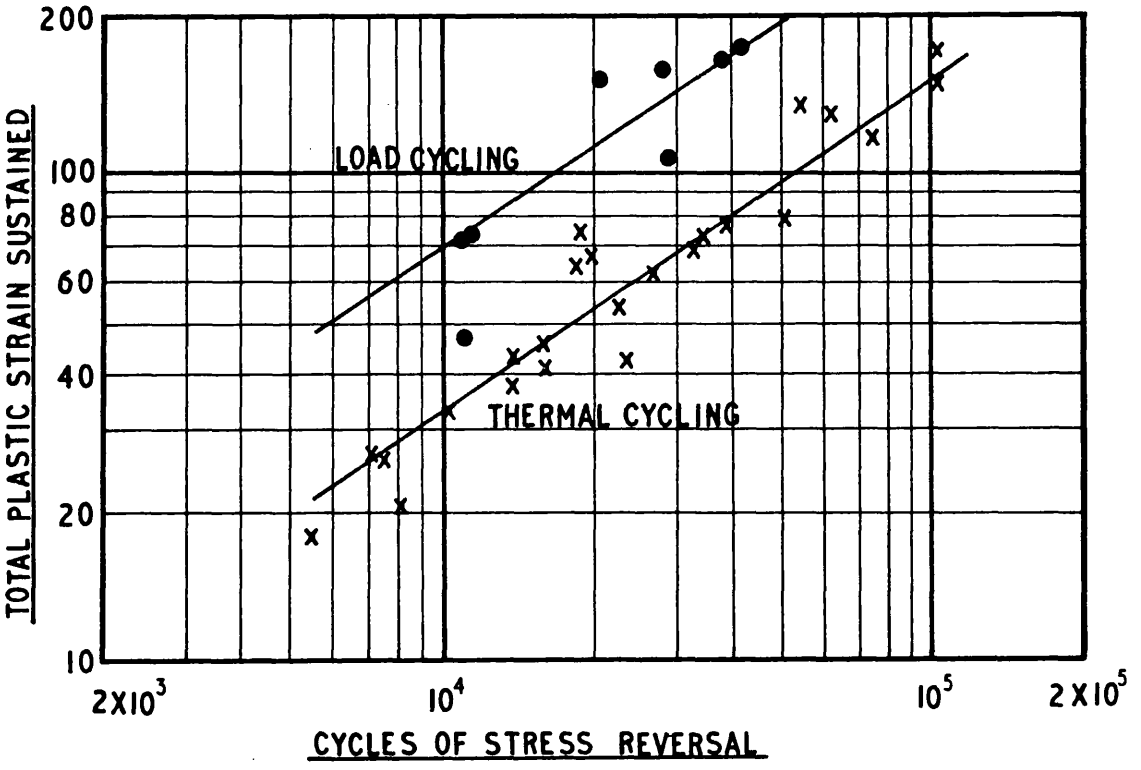

FIGURE A1.16

COMPARISON OF PREDICTED AND ACTUAL PLASTIC STRAIN FOR STATIC TENSILE TEST.

TYPE OF TEST	MATERIAL	PLASTIC STRAIN FOR $N=\frac{1}{4}$	TENSION TEST RESULTS		
			Total Strain in 2.0"	Area Reduction	Mean Temp. ^{o} F.
Load Cycling	TI-75A	0.45	0.40	0.68	575
Thermal Cycling	TI-75A	0.11	0.40	0.68	575
Load Cycling	'A' Ni	0.12	-	0.71	525
Thermal Cycling	'A' Ni	0.07	-	0.71	525

FIGURE A1.17

COMPARISON OF LOAD CYCLING AND THERMAL CYCLING: EFFECT OF PLASTIC STRAIN RANGE ON LIFE OF AISI TYPE 347 STAINLESS STEEL.

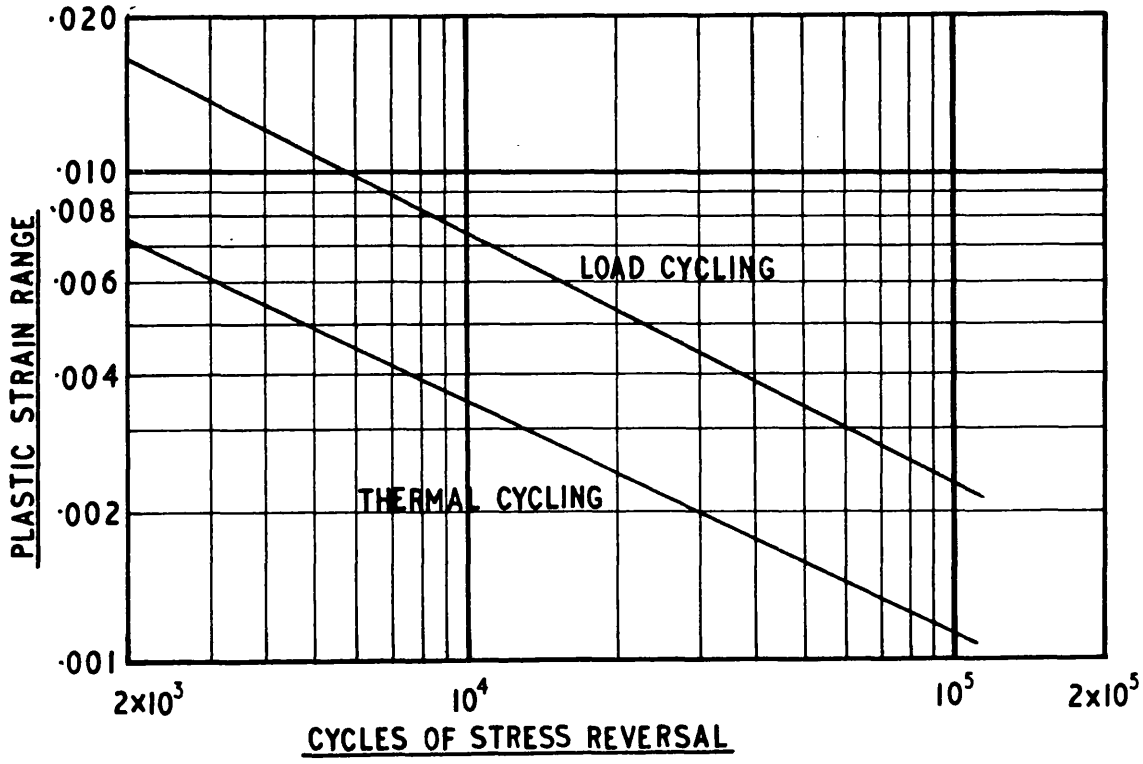

FIGURE A1.18

COMPARISON OF VARIOUS MATERIALS UNDER LOAD CYCLING: EFFECT OF PLASTIC STRAIN RANGE ON LIFE.

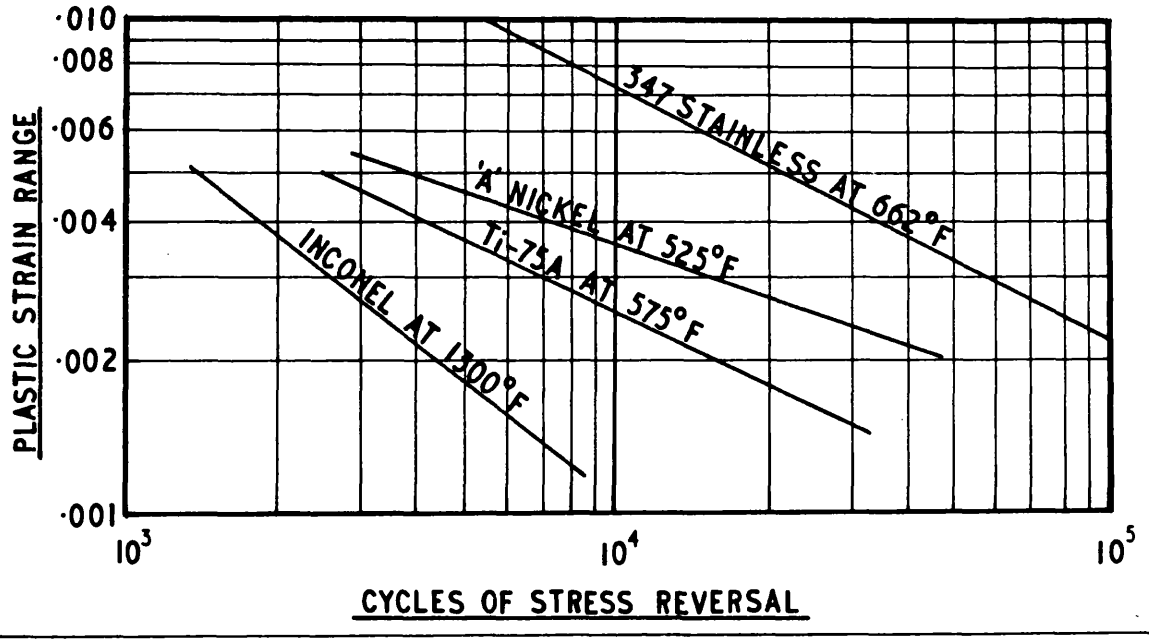

FIGURE A1.19

COMPARISON OF LOAD CYCLING AND THERMAL CYCLING: VALUES OF MATERIAL CONSTANTS K AND C IN COFFIN'S EMPIRICAL EXPRESSION

$$N^{K}\Delta\varepsilon_{p} = C$$

FOR VARIOUS MATERIALS.

MATERIAL	HEAT TREATMENT	TYPE OF TEST	K	C	TEMP. ^{O}F.
INCONEL	Annealed for 2 hrs. at 2050^{O}F.	Load cycling	0.82	1.91	1300
INCONEL	As received small grain	Load cycling	0.81	1.27	1300
347 STAINLESS STEEL	Extruded bar. Annealed for 30 mins. at 1922^{O}F ASTM 7.	Load cycling	0.52	0.87	662
TI-75A	Annealed at 1200^{O}F ASTM 6.	Load cycling	0.48	0.23	575
'A' NICKEL	Annealed at 1300^{O}F ASTM 5.	Load cycling	0.35	0.087	525
INCONEL	As received small grain	Thermal cycling	0.72	1.14	1300
347 STAINLESS STEEL	Annealed. Red at 2010^{O}F in dry hydrogen atmosphere	Thermal cycling	0.50	0.36	662
Ti-75A	Annealed rod at 1200^{O}F ASTM 6.	Thermal cycling	0.51	0.052	575
'A' NICKEL	Annealed at 1300^{O}F ASTM 5.	Thermal cycling	0.35	0.043	525

FIGURE A1.20

EFFECT OF PRIOR COLD WORK ON LIFE OF AISI TYPE 347 STAINLESS STEEL UNDER THERMAL CYCLING.

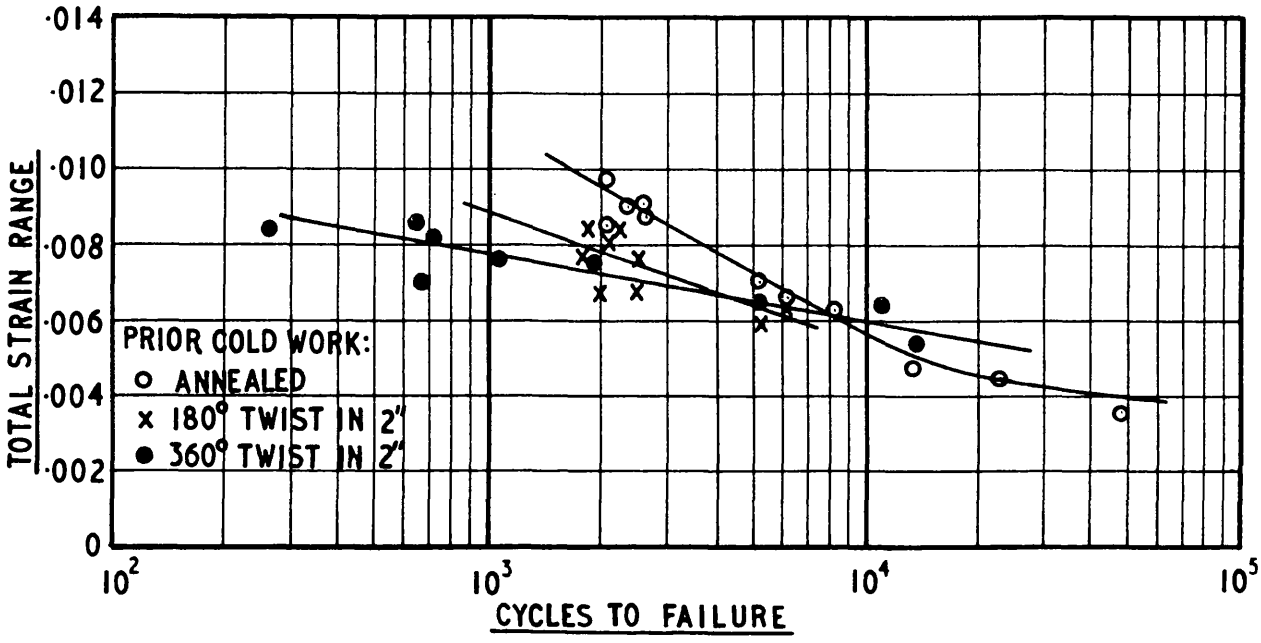

FIGURE A1.21

EFFECT OF PRIOR COLD WORK ON LIFE OF AISI TYPE 347 STAINLESS STEEL UNDER LOAD CYCLING.

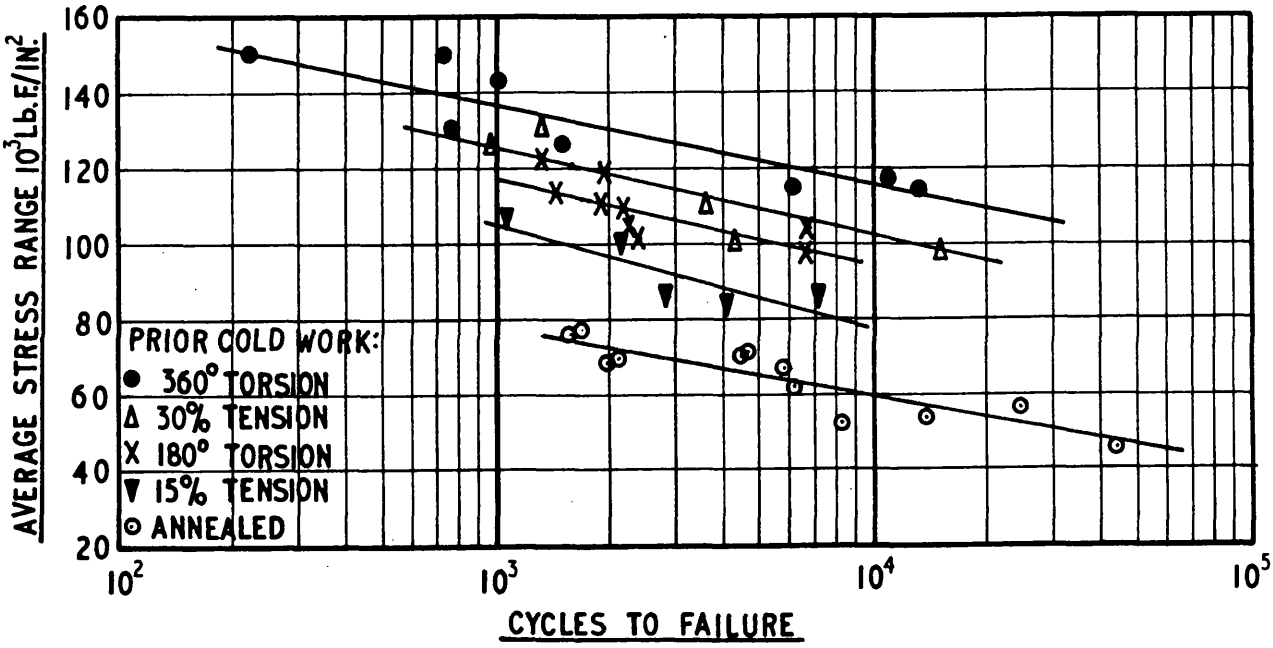

FIGURE A1.22

VARIATION OF STRESS RANGE WITH STRAIN RANGE AFTER 1000 TEMPERATURE CYCLES. AISI TYPE 347 STAINLESS STEEL.

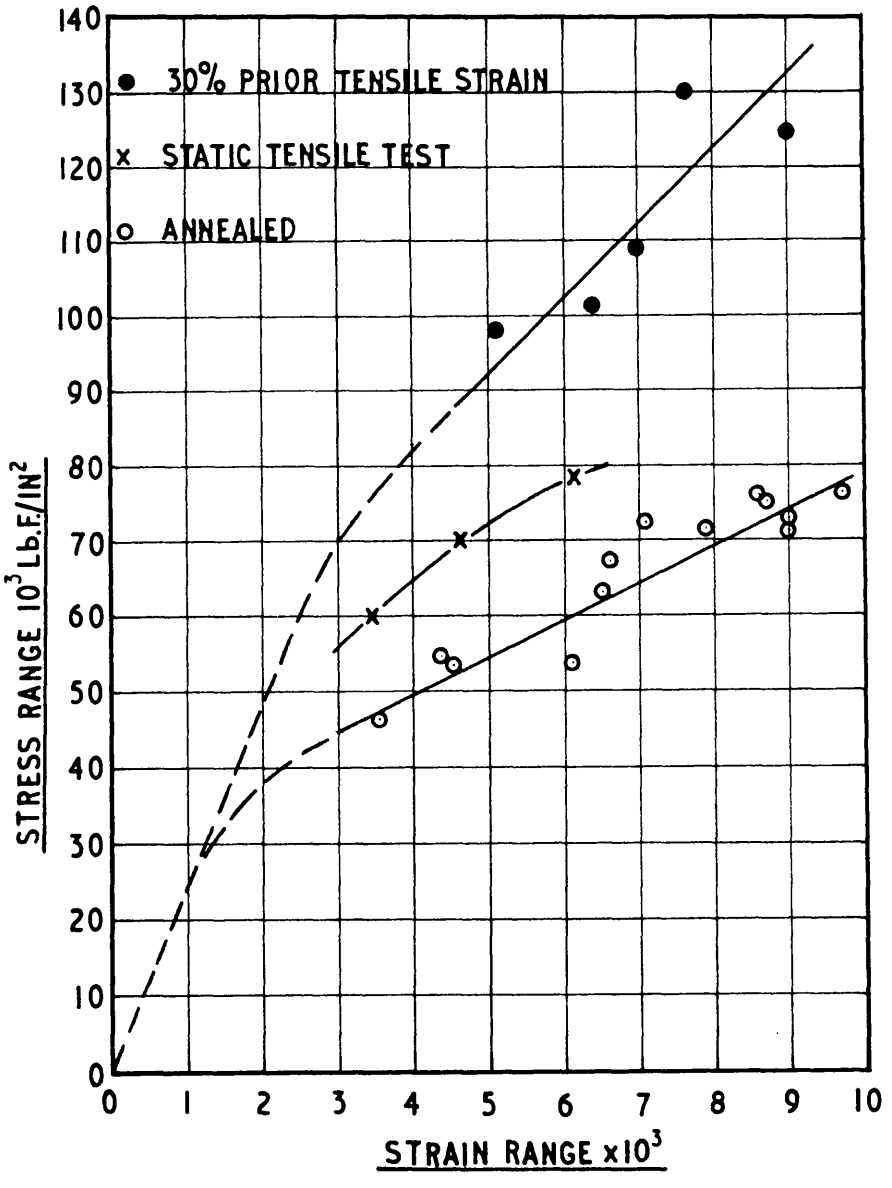

FIGURE A1.23

VALUES OF K AND C IN THE EXPRESSION $N^K \Delta\varepsilon_p = C$ FOR SEVERAL MATERIALS AND TEST CONDITIONS

MATERIAL	TEMP.	K	C	TEST CONDITIONS
Annealed AISI type 347 stainless steel	Cycled	0.50	0.36	Constrained thermal cycling
Cold worked AISI type cycled 347 stainless steel	Cycled	0.54	0.10	Constrained thermal cycling
Annealed AISI type 347 stainless steel	350°C	0.43	0.28	Constant temp. strain cycling
24S-T aluminium	20°C	0.50	0.27	Constant temp. strain cycling

FIGURE A1.24

THERMAL CYCLING OF TYPE 347 STAINLESS STEEL WITH CONSTANT TOTAL STRAIN

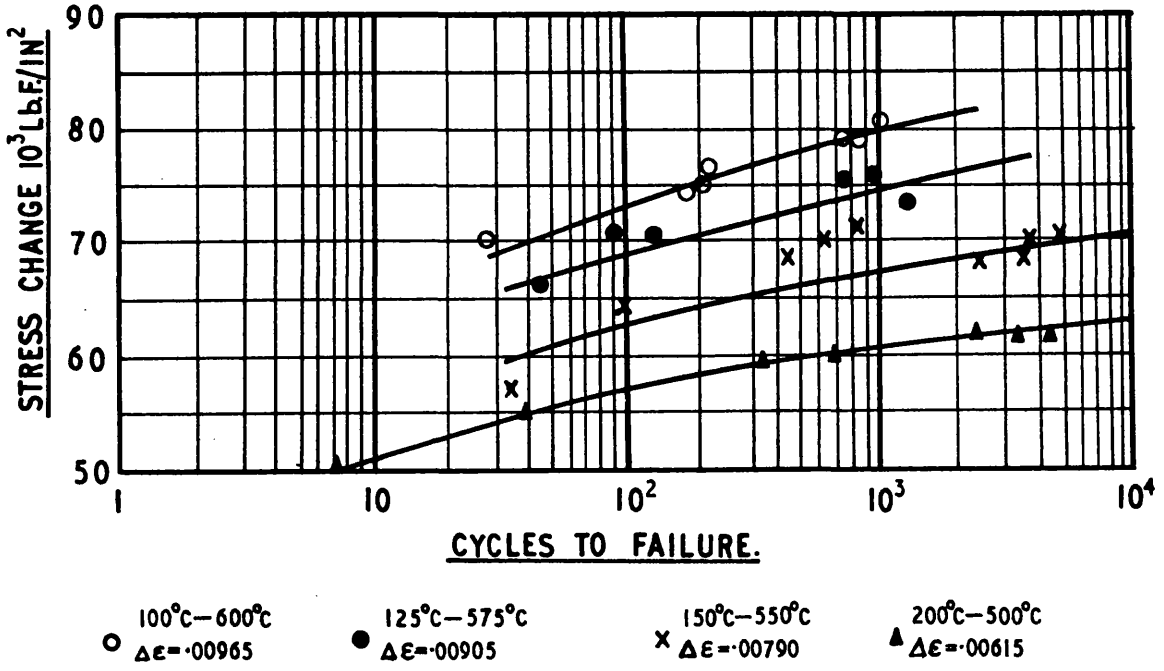

FIGURE A1.25

EFFECT OF CYCLIC TEMPERATURE AMPLITUDE ON THE FATIGUE LIFE OF TYPE 347 STAINLESS STEEL

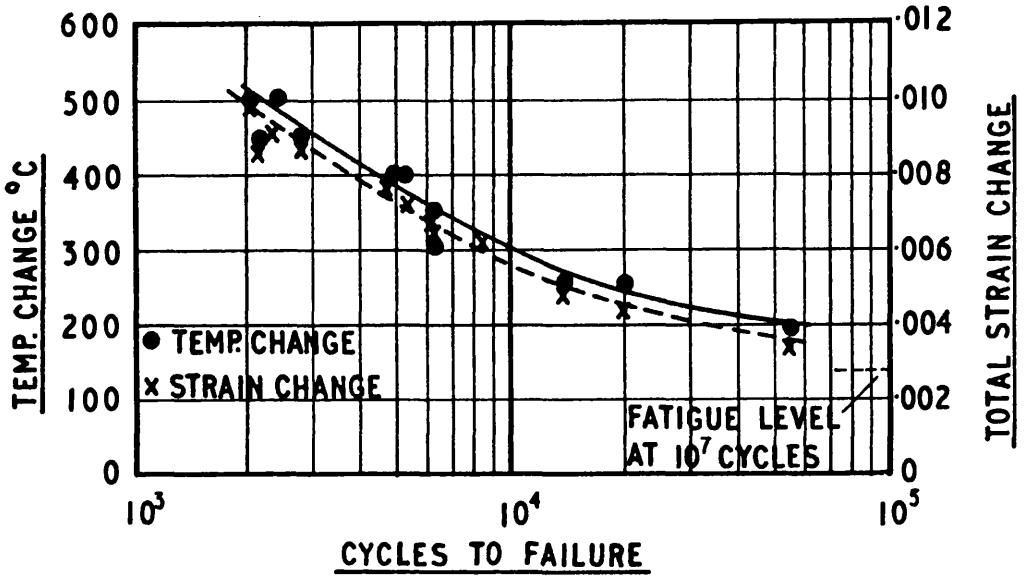

MEAN TEMPERATURE = 350°C

FIGURE A1.26

EFFECT OF A STRESS CONCENTRATION ON THE FATIGUE LIFE OF TYPE 347 STAINLESS STEEL UNDER THERMAL CYCLING CONDITIONS

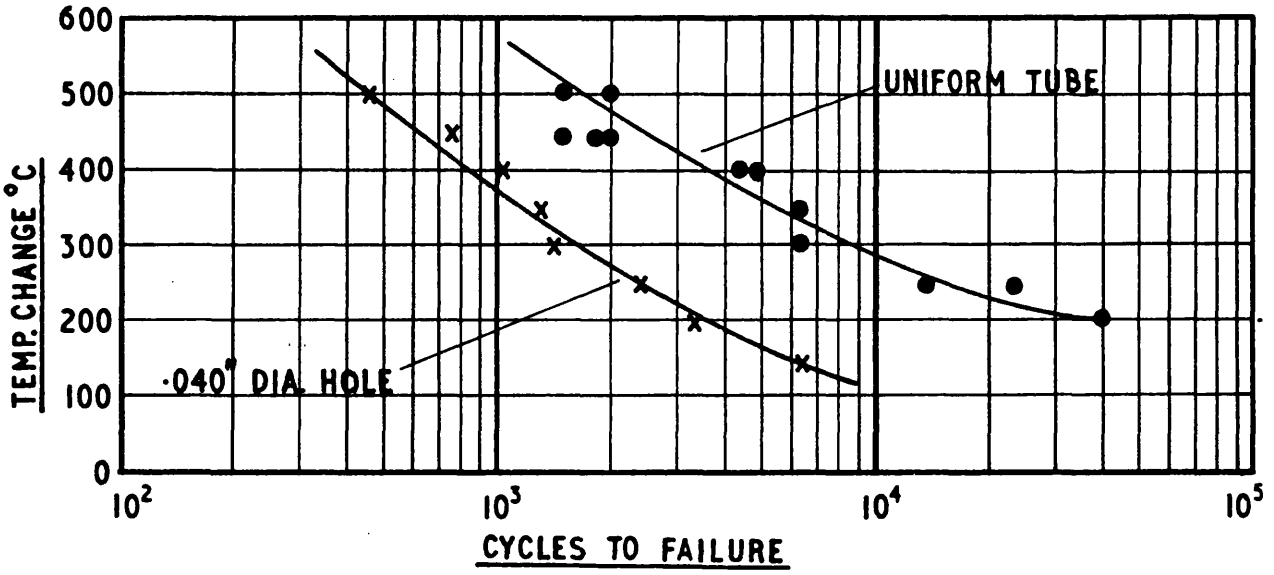

MEAN TEMPERATURE = 350°C

FIGURE A1.27

EFFECT OF ANNEALING ON THE FATIGUE LIFE OF TYPE 347 STAINLESS STEEL UNDER THERMAL CYCLING CONDITIONS

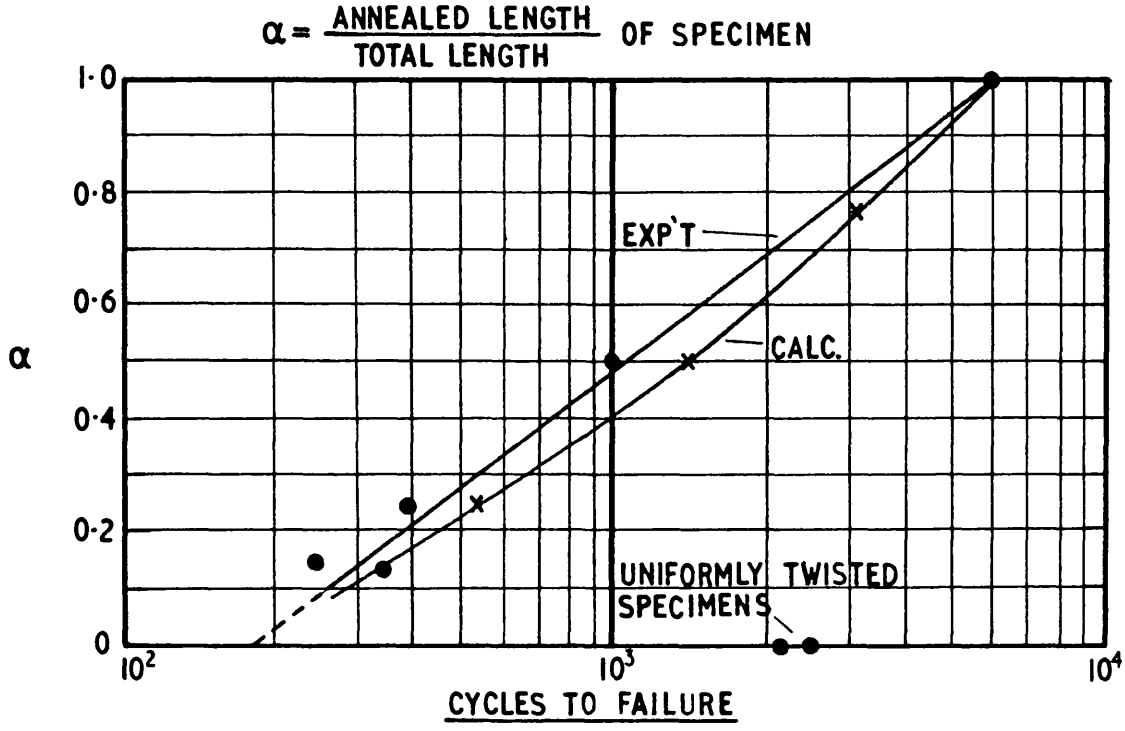

FIGURE A1.28

COMPARISON OF THERMAL CYCLING AND STRAIN CYCLING OF TYPE 347 STAINLESS STEEL

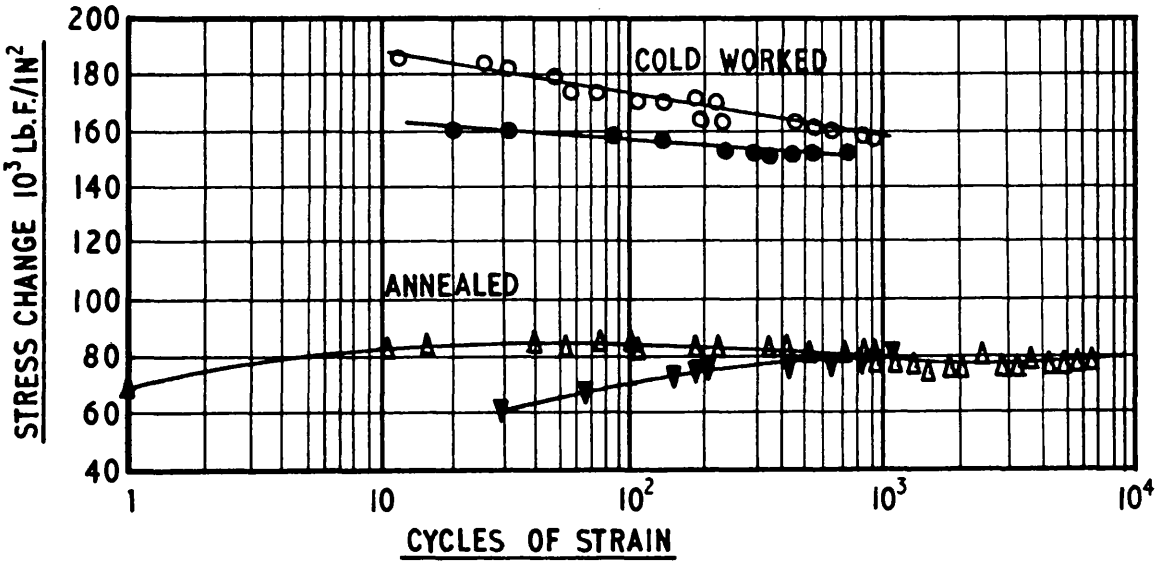

Δε = ·010

OPEN POINTS: STRAIN CYCLED AT 350°C

CLOSED POINTS: THERMALLY CYCLED 100°C - 600°C

FIGURE AI.29

COMPARISON OF THERMAL CYCLING AND STRAIN CYCLING OF TYPE 347 STAINLESS STEEL

CONDITION	CYCLES TO FAILURE			
	THERMAL CYCLING 100-600°C		STRAIN CYCLING 350°C	
Annealed	1760	2260	5820	5950
Cold worked	650	880	2130	

FIGURE AI.30

STRAIN CYCLING DATA FOR TYPE 347 STAINLESS STEEL

STRAIN CHANGE	AVERAGE STRESS CHANGE P.S.I.	PLASTIC STRAIN CHANGE	CYCLES TO FAILURE
0.01	80,000	.0068	5820 5950
0.02	109,000	.0156	1210
0.03	144,000	.0242	232

FIGURE A1.31

COMPARISON OF THERMAL CYCLING AND STRAIN CYCLING OF TYPE 347 STAINLESS STEEL